The Pennsylvania State University

The Graduate School

College of Earth and Mineral Science

CHEMICAL AND PHYSICAL WEATHERING IN REGOLITH: AN INVESTIGATION OF THREE DIFFERENT FE-RICH SITES OF VARYING CLIMATE AND LITHOLOGY

A Dissertation in

Geosciences and Biogeochemistry

by

Tiffany A. Yesavage

Submitted in Partial Fulfillment
of the Requirements
for the Degree of

Doctor of Philosophy

May 2014

The dissertation of Tiffany A. Yesavage was reviewed and approved* by the following:

Susan L. Brantley
Distinguished Professor of Geosciences
Dissertation Advisor
Chair of Committee

Matthew Fantle
Assistant Professor of Geosciences

Peter Heaney
Professor of Geosciences

Mary Ann Bruns
Associate Professor of Soil Science/Microbial Ecology

Chris Marone
Professor of Geosciences and Associate Head Graduate Programs

*Signatures are on file in the Graduate School.

Abstract

The goal of this thesis is to understand chemical weathering in regolith at three very different sites that vary with respect to climate and lithology. The first study involves an analysis of chemical weathering and Fe isotope fractionation in soils from a shale-derived catchment in central Pennsylvania. Our investigation of this site is unique in the sense that we sampled regolith not only as a function of depth, but also from along a transect from the ridge to the valley floor of the watershed. The oxidation of Fe(II) occurs in a gradual manner in the augerable soil at this site, with no abrupt oxidation fronts with depth noted across the soil profile. Ultimately, we observed that both bulk and amorphous Fe become isotopically lighter in moving from the younger, shallow ridge top regolith into the older, deeper valley floor. One explanation for this trend involves dissolution processes (i.e., ligand-promoted dissolution and dissimilatory Fe reduction) that preferentially release isotopically light Fe during weathering. As weathering proceeds, we suggest that this isotopically light Fe travels along preferential zones of flow and is then partially precipitated, accumulating in the older valley floor. A second explanation for these trends involves the inference that the accumulation preferentially retains isotopically light Fe oxides. Although dissolved Fe in most streams is thought to be isotopically light, this second mechanism requires the loss of heavy Fe from the Shale Hills watershed.

In addition to the shale-derived watershed, we also investigated regolith weathering in two very different profiles developed on basaltic material. The first of these profiles is located at the Sverrefjell volcano, a Mars analog site in the Arctic Circle characterized by a cold, dry climate (described in Chapter 3). Despite the limited amount of time for weathering, very high concentrations of amorphous Al, Fe and Si were observed. Analysis of the clay-sized fraction from this site documents allophane as the predominant secondary phase, while abundant silica coatings of up to 100 μm on rock surfaces may help to explain anomalously low extracted amorphous Al/Si ratios. Based on batch experiments designed to study colloidal dispersion, elements such as Na, Mg and Ca are lost from the regolith in the dissolved form, while Al, Fe and Ti are mobilized as colloids in the 260-415 nm size range. In contrast, Si is mobilized simultaneously both in the dissolved and colloidal fractions. Findings from these colloidal dispersion experiments help to explain the relative loss of specific elements from regolith (Na, K >Ca, Mg >Si >Fe, Al, Ti) as well as the presence of silica coatings on weathered rocks.

In the final regolith profile studied (Chapter 4), analysis of pore-water samples in weathering diabase regolith allows for a further understanding of how various constituents (pH, DOC, anion and cation concentrations) change as a function of depth and season. In contrast to the other two sites, Fe(II) has been oxidized in close proximity to the bedrock/regolith interface of the Pennsylvania diabase profile. Elevated amorphous Fe concentrations near the bedrock/regolith interface are attributed to the release of Fe(II) and precipitation of amorphous Fe in a zone inferred to have originally been a set of rindlets created during spheroidal weathering. While bulk Fe isotope signatures within the diabase regolith did not vary significantly with depth, amorphous Fe values are isotopically lighter near the bedrock/regolith interface. Isotopically light Fe at depth is explained as resulting from kinetic effects during the rapid precipitation of Fe oxides from Fe(III) in solution. Similar observations at sites in Virginia and Puerto Rico suggest that spheroidal weathering results in unique chemical and Fe isotopic trends.

TABLE OF CONTENTS

LIST OF FIGURES

LIST OF TABLES

ACKNOWLEDGEMENTS

I would like to thank Sue for lots of great help and all of my funding sources. I am glad that I got to use the best equipment to collect my data. Laura helped me a lot to learn many of these techniques. Finally, I want to thank Grandma and Grandpa, Melanie, Moab and Tina.

Chapter 1: Introduction

Although the C horizon has often been ignored in many studies pertaining to soil weathering (Richter and Markewitz, 1995), a growing body of evidence indicates that important mineralogical, chemical and biological reactions occur deep within the regolith profile (e.g., Eswaran and Bin, 1978; Gilkes and Suddhiprakan, 1979; Calvert et al., 1980; Rice et al., 1985; Graham et al., 1989; Buol and Weed, 1991; White et al., 1998; Buss et al., 2005; Jin et al., 2011; Minyard et al., 2011; Minyard et al., 2012; Bazilevskaya et al., 2013). Of particular interest are reactions related to Fe cycling (including solubilization, oxidation, precipitation, colloidal transport and Fe isotope fractionation) in deeper horizons of the regolith profile (Buss et al., 2005; Fletcher et al., 2006; Buss et al., 2010). The goal of this thesis is to apply several techniques to better understand chemical weathering with depth in soils and regolith at three very different sites that vary with respect to climate and lithology. In addition to more traditional methods such as bulk chemical soil analysis, particle size analysis and sequential extractions, several other less conventional approaches were used. These less traditional approaches include the following: a) the analysis of the stable isotope values of Fe in regolith (for both bulk and amorphous Fe), b) batch experiments performed to better understand the size and chemistry of dispersed colloidal material from regolith under various redox and pH conditions, and c) the analysis of pore-water concentrations within soil profiles for the purpose of understanding changes in chemistry with depth and season.

Chapter 2: Fe cycling in the Shale Hills Critical Zone Observatory, Pennsylvania: An analysis of biogeochemical weathering and Fe isotope fractionation:

As the fourth most abundant element in the Earth's crust, iron (Fe) makes up an average of 2.6 wt. % of all soils (Essington, 2004). During weathering, Fe in primary minerals can be solubilized in the ferrous state at depths where oxygen is depleted (Bazilevskaya et al., 2013), solubilized by ligands in oxygen-containing soil waters (Hersman, 2000), or reduced from ferric species by bacteria (Lovley and Phillips, 1986) and released as ferrous Fe into soil pore waters. Such solubilized Fe may then move along preferential flow paths and sometimes be re-precipitated as secondary phases in soils. Precipitates often consist of poorly crystalline Fe (oxyhydr)oxide minerals such as ferrihydrite (Cornell and Schwertmann, 2003). During soil

development, these poorly crystalline minerals transform into more crystalline Fe (oxyhydr)oxide minerals such as goethite and hematite (Violante et al., 2002).

To understand these processes across an entire catchment, we analyzed Fe chemistry and isotopic composition in regolith of the Shale Hills watershed, a Critical Zone Observatory in central Pennsylvania overlying iron-rich shale of the Rose Hill Formation (Yesavage et al., 2012). The Rose Hill Formation is comprised of an organic-poor (~0.05% total carbon) shale that is Silurian in age. The shale contains illite (58 wt.%), quartz (30 wt.%), "chlorite" (12%), feldspar, and smaller amounts of magnetite and hematite (Jin et al., 2010). Elemental concentrations were measured in soil as a function of depth from a well-drained transect on a north-facing planar hillslope. Both total and ferrous iron are depleted (with losses of up to 80% and 75%, respectively) from soils relative to the bedrock. However, these changes take place gradually with depth in the 25-90 cm-thick soil profiles, with no evidence for an abrupt layer of extensive depletion. In contrast, subsequent work at this site has demonstrated that two notable zones of Fe(II) oxidation (presumed to be reaction fronts) occur at significant depths below the bedrock/regolith interface (at 23 and 5 meters below at the ridge) in drilled bedrock (Brantley et al., 2013).

Due to analytical difficulty, the precise and accurate analysis of the stable isotope values of Fe (referred to as the δ^{56}Fe value) was not possible until around the year 2000. Consequently, only a limited number of studies exist examining the Fe isotope signatures of soil and regolith. Although many of the earliest published Fe isotope values were obtained using thermal ionization mass spectrometry (TIMS), multi-collector inductively-coupled plasma mass spectrometry (MC-ICP-MS) has since become the preferred method for the analysis of most non-traditional stable isotopes (Beard and Clark, 2004). Although the existence of isobars derived from the Ar plasma used with MC-ICP-MS presents a special challenge in the form of isobaric interferences ($^{40}Ar^{14}N$ has roughly the same mass as ^{54}Fe, while ^{40}ArO has a similar mass to ^{56}Fe), the high ionization efficiency of this method allows for rapid sample throughput.

Although many studies have analyzed Fe isotope values within soils (Brantley et al., 2001; Fantle and DePaolo, 2004; Emmanuel et al., 2005; Thompson et al., 2007; Wiederhold et al., 2007a; Wiederhold et al., 2007b; Poitrasson et al., 2008), much of this work was limited in nature. For instance, in some cases fewer than three samples were analyzed from the soil profile

(Brantley et al., 2001; Thompson et al., 2007) or the parent material was poorly constrained (Wiederhold et al., 2007a, 2007b). In contrast, in the second chapter of this thesis, I present Fe isotopic analyses on soil samples which were all derived from shale bedrock. Many processes in soils may contribute to Fe isotope fractionation. While some of the processes are bacterial in nature (Beard et al., 1999), others are strictly inorganic (Skulan et al., 2002; Icopini et al., 2004). Moreover, mineral incubation experiments, including experiments with the shale underlying the Shale Hills catchment (Liermann et al., 2011), indicate that organic ligands preferentially release isotopically light Fe into solution relative to the starting material (Beard et al., 1999; Brantley et al., 2001; Brantley et al., 2004). Considering the wide variety of different processes that are known to fractionate Fe, we were interested in whether any consistent trends could be observed across the Shale Hills watershed as a whole.

The isotopic compositions (δ^{56}Fe, relative to IRMM-014) of bulk Fe and amorphous Fe (extracted with 0.5 N HCl) range between -0.3 and +0.3‰, with $\Delta^{56}Fe_{bulk\text{-}extractable}$ values between ~0.2 and 0.4‰. Due to the very good precision of Fe isotope measurements (often as low as 0.05‰), these differences are significant. Throughout the watershed, δ^{56}Fe signatures of both bulk and HCl-extracted Fe become isotopically lighter from the ridge toward the valley floor as the extent of weathering proceeds. Two different mechanisms were invoked to explain the accumulation of light Fe in the valley floor (Yesavage et al., 2012). The first mechanism involves Fe fractionation during dissolution of the parent material (via ligand-promoted dissolution and dissimilatory Fe reduction) and the subsequent precipitation of this isotopically-depleted solubilized Fe in the older valley floor. The second mechanism, invoked to explain why the entire hillslope transect shows loss of heavy Fe, requires that the precipitation in the valley floor be incomplete, preferentially retaining isotopically light Fe oxides. Although dissolved Fe in most streams is thought to be isotopically light (Fantle and DePaolo, 2004), this second mechanism would require loss of Fe from the watershed as isotopically heavy colloidal particles or solutes. Subsequent research since the publication of this manuscript has documented extreme fractionation of Fe in colloidal matter as a function of particle size (Ilina et al., 2013), with smaller particles (10 kDa) in streams up to 4‰ lighter than larger particles (100 μm). The relative enrichment of 1-10 kDa ultrafiltrates in heavy istotopes was attributed to the fact that low molecular weight ligands bind Fe more strongly than Fe oxides, in accordance with quantum

mechanical predictions (Ilina et al., 2013). In the case of the Shale Hills watershed, isotopically heavy Fe may therefore be lost as very small colloidal particles that are not precipitated.

Chapter 3: Basalt Weathering in an Arctic Mars Analog Site

While the first of our three sites is underlain entirely by an iron-rich shale, the second two sites are underlain by mafic rocks (a basalt and a diabase). The first of these profiles is located at the Sverrefjell volcano, a Mars analog site in the Arctic Circle characterized by a cold, dry climate. Because this site was deglaciated beginning only about 10,000 years ago, it is thought that observations from this location will elucidate early-stage weathering processes on Mars. Evidence indicates that weathering has previously occurred on Mars and may intermittently occur today. Although such weathering in cold, dry climates is often assumed to be dominated by physical processes (Campbell and Claridge, 1987), chemical weathering also occurs. In Chapter 3 of this thesis, I quantify the extent of chemical weathering, identify secondary phases that are forming in the regolith during weathering, and estimate the rate of physical spalling of particles from the regolith due to freeze/thaw and drying/wetting.

Analysis of a ~75-cm core of rubbly regolith formed on a basaltic flow documents concentrations of amorphous phases similar to those observed in warmer, wetter volcanic ash soils. FT-IR and TEM analysis of the clay-sized regolith fraction indicate allophane as the predominant secondary phase, with no evidence for halloysite. Allophane is a common constituent of volcanic soils (Dahlgren et al., 1993), and thermal emission spectrometer data from Mars suggest that allophane may be present at different latitudes across the surface of the planet (Rampe et al., 2012). The relative order of loss of elements from the clay-sized fraction of the regolith is observed to be: (Na, K) > (Ca, Mg) > Si > (Fe, Al, Ti). The Al/Si ratio of the amorphous portion (extracted with acid ammonium oxalate) of the regolith is lower than in volcanic soils reported for other localities, perhaps reflecting extraction of the silica-rich layers observed to coat weathered rocks from the regolith. The fact that abundant Si coatings appear on weathered Sverrefjell rocks may lend support to the argument that has been advanced from thermal emission spectrometer data that silica coatings are common on Martian rocks (Kraft et al., 2003).

Because allophane occurs as colloidal-sized particles (Karube et al., 1996), we performed a series of batch experiments to understand dissolved and colloidal dispersion from regolith samples under oxic and anoxic conditions. Soil colloids are operationally defined as particles between 1 nm and 10 μm in diameter (de Jong et al., 2004) and include layer silicates, Fe and Al oxides, organic molecules, bacteria and viruses. Due to their high specific surface areas, colloids have a high sorptive capacity and therefore readily adsorb a wide variety of contaminants, including heavy metals, organics, pesticides and radionuclides (Sen and Khilar, 2006). Two techniques that have allowed for the improved chemical characterization of colloidal material as a function of particle size include ultrafiltration and dialysis. Although a wide variety of studies have been devoted to colloidal characterization in aquatic environments including rivers, lakes and seawater, fewer studies have focused more specifically upon soil solutions (Pokrovsky et al., 2005).

For the colloidal dispersion experiments, solutions of known ionic strength were added to regolith, and microcentrifugation and ultrafiltration were used to separate different size fractions, which were then analyzed for chemistry. Similar results were found for experiments performed between pH 5-8.5, a range that encompasses the measured regolith pore-water pH of ~7. While elements such as Na, Mg and Ca are dispersed in the dissolved form, Al, Fe and Ti are present predominantly as larger colloids in the 260-415 nm size range. In contrast, Si is present simultaneously in both the dissolved and larger colloidal size fractions. The Fe/Al/Si ratio of the dispersed colloids under oxic conditions is consistent with the dispersion of allophane and ferrihydrite. Under anoxic conditions, the average size of dispersed particles decreased over time, an observation attributed to ongoing dissolution of Fe oxide cements followed by release of fines.

Not only do the colloidal dispersion experiments elucidate the size fractions of colloidal material, but they also help to explain regolith chemistry as well as the abundance of silica coatings on weathered rocks. In the case of clay-sized regolith at Sverrefjell volcano, Na, K, Mg and Ca are lost as the extent of weathering increases from the bottom of the profile toward the surface. Despite the very dry climate at Sverrefjell, the solubilization of these elements allows them to exit the soil profile. In contrast, the retention of Al, Fe and Ti may be explained based on the fact that these elements are associated with larger colloidal-sized particles (predominantly

260-415 nm in size); the dry climate of Sverrefjell may inhibit the loss of these larger particles from the regolith profile. In the case of Si, the dissolution of Si from rocks in all batch experiments ranging from pH 4 to 10 explains loss of this element from the profile relative to Fe and Al. Finally, the abundance of Si coatings on weathered rock surfaces may likewise be explained as resulting from Si dissolution across the pH range (pH 5-8) relevant to the Sverrefjell regolith. Such dissolved Si may then precipitate as coatings during particularly dry periods. In contrast, significant Al is dissolved only at very low and high pH values (of 4.5 and 10, respectively) that are not environmentally relevant to the regolith profile at Sverrefjell.

Based upon estimates of retreat from the sum of both chemical and physical weathering, we infer high rates of weathering at this site that are comparable to rates observed in temperate climates. We were interested in testing the hypothesis that freeze/thaw plays a crucial role in enhancing the rates of basalt disintegration. To investigate mechanisms of elemental loss, pristine Svalbard parent regolith was subjected to wetting, freezing and drying in the laboratory. Cyclic freezing does not disintegrate the rock faster than wetting and drying alone: all treatments resulted in ~0.2% mass loss over ~200 cycles. These experiments are in agreement with previous research suggesting that high weathering rates in cold, dry climates such as Sverrefjell volcano and Mars need not be attributed exclusively to freeze/thaw processes. On the contrary, sorptive processes taking place during wetting and drying may more readily disintegrate rock than freeze/thaw cycling (Dunn and Hudec, 1972).

Chapter 4: Chemical Weathering and Fe Isotope Fractionation in Regolith Overlying a Diabase: Fe Cycling at the Bedrock/Regolith Interface in Pennsylvania (U.S.A.)

The goal behind this final chapter is to understand changes in mineralogy, chemistry and Fe isotope signatures in a 4-m thick Pennsylvania regolith profile underlain entirely by rocks of basaltic composition (diabase). While the Shale Hills project investigated chemical and isotopic changes taking place across an entire hillslope, the goal of this chapter was to focus specifically upon changes associated with the transformation of bedrock into soil in the deeper 4-m diabase profile. Samples were collected from a forested ridge-top site at a remote location along the Appalachian Trail to avoid contributions from downslope mass movements. In contrast to the 70-cm regolith profile at the Sverrefjell volcano, concentrations of amorphous-extracted phases

were much lower at this site. Furthermore, while the predominant weathering product at Sverrefjell was amorphous allophane, the clay-sized regolith fraction in the Pennsylvania diabase is dominated by a 14 Å phyllosilicate phase (presumably a phase containing smectite±chlorite±illite) and 7 Å halloysite/kaolinite. The abundance of more crystalline phases in the diabase profile compared to the Svalbard profile is likely the result of the following: a) a lack of glass, a precursor to allophane (Dahlgren et al., 1993), b) the warmer, wetter climate of Pennsylvania, which promotes more extensive recrystallization, and c) the longer periods of time for weathering in this 4-m profile. In further contrast to the Sverrefjell volcano, rock at the diabase site is also undergoing spheroidal weathering. Spheroidal weathering is thought to occur when the diffusion of oxygen into corestones initiates oxidation of Fe(II) minerals. A volumetric increase accompanying oxidation and/or precipitation of Fe oxides then results in an elastic strain energy in the rock that creates a concentric set of fractures (referred to as rindlets) that slowly transform to saprolite (Fletcher et al., 2006).

In contrast to the shallow soil profile at Shale Hills and the minimal weathering profile at Sverrefjell, we document abrupt reactions taking place in the deep regolith near the bedrock/regolith interface at this site. Total sulfur concentrations decrease from 1,000 ppm in the bedrock to 0-150 ppm in the regolith, documenting the oxidation of iron sulfides at some unknown depth below the bedrock/regolith interface. While total Fe is largely retained in the lower portion of the profile, Fe(II) is oxidized in the lowermost 30 cm. Elevated concentrations of amorphous Fe are observed both in this depth range near the bedrock/regolith interface as well as toward the surface of the profile. Similar trends in a spheroidally weathering Puerto Rico granodiorite profile indicate that spheroidal weathering may release Fe(II) that is rapidly oxidized in the rindlet zone of the deep profile and precipitated as amorphous Fe oxides. δ^{56}Fe values of bulk samples show very little variation with depth, whereas δ^{56}Fe values of amorphous Fe (extracted with 0.5 N HCl) are depleted both in the upper meter and near the bedrock/regolith interface. We explain isotopically light Fe at depth as resulting from kinetic effects during the rapid precipitation of Fe(III) to form Fe oxides–these reactions could be abiotic or promoted by bacteria.

Suction lysimeters were installed in the upper two meters of the diabase profile to understand the pore-water chemistry as a function of depth and season. The concept behind this

technique involves the creation of a vacuum that exceeds the soil water tension, therefore causing water to flow through a ceramic cup into the lysimeter. Although the earliest lysimeters were used to collected unsaturated pore water beginning in 1904 (Peters and Healy, 1988), the method was refined by the U.S. Environmental Protection Agency in the 1980s in order to improve vadose zone monitoring around landfills and contaminated sites (Durant et al., 1993).

While a great deal of variation exists, average nitrate and dissolved organic carbon (DOC) concentrations in regolith pore fluids decrease with depth in the profile. Concentrations of DOC do not show predictable seasonal variability, nor are they correlated to the amount of recent precipitation. The pH values of pore-water samples decrease from the B to C horizons, presumably due to higher concentrations of carbon dioxide at greater depths. This finding may be due in part to higher concentrations of carbon dioxide with depth in the soil (Stinchcomb et al., in prep.). These elevated carbon dioxide concentrations may be the result of lower hydraulic conductivity in the BC horizon (Buol and Week, 1991), which may restrict the upward diffusion of carbon dioxide. Lower hydraulic conductivity within the BC horizon may also explain elevated concentrations of DOC, dissolved Fe and dissolved Al near the Bt/BC horizon at 60 cm in the profile, which presumably acts as a preferential flow zone. Pore-water cation concentrations (especially Fe and Al) correlate with DOC throughout the year, suggesting metal complexation.

To better understand the weathering system, we compare solid- and solute-based weathering rates for the upper two meters of the diabase profile for which pore-water chemistry was measured. In theory, steady state conditions in which the bedrock has attained a constant thickness over time would result in similar values for both of these rates (White et al., 2002). Given the error entailed in estimating the long-term values of the hydrologic flux density as well as the regolith residence time at this site, the similar values of the solid- and solute-based rates lead to the conclusion that the site is in, or close to, steady state.

References:

Amiotte-Suchet, P., Probst, J.L., and Ludwig,W., 2003, Worldwide distribution of continental rock lithology: Implications for the atmospheric/soil CO_2 uptake by continental weathering and alkalinity river transport to the oceans. Global Biochem. Cycles. 17: 1038-1051.

Bazilevskaya, E., Lebedeva, M., Pavich, M., Rother, G., Parkinson, D.Y., Cole, D., Brantley, S.L., 2013, Where fast weathering creates thin regolith and slow weathering creates thick regolith. Earth Surface Processes and Landforms. 38: 847-858.

Beard, B.L., Johnson, C.M., Cox, L., Sun, H., Nealson, K.H., and Aguilar, C., 1999, Iron isotope biosignatures. Science. 285: 1889-1892.

Beard, B.L., and Johnson, C.M., 2004, Fe isotope variations in the modern and ancient earth and other planetary bodies. Reviews in Mineralogy & Geochemistry. Volume 55. Geochemistry of Non-traditional Stable Isotopes. (eds. C.M. Johnson, B.L. Beard, and F. Albarede). Mineralogical Society of America Geochemical Society, Washington, DC. pp. 319-357.

Brantley, S.L., Liermann, L., Bullen, T.D., 2001, Fractionation of Fe isotopes by soil microbes and organic acids. Geology. 29: 535-538.

Brantley, S.L., Liermann, L.J., Guynn, R.L., Anbar, A., Icopini, G.A., Barling, J., 2004, Iron isotope fraction during mineral dissolution with and without bacteria. Geochim. Cosmochim. Acta. 68: 3189-3204.

Brantley, S.L., Holleran, M.E., Jin, L., and Bazilevskaya, E., 2013, Probing deep weathering in the Shale Hills Critical Zone Observatory, Pennsylvania (USA): the hypothesis of nested chemical reaction fronts in the subsurface. Earth Surface Processes and Landforms. 38: 1280-1298.

Buol, S.W., and Weed, S.B., 1991, Saprolite-soil transformations in the Piedmont and Mountains of North Carolina. Geoderma. 51: 15-28.

Buss, H.L., Bruns, M.A., Schultz, M.J., Moore, J., Mathur, C.F., Brantley, S.L., 2005, The coupling of biological iron cycling and mineral weathering during saprolite formation, Luquillo Mountains, Puerto Rico. Geobiology. 3: 247–260.

Buss, H.L., Mathur, R., White, A.F., and Brantley, S.L., 2010, Phosphorus and iron cycling in deep saprolite, Luquillo Mountains, Puerto Rico. Chemical Geology. 269: 52-61.

Calvert, C.S., Buol, S.W., and Weed, S.B., 1980, Mineralogical characteristics and transformations of a vertical rock-saprolite-soil sequence in the North Carolina Piedmont: II.

Feldspar alteration products-Their transformations through the profile. Soil Sci. Soc. Am. J. 44: 1104-1112.

Campbell. I.B., and Claridge, G.G.C., 1987, Antarctica: Soils, Weathering Processes and Environment. Developments in Soil Science 16. Elsevier Science Publishing Company Inc. New York, NY.

Cornell, R.M., and Schwertmann, U., 2003, The Iron Oxides: Structure, Properties, Reactions, Occurrences and Uses. Wiley-VCH, Weinheim, Germany.

Dahlgren, R., Shoji, S. and Nanzyo, M., 1993, Chapter 5: Mineralogical characteristics of volcanic ash soils. In Volcanic Ash Soils: Genesis, Properties and Utilization. Eds. Shoji, S., Nanzyo, M., and Dahlgren, R.A., Developments in Soil Science 21. Elsevier. Amsterdam, The Netherlands. pp. 101-143.

de Jonge, L.W., Kjaergaard, C., and Moldrup, P., 2004, Colloids and colloid-facilitated transport of contaminants in soils: An introduction. Vadose Zone Journal. 3: 321-325.

Dessert, C., Dupre, B., Gaillardet, J., Francois, L.M., and Allegre, C.J., 2003, Basalt weathering laws and the impact of basalt weathering on the global carbon cycled. Chemical Geology. 202: 257-273.

Dunn, J.R., and Hudec, P.P., 1972, Frost and sorption effects in argillaceous rocks. Highway Research Record. 393: 65-78.

Durant, N.D., Myers, V.B., and Eccles, L.A., 1993, EPA's approach to vadose zone monitoring at RCRA facilities. Winter 1993. GWMR. 151-158.

Emmanuel, S., Erel, Y., Matthews, A., and Teutsch, N., 2005, A preliminary mixing model for Fe isotopes in soils. Chemical Geology. 222: 23-34.

Essington M. E., 2004, Soil and Water Chemistry: An Integrative Approach. CRC Press, Boca Raton. pp. 1-34.

Eswaran, H., and Bin, W.C., 1978, A study of a deep weathering profile on granite in Penninsular Malaysia: III. Alteration of feldspars. Soil Sci. Soc. Am. J. 42: 154-158.

Fantle, M.S., and DePaolo, D.J., 2004, Iron isotopic fractionation during continental weathering. Earth and Planetary Science Letters. 228: 547-562.

Fletcher, R.C., Buss, H.L., Brantley, S.L., 2006, A spheroidal weathering model coupling porewater chemistry to soil thickness during steady-state denudation. Earth and Planetary Science Letters. 244: 444-457.

Gilkes, R.J., and Suddhiprakarn, A., 1979, Biotite alteration in deeply weathered granite. Morphological, mineralogical, and chemical properties. Clays and Clay Minerals. 5: 349-360.

Graham, R.C., Weed, S.B., Bowen, L.H., Amarasiriwardena, D.D., and Buol, S.W., 1989, Weathering of iron-bearing minerals in soils and saprolite on the North Carolina Blue Ridge Front: II. Clay mineralogy. Clays and Clay Minerals. 37: 29-40.

Hausrath, E.M., Navarre-Sitchler, A.K., Sak, P.B., Williams J.Z., and Brantley, S.L., 2011, Soil profiles as indicators of mineral weathering rates and organic interactions for a Pennsylvania diabase. Chemical Geology. 290: 89-100.

Hersman L. E., (2000) The role of siderophores in iron oxide dissolution. In Environmental Microbe-Metal Interactions (ed. D.R. Lovley). ASM Press, Washington, D.C. pp.145-157.

Icopini G.A., Anbar A.D., Ruebush S.S., Tien, M., and Brantley S. L., 2004, Iron isotope fractionation during microbial reduction of iron: the importance of adsorption. Geology. 32: 205–208.

Jin, L., Rother, G., Cole, D.R., Mildner, D.F.R., Duffy, C.J., Brantley, S.L., 2011, Characterization of deep weathering and nanoporosity development in shale—a neutron study. American Mineralogist. 96: 498-512.

Karube, J., Nakaishi, K., Sugimoto, H., and Fujihira, M., 1996, Size and shape of allophane partices in dispersed aqueous systems. Clays and Clay Minerals. 44: 485-491.

Kraft, M.D., Michalski, J.R., and Sharp, T.G., 2003, Effects of pure silica on thermal emission spectra of basaltic rocks: Considerations for Martian surface mineralogy. Geophysical Research Letters. 30: 2288, doi:10.1029/2003GL018848.

Lovley D. R., and Phillips E. J. P., 1986, Organic matter mineralization with reduction of ferric iron in anaerobic sediments. Appl. Environ. Microbiol. 51, 683-689.

Minyard, M.L., Bruns, M.A., Liermann, L.J., Buss, H.L., and Brantley, S.L., 2011, Halloysite nanotubes and bacteria at the saprolite-bedrock interface, Rio Icacos watershed, Puerto Rico. Soil Sci. Soc. Am. J. 75: 348-356.

Minyard, M.L., Bruns, M.A., Liermann, L.J., Buss, H.L., and Brantley, S.L., 2012, Bacterial associations with weathering minerals at the regolith-bedrock interface, Luquillo Experimental Forest, Puerto Rico. Geomicrobiology Journal. 29: 792-803.

Peters, C.A., and Healy, R.W., 1988, The Representativeness of pore water samples collected from the unsaturated zone using pressure-vacuum lysimeters. GWMR. Spring 96-101.

Pokrovsky, O.S., Dupre, B., and Schott, J., 2005, Fe-Al-organic colloids control of trace elements in peat soil solutions: Results of ultrafiltration and dialysis. Aquatic Geochemistry. 11: 241-278.

Poitrasson, F., Viers, J., Martin, F. and Braun, J.J., 2008, Limited iron isotope variations in recent lateritic soils from Nsimi, Cameroon: Implications for the global Fe geochemical cycle. Chemical Geology. 253: 54-63.

Rampe, E.B., Kraft, M.D., Sharp, T.G., Golden, D.C., Ming, D.W., and Christensen, P.R., 2012, Allophane detection on Mars with thermal emission spectrometer data and implications for regional-scale chemical weathering processes. Geology. 40: 995-998.

Rice, T.J., Buol, S.W., and Weed, S.B., 1985, Soil-saprolite derived from mafic rocks in the North Carolina Piedmont: I. Chemical, morphological, and mineralogical charateristics and transformations. Soil Sci. Soc. Am. J. 49: 171-178.

Richter, D.D., Markewitz, D., 1995, How deep is soil? BioScience. 45: 600-609.

Schwertmann U., 1988, Chapter 11: Occurrence and formation of iron oxides in various pedoenvironments. In Iron in Soils and Clay Minerals (eds. J.W. Stucki, B.A. Goodman and U. Schwertmann). D. Reidel Publishing Company, Dordrecht.

Sen, T.K., Khilar, K.C., 2006, Review on subsurface colloids and colloid-associated contaminant transport in saturated porous media. Advances in Colloid and Interface Science. 119: 71-96.

Skulan, J.L., Beard, B.L., and Johnson, C.M., 2002b, Kinetic and equilibrium Fe isotope fractionation between aqueous Fe(III) and hematite. Geochimica et Cosmochimica Acta, 66: 2995-3015.

Stinchcomb, G. E., et al., in preparation, Quantitative links between biota, mass-balance geochemistry and the soil atmosphere: An example from a diabase weathering profile in northeastern USA.

Thompson, A., Chadwick, O.A., Boman, S., Chorover, J., 2006, Colloid mobilization during soil iron redox oscillations. Environ. Sci. Technol. 40: 5743-5749.

Thorn, C.E., 1979, Bedrock freeze/thaw weathering regime in an alpline environment, Colorado Front Range. Earth Surface Processes, 4: 211-228.

Violante, A., Krishnamurti, G.S.R., and Huang P.M., 2002, Impact of organic substances on the formation and transformation of metal oxides in soil environments. In Interactions between Soil Particles and Microorganisms. (eds. P.M. Huang, J.M. Bollag and N. Senesi). John Wiley & Sons. Ltd, New York City. pp. 133-188.

White, A.F., Blum, A.E., Schulz, M.B., Vivit, D.V., Stonestrom, D.A., Larsen, M., Murphy, S.F., and Eberl, D., 1998, Chemical weathering in a tropical watershed, Luquillo Mountains, Puerto Rico: I. Long-term versus short-term weathering fluxes. Geochimica et Cosmochimica Acta. 62: 209-226.

White, A.F., 2002, Determining mineral weathering rates based on solid and solute weathering gradients and velocities: application to biotite weathering in saprolites. Chemical Geology. 190: 69-89.

Wiederhold, J.G., Teutsch, N., Kraemer, S.M., Halliday, A.N., and Kretzschmar, R., 2007a, Iron isotope fractionation during pedogenesis in redoximorphic soils. Soil Science Society of America Journal. 71: 1840-1850.

Wiederhold, J.G., Teutsch, N., Kraemer, S.M., Halliday, A.N., and Kretzschmar, R., 2007b, Iron isotope fractionation in oxic soils by mineral weathering and podzolization. Geochimica et Cosmochimica Acta. 71: 5821-5833.

Yesavage, T.A., Fantle, M.S.,Vervoort, J., Mathur, R., Jin, L., Liermann, L.J., and Brantley, S.L., 2012, Fe cycling in the Shale Hills Critical Zone Observatory, Pennsylvania: an analysis of biogeochemical weathering and Fe isotope fractionation. Geochimica et Cosmochimica Acta. 99: 18-38.

Chapter 2: Fe cycling in the Shale Hills Critical Zone Observatory, Pennsylvania: An analysis of biogeochemical weathering and Fe isotope fractionation

Tiffany Yesavage[1], Matthew S. Fantle[1], Jeffrey Vervoort[2], Ryan Mathur[3], Lixin Jin[4], Laura J. Liermann[1] and Susan L.Brantley[1]

[1]Department of Geosciences, the Pennsylvania State University, University Park, Pennsylvania 16802, USA
[2]School of Earth and Environmental Sciences, Washington State University, Pullman, Washington 99164
[3]Department of Geology, Juniata College, Huntington, Pennsylvania 16652, USA
[4]Department of Geological Sciences, University of Texas at El Paso, TX 79968, USA
**Corresponding author: tay120@psu.edu*

2. ABSTRACT

During weathering, Fe in primary minerals is solubilized by ligands and/or reduced by bacteria and released into soil porewaters. Such Fe is then removed or reprecipitated in soils. To understand these processes, we analyzed Fe chemistry and isotopic composition in regolith of the Shale Hills watershed, a Critical Zone Observatory in central Pennsylvania overlying iron-rich shale of the Rose Hill Formation. Elemental concentrations were measured in soil from a well-drained catena on a planar hillslope on the south side of the catchment. Based upon X-ray diffraction and bulk elemental data, loss of Fe commences as clay begins to weather ~15 cm below the depth of auger-refusal. More Fe(III) was present than Fe(II) in all soil samples from the ridge top to the valley floor. Both total and ferrous iron are depleted from the land surface of catena soils relative to the bedrock. Loss of ferrous Fe is attributed mostly to abiotic or biotic oxidation. Loss of Fe is most likely due to transport of micron-sized particles that are not sampled by porous-cup lysimeters, but which are sampled in stream and ground waters. The isotopic compositions (δ^{56}Fe, relative to IRMM-014) of bulk Fe and 0.5 N HCl-extracted Fe (operationally designed to remove amorphous Fe (oxyhydr)oxides) range between -0.3 and +0.3‰, with $\Delta^{56}Fe_{bulk\text{-}extractable}$ values between ~0.2 and 0.4‰. Throughout the soils along the catena, δ^{56}Fe signatures of both bulk Fe and HCl-extracted Fe become isotopically lighter as the extent of weathering proceeds. The isotopic trends are attributed to one of two proposed mechanisms. One mechanism involves Fe fractionation during mobilization of Fe from the parent material due to either Fe reduction or ligand-promoted dissolution. The other mechanism involves fractionation during immobilization of Fe (oxyhydr)oxides. If the latter mechanism is true, then shale--which comprises one quarter of continental rocks--could be an important source of isotopically heavy Fe for rivers.

2-1. INTRODUCTION

As the fourth most abundant element in the Earth's crust, iron (Fe) makes up an average of 2.6 wt. % of all soils (Essington, 2004). Fe is cycled rapidly within soils by microorganisms that use Fe as an electron acceptor (Lovley and Phillips, 1986) or that solubilize the Fe with organic ligands (Hersman, 2000). In well drained soils, Fe(II) released during weathering is rapidly oxidized and precipitated as poorly crystalline Fe (oxyhydr)oxide minerals such as ferrihydrite (Cornell and Schwertmann, 2003). During soil development, these poorly crystalline minerals transform into more crystalline Fe (oxyhydr)oxide minerals such as goethite and hematite (Violante et al., 2002). Other processes, such as clay translocation, further transform the distribution of Fe-bearing phases within a given watershed, affecting Fe fluxes in soils and rivers (Laffan et al., 1989). To understand these processes in regolith requires investigations of weathering in many lithologies and surficial environments.

Weathering of one lithology, shale, which constitutes 25% of continental rocks (Amiotte-Suchet et al., 2003), has only been investigated in a limited number of studies (Littke et al., 1991; Pierson-Wickmann et al., 2002; Tuttle and Breit, 2009; Woodruff et al., 2009; Jin et al., 2010). Although shales are primarily assumed to undergo physical weathering (Schaetzl and Anderson, 2009), proton-mediated dissolution, ligand-promoted dissolution, and reductive dissolution are known to affect both Fe (oxyhydr)oxides and Fe-bearing silicates (Brantley et al., 2006; Jin et al., 2010; Liermann et al., 2011).

The goal of this study is to understand Fe transformations in a catchment underlain entirely by shale and to investigate how these various processes affect isotopic fractionation of Fe. Accordingly, we have sampled soils from a catena along the Shale Hills watershed of Pennsylvania and analyzed them for bulk chemistry, abundance of Fe-related bacteria, and Fe isotope values. The data we collected elucidate the effects of chemical weathering on shale and how that weathering affects the Fe isotope composition of surface streams and groundwater.

2-1.1. Fe isotopes, soils, and rivers

Fe has four naturally occurring isotopes: ^{54}Fe (5.85%), ^{56}Fe (91.75%), ^{57}Fe (2.12%) and ^{58}Fe (0.28%) (Dauphas and Rouxel, 2006). Variations among these isotopes are reported as δ^{56}Fe values (‰):

$$\delta^{56}Fe = \left(\frac{\left(\frac{^{56}Fe}{^{54}Fe} \right)_{sample}}{\left(\frac{^{56}Fe}{^{54}Fe} \right)_{std}} - 1 \right) * 10^{3} \qquad (2\text{-}1)$$

The international Fe reference material IRMM-014 is used as a standard, which is ~0.09‰ lighter than the average of igneous rocks. The precision of δ^{56}Fe values is generally reported at ±0.05 to ±0.15‰ (Beard and Johnson, 2004). While the extent of Fe isotopic variation is limited in bulk igneous rocks (which cluster around 0‰), soils often show a greater degree of fractionation. For instance, the range of δ^{56}Fe measured for bulk Fe in different soil samples is ~1.5‰ (Wiederhold et al., 2007a).

Many processes in soils may contribute to Fe isotope fractionation. For instance, mineral incubation experiments indicate that organic ligands preferentially release isotopically light Fe into solution relative to the starting material, including experiments with the shale underlying the Shale Hills catchment (Brantley et al., 2001; Brantley et al., 2004; Liermann et al., 2011). Wiederhold et al. (2007a) further measured isotopically lighter Fe in the Bh horizon where organic matter accumulates in a Spodosol. The authors attributed this isotopic shift to ligand-promoted dissolution that preferentially removed isotopically light Fe from upper horizons and deposited it as isotopically light material in the Bh horizon.

Bacterially mediated reductive dissolution may also cause Fe isotopic variations. For example, dissimilatory iron reduction in clay minerals and Fe (oxyhydr)oxides occurs when microorganisms use Fe(III) as an electron acceptor. Beard et al. (1999) demonstrated that the δ^{56}Fe value of dissolved Fe(II) produced by dissimilatory iron-reducing bacteria was lighter than the remaining ferrihydrite substrate by ~1.3‰. In soils therefore, dissimilatory iron reduction might release isotopically light Fe into solution, leaving behind isotopically heavier residual Fe. Indeed, Wiederhold et al. (2007b) attributed ^{56}Fe enrichment within iron-depleted zones of a

German Inceptisol as the result of reductive loss of isotopically light Fe. In contrast, Fe-enriched zones, in which reduction presumably was not very important, were isotopically lighter. In a study of basaltic soils in Maui where mean annual rainfall increases from 2800 to 4200 mm per year, Thompson et al. (2007) likewise suggested that reductive dissolution led to loss of light Fe, causing increasingly heavy isotopic signatures of Fe in the bulk soils with increased precipitation.

Although many studies have analyzed Fe isotope values within soils (Brantley et al., 2001; Fantle and DePaolo, 2004; Emmanuel et al., 2005; Thompson et al., 2007; Wiederhold et al., 2007a; Wiederhold et al., 2007b; Poitrasson et al., 2008), much of this work was limited in nature. For instance, in some cases fewer than three samples were analyzed from the soil profile (Brantley et al., 2001; Thompson et al., 2007) or the parent material was poorly constrained (Wiederhold et al., 2007a, 2007b). In contrast, in this study, samples were collected not only from pedons along a hillslope but also from bedrock. This approach allows fuller understanding of how pedogenic processes affect Fe isotope composition during weathering.

2-2. METHODS

2-2.1. Site Description

The Susquehanna/Shale Hills Critical Zone Observatory is a catchment in Huntington County, Pennsylvania. The catchment is underlain entirely by the Rose Hill formation, and has been characterized with regard to hydrologic flow (Lin, 2006; Qu and Duffy, 2007; Kuntz et al., 2011), soil properties (Lin, 2006; Lin et al., 2006), soil chemistry and elemental fluxes (Jin et al., 2010; Jin et al., 2011a; Jin et al., 2011b; Ma et al., 2011), organic carbon content (Andrews et al., 2011), and regolith production rates (Ma et al., 2010). The 8-hectare catchment has a mean annual temperature of 10^{o}C and a mean annual precipitation of about 110 cm (NOAA, 2007). A first-order ephemeral stream flows from east to west in the catchment (Figure 2-1), with peak flow in the spring months (Andrews et al., 2011). Deciduous trees (including maple, oak and hickory) are dominant on ridges and middle slopes, while eastern hemlock conifers are prevalent on the valley floor (Lin et al., 2006).

The Rose Hill Formation is comprised of an organic-poor (~0.05% total carbon) shale that is Silurian in age. The Rose Hill shale contains illite (58 wt.%), quartz (30 wt.%), "chlorite" (12%), feldspar, and smaller amounts of magnetite and hematite (Jin et al., 2010). "Chlorite," as determined from quantitative X-ray diffraction (XRD), is a term that here encompasses chlorite, vermiculite, hydroxy-interlayered vermiculite (HIV) and/or mixtures of these phases. The majority (90%) of Fe in the shale bedrock resides in illite and vermiculated chlorite, with ~10% of Fe in magnetite and hematite (Jin et al., 2010). As weathering proceeds, illite and vermiculated chlorite transform into vermiculite, hydroxy-interlayered vermiculite, kaolinite, and various Fe oxyhydroxides (Jin et al., 2010).

Five different soil series, including three Inceptisols and two Ultisols (Lin et al., 2006), have been characterized within the Shale Hills catchment. Soils from the ridge top, middle slope and footslope are well-drained Inceptisols of the Weikert (loamy-skeletal, mixed, active, mesic Lithic Dystrudepts) and Berks series (loamy-skeletal, mixed, active, mesic Typic Dystrudepts) that tend to be dry throughout much of the year (Lin et al., 2006). In contrast, soils from the toeslope are more poorly drained Ultisols of the Ernest (fine-loamy, mixed, superactive, mesic Aquic Fragiudults) and Blairton series (fine-loamy, mixed, active, mesic Aquic Hapludults) that are wetter and show redoximorphic features (Lin et al., 2006). These features include gleying, a bluish or greenish color that is observed under reduced conditions.

Uranium-series isotope measurements indicate that the residence time for particles in the ridge top increases from 7 kyr at the ridge top to 34 kyr at the middle slope and 40 kyr at the valley floor footslope (Ma et al., 2010). The catchment-averaged erosion rate as determined using ^{10}Be on valley-floor sediments is ~15 m/Ma (Jin et al., 2010).

2-2.2 Sample Collection

Regolith samples were collected along a transect on the south "planar" hillslope with a 2-inch hand auger. The hillslope is planar in that it does not support significant convergent water flow; however, the upper part of the hillslope is somewhat convex-upward while the lower part is concave-upward. Regolith (or soil) is used here to refer to material that can be sampled by hand augering, i.e., material above the depth of refusal for the auger. The zero depth was defined as

the interface between the mineral soil and the organic layer. A stream sediment sample was also collected from the surface of the stream directly below the transect.

Samples were obtained from four positions (Fig. 2-1): south planar ridge top (SPRT), middle slope (SPMS), valley floor footslope (SPVF(FS)) and valley floor toeslope (SPVF(TS)) (Figure 1). The footslope and toeslope samples were collected from positions that were both about 1 meter higher than the channel and about 3 meters away from each other. Overflow of the ephemeral stream to toeslope level has not been observed. Bedrock samples that we discuss here were derived from the 30-m drillcore (referred to as DC1) obtained from the northern ridge top as described by Jin et al. (2010)(Fig. 2-1).

A second set of cores, the SPRT2 and SPMS2 cores, were augered at the same elevations and within 3 meters of the ridge top (SPRT) and middle slope (SPMS) sites reported by Jin et al. (2010). The footslope cores analyzed here are referred to as "SPVF(FS1)" and "SPVF(FS2)," while the toeslope cores are referred to as "SPVF(TS1)" and "SPVS(TS2)." SPVF(FS1) is identical to the south planar valley floor (SPVF) sample set reported by Jin et al. (2010). For microbiological analysis, two soil footslope cores (July of 2008 and October of 2009) and two toeslope cores (May of 2009 and October of 2009) were obtained. The following new data were collected for this study from the following profiles: SPRT2 (chemistry, Fe isotopes and microbiology), SPMS2 (chemistry, Fe isotopes and microbiology), SPVF(FS1) (Fe isotopes) SPVF(FS2) (microbiology only), SPVF(FS3) (microbiology only), SPVF(TS1) (chemistry, Fe isotopes and microbiology) and SPVF(TS2) (microbiology only).

During the summer and spring of 2010 and 2011, a series of stream-, ground- and pore-water samples were obtained for chemical analysis (Fig. 2-1 for locations). In order to sample pore waters, porous cup tension lysimeters (Soil Moisture Inc., 1900 and 1920 F1 Series) were installed in 2009 at 10-cm intervals at SPRT, SPMS, and SPVF, as discussed previously (Jin et al., 2011a). The sampling locations for cores reported here from SPRT, SPMS, and SPVF(FS) are roughly identical to the lysimeter installation sites. In addition, during the spring of 2011, flow emerging into the stream from a ~2-cm diameter tubular pore (referred to here as a "macropore") in the streambank was also sampled (Fig. 2-1). Filtered and unfiltered stream samples were collected and acidified during spring and summer of 2010 and spring of 2011, while porewater and groundwater samples were collected during the summer of 2010 (Fig. 2-1 for locations).

Water samples were added to 15-mL metal-free Falcon tubes to which 0.1 mL of Ultrex® Ultrapure HNO_3 from J.T. Baker were added to minimize precipitation and then stored in the refrigerator prior to analysis. For this study, dissolved Fe was operationally defined as the fraction of the Fe that passed through VWR International 25-mm, 0.45-µm Nylon syringe filters (North American Cat. No. 28145-489) or into the lysimeters (pore size of ceramic cup, 1.3 µm).

2-2.3. Dissolved Oxygen Concentrations

Dissolved oxygen concentrations and soil temperatures were measured in the valley floor with Apogee oxygen sensors (SO-111) installed in August of 2009 in the valley floor at depths of 10, 40, and 60 cm. One set of three sensors was installed beneath the south planar transect analyzed for soil chemistry as part of this study, while a second set of three sensors was installed farther up the catchment at the termination of a swale on the south side (Fig. 2-1). The sensors consist of a lead anode and a gold cathode. The current between these is proportional to the partial pressure of oxygen in the soil gas. The sensors were connected to a Campbell Scientific CR1000 datalogger, and current and temperature were measured every 10 minutes.

2-2.4. Sample Preparation and Analysis

In the laboratory, augered soil samples were weighed and maintained at 40°C as in Wiederhold et al. (2007a; 2007b) until a constant soil mass was attained (10 days); samples were then re-weighed to determine gravimetric soil moisture content (g water/g dry soil). A mortar and pestle were used to grind bulk samples after drying, including all rock fragments, and sieved to <150 µm. Bulk soil samples were fused with lithium metaborate and analyzed for elemental concentrations with inductively coupled plasma-atomic emission spectroscopy (Perkin-Elmer ICP-AES 5300DV). The estimated precision for most elements is ± 3%, although the error with Zr is closer to ±10%. 100 mg of the stored ground sample were fused with lithium metaborate at 850°C for 10 minutes and then redissolved in dilute nitric acid.

Concentrations of Fe(II) in soils were also determined (Goldich, 1984). The method involves boiling 1 gram of soil in the presence of hydrofluoric and sulfuric acid and titrating with

potassium dichromate to determine Fe(II) (wt. %). The method of standard additions using an acidified ferrous ammonium sulfate standard indicated that matrix effects are minimal in organic-poor soil samples such as those reported here (Table C-1). Specifically, calibration slopes obtained upon adding standard additions of ferrous ammonium sulfate to a soil sample were similar to control standards (Table C-1). Precision for these analyses was estimated at $\pm$20% by multiple measurements on individual samples. To ascertain whether sample preparation or aging affected Fe(II) concentrations, stream sediment samples were collected and processed by air drying, oven drying or drying in a desiccator. Fe(II) concentrations were not significantly different in samples dried in different ways (Table C-2).

Total carbon and nitrogen (wt. %) were measured with an Elementar vario MAX Macro Nitrogen Analyzer in the Agricultural Analytical Service Lab of Penn State University. Error was estimated equal to $\pm$ 5% at the concentration levels reported here.

Concentrations of total Fe and Al in streams, porewaters, and groundwater were determined for both filtered (0.45 μm filter) and unfiltered samples with a Thermo Scientific XSERIES 2 ICP-MS (inductively-coupled plasma-mass spectrometer). The estimated detection limits for Fe and Al in solution were 0.01 μM and 0.03 μM, respectively. Concentrations of all elements in the stream and macropores during the spring of 2011 were determined by ICP-AES (Perkin-Elmer ICP-AES 5300DV). Well samples were obtained with the use of an extraction kit from Soilmoisture (1900K3).

2-2.5. Microbiological methods

Samples for microbiological analysis were collected aseptically with sterile spatulas and placed in sterile bags on ice in the field. Within a few hours, samples were refrigerated. Within several weeks, samples were plated onto an R2A agar specific for heterotrophic bacteria (Reasoner and Geldreich, 1985). Total cell counts were enumerated with acridine orange stain (Watson et al., 1977). A dilution of soil in PBS (phosphate buffered saline) was first treated with sodium dithionite to remove interfering mineral particles and then vacuum-filtered onto a Whatman Nucleopore 0.2 mm black filter and stained with a 0.01% acridine organic solution for 1 minute. The slide was then viewed and counted under oil immersion on a Nikon Eclipse 80I light microscope using a blue FITC filter cube and a counting grid.

In soil profiles, redox gradient tests (BART™ tests manufactured by Droycon Bioconcepts Inc) were used to document iron-related bacteria, i.e., both iron-oxidizing and iron-reducing microorganisms. With these tests, we suspended ~1 gram of sample in 15 mL of autoclaved PBS buffer and then added the suspension to each test vial. Vials contained ferric ammonium citrate, the active ingredient for the growth of Fe-oxidizing and Fe-reducing bacteria (referred to as "Fe-related bacteria") as well as a plastic ball used to create a redox gradient across the tube (Buss et al., 2005). After 8 days of storage in the dark, samples were compared to a control with only PBS buffer. Foam rings in the test vials indicate the presence of anaerobic Fe-reducing microorganisms, while a brown cloud extending upward from the bottom of the tube without foam rings documents aerobic Fe-related bacteria.

To document the specific presence of dissimilatory iron-reducing bacteria, a refrigerated soil from each sample was suspended in a PBS buffer and then inoculated into a medium specific for the iron-reducing genus *Shewanella*, with Fe(III)-citrate as the electron acceptor and lactic acid as the electron donor following published procedures (Ruebush et al., 2006). Serum vials were stored in the dark during incubation. In the presence of iron-reducing organisms, the medium changes from yellow to green (Table C-3). The ferrozine assay (Stookey, 1970) was used to confirm that Fe(II) was produced.

2-2.6. Stable iron isotopes

Dried regolith samples were analyzed for both bulk and HCl-extracted Fe isotope compositions. All soils were digested in a perchloric acid hood, in a clean box prior to Fe isotope analysis. About 100 mg of oven-dried bulk soil were dissolved in acid-washed Savillex vials using a 1 mL: 3 mL mixture of HNO_3 (16 N): HF (29 N). Samples were digested at 90°C for 24 h. 1 mL of full-strength perchloric acid ($HClO_4$, 11.6 N) was then added to each vessel and the solutions evaporated at 120°C until only ~1 mL of $HClO_4$ remained. With ~1 mL of $HClO_4$ remaining in each vial, the vessels were resealed and heated at 150°C for 24 h. Samples (with ~1 mL $HClO_4$) were resuspended in a 3:1:1 mixture of HNO_3 (16 N): HF (29 N): HCl (12 N), reacted for 2 h at room temperature, sealed and heated overnight at 150°C. Samples were subsequently evaporated to dryness and resuspended in HNO_3 (16 N) and ultrapure H_2O_2 until dissolved. Samples containing large amounts of organic matter required up to 15 mL H_2O_2 to

remove all visible organic matter. Samples were dried down in concentrated HNO_3 to ensure complete Fe oxidation and resuspended in 7 N HCl. All digestion reagents were ultrapure grade (Aristar®ultra HF, OmniTrace Ultra™ high purity $HClO_4$ and Ultrex® Ultrapure HCl, H_2O_2 and HNO_3 from J.T. Baker); Millpore 18.2 MΩ-cm deionized water was used for all dilutions. Process blanks for the digestion procedure had Fe concentrations below the detection limit of ICP-AES (0.01 mg/L).

Extractions using 0.5 N HCl to release Fe from Fe oxides do not fractionate Fe (Kiczka et al., 2010; Skulan et al., 2002; Wiederhold et al., 2006). Therefore, we used 0.5 N HCl to extract poorly crystalline Fe oxides following Wiederhold et al. (2007a; 2007b). In the first step of the extraction, 0.2 grams of sample were weighed into 15-mL metal-free tubes to which 4 mL of 0.5 N HCl were added. The tubes were shaken gently on an end-over-end shaker for 24 h at room temperature. Tubes were then centrifuged at 3,400 g for 15 min. The resulting supernatant was decanted and filtered through 18.2 MΩ-cm rinsed 0.45-µm VWR Nylon filters. The centrifugate was then washed with distilled water, centrifuged a second time, and the resulting supernatant was filtered and combined with the first solution. The combined supernatant was dried down on a hotplate and resuspended in 7 N HCl.

Iron in all digested and extracted samples was chromatographically purified prior to isotopic analysis using BioRad's AG MP-1 anion exchange resin. After loading into the columns (with a bed volume of ~2 mL), the resin was washed with 7 mL 0.5 N HCl and conditioned with 9 mL 7 N HCl. Approximately 90 µg of Fe were loaded onto the column in 7 N HCl, rinsed three times with 9 mL 7 N HCl, and the Fe eluted in 9 mL 0.5 N HCl. All eluant Fe solutions were dried and resuspended in ~0.45 N HNO_3. Because incomplete recovery of Fe from the resin causes isotopic fractionation (Anbar et al., 2000), the Fe in our samples was measured before and after column chemistry to determine yields, which contained > 95% of the pre-column Fe mass. Fe concentrations in post-column blanks fell below the detection limit of ICP-AES of 0.01 mg/L. The ratio of Fe:Cr in 8 post-column samples analyzed for both elements was > 10,000:1 (Table C-3). Column chemistry aliquots were collected during the Fe purification of a synthetic solution containing ~500 mg/L of both Fe and Cr. Analysis of the various aliquots confirmed that no detectable Cr elutes within the Fe peak (Table C-4).

Iron isotope compositions were measured by multiple collector inductively-coupled plasma mass spectrometry (MC-ICP-MS) using a Thermo Fisher Scientific Neptune at

Washington State University (WSU). Medium resolution mode was used to avoid molecular interferences ($^{40}Ar^{16}O^{+}$, $^{40}Ar^{14}N^{+}$). Fe concentrations were adjusted to 3 ppm in 0.5 N HNO_3, and a 3 ppm Cu standard was added to correct for instrumental mass bias. A standard-sample bracketing approach with an exponential law correction was used to correct for instrumental mass bias and machine drift (Schoenberg and von Blanckenburg, 2005). Single-element standards with known Fe concentrations were run before and after ion exchange separation of Fe to verify that column chemistry did not result in fractionation. All delta values are reported relative to IRMM-014; the standard deviation for a series of IRMM-014 standards run daily over a 10-day period was 0.07‰ (2σ=0.14‰). As a check for accuracy, the goethite sample analyzed by Icopini et al. (2004) was previously run six times by our laboratory group, and the values measured were δ^{56}Fe=-0.27‰ ($\pm 2\sigma$=0.14‰) (Jang et al., 2008), in agreement with the previously published value of -0.27‰ (Icopini et al., 2004).

2-3. RESULTS

2-3.1. Field observations

Elevation change from ridge to valley floor on the south planar hillslope equals ~30 meters (Figure 2-1). Soils at the ridge top, middle slope and valley floor footslope have a reddish hue (7.5YR) compared to soils in the toeslope, which have a more yellow hue (10YR). Moderate gleying is also visible in the lower half of the toeslope profile, which is wetter than the other profiles. Rock fragments (shale channeries) comprise up to 90% of the material in deeper layers of the ridge top, middle slope and footslope soils, but are mostly absent in the toeslope profile, which is finer in texture. The average soil depth increases from around 30 cm at the ridge top to 1.5 m in the valley floor footslope and toeslope along the south planar catena.

2-3.2. Soil oxygen and temperature

As measured with the oxygen probes at the planar and swale valley floor positions, the footslope soils at all depths are well oxygenated, with oxygen concentrations in the soil atmosphere varying from 19-21% (molar abundance) throughout most of the year (Fig. 2-2). Oxygen concentrations tend to decrease slightly with depth during wet periods at the two sites,

and vary together with time. During the winter of 2009-2010, the oxygen concentrations were as low as 10% at the 60-cm depth in the south planar valley floor footslope (Fig. 2-2a). Temperatures vary from ~15-20°C in the summer months to ~0-5°C in the winter (Fig. 2-2). Temperatures at 10 cm vary more than those measured at 40 and 60 cm (Fig. 2-2).

2-3.3. Chemical analysis

As reported previously (Jin et al., 2010), abundance of Fe oxides estimated from quantitative XRD ranges from 0.8% in the bedrock to 1.0 to 2.2% in regolith (Table 2-1). Based upon quantitative XRD analysis and mineral stoichiometries from Jin et al. (2010), ~70% of the Fe in the bedrock is present in illite, ~20% in "chlorite" and ~10% in Fe (oxyhydr)oxides (see Table 2-1 for explanation).

Plots of the mass transfer coefficient ($\tau_{i,j}$) were made using the following expression (Anderson et al., 2002; Brimhall and Dietrich, 1987):

$$\tau_{i,j} = \frac{C_{j,w}C_{i,p}}{C_{j,p}C_{i,w}} - 1 \qquad (2\text{-}2)$$

Here, C refers to the concentrations of the immobile (i) and mobile (j) elements in the weathered (w) or parent (p) material. The following equation was used to determine the uncertainty, $\varepsilon(\tau_{i,j})$, by propagating uncertainty in the chemical measurement of each sample:

$$\varepsilon(\tau_{i,j}) = (\tau_{i,j} + 1)\left[\left(\varepsilon(C_{i,p})\right)^2 + (\varepsilon(C_{i,w}))^2 + \left(\varepsilon(C_{j,p})\right)^2 + (\varepsilon(C_{j,w}))^2\right]^{1/2} \qquad (2\text{-}3)$$

Error in parent concentration ($\varepsilon(C_{j,p})$) was estimated as the percent standard deviation of concentration in bedrock as summarized by Jin et al. (2010), while the error in soil samples ($\varepsilon(C_{j,w})$) was estimated to equal the analytical error (3% for most elements) for ICP-AES. Normalization to an immobile element (in this case, Zr) accounts for concentration changes resulting from depletion and addition of other elements. Values of $\tau_{Zr,j} > 0$ indicate that Fe is enriched in soil relative to bedrock, while $\tau_{Zr,j} < 0$ indicates depletion, where the absolute value of $\tau_{Zr,j}$ reveals the fraction of *j* left in the soil relative to parent for depleted samples. A few samples were also measured with ICP-MS instead of ICP-AES after Li metaborate fusion on a Thermo Scientific XSERIES 2 ICP-MS in the Materials Characterization Laboratory of Penn

State. With one exception, Zr concentrations of several samples measured with ICP-MS were within 5% of those measured with ICP-AES (Table C-5).

To estimate parent material composition, we followed Jin et al. (2010) and used the composition of bedrock cuttings drilled at the north ridge top (borehole DC1 in Jin et al., 2010) above a deep carbonate-containing zone. The mean Fe composition, 5.50 $\pm$ 0.19 wt. % (n = 14, 1σ), from a depth interval of 0.3 to 20 meters, was used here for $C_{Fe,p}$. This value excluded one anomalous sample of high Fe content, inferred to be a fracture zone at 4.4 m. Three additional sets of samples drilled to depths of 16 m each at the valley floor showed a similar mean Fe composition, 5.6 wt.% $\pm$ 0.5% (1σ) (n=53). In addition, Jin et al. (2010) reported that the bottommost soil samples from cores throughout the catchment showed average concentrations that were similar to the parent material within 1 standard deviation.

Present in the high-density, insoluble mineral zircon in Rose Hill shale, Zr has been previously shown to be the least mobile element in this watershed (Jin et al., 2010; Jin et al., 2011a). Zr is immobile in the Shale Hills watershed even in comparison to Ti, an element that was observed to be depleted in upper soil layers. Recent work at other sites has further indicated that Ti is often preferentially lost relative to Zr from weathering profiles as colloidal-sized particles (Bern et al. 2011; Bern and White, 2011). Values of $\tau_{Zr,\text{ Fe in ``chlorite''}}$, $\tau_{Zr,\text{Fe in illite}}$ and $\tau_{Zr,\text{ Fe in Fe oxide}}$ for soil samples were also defined by calculating the amount of Fe residing within each mineral based on quantitative XRD data and mineral stoichiometries from Jin et al. (2010)(Table1). $\tau_{Zr,\text{Fe in ``chlorite''}}$ is defined as:

$$\tau_{Zr,Fe\_in\_"chlorite"} = \frac{C_{Chl,w}C_{Zr,p}}{C_{Chl,p}C_{Zr,w}} - 1 \qquad (2\text{-}4)$$

Here, a subscript "Chl" refers to the fraction of Fe in the sample that is contained in "chlorite." Values for "Fe in illite" and "Fe in Fe oxides" were defined analogously (see Table 1 for more details).

Values of $\tau_{Zr,Fe}$ are ≤ 0 in all but one sample along the transect (Table 2-2, Fig. 2-3), indicating overall Fe loss ranging from ridge top (<20%) to middle slope (<40%) to valley floor footslope (<77%) (Table 2-2). $\tau_{Zr,Fe}$ values are also negative for the toeslope, except for 64-72 cm (Table 2-2). The $\tau_{Zr,j}$ values for other elements generally resemble those for Fe (Table C-6). As

discussed by Jin et al. (2010), many of the $\tau_{Zr,j}$ values do not return to 0 in the lowermost samples because weathering has occurred in material tens of centimeters below depth of hand augering.

In the upper 12 m of DC1 (used here as an estimate of parent) and in the footslope, about 24% of the Fe is present as Fe(II)(Table 2-2). In contrast, the Fe(II)/Fe(total) fraction is lower in the ridge top, middle slope and toeslope regolith. In the soils, $\tau_{Zr,Fe(II)}$ is negative in all but two samples (Table 2-2, Fig. 2-3), documenting loss of Fe(II). $\tau_{Zr,Fe(II)}$ is generally more negative than $\tau_{Zr,Fe}$ in the ridge top and toeslope (Fig. 2-3).

Fe contained in illite and "chlorite" was lost during weathering relative to Zr (i.e., negative values of $\tau_{Zr,Fe\ in\ illite}$ and $\tau_{Zr,Fe\ in\ chlorite}$ in all soil profiles (Table 2-1). In contrast, Fe (oxyhydr)oxides have increased in concentration relative to Zr (positive $\tau_{Zr,Fe\ in\ Fe\ oxide}$ values, Table 1). Consistent with this, the portion of HCl-extractable Fe at each depth (Table 2-2) tends to increase toward the surface of most profiles and is particularly high in stream sediments and the surface of the footslope and toeslope (Table 2-2).

The net Fe mass flux values, m_{Fe}, from each augerable profile for total Fe and Fe(II) (g Fe/m^2) were calculated as defined by Chadwick et al. (1990) after correction for strain (Egli and Fitze, 2000), using an equation amended by Brantley and Lebedeva (2011):

$$m_{Fe} = \rho_p C_{Fe,p} \int_{z=o}^{z=L} \frac{\tau_{Fe(z)}}{(\varepsilon_j(z)+1)} dz \tag{2-5}$$

Here, ρ_p is the bulk density of the parent material and L is the total depth of the soil profile. The strain for soil from each depth interval (noted as the bottom of the interval, z), $\varepsilon_j(z)$ was calculated from Anderson et al. (2002):

$$\varepsilon_j(z) = \frac{\rho_p C_{Zr,p}}{\rho_w(z) C_{Zr,w}(z)} - 1 \tag{2-6}$$

This calculation requires an estimate of bulk density, $\rho_w(z)$, for each soil at each interval. To estimate this, we used a regression based upon bulk density data for 28 samples collected throughout the watershed by Lin (2006) (see Table 2-3 footnote). Note that in Equation 2-6 we also explicitly noted that $C_{Zr,w}$ varies with depth.

Values of m_{Fe} are negative in all four profiles, indicating increasing loss of Fe from 2,500 g Fe/m^2 at the ridge to 27,000 g Fe/m^2 at valley floor footslope (Table 2-3). Values of $m_{Fe(II)}$,

defined analogously to (2-5), are also negative, documenting increasing loss from 1,500 g Fe(II)/m^2 at the ridge to 9,000 g Fe(II)/m^2 at toeslope (Table 2-3).

Finally, the total integrated fraction of Fe lost from each profile estimated for a core of depth L can be expressed as (Brantley and Lebedeva, 2011):

$$f_{Fe} = \frac{m_{Fe}}{C_{Fe,p}\rho_p L} \tag{2-7}$$

Assuming a homogeneous parent material, this fraction increases from a minimum of 7% at the ridge top to a maximum of 30% in the toeslope (Table 2-3).

2-3.4. Chemical composition of water samples

Concentrations of both Fe and Al were typically ~1 μM in filtered stream and "macropore" samples (<0.45 μm) versus 2-10 μM in unfiltered samples (Table C-7). In soil porewaters, Al concentrations were roughly identical for filtered versus unfiltered samples (~1 μM). On the other hand, concentrations of filtered and unfiltered Fe in porewaters from lysimeters were near the detection limit for ICP-MS, 0.01 μM, two orders of magnitude lower than dissolved stream Fe. Like Fe and Al, unfiltered stream and "macropore" waters also had higher concentrations of Ti and Si than filtered stream waters (Table C-7). In contrast, filtered and unfiltered stream and macropore samples have similar K, Ca, and Na concentrations. In general, the macropore chemistry was similar to that of the stream (Table C-7).

Filtered and unfiltered concentrations of both Fe and Al sampled in the summer of 2010 from groundwater wells (Fig. 2-1) are higher in concentration than stream waters, ranging from ~0.3-30 μM, and are about twice as high in unfiltered as compared to filtered samples (Table C-7).

2-3.5. Microbiological, C, and N observations

Total nitrogen and carbon concentrations were highest at the surface: 0.1-0.2 wt. % and 1-3 wt. %, respectively (Table C-8; Figure C-1). Concentrations decreased by a factor of 2-10 with depth below 20 cm, regardless of hillslope position. Total concentrations in the lowermost

soil samples approached parent concentrations for N (0.06 wt.%) but remained 10 times higher than parent for C (0.04 wt. %, Table C-8).

Total measured cell counts were highest at the surface and decreased with depth (Table C-9; Figure C-2). No significant differences were observed between two toeslope cores (SPVF(TS1) and SPVF(TS2)), collected in May and October of 2009 (Figure C-2). Heterotrophic counts were more variable with depth. Heterotrophic counts tended to be higher at interfaces of soil horizons where permeability contrasts have been documented (Lin et al., 2006) and where porewaters are more dilute (Jin et al., 2011a). Higher heterotrophic counts were observed a) in the ridge top at ~25 cm near the regolith/bedrock horizon interface, b) in the middle slope at both 25 and 50 cm at the Bw/C and regolith/bedrock interfaces respectively, c) in the footslope at ~30 cm near the Bw/Bt interface and d) near the regolith/bedrock interface of the toeslope profile.

From the redox gradient tests, we observed evidence for Fe-related bacteria i) within 15 cm of the bedrock-regolith interface and ii) near the land surface along the entire catena. Specifically, the presence of aerobic Fe-related bacteria is consistent with the brown color we observed from the test (http://www.dbi.ca). Furthermore, the redox tests showed no evidence for iron-reducing bacteria (i.e., no foam rings formed in the tubes). All of the control tests remained yellow, consistent with no bacterial activity. Despite the lack of foam rings in the redox gradient tests, we were able to culture Fe-reducing organisms in the *Shewanella* medium in the upper toeslope (Figure C-3), indicating that Fe reducers were present.

2-3.6. Iron stable isotope results

The range of $\delta^{56}Fe$ values measured for bulk samples varied from -0.12 to 0.31‰, while the HCl-extracted range varied from -0.31 to 0.08‰ (Table 2-2; Fig. 2-4). The Fe isotopic composition ($\delta^{56}Fe_{IRMM\text{-}014}$) of bedrock at Shale Hills is 0.31 ± 0.06‰ (n=2 samples; Table 2-2). Five of six samples from the ridge and middle slope did not differ significantly from bedrock ($\pm$ 1σ, Table 2-2, Fig. 2-4). In contrast, foot- and toeslope samples ranged from -0.12 to +0.25‰, with surface soils significantly lighter than bedrock (Table 2-2, Fig. 2-4). A stream sediment sample (collected below the transect in the stream channel) was also ~0.2‰ lighter than bedrock ($\delta^{56}Fe$ = 0.10‰) and statistically similar to bulk foot- and toeslope soils. HCl-extracted Fe

varied from ~0.0‰ (bedrock and ridge-top soils) to -0.3‰ (stream sediment) and generally becomes isotopically lighter toward the surface.

HCl-extractable Fe comprises 3.1 to 13.8% of the total soil (Table 2-2), and δ^{56}Fe values of this fraction are ~0.2 to 0.4‰ lighter than bulk soil Fe ($\Delta_{bulk\text{-}extracted} = \delta^{56}Fe_{bulk} - \delta^{56}Fe_{extracted}$, Table 2-2). Depth and bulk density-weighted δ^{56}Fe values for HCl-extractable Fe (Table 2-4) show similar trends as bulk Fe (i.e., increasingly depleted isotopic signatures from the ridge top to the valley floor and stream sediments). Values were weighted with the following equation:

$$[\delta^{56}Fe_{bulk}]_{wt} = \frac{\sum_i [\delta^{56}Fe_{bulk}]_i (z_i^{top} - z_i^{bottom}) \rho_w (z_i^{mid})}{\sum_i (z_i^{top} - z_i^{bottom}) \rho_w (z_i^{mid})} \quad (2\text{-}7)$$

Here, $[\delta^{56}Fe_{bulk}]_i$ is the isotopic composition of bulk Fe from some interval *i*, z_i^{top} is the top of the sampling interval *i*, z_i^{bottom} is the bottom of sampling interval *i,* and $\rho_w(z_i^{mid})$ is the estimated bulk density for the middle depth of each sample. Note that where samples were taken over intervals that did not sum to L, we assumed that the concentration of samples could be extrapolated over sampling intervals that sum to L.

2-4. DISCUSSION

2-4.1. Abiotic and Biotic Iron Transformations

Along the hillslope, Fe was lost due to the weathering of illite and chlorite (Table 2-1, see also Jin et al. (2010)). Furthermore, based on the $\tau_{Zr,Fe\ in\ illite}$ and $\tau_{Zr,Fe\ in\ "chlorite"}$ values (Table 2-1), a larger fraction of Fe was lost from illite than from "chlorite" at the ridge top. In contrast, in the valley floor, the fractional loss of Fe from illite and "chlorite" is equivalent. Differences between Fe loss from the ridge versus valley might therefore be due to weathering initiating as illite dissolution, followed by later weathering of "chlorite." Indeed, weathering of illite is thought to initiate beneath the bedrock-regolith interface (Jin et al., 2010; 2011a). As weathering progresses, Fe is subsequently lost from "chlorite" (Table 2-1).

The nature of the lost Fe from the hillslope is not well understood. Iron can be transported in soils as aqueous organic complexes, as clays or as Fe $\pm$ Si $\pm$ Al $\pm$ organic colloids up to 1 μm in diameter (Buffle et al., 1998; Riise et al., 2000). The 1.3-μm pores of the lysimeters should allow for the entry of Fe-bearing complexes or colloids. The observation of depletion profiles for Fe along the hillslope in combination with the lack of significant Fe in both filtered and unfiltered lysimeter samples is consistent with Fe transport as particulates larger than 1.3 μm. Particulate Fe (with Al, Si and Ti) is also likely to be present in ground-, stream- and macropore-water because we observed different concentrations of those elements in unfiltered versus filtered samples (Table C-7). Since macropore flow at the stream channel was only observed during high water table periods, ground- or stream-water may be flowing within stream channel macropores during those storm periods. When the water table is low, the stream water may be dominated by ground water.

Although net Fe is lost overall from the catena, positive $\tau_{Zr,Fe\ in\ Fe\ oxide}$ values document retention of some Fe as reprecipitated Fe (oxyhydr)oxides (Table 2-1). The identity of reprecipitates has not been established due to their low abundance. However, reddish coloration in upslope soils is consistent with hematite and/or ferrihydrite whereas the yellow hue in the toeslope is consistent with goethite, a mineral which precipitates under wetter conditions (Violante et al., 2002). Wetter conditions are indeed expected at the toeslope as the groundwater table rises and falls. Similar red to yellow soil toposequences have previously been noted in Brazil and Malawi (Schwertmann, 1988).

Values of $\tau_{Zr,Fe(II)}$ and $\tau_{Zr,Fe}$ along the catena clarify how and where these processes occur. At the ridge top, more negative values of $\tau_{Zr,Fe(II)}$ than $\tau_{Zr,Fe}$ indicate that more Fe(II) than total Fe was lost. This finding is likely due to either i) preferential removal of Fe(II) compared to Fe(III), or ii) oxidation of Fe(II) to Fe(III) without net Fe loss. The second scenario is more likely based on arguments of mass balance. Specifically, Equation 2-5 yields calculated losses from the ridge top cores of $m_{Fe(II)}$ = 1,500 g Fe(II)/m^2 and m_{Fe} = 2,500 g Fe/m^2 (Table 2-3). The ratio of Fe(II)/Fe(total) in the "lost" Fe is therefore 60% (1,500 g Fe(II) m^{-2}/2500 g Fe(II) m^{-2}), much higher than the ratio in parent shale (~25%). It is unlikely that extensive Fe reduction occurs in regolith at the ridge top given the red hue. In addition, we observed evidence for Fe oxidizers but not reducers in the ridge top soils (Table C-3). Therefore, ~50% of the Fe(II) (~750 g Fe(II)/m^2) at the ridge top was likely released from bedrock, oxidized biotically or abiotically and

precipitated *in situ* while the other 50% was lost either as dissolved or particulate Fe. Like the ridge top, middle slope soils are also reddish and showed evidence for the presence of Fe oxidizers. Therefore, the more depleted $\tau_{Zr,Fe(II)}$ relative to $\tau_{Zr,Fe}$ values in the upper portions of the middle slope are also attributed to oxidation and reprecipitation of Fe(II) released from "chlorite" or illite.

Toeslope soils also have more depleted values of $\tau_{Zr,Fe(II)}$ relative to $\tau_{Zr,Fe}$ (Fig. 2-3D). Furthermore, there is no evidence for elevated Fe(II)/total Fe ratios in the toeslope samples (Table 2-2). This observation may appear to be contradictory, however, because the toeslope is the wettest of the four topographic positions. In the toeslope, for example, gravimetric soil moisture levels as high as 0.72 g water/g dry soil were measured in comparison to maximum values of 0.16 and 0.13 g/g at the ridge top and middle slope, respectively (Table C-9). In addition, the oxygen sensors documented that anoxia occasionally occurs in the valley floor (Fig. 2-2). Consistent with anoxia, moderate gleying, a feature that is generally associated with low redox potential (Vodyanitskii, 2007), was observed in the lower portion of the toeslope profile. Gleying generally results from the removal of Fe (oxyhydr)oxides (e.g.,Vodyanitskii et al., 2007) and is commonly associated with increased Fe(II) content (Vodyanitskii et al., 2007). The adsorption of as little as 10% Fe(II) onto Fe (oxyhydr)oxide minerals can produce gleying (Vodyanitskii et al., 2007). Finally, the toeslope was the only location from which Fe-reducing bacteria were cultured using the *Shewanella* medium (Figure C-3).

Based upon the above evidence, it might therefore be expected that the toeslope would be a site of Fe(II) accumulation. The fact that the toeslope is instead a site of Fe(III) accumulation may be due to the fact that it is made up largely of well-oxidized material derived from upslope positions. In other words, much of the accumulated Fe in the toeslope may actually have precipitated at higher hillslope positions and have then been transported to the toeslope postion. Furthermore, while Fe(II) may indeed be produced by Fe reduction in the valley floor, the proximity of the toeslope to the stream suggests that any accumulated Fe(II) might be periodically flushed out of the profile.

This geochemical evidence is consistent with the microbiological observations. Specifically, aerobic Fe-related bacteria were documented at all locations along the catena, especially in the uppermost soil horizons and within 15 cm of the soil/bedrock interface (Figure

C-3). In contrast, the culturing experiments documented that Fe reducing cells could only be cultured from the upper layers of the valley soils.

The pattern of Fe oxidizing bacteria with respect to landscape position and depth (Figure C-3) contrasts markedly with the data for total bacterial cell counts. Total cell counts decrease with depth at Shale Hills (Table C-9; Figure C-2), as observed in the Puerto Rico site as well as other topsoils (Brady and Weil, 2008; Maier et al., 2009). Some of this decrease is likely related to the decrease in total C and N with depth (Table C-8). Likewise, the presence or absence of Fe oxidizers is in contrast to the observations of heterotrophic cell abundance. At Shale Hills as well as in other locations (Bundt et al., 2001), the density of heterotrophic cells roughly vary with the concentrations of dissolved organic carbon (DOC). For example, the Bw/Bt interface at 30-cm depth in the footslope is high in both DOC (Andrews et al., 2011) and concentration of heterotrophs (Table C-9). Therefore, while total cell counts and heterotroph cell densities vary with soil properties related to C and/or N, the abundance of Fe oxidizers appears to be related more closely to the presence or absence of specific mineral weathering reactions.

In fact, Fe oxidation, possibly catalyzed by Fe-oxidizing bacteria near the bedrock-regolith interface, has been invoked as a possible initiator of weathering in some systems. Specifically, a lithoautotrophic Fe(II)-oxidizing community was identified at the bedrock-regolith interface of quartz diorite in Puerto Rico (Buss et al., 2005; Minyard et al., 2011). Buss et al. (2005; 2010) argued that the bacteria are coupled to the transformation of bedrock into regolith because the density of Fe oxidizers was high in topsoil (upper meter), low in saprolite at mid-depth, but again high at the bedrock interface (5 meters depth) – a pattern also exhibited for the much shallower Shale Hills soil (Figure C-3). It is therefore possible that Fe oxidation, possibly catalyzed by Fe oxidizing bacteria, also contributes to the weathering-driven disaggregation of bedrock in Shale Hills.

2-4.2. Hillslope Mass Balance

This discussion of Fe transport along the hillslope can be elucidated by calculating mass balance for a "reactor-on-a-slope" model. Net weathering fluxes were calculated by simulating the transect as a series of reservoirs (see Appendix C, Jin et al., 2010, for details). The model assumes a steady-state soil thickness and chemistry and incorporates both erosion (= loss of soil

that has the same composition as the average soil) and weathering (= loss of material whose composition differs from the average soil). The model also utilizes values of the measured soil production rate for each position (Ma et al., 2010). Calculated net weathering fluxes (W_{Fe} and $W_{Fe(II)}$, g Fe m^{-2} yr^{-1}) were determined for each topographic position. Furthermore, inputs into the middle slope were set equal to the output from the ridge top and inputs into the valley floor were set equal to output from the middle slope.

Positive values for the total Fe weathering flux at the ridge top and middle slope (W_{Fe} in Table C-11) are consistent with net loss of total Fe during weathering from these positions (Table C-11), while negative values in the footslope and toeslope are consistent with net accumulation of total Fe. Similar values are obtained regardless of whether constant or varying soil production rates (from Ma et al., 2010) are used (Table C-11)). These values indicate that, despite negative $\tau_{Zr,Fe}$ values in the valley floor indicative of Fe loss from the profile over the history of the catchment, the valley floor is currently a site of Fe accumulation. Consistent with conclusions from Section 2-4.1, $W_{Fe(II)}$ values indicate net transport of Fe(II) out of the ridge top, middle slope and toeslope (positive values, Figure C-11) but net accumulation of Fe(II) in the footslope.

2-4.3. Iron Isotope Systematics in the Shale Hills Watershed

2-4.3.1 Significance of Iron Isotope Systematics During Shale Weathering

The long-term evolution of the Fe isotopic signature of the ocean is determined partly by riverine $\delta^{56}Fe$, and controls on this value are not well constrained. Various studies have shown that riverine Fe is generally isotopically light relative to continental rocks, though more complicated river systematics have been invoked (Fantle and DePaolo, 2004; Bergquist and Boyle, 2006; Ingri et al., 2006). Furthermore, the utility of Fe isotopes as a marine proxy for examining the past depends on knowing which processes can alter the isotopic composition of the ocean. Our study contributes to a developing understanding of the effects of weathering on Fe isotopic composition. Extrapolating from the results summarized here, Fe is apparently mobilized during shale weathering as micron-sized particles with an Fe isotopic composition of ~0.8‰ ±0.3‰. This differs from previous weathering studies on other lithologies and may help

explain observations in rivers of isotopically heavy Fe in (oxyhydr)oxide colloids (Ingri et al., 2006).

In addition to providing insight into global fluxes, Fe isotopes can be a useful tracer of processes within a catchment. Determining which processes are acting in the local Fe cycle is fundamental from a variety of perspectives, from understanding nutrient loss over time to the successful coupling of local- and regional-scale Fe cycles to complex global climate models. Previous work indicates that reduction- and ligand-promoted dissolution of minerals preferentially releases the light isotopes into solution, creating residual soil Fe that is isotopically heavy (Beard et al., 1999; Brantley et al., 2001; Liermann et al. 2011). Using Fe isotopes, researchers have thus been able to hypothesize the processes responsible for Fe mobilization (Thompson et al. 2007; Wiederhold et al. 2007b).

Previous experimental work demonstrated that Fe released during dissolution of the Rose Hills shale in the presence of siderophores was isotopically fractionated (Δ~ -0.15‰) relative to the starting rock (Liermann et al., 2011). Extrapolating this laboratory work to the catchment, we expected to see isotopically enriched Fe in the soils. However, at Shale Hills, our observation is that the regolith becomes *lighter* with increasing extent of Fe loss (i.e., more negative $\tau_{Zr,Fe}$ values; Fig. 2-5). Furthermore, in contrast to the findings of Buss et al. (2010) in an Puerto Rico quartz diorite, there was no clear evidence of a relationship between δ^{56}Fe values of HCl-extracted Fe and the abundance of Fe-oxidizing bacteria. In order to explain data at Shale Hills, we therefore propose two models: the first invokes Fe isotopic fractionation during mobilization of Fe, while the second invokes fractionation during the immobilization of Fe (Fig. 2-6).

2-4.3.2. Mechanism I

The first model (Fig. 2-6), which is based on the assumption that fractionation depends solely upon Fe mobilization, is driven by the observation of Fe loss from the ridge top to the footslope (valley floor). Coincident with this trend in Fe loss are the observations that all 0.5 N HCl leachates are isotopically lighter than bulk Fe, and bulk δ^{56}Fe values also get lighter from the ridge top to footslope. According to this model, this is explained by a mobile phase that is isotopically lighter than the soil/parent.

Specifically, we hypothesize in Mechanism I that weathering mobilizes Fe that is isotopically lighter than the parent. Such a process is consistent with the batch experiments by Liermann et al. (2011) where the Fe that accumulated in a solution containing a strong siderophore was isotopically light ($\delta^{56}Fe_{solution}$-$\delta^{56}Fe_{solid}$ = -0.15‰) after 21 days of incubation with Rose Hill shale. Regardless of how fractionation occurs during mobilization, however, Fe moves out of the upslope soil profiles under wetter conditions in this scenario and is transported down hillslopes in pore waters largely at soil/horizon interfaces (Jin et al., 2011a). In downslope accumulation zones, Fe (oxyhydr)oxides partially precipitate, either due to biotic or abiotic causes. According to published reports, iron (oxyhydr)oxides can be either similar or isotopically depleted relative to $Fe(III)_{aq}$ from which they have precipitated, depending upon whether equilibrium or kinetic conditions prevail (Skulan et al., 2002).

In effect, the proposed model suggests that isotopically light Fe is generated by dissolution, perhaps mediated by organic complexes or bacterially-mediated processes; this Fe is then moved through the ridge top and middle slope soils and partially reprecipitates in foot- and toeslope soils. It is likely that iron is initially immobilized as amorphous Fe (oxyhydr)oxides (e.g., ferrihydrite), which explains the isotopically light HCl extracts. As the amorphous phase ages, crystalline minerals such as hematite and goethite form, taking on the $\delta^{56}Fe$ of the precursor phase.

It is of course also possible that plants preferentially extract isotopically light Fe along the hillslope (Guelke and von Blanckenburg, 2007). However, there is no clear isotopic evidence for this process at Shale Hills. For instance, $\delta^{56}Fe$ values in surface horizons of the ridge top, in which organic carbon is abundant (Table C-8), are not substantially lighter than the underlying soils (Fig. 2-4). This is true for both total and HCl-extracted Fe (Fig. 2-4). Thus, plant uptake is not thought to be a major mechanism for Fe isotope fractionation in the watershed.

Complications arise with this model, however, when one considers a watershed-scale mass balance. According to this model, the generation of a mobile Fe pool that is isotopically light implies that Fe lost from the watershed is likewise light; this then requires a pool of isotopically heavy Fe to be present in the watershed. At this point, this pool has not been identified. On the contrary, all measured soil samples were isotopically lighter than bedrock values (Table 2-2; Fig. 2-4); weighted $\delta^{56}Fe$ values of bulk Fe decrease from 0.31‰ in the bedrock to 0.27‰ at the ridge top and 0.22‰ in the middle slope (Table 2-4).

One possible explanation for this contradiction may be that the two bedrock samples analyzed are not representative of the isotopic composition of bedrock underlying the south planar hillslope. The bedrock analyzed was obtained from a location with steeply-dipping bedding at the northern ridge top. Based upon three 18-meter cores obtained from the valley floor of the watershed, however, the mean Fe composition was 5.6 wt.% $\pm$ 0.5% (1σ) (n=53) (unpub. data), documenting chemical homogeneity of Fe in the Rose Hill section.

However, Liermann et al. (2010) report the Fe isotopic composition (+0.11‰) of a consolidated shale sample made up of over ten sampling depths from the upper 17 m from the north drillcore DC1. In the present work, we considered that the upper 1-meter and 6- meter bedrock layers of DC1 were better indicators of the parent isotopic composition than the deeper layers of DC1. If, instead, we considered the Liermann et al. value as parent, this value is 0.2‰ heavier than that used in our calculations. Even with this assumption of a different parent isotopic composition, however, the hillslope data shows overall loss of isotopically heavy Fe that cannot be completely explained.

2-4.3.3. Mechanism II

We present an alternative model in which we assume that Fe mobilization occurs without fractionation, releasing both aqueous Fe(II) and Fe(III) with a value of $\delta^{56}Fe = 0.3‰$ as observed in the bedrock (Fig. 2-6). The assumption of no fractionation during mobilization seems plausible; the well-oxidized conditions at the ridge top limit the extent of dissimilatory iron reduction and favor proton-promoted dissolution, which may not fractionate isotopically (Wiederhold et al., 2006). Due to the well-oxidized nature of most of the hillslope, it is further assumed that all $Fe(II)_{aq}$ is completely oxidized to $Fe(III)_{aq}$ in upslope positions. In contrast with Model 1, the second model assumes that fractionation occurs as secondary Fe (oxyhdr)oxides are precipitated.

As discussed in Section 2-4.1, the yellow hue observed in the toeslope is consistent with goethite, a precipitate which is favored by wetter conditions (Violante et al., 2002). Skulan et al. (2002) have shown that, due to kinetic effects during precipitation, Fe (oxyhydr)oxides (hematite) can be isotopically lighter than $Fe(III)_{aq}$ by 1.3‰ (i.e., $10^3 \ln\alpha = -1.3$; $\alpha = 0.9987$ between hematite and $Fe(III)_{aq}$). In one soil, Mansfeldt et al. (2011) further noted an inverse

relationship between soil δ^{56}Fe and goethite abundance that could be interpreted as a control by goethite precipitation.

In order to gauge the appropriateness of the model, we constructed a mass balance equation that describes the δ^{56}Fe of Fe lost to the mobile reservoir from each soil profile:

$$\delta^{56}Fe_{mobile} = \frac{\delta^{56}Fe_{parent} - [\delta^{56}Fe_{soil}]_{wt} f_{soil}}{f_{mobile}} \quad (2\text{-}8)$$

Where $\delta^{56}Fe_{parent}$ is the isotopic composition of parent material, $[\delta^{56}Fe_{soil}]_{wt}$ is the depth and bulk density-weighted δ^{56}Fe value for each soil profile as determined by Equation 7 (Table 2-4), and f_{mobile} is the fraction of Fe lost from each profile, as determined by $\tau_{Zr,Fe}$ values (Equation 2-7; Table 2-3); we also assumed $f_{mobile} = 1 - f_{soil}$. The average calculated δ^{56}Fe value for Fe lost from the profiles, $\delta^{56}Fe_{mobile}$, is ~0.8‰ (Table 2-5). The calculated δ^{56}Fe of the mobile pool at each site ranges from 0.6‰ (middle slope) to 1.3‰ (toeslope) (Table 2-5).

Assuming that precipitation of Fe (oxyhydr)oxides occurs in a single step, we use a Rayleigh model to estimate the fraction of Fe removed from solution during precipitation:

$$\delta^{56}Fe(III)_{aq} = (\delta^{56}Fe(III)_{aq,i} + 10^3) f^{\alpha-1} - 10^3 \quad (2\text{-}9)$$

$$\delta^{56}Fe_{ppt,inst} = (\delta^{56}Fe(III)_{aq,i} + 10^3)\alpha f^{\alpha-1} - 10^3 \quad (2\text{-}10)$$

$$\delta^{56}Fe_{ppt,cum} = (\delta^{56}Fe(III)_{aq,i} - (f * \delta^{56}Fe(III)_{aq}))/(1-f) \quad (2\text{-}11)$$

Where $\delta^{56}Fe(III)_{aq}$ is the composition of Fe(III) remaining in solution during precipitation (set equal to $\delta^{56}Fe_{mobile}$ for each profile), $\delta^{56}Fe_{ppt,inst}$ refers to the instantaneous isotopic composition of the precipitate during precipitation, and $\delta^{56}Fe_{ppt,cum}$ refers to the cumulative composition of the precipitate that has accumulated. In each equation, $\delta^{56}Fe(III)_{aq,i}$ is the composition of the Fe initially dissolved from the mineral prior to any reprecipitation (set equal to $\delta^{56}Fe_{bedrock}$ = 0.31‰), α is the assumed isotopic fractionation factor between $Fe(III)_{aq}$ and precipitated Fe (α = 0.9987, from Skulan et al., 2002), and f is the fraction of $Fe(III)_{aq}$ remaining in solution.

If a single cycle of precipitation is appropriate for simulating the Fe isotope systematics in these soils, our analysis implies that ~20-50% of all Fe released into solution during soil

weathering in the catchment precipitates as an Fe (oxyhydr)oxide phase (Table 2-5; Fig. 2-7). These calculated values range from a minimum of 20% in the middle slope to a maximum of 52% in the toeslope (Table 2-5). Because there must be an isotopic offset expressed between parent and bulk soil, we hypothesize that the remaining 50-80% of the Fe is lost from the hillslope (perhaps as isotopically-heavy colloids).

According to the predictions of Mechanism 2, the precipitated Fe (oxydr)oxide phases in each soil profile are isotopically lighter than bedrock and can therefore explain the isotopically depleted HCl-extracted fractions throughout the hillslope. However, the predicted isotopic values of HCl-extracted Fe (designed to remove secondary precipitated phases) are lighter than the actual values by up to 0.5‰. For example, these calculated values from Equation 2-11 range from -0.80‰ to -0.86‰ in the ridge top, middle slope and footslope, and -0.58‰ in the toeslope (Table 2-5). Several reasons may explain HCl-extracted values that are less depleted than those calculated by Mechanism 2. For example, the α value (Skulan et al., 2002) used in Equations 9-11 may be too large to describe processes occurring in Shale Hills.

A second possibility for the discrepancies noted above involve possible artifacts in the HCl extraction. For example, Chapman et al. (2009) suggested that HCl extractions of granites and basalts resulted in the release of very small amounts of Fe from silicates (with 0.5% of the silicates being leached over 48 hours). The amount of aluminum released into solution by the HCl extraction in this study was up to 5% of the total amount of Al by mass (Table C-10), indicating that a possible contribution from isotopically heavier Fe from silicate leaching may enrich the HCl-extracted fraction. While some of the Al may be associated with Fe (oxyhydr)oxide phases, we cannot rule out the possibility that a small amount may be derived from the dissolution of silicate minerals.

The hypothesis that isotopically heavy Fe-rich colloids form in soils, and are then transported out of soils to streams, is consistent with previous work suggesting isotopic fractionation during particle formation. Escoube et al. (2009) measured dissolved Fe (<0.22 μm) that was isotopically heavier than particulate Fe (>0.22 μm) in the North River of Massachusetts by 0.5‰. Just as we hypothesize is happening at Shale Hills, Escoube et al. (2009) attributed these differences to the preferential enrichment of ^{56}Fe in solution as isotopically light Fe-bearing precipitates form. Bergquist and Boyle (2006) also observed isotopically enriched dissolved Fe relative to particulate Fe in the Negro River of the Amazon System.

At the moment, the role that lithology plays in determining the isotopic signature of Fe mobilized from a given watershed is not definitive. Mechanism 2 suggests that shales may behave distinctly from other rock types in terms of Fe isotope fractionation during weathering. In contrast, Mechanism 1 implies the loss of isotopically light iron into streams, and such losses have been noted for other lithologies as well.

2-5. CONCLUSIONS

This study provides the first Fe isotopic data for a weathering hillslope. Both total Fe and Fe(II) are lost from all topographic positions along the hillslope developed on Rose Hill shale as weathering proceeds, with much of the mobilized Fe(II) ultimately being reprecipitated as Fe(III) (oxyhydr)oxides. It is possible that some or all of this oxidation is mediated by Fe-oxidizing bacteria because we observed evidence for their presence throughout the hillslope. The lack of dissolved Fe in pore-water samples is consistent with the conclusion that Fe (along with Al, Ti and Si) is lost mostly as micron-sized particles. Such particles are present in groundwater beneath the catchment valley floor, in the stream and in fluids emitting from stream banks during high water conditions. This work indicates that the isotopic signature of bulk soil Fe becomes increasingly light with increased weathering along the hillslope, a finding that was initially unexpected. Two simplified models were invoked to explain isotopic fractionation in the Shale Hills watershed. The first model involves fractionation upon mobilization of Fe as a result of processes such as dissimilatory iron reduction or ligand-promoted dissolution, both of which are capable of producing isotopically light iron in solution. According to this first model, fractionation occurs upon dissolution rather than during the precipitation of Fe (oxyhydr)oxides. Precipitation of the light Fe in soils near the valley floor leaves those soils isotopically depleted. The second simplified model involves fractionation not with the dissolution step but rather during the precipitation step. Future work is needed to isolate and analyze micron-sized particles from the watershed. While the first model suggests that these particles will be isotopically depleted in Fe, the second model suggests isotopic enrichment. If the latter model is true, shales, which comprise almost one quarter of continental rocks (Amiotte-Suchet et al., 2003), could be important sources of isotopically heavy Fe to rivers worldwide.

Acknowledgements. We thank H. Gong and W. Castro for ICP-AES and ICP-MS analysis and Katherine Lindeburg for advice. Funding for this project was provided by National Science Foundation under Grant No. CHE-0431328 for Center for Environmental Kinetics Analysis (SLB) and by Grant No. EAR-0725019 to Chris Duffy (PSU) for the Susquehanna/Shale Hills Critical Zone Observatory. Liermann was supported by NSF EAR 05-19144. Logistical support and/or data were provided by the NSF-supported Shale Hills Susquehanna Critical Zone Observatory.

REFERENCES:

Amiotte-Suchet, P., Probst, J. L., and Ludwig, W., 2003, Worldwide distribution of continental rock lithology: Implications for the atmospheric/soil CO_2 uptake by continental weathering and alkalinity river transport to the oceans. Global Biogeochem. Cycles 17: 1038-1051.

Anbar, A.D., Roe, J.E., Barling, J., and Nealson, K.H., 2000, Nonbiological fractionation of iron isotopes. Science 288: 126-128.

Anderson, S.P., Dietrich, W.E., and Brimhall, G.H., 2002, Weathering profiles, mass-balance analysis, and rates of solute loss: Linkages between weathering and erosion in a small, steep catchment. Geol. Soc. Am. Bull. 114: 1143-1158.

Andrews, D.M., Lin, H., Zhu, Q., Jin, L., and Brantley, S.L., 2011, Hot Spots and Hot Moments of Dissolved Organic Carbon Export and Soil Organic Carbon Storage in the Shale Hills Catchment. Vadose Zone J. 10: 943-954.

Beard, B.L., and Johnson, C.M., 2004, Fe isotope variations in the modern and ancient Earth and other planetary bodies. In Reviews in Mineralogy and Geochemistry: Geochemistry of non-traditional Stable Isotopes (eds. C. M. Johnson, B.L. Beard and F. Albarede). The Mineralogical Society of America, Washington, D.C. pp. 319-357.

Beard, B.L., Johnson, C.M., Cox, L., Sun, H., Nealson, K.H., and Aguilar, C., 1999, Iron isotope biosignatures. Science 285: 1889-1892.

Bergquist, B.A., and Boyle, E.A., 2006, Iron isotopes in the Amazon River system: Weathering and transport signatures. Earth Planet. Sc. Lett. 248: 54-68.

Bern, C.R., and White, A.F., 2011, A model for assessing, quantifying, and correcting for index element mobility in weathering studies. Appl. Geochem. 26: S9-S11.

Bern, C.R., Chadwick, O.A., Hartshorn, A.S., Khomo, L.M., and Chorover, J., 2011, A mass-balance model to separate colloidal and solute redistributions in soil. Chem. Geol. 282: 113-119.

Brady, N.C., and Weil, R.R., 2008, The Nature and Properties of Soils. Pearson Prentice Hall, Upper Saddle River, New Jersey. pp. 495-541.

Brantley, S.L., and Lebedeva, M., 2011, Learning to read the chemistry of regolith to understand the critical zone. Annu. Rev. Earth Planet. Sci. 39: 387-416.

Brantley, S.L., Liermann, L., and Bullen, T.D., 2001, Fractionation of Fe isotopes by soil microbes and organic acids. Geology 29: 535-538.

Brantley, S.L., Liermann, L.J., Anbar, A., Icopini, G.A., Guynn, R.L., and Barling, J., 2004, Fe isotopic fractionation during mineral dissolution with and without bacteria. Geochim. Cosmochim Ac. 68: 3189-3204.

Brantley, S.L., Ruebush, S., Jang, J., and Tien, M., 2006, Analysis of (bio)geochemical kinetics of Fe(III) oxides. In Methods of Investigating Microbial-Mineral Interactions (eds. P.A. Maurice and L. Warren). The Clay Minerals Society, Chantilly, VA. pp. 79-116.

Brimhall, G.H., and Dietrich, W.E., 1987, Constitutive mass balance relations betweenchemical composition, volume, density, porosity, and strain in metasomatic hydrochemical systems: Results on weathering and pedogenesis. Geochim. Cosmochim. Ac. 51: 567-587.

Buffle, J., Wilkinson, K.J., Stoll, S., Filella, M., and Zhang, J.W., 1998, A generalized description of aquatic colloidal interactions: The three-colloidal component approach. Environ. Sci. Technol. 32: 2887-2899.

Bundt, M., Jaggi, M., Blaser, P., Siegwolf, R., and Hagedorn, F., 2001, Carbon and nitrogen dynamics in preferential flow paths and matrix of a forest soil. Soil Sci. Soc. Am. J. 65: 1529-1538.

Buss, H.L., Bruns, M.A., Schultz, M.J., Moore, J., Mathur, C. F., and Brantley, S. L., 2005, The coupling of biological iron cycling and mineral weathering during saprolite formation, Luquillo Mountains, Puerto Rico. Geobiology 3: 247-260.

Buss, H.L., Mathur, R., White, A.F., and Brantley, S.L., 2010, Phosphorus and iron cycling in deep saprolite, Luquillo Mountains, Puerto Rico. Chem. Geol. 269: 52-61.

Chadwick, O.A., Brimhall, G.H., and Hendricks, D.M., 1990, From a black to a gray box-a mass balance interpretation of pedogenesis. Geomorphology 3: 369-390.

Chapman, J. B., Weiss, D.J., Shan, Y., and Lemburger, M., 2009, Iron isotope fractionation during leaching of granite and basalt by hydrochloric and oxalic acids. Geochim. Cosmochim. Ac. 73: 1312-1324.

Cornell, R.M., and Schwertmann, U., 2003. The Iron Oxides: Structure, Properties, Reactions, Occurrences and Uses. Wiley-VCH, Weinheim, Germany.

Dauphas, N., and Rouxel, O., 2006, Mass spectrometry and natural variations of iron isotopes Mass Spectrom. Rev. 25: 831-832.

Egli, M., and Fitze, P., 2000, Formulation of pedologic mass balance based on immobile elements: A revision. Soil Sci. 165: 437-443.

Emmanuel, S., Erel, Y., Matthews, A., and Teutsch, N., 2005, A preliminary mixing model for Fe isotopes in soils. Chem. Geol. 222: 23-34.

Escoube, R., Rouxel, O. J., Sholkovitz, E., and Donard, O.F.X., 2009, Iron isotope systematics in estuaries: The case of North River, Massachusetts (USA). Geochim. Cosmochim. Ac. 73: 4045-4059.

Essington, M.E., 2004, Soil and Water Chemistry: An Integrative Approach. CRC Press, Boca Raton. pp. 1-34.

Fantle, M.S., and DePaolo, D.J., 2004, Iron isotopic fractionation during continental weathering. Earth Planet. Sc. Lett. 228: 547-562.

Guelke, M., and von Blanckenburg, F., 2007, Fractionation of stable iron isotopes in higher plants. Environ. Sci. Technol. 41: 1896-1901.

Goldich, S.S., 1984, Determination of ferrous iron in silicate rocks. Chem. Geol. 42: 343-347.

Hersman, L.E., 2000, The role of siderophores in iron oxide dissolution. In Environmental Microbe-Metal Interactions (ed. D.R. Lovley). ASM Press, Washington, D.C. pp.145-157.

Icopini, G.A., Anbar, A.D., Ruebush, S.S., Tien, M., Brantley, S.L., 2004. Iron isotope fractionation during microbial reduction of iron: the importance of adsorption. Geology. 32: 205–208.

Ingri, J., Malinovsky, D., Rodushkin, I., Baxter, D.C., Widerlund, A., Andersson, P., Gustafsson, O., Forsling, W., and Ohlander, B., 2006, Iron isotope fractionation in river colloidal matter. Earth Planet. Sci. Lett. 245: 792-798.

Jang, J.H., Mathur, R., Liermann, L.J., Ruebush, S., Brantley, S.L., 2008, An iron isotope signature related to electron transfer between aqueous ferrous iron and goethite. Chem. Geol. 250: 40–48.

Jin, L., Ravella, R., Ketchum, B., Bierman, P. R., Heaney, P., White, T. S., and Brantley, S. L., 2010, Mineral weathering and elemental transport during hillslope evolution: regolith formation on shale at Shale Hills Critical Zone Observatory. Geochim Cosmochim. Ac. 74: 3669-3691.

Jin, L., Andrews, D. M., Holmes, G. H., Lin, H., and Brantley, S. L., 2011a, Opening the "Black Box": Water Chemistry Reveals Hydrological Controls on Weathering in the Susquehanna Shale Hills Critical Zone Observatory. Vadose Zone J. 10: 928-942.

Jin, L., Rother, G., Cole, D. R., Mildner, D. F. R., Duffy, C. J., and Brantley, S. L., 2011b, Characterization of deep weathering and nanoporosity development in shale--A neutron study. Am. Mineral. 96: 498-512.

Kappler, A., Johnson, C. M., Crosby, H. A., Beard, B. L., and Newman, D. K., 2010, Evidence for equilibrium iron isotope fractionation by nitrate-reducing iron(II)-oxidizing bacteria. Geochim. Cosmochim. Ac. 74: 2826-2842.

Kiczka, M., Wiederhold, J. G., Frommer, J., Kraemer, S. M., Bourdon, B., and Kretzschmar, R., 2010, Iron isotope fractionation during proton- and ligand-promoted dissolution of primary phyllosilicates. Geochim. Cosmochim. Ac. 74: 3112-3128.

Kuntz, B.W., Rubin, S., Berkowitz, B., and Singha, K., 2011, Quantifying solute transport at the Shale Hills Critical Zone Observatory. Vadose Zone J. 10: 843-857.

Laffan, M.D., Daly, B.K., and Whitton, J.S., 1989, Soil patterns in weathering, clay translocation and podzolisation on hilly and steep land at port underwood, Marlborough Sounds, New Zealand: Classification and relation to landform and altitude. Catena 16: 251-268.

Liermann, L.J., Mathur, R., Wasylenki, L.E., Nuester, J., Anbar, A.D., and Brantley, S. L., 2011, Extent and isotopic composition of Fe and Mo release from two Pennsylvania shales in the presence of organic ligands and bacteria. Chem. Geol. 281: 167-180.

Lin, H., 2006, Temporal stability of soil moisture spatial pattern and subsurface preferential flow pathways in the shale hills catchment. Vadose Zone J. 5: 317-340.

Lin, H.S., Kogelmann, W., Walker, C., and Bruns, M.A., 2006, Soil moisture patterns in a forested catchment: A hydropedological perspective. Geoderma 131: 345-368.

Littke, R., Klussmann, U., Krooss, B., and Leythaeuser, D., 1991, Quantification of loss of calcite, pyrite, and organic matter due to weathering of Toarcian black shales and effects on kerogen and bitumen characteristics. Geochim. Cosmochim. Ac. 55: 3369-3378.

Lovley, D.R., and Phillips, E.J.P., 1986, Organic matter mineralization with reduction of ferric iron in anaerobic sediments. Appl. Environ. Microbiol. 51: 683-689.

Ma, L., Chabaux, F., Pelt, E., Blaes, E., Jin, L., and Brantley, S.L., 2010, Regolith production rates calculated with uranium-series isotopes at Susquehanna/Shale Hills Critical Zone Observatory. Earth Planet. Sc. Lett. 297: 211-225.

Ma, L., Jin, L., and Brantley, S.L., 2011, Geochemical behaviors of different element groups during shale weathering at the Susquehanna/Shale Hills Critical Zone Observatory. Appl. Geochem. 26: S89-S93.

Maier, R.M., Pepper, I.L., and Gerba, C.P., 2009, Environmental Microbiology, Second Edition. Elsevier Academic Press, Amsterdam. pp. 57-82.

Mansfeldt, T., Schuth, S., Hausler, W., Wagner, F., Kaufhold, S., and Overesch, M., 2012, Iron oxide mineralogy and stable iron isotope composition in a Gleysol with petrogleyic properties. J. Soil Sediment 12: 97-114.

Minyard, M.L., Bruns, M.A., Liermann, L.J., Buss, H.L., and Brantley, S.L., 2012, Bacterial associations with weathering minerals at the regolith-bedrock interface, Luquillo Experimental Forest, Puerto Rico. Geomicrobiology Journal. 29: 792-803.

NOAA, (National Oceanic and Atmospheric Administration) (2007) U.S. divisional and station climatic data and normals: Asheville, North Carolina, U.S. Department of Commerce, National Oceanic and Atmospheric Administration, National Environmental Satellite Data and Information Service, National Climatic Data Center.

Pierson-Wickmann, A., Reisberg, L., and France-Lanord, C., 2002, Behavior of Re and Os during low-temperature alteration: Results from Himalayan soils and altered black shales. Geochim. Cosmochim. Ac. 66: 1539-1548.

Poitrasson, F., Viers, J., Martin, F., and Braun, J., 2008, Limited iron isotope variations in recent lateritic soils from Nsimi, Cameroon: Implications for the global Fe geochemical cycle. Chem. Geol. 253: 54-63.

Qu, Y., and Duffy, C.J., 2007, A semidiscrete finite volume formulation for multiprocess watershed simulation. Water Resour. Res. 43, W08419.

Reasoner, D.J., and Geldreich, E.E., 1985, A new medium for the enumeration and subculture of bacteria from potable water. Appl. Environ. Microbiol. 49: 1-7.

Riise, G., Van Hees, P., Lundström, U., and Tau Strand, L., 2000, Mobility of different size fractions of organic carbon, Al, Fe, Mn and Si in podzols. Geoderma 94: 237-247.

Roden, E., 2008, Microbial controls on geochemical kinetics 1: fundamental and case study on microbial Fe(III) oxide reduction. In Kinetics of Water-Rock Interaction. (eds. S.L. Brantley, J.D. Kubicki and A.F. White). Springer, New York. pp. 335-415.

Ruebush, S.S., Icopini, G.A., Brantley, S.L., and Tien, M., 2006, In vitro enzymatic reduction kinetics of mineral oxides by membrane fractions from Shewanella oneidensis MR-1. Geochim. Cosmochim. Ac. 70: 56-70.

Schwertmann, U., 1988, Chapter 11: Occurrence and formation of iron oxides in various pedoenvironments. In Iron in Soils and Clay Minerals (eds. J.W. Stucki, B.A. Goodman and U. Schwertmann). D. Reidel Publishing Company, Dordrecht.

Schaetzl, R., and Anderson, S., 2009, In Soils: Genesis and Geomorphology. Cambridge University, New York. p. 483.

Schoenberg, R., and von Blanckenburg, F., 2005, An assessment of the accuracy of stable Fe isotope ratio measurements on samples with organic and inorganic matrices by high-resolution multicollector ICP-MS. Int. J. Mass Spectrom. 242: 257-272.

Skulan, J.L., Beard, B.L., and Johnson, C.M., 2002, Kinetic and equilibrium Fe isotope fractionation between aqueous Fe(III) and hematite. Geochim. Cosmochim. Ac. 66: 2995-3015.

Stookey, L.L., 1970, Ferrozine---a new spectrophotometric reagent for iron. Anal. Chem. 42: 779-781.

Thompson, A., Chadwick, O.A., Rancourt, D.G., and Chorover, J., 2006, Iron-oxide crystallinity increases during soil redox oscillations. Geochim. Cosmochim. Ac. 70: 1710-1727.

Thompson, A., Ruiz, J., Chadwick, O. A., Titus, M., and Chorover, J., 2007, Rayleigh fractionation of iron isotopes during pedogenesis along a climate sequence of Hawaiian basalt. Chem. Geol. 238: 72-83.

Tuttle, M.L.W., and Breit, G.N., 2009, Weathering of the New Albany Shale, Kentucky, USA: I. Weathering zones defined by mineralogy and major-element composition. Appl. Geochem. 24: 1549-1564.

Violante, A., Krishnamurti, G.S.R., and Huang, P.M., 2002, Impact of organic substances on the formation and transformation of metal oxides in soil environments. In Interactions between Soil Particles and Microorganisms. (eds. P.M. Huang, J.M. Bollag and N. Senesi). John Wiley & Sons. Ltd, New York City. pp. 133-188.

Vodyanitskii, Y., 2007, Reductive biogenic transformation of Fe(III)-containing phyllosilicates (review of publications). Eurasian Soil Sci. 40: 1355-1363.

Watson, S.W., Novitsky, T.J., Quinby, H.L., and Valois, F.W., 1977, Determination of bacterial number and biomass in the marine environment. Appl. Environ. Microbiol. 33: 940-946.

Wiederhold, J.G., Kraemer, S.M., Teutsch, N., Borer, P. M., Halliday, A.N., and Kretzschmar R., 2006, Iron isotope fractionation during proton-promoted, ligand-controlled, and reductive dissolution of goethite. Environ. Sci. Technol. 40: 3787-3793.

Wiederhold, J.G., Teutsch, N., Kraemer, S.M., Halliday, A.N., and Kretzschmar, R., 2007a, Ironisotope fractionation during pedogenesis in redoximorphic soils. Soil Sci. Soc. Am. J. 71: 1840-1850.

Wiederhold, J.G., Teutsch, N., Kraemer, S.M., Halliday, A.N., and Kretzschmar, R., 2007b, Iron isotope fractionation in oxic soils by mineral weathering and podzolization. Geochim. Cosmochim. Ac. 71: 5821-5833.

Woodruff, L.G., Cannon, W.F., Eberl, D.D., Smith, D.B., Kilburn, J. E., Horton, J. D., Garrett R.G., and Klassen, R.A., 2009, Continental-scale patterns in soil geochemistry and mineralogy: Results from two transects across the United States and Canada. Appl. Geochem. 24: 1369-1381.

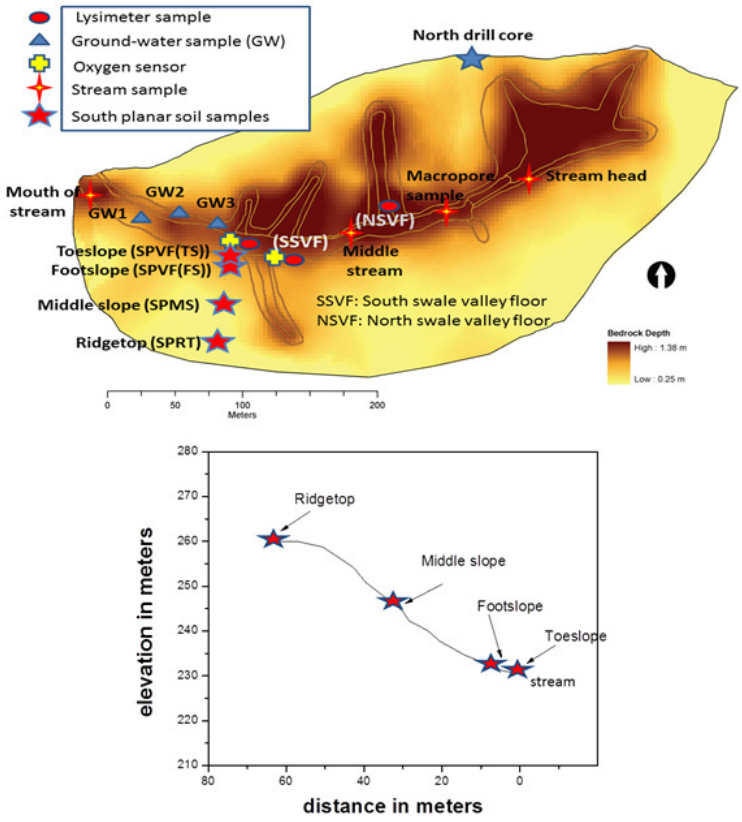

Figure 2.1. Above: An Arc-GIS map of the Shale Hills watershed showing sampling locations and depth to bedrock, where shading increases with depth of regolith (modified from Lin et al., 2006). Oxygen sensors are located at SPVF (south planar valley floor) and SSVF (south swale valley floor). Lysimeter nests are located at SPVF (south planar valley floor), SSVF (south swale valley floor) and NSVF (north swale valley floor). Below: Plot of elevation versus position down the south planar hillslope showing positions from upper map. Stars represent sampling locations, while solid line follows surface locations from which GPS measurements were taken along the transect.

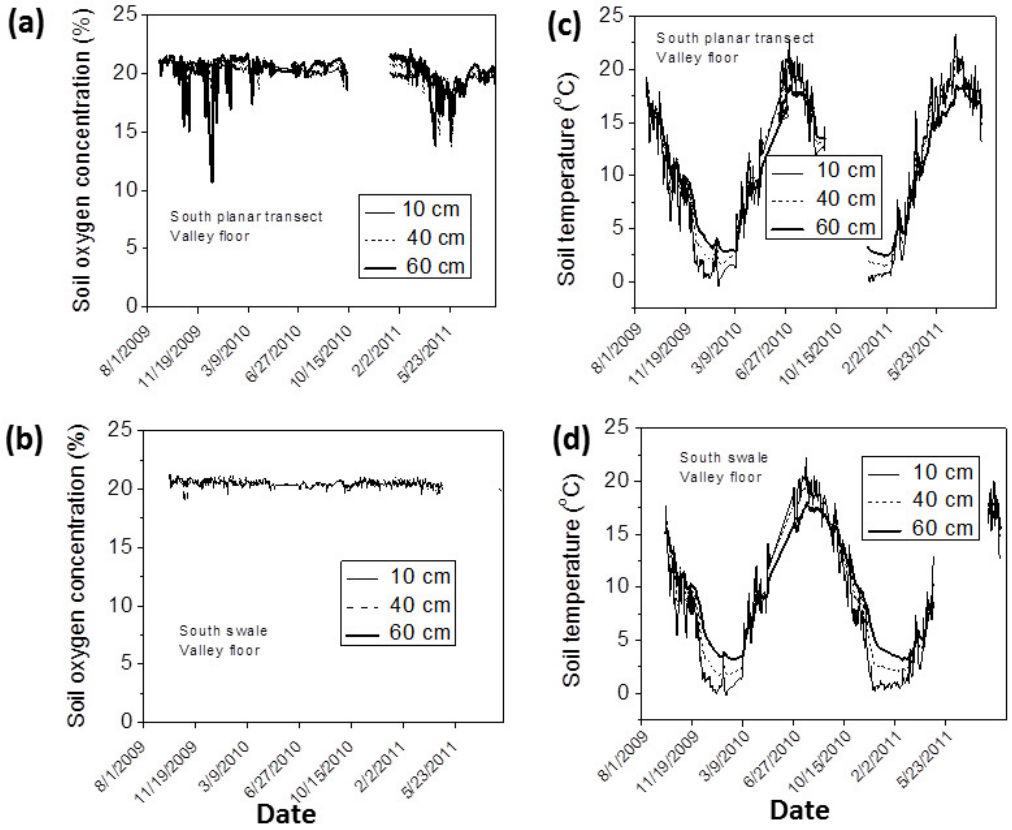

Figure 2-2. Soil oxygen concentrations in the valley floor (footslope) of the south planar (a) and south swale (b) transects plotted versus date of measurement. Similar plots for temperature at the valley floor (footslope) of the south planar hillslope (c) and south swale (d). Measurements at different depths using Apogee oxygen sensors are noted. All data were measured at 2:00 AM.

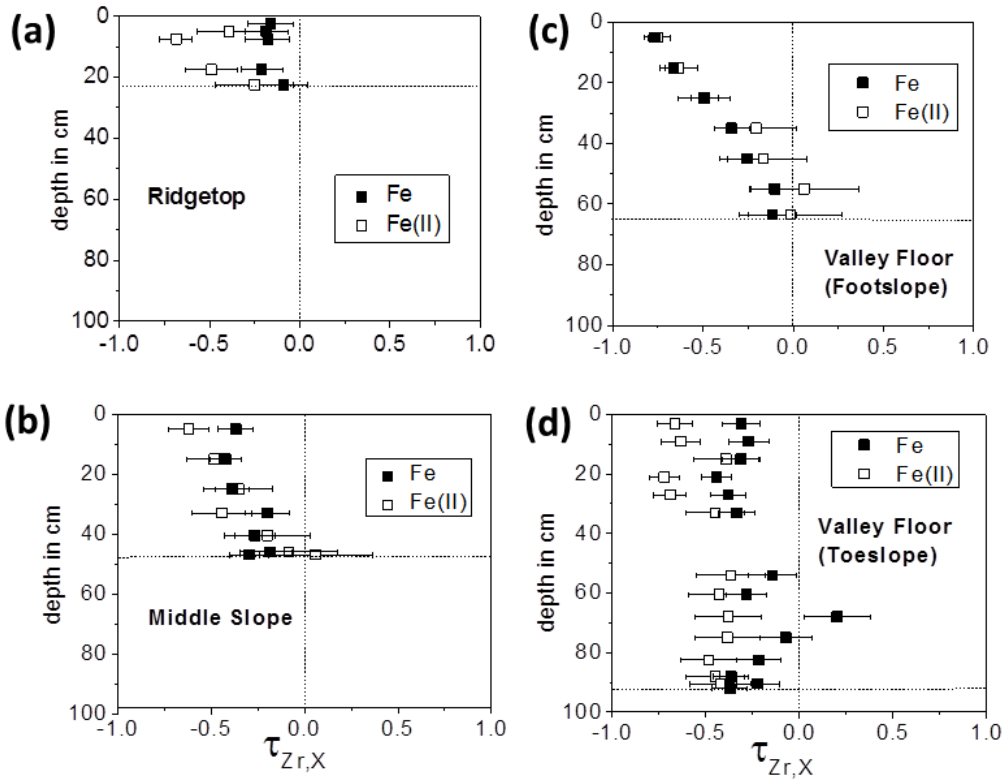

Figure 2-3. $\tau_{Zr,Fe}$ and $\tau_{Zr,Fe(II)}$ values versus depth at the ridge top (a), middle slope (b), valley floor footslope (c) and valley floor toeslope (d) for south planar transect. Characteristic error bars based upon an assumed analytical error of 3%, 10% and 20% for Fe, Zr and Fe(II) concentrations, respectively. Horizontal lines indicate depth to refusal.

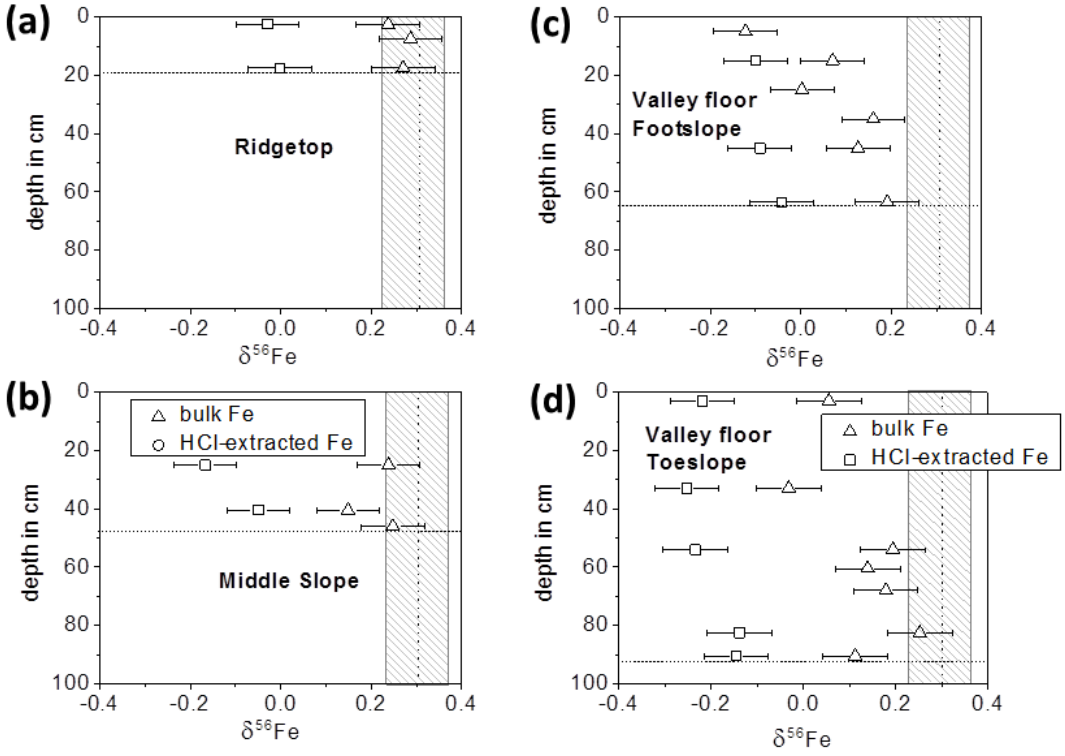

Figure 2-4. δ^{56}Fe values in bulk soil and in 0.5 N HCl-extractable Fe at the ridge top (a), middle slope (b), valley floor footslope (c) and valley floor toeslope (d). Error bars represent 1σ for replicate measurements of the IRMM-014 standard over a 10-day period. Vertical lines indicate the average composition of bulk Fe in the bedrock. Horizontal lines indicate depth to refusal.

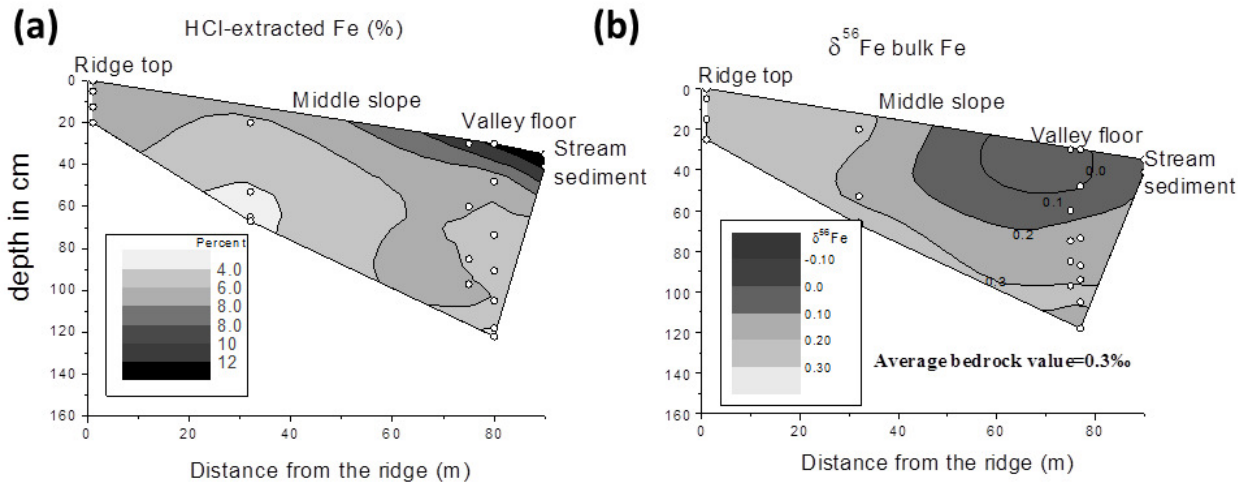

Figure 2-5. Contour maps showing the distribution of concentrations of HCl-extractable Fe (a) and δ^{56}Fe values in bulk Fe (b) across the south planar transect. Small circles indicate locations from which samples were obtained.

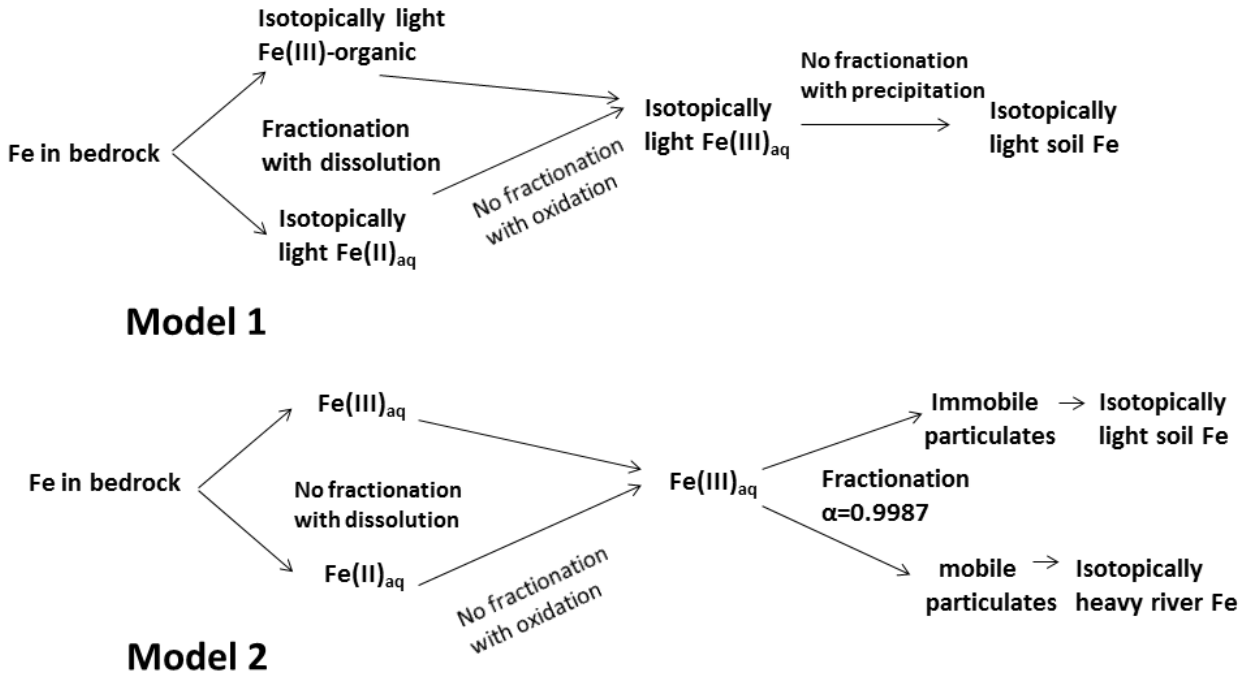

Figure 2-6. Two simplified models invoked to explain isotopic fractionation in the Shale Hills watershed. The first model involves fractionation upon dissolution as a result of processes such as dissimilatory iron reduction and ligand-promoted dissolution, both of which are capable of producing isotopically light iron in solution. According to the first model, fractionation does not occur upon precipitation of Fe (oxyhydr)oxides, only during dissolution. The second simplified model involves the same two steps, but fractionation does not occur with dissolution but rather during precipitation. During weathering under the second model, it is assumed that $Fe(II)_{aq}$ and $Fe(III)_{aq}$ are released from bedrock material without fractionation. $Fe(II)_{aq}$ is then assumed to be oxidized completely to $Fe(III)_{aq}$. Observed fractionation in the watershed is then explained using a fractionation factor between the retained Fe precipitate and the mobile Fe phase of 0.9987 (Skulan et al., 2002).

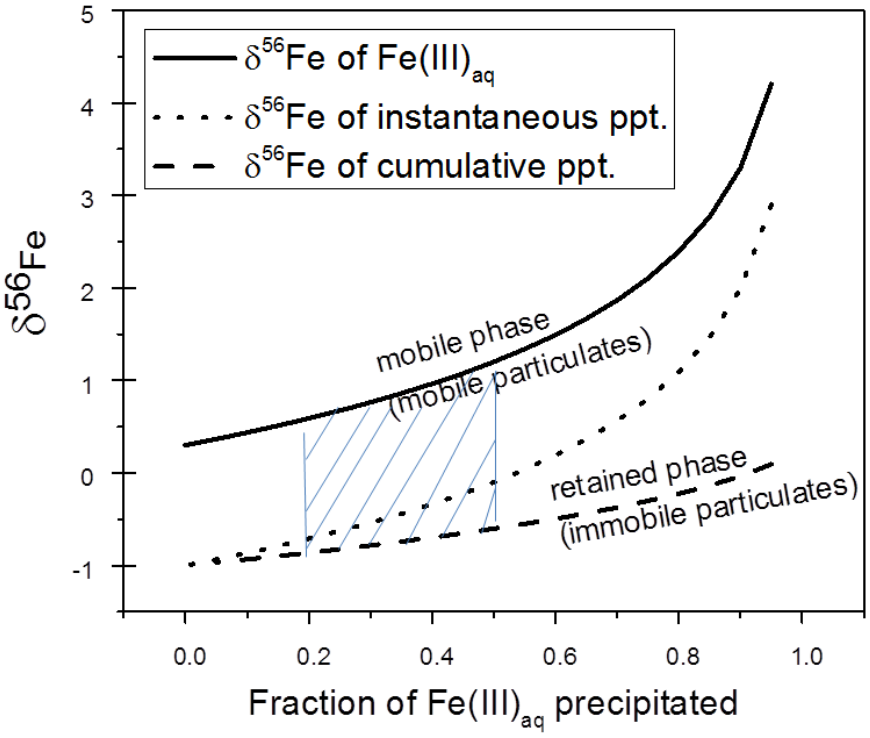

Figure 2-7. Changes in the Fe isotopic composition of $Fe(III)_{aq}$ (where $Fe(III)_{aq}$ could be true solute or colloidal Fe) and cumulative and instantaneous Fe (oxyhydr)oxide precipitate as the fraction of Fe precipitated from $Fe(III)_{aq}$ increases. A fractionation factor of α=0.9987 between hematite and $Fe(III)_{aq}$ from Skulan et al. (2002) is used. The upper line of the dashed box indicates the presumed isotopic composition of $Fe(III)_{aq}$ mobilized during weathering, which ranges from 0.6 to 1.3‰ based upon results from Equation 2-8. Assuming a single precipitation step, this implies that ~20-50% of the $Fe(III)_{aq}$ is precipitated.

Table 2-1: Fe mineralogy in regolith and bedrock

Sample name	Sampling location	Zr concentration (ppm)[1]	% "Chlorite"[2,3]	% Illite[2]	% Fe (oxyhyr)oxides[2,4]	% Total Fe as "chlorite"[5]	% Total Fe as illite[5]	% Total Fe as Fe (oxyhydr)oxide[5]	$\tau_{Zr,Fe\ in\ "chlorite"}$[6]	$\tau_{Zr,Fe\ in\ illite}$[6]	$\tau_{Zr,Fe\ in\ Fe\ (oxyhdr)oxides}$[6]
SPRT (0-10 cm)[7]	ridgetop	273	5.9	28.7	2.2	19.4	47.0	33.7	-0.4	-0.5	1.1
SPRT (20-30 cm)[7]	ridgetop	246	7.4	28.1	1.9	24.3	46.1	29.5	-0.2	-0.5	1.3
SPMS (0-10 cm)[7]	middle slope	351	5.9	24.8	1.9	21.7	45.5	32.7	-0.5	-0.7	0.7
SPMS (20-30 cm)[7]	middle slope	295	5.8	23.9	1.7	22.5	45.8	31.7	-0.4	-0.6	1.0
SPMS (50-59 cm)[7]	middle slope	266	7.6	31.8	1.7	23.9	50.1	25.9	-0.3	-0.5	0.7
SPVF(FS1) (0-10 cm)[7]	valley floor, footslope	349	4.2	21.5	1.4	19.3	49.3	31.4	-0.6	-0.6	0.6
SPVF(FS1) (30-40 cm)[7]	valley floor, footslope	219	7.5	44.5	1.0	21.7	64.0	14.3	-0.2	-0.2	0.2
SPVF(FS1) (60-67 cm)[7]	valley floor, footslope	191	7.6	55.8	1.2	18.5	67.6	13.9	-0.2	-0.1	0.3
Borehole DC1[8]	north ridge top	178	8.8	54.0	0.8	22.3	67.7	10.0	-	-	-

(1) As reported by Jin et al. (2010)

(2) Based upon quantitative XRD from Jin et al. (2010)

(3) Includes chlorite, illite and hydroxy-interlayered vermiculite

(4) Includes magnetite, hematite, goethite and maghemite

(5) Estimated using quantitative XRD data and mineral stoichiometries from Jin et al. (2010)

(6) Normalized to Zr as the immobile element

(7) Cores previously described by Jin et al. (2010); SPVF(FS1) is the same as SPVF in Jin et al. (2010)

(8) Analysis used for parent material, based upon averages from five drill core samples analyzed by Jin et al. (2010)

Table 2-2: Fe chemistry and isotope data

	mid-depth (cm)	Fe (wt. %)[1]	Fe(II) (wt. %)	Zr (ppm)[1]	$\tau_{Zr,Fe}$	$\tau_{Zr,Fe(II)}$	% Fe(II)/ total Fe	% Fe extractable[2]	δ^{56}Fe in bulk Fe	1 σ	n	δ^{56}Fe in HCl-extracted Fe	1 σ	n	Δ^{56}Fe[3]	δ^{56}Fe in non-extractable Fe[4]
ridgetop:																
SPRT2 (0-5 cm)	2.5	4.23	-	163	-0.16	-	-	6.6	0.24	0.03	3	-0.03	0.07	3	0.27	0.26
SPRT2 (5-10 cm)	7.5	4.87	0.8	194	-0.19	-0.39	17	6.8	0.29	0.06	3	-	-	-	-	-
SPRT2 (10-15 cm)	12.5	4.90	0.4	192	-0.18	-0.68	9	-	-	-	-	-	-	-	-	-
SPRT2 (15-20 cm)	17.5	4.79	0.7	196	-0.21	-0.49	14	7.8	0.27	0.03	2	0.00	0.03	3	0.27	0.29
SPRT2 (20-25 cm)	22.5	5.14	0.9	183	-0.09	-0.25	18	-	-	-	-	-	-	-	-	-
middle slope:																
SPMS2 (0-10 cm)	5	4.29	0.6	220	-0.37	-0.62	13	-	-	-	-	-	-	-	-	-
SPMS2 (10-20 cm)	15	4.44	0.9	249	-0.42	-0.49	20	-	-	-	-	-	-	-	-	-
SPMS2 (20-30 cm)	25	4.40	1.0	233	-0.39	-0.35	24	5.5	0.24	0.03	3	-0.17	0.05	3	0.41	0.26
SPMS2 (30-36 cm)	33	5.15	0.8	208	-0.20	-0.44	16	-	-	-	-	-	-	-	-	-
SPMS2 (36-45 cm)	41	4.80	1.2	212	-0.27	-0.20	24	3.7	0.15	0.06	3	-0.05	0.07	2	0.20	0.16
SPMS2 (45-47 cm)	46	5.04	1.3	200	-0.19	-0.08	25	3.6	0.25	0.05	2	-	-	-	-	-
SPMS2 (lowermost)	47	4.71	1.6	217	-0.30	0.06	34	-	-	-	-	-	-	-	-	-
footslope:																
SPVF(FS1) (0-10 cm)[5]	5	2.50	0.6	349	-0.77	-0.75	24	-	-0.12	-	-	-	-	-	-	-
SPVF(FS1) (10-20 cm)[5]	15	3.31	0.8	318	-0.66	-0.64	24	10.9	0.07	0.02	3	-0.10	0.01	3	0.17	0.09
SPVF(FS1) (20-30 cm)[5]	25	4.08	0.9	258	-0.49	-0.50	22	-	0.00	-	-	-	-	-	-	-
SPVF(FS1) (30-40 cm)[5]	35	4.45	1.2	219	-0.34	-0.21	27	-	0.16	-	-	-	-	-	-	-
SPVF(FS1) (40-50 cm)[5]	45	4.79	1.2	208	-0.25	-0.17	25	7.6	0.13	0.02	3	-0.09	0.02	3	0.22	0.15
SPVF(FS1) (50-60 cm)[5]	55	5.04	1.3	182	-0.10	0.06	26	-	-	-	-	-	-	-	-	-
SPVF(FS1) (60-67 cm)[5]	64	5.22	1.3	191	-0.12	-0.02	25	7.0	0.19	0.03	2	-0.04	0.06	3	0.23	0.21
toeslope:																
SPVF(TS1) (0-6 cm)	3	4.11	-	193	-0.31	-	-	13.3	0.05	0.01	2	-0.22	0.06	2	0.27	0.09
SPVF(TS1) (6-12 cm)	9	4.87	0.5	217	-0.27	-0.67	10	-	-	-	-	-	-	-	-	-
SPVF(TS1) (12-18 cm)	15	5.05	0.6	238	-0.31	-0.63	12	-	-	-	-	-	-	-	-	-
SPVF(TS1) (18-24 cm)	21	4.41	1.1	256	-0.44	-0.39	24	-	-	-	-	-	-	-	-	-
SPVF(TS1) (24-30 cm)	27	5.04	0.5	263	-0.38	-0.72	10	-	-	-	-	-	-	-	-	-
SPVF(TS1) (30-36 cm)	33	5.85	0.6	285	-0.33	-0.69	10	4.2	-0.03	0.00	2	-0.25	0.01	3	0.22	-0.02
SPVF(TS1) (51-57 cm)	54	5.19	0.7	197	-0.15	-0.45	14	3.9	0.19	0.09	3	-0.23	0.03	2	0.43	0.21
SPVF(TS1) (57-64 cm)	61	4.37	0.9	197	-0.28	-0.37	20	-	0.14	0.01	-	-	-	-	-	-
SPVF(TS1) (64-72 cm)	68	7.76	0.8	209	0.20	-0.43	11	3.1	0.18	0	-	-	-	-	-	-
SPVF(TS1) (72-78 cm)	75	5.41	0.8	189	-0.07	-0.38	15	-	-	-	-	-	-	-	-	-
SPVF(TS1) (78-87 cm)	83	4.99	0.9	207	-0.22	-0.39	18	7.2	0.25	0.01	2	-0.14	0.01	2	0.39	0.28
SPVF(TS1) (87-89 cm)	88	4.55	0.8	232	-0.37	-0.49	18	-	-	-	-	-	-	-	-	-
SPVF(TS1) (89-92 cm)	91	5.80	0.9	242	-0.22	-0.45	16	3.3	0.11	0.03	3	-0.15	0.05	3	0.26	0.12
SPVF(TS1) (lowermost)	92	4.91	1.0	253	-0.37	-0.42	21	-	-	-	-	-	-	-	-	-
stream sediment:	-	4.46	-	220	#REF!	-	-	13.8	0.10	0.02	3	-0.31	0.02	2	0.41	0.17
north drill core:																
DC1-8 (1.1-1.2 m)[5]	115	5.44	1.2	179	-	-	23	5.7	0.31	0.04	4	0.08	0.03	2	0.23	0.32
DC1-26 (6.1-6.3 m)[5]	620	5.97	1.1	172	-	-	18	8.8	0.30	0.09	3	0.02	0.06	3	0.28	0.33

(1) Measured with ICP-AES

(2) Mass of 0.5 N HCl-extracted Fe/mass of total Fe in bulk sample. Method of Wiederhold et al. (2007a, 2007b)

(3) Defined as $\delta^{56}Fe_{bulk\ Fe}$-$\delta^{56}Fe_{0.5N\ HCl\text{-}extracted\ Fe}$

(4) Calculated from above values using mass balance : $\delta^{56}Fe_{bulk\ Fe}$*wt.% bulkFe = $\delta^{56}Fe_{non\text{-}extracted\ Fe}$*wt.% non-extracted Fe + $\delta^{56}Fe_{extracted\ Fe}$*wt.% extracted Fe

(5) Elemental concentration data from Jin et al. (2010)

Table 2-3: Integrated Fe fluxes and masses in regolith

	mid-depth (cm)	$\rho_w(z)$ $(g/cm^3)^1$	strain $(\varepsilon(z))^2$	mass flux m_{Fe} (g Fe/m^2)	Σm_{Fe} (g Fe/m^2)	mass flux $m_{Fe(II)}$ (g Fe/m^2)	$\Sigma m_{Fe(II)}$ (g Fe/m^2)	f_{Fe} (%)
ridgetop:								
SPRT2 (0-5 cm)	2.5	0.7	3.0	-264		-167		
SPRT2 (5-10 cm)	7.5	1.0	1.3	-534		-253		
SPRT2 (10-15 cm)	12.5	1.1	1.0	-584		-505		
SPRT2 (15-20 cm)	17.5	1.2	0.8	-769		-400		
SPRT2 (20-25 cm)	22.5	1.3	0.8	-319	-2500	-203	-1500	7
middle slope:								
SPMS2 (0-10 cm)	5	0.8	1.3	-2126		-803		
SPMS2 (10-20 cm)	15	1.2	0.5	-3785		-969		
SPMS2 (20-30 cm)	25	1.3	0.4	-3669		-745		
SPMS2 (30-36 cm)	33	1.4	0.5	-1056		-529		
SPMS2 (36-45 cm)	41	1.4	0.4	-2285		-380		
SPMS2 (45-47 cm)	46	1.5	0.5	-339		-34		
SPMS2 (lowermost)	47	1.5	0.3	-294	-13500	13	-3400	22
footslope:								
SPVF(FS1) (0-10 cm)[3]	5	0.8	0.5	-7036		-1539		
SPVF(FS1) (10-20 cm)[3]	15	1.2	0.2	-7567		-1623		
SPVF(FS1) (20-30 cm)[3]	25	1.3	0.3	-5084		-982		
SPVF(FS1) (30-40 cm)[3]	35	1.4	0.4	-3248		-439		
SPVF(FS1) (40-50 cm)[3]	45	1.5	0.4	-2412		-156		
SPVF(FS1) (50-60 cm)[3]	55	1.5	0.5	-893		114		
SPVF(FS1) (60-67 cm)[3]	64	1.6	0.4	-750	-27000	87	-4500	30
toeslope:								
SPVF(TS1) (0-6 cm)	3	0.7	2.2	-782		225		
SPVF(TS1) (6-12 cm)	9	1.0	1.0	-1108		-607		
SPVF(TS1) (12-18 cm)	15	1.2	0.6	-1601		-727		
SPVF(TS1) (18-24 cm)	21	1.3	0.3	-2643		-525		
SPVF(TS1) (24-30 cm)	27	1.3	0.2	-2467		-1048		
SPVF(TS1) (30-36 cm)	33	1.4	0.1	-2450		-1132		
SPVF(TS1) (36-57 cm)	54	1.5	0.4	-2830		-1962		
SPVF(TS1) (57-64 cm)	61	1.6	0.4	-1883		-546		
SPVF(TS1) (64-72 cm)	68	1.6	0.3	1647		-790		
SPVF(TS1) (72-78 cm)	75	1.6	0.4	-414		-482		
SPVF(TS1) (78-87 cm)	83	1.6	0.3	-2066		-814		
SPVF(TS1) (87-89 cm)	88	1.7	0.1	-871		-259		
SPVF(TS1) (89-92 cm)	91	1.7	0.1	-557		-251		
SPVF(TS1) (lowermost)	92	1.7	0.0	-487	-18500	-124	-9000	15

(1) Estimated using regression based upon data from Lin (2006): $\rho_w(z)=0.2839*\ln(z/140) + 1.7954$; z=depth in cm

(2) Strain estimated using Equation 6

(3) Samples from Jin et al. (2010)

Table 2-4: Values weighted for depth and bulk density[1]

	$[\delta^{56}Fe_{bulk}]_{wt}$	$[\delta^{56}Fe_{0.5N\ HCl\text{-}extracted\ Fe}]_{wt}$
Bedrock	0.31	0.05
Ridge top[1]	0.27	-0.01
Middle slope[1]	0.22	-0.13
Footslope[1]	0.12	-0.09
Toeslope[1]	0.13	-0.21
Stream sediment	0.10	-0.31

(1) Weighted for depth and bulk density according to Equation 7

Table 2-5: Mass balance calculations along hillslope for $\delta^{56}Fe$ (‰)

	$\delta^{56}Fe_{mobile}$[1]	Fraction $Fe(III)_{aq}$ precipitated[2]	$\delta^{56}Fe_{precipitated\ phase}$[3]
Ridge top	0.70	0.27	-0.81
Middle slope	0.58	0.20	-0.86
Footslope	0.72	0.28	-0.80
Toeslope	1.26	0.52	-0.58

(1) Calculated from Equation 8 using weighted values from Table 4

(2) defined as 1-f where f calculated from Equation 9 and assuming $\delta^{56}Fe(III)_{aq,i}$=0.3‰ and α=0.9987 (Skulan et al., 2002)

(3) Calculated from Equation 11

Chapter 3: Basalt Weathering in an Arctic Mars-Analog Site

Tiffany Yesavage[a]*, Aaron Thompson[b], Elisabeth M. Hausrath[c], and Susan L.Brantley[a,d]

[a]302 Hosler Building, Department of Geosciences, the Pennsylvania State University, University Park, Pennsylvania 16802, USA.

[b]3101 Miller Plant Sciences Building, The University of Georgia, the University of Georgia, Athens, Georgia 30602-7272, USA. AaronT@uga.edu.

[c]SEB 4132 Department of Geoscience, The University of Nevada, Las Vegas, Nevada 89154-4010, USA. elisabeth.hausrath@unlv.edu.

[d]2217 EES Building, Earth and Environmental Systems Institute, Pennsylvania State University, University Park, PA 16802, USA. sxb7@psu.edu.

**Corresponding author: e-mail: tay120@psu.edu*

Phone: +1-720-201-7880

Keywords: Mars analog site; amorphous phases; allophane; volcanic ash soils; chemical weathering in cold climates

3: Abstract

Weathering is thought to have occurred in the past and may occur intermittently today on Mars. We investigate weathering at Sverrefjell volcano, a cold, dry site that lies above the Arctic Circle, as an analog to weathering on Mars. At Sverrefjell, Quaternary-aged basalt lava flows have weathered since deglaciation ~10,000 years ago. Analysis of a ~75-cm core of rubbly regolith formed on a basaltic flow documents concentrations of amorphous phases similar to those observed in warmer, wetter volcanic ash soils. Infrared and electron microscopic analyses of the clay-sized fraction are consistent with allophane as the predominant secondary phase. The Al/Si ratio of the amorphous portion of this regolith is lower than in volcanic soils reported for other localities, perhaps reflecting the abundance of Si-rich coatings. The relative order of loss from regolith was observed to be: (Na, K) > (Ca, Mg) > Si > (Fe, Al, Ti). If the Sverrefjell volcano is indeed a good Mars analog site, then we expect secondary allophane and a similar relative loss of elements from Martian regolith developed under circumneutral pH.

Dissolved and colloidal loss from regolith samples was quantified in oxic and anoxic batch incubation experiments. Under oxic conditions at circumneutral pH, Al, Fe and Ti were dispersed primarily as 260-415 nm particles; in contrast, Ca, Mg and Na were lost as solutes, while significant Si was lost both in the colloidal and dissolved forms. The Fe/Al/Si ratios of the dispersed colloids under oxic conditions are consistent with mobilization of allophane and ferrihydrite. Under anoxic conditions, dissolution of Fe oxide cements may accompany release of fines. Colloidal batch experiments help to explain the relative order of elemental loss from the clay-sized regolith fraction: Ca, Mg and Na are lost as solutes, while Fe, Al and Ti colloids are mostly retained; Si is lost to an intermediate extent as it exists both in the colloidal and solute form. The solubility of Si across the entire pH range of the study is large enough to explain extensive Si-rich coatings. We expect that colloidal material could be abundant in Mars regolith, with similar elemental fractionation trends to those observed in the colloidal dispersion experiments.

Surface retreat distances on Sverrefjell rock surfaces imply high rates of both physical and chemical weathering at this site. Wetting/drying was just as effective as freeze/thaw in facilitating material loss. The occasional cyclic adsorption of water (either as a liquid or vapor) onto rocks in this very dry climate may result in strong sorptive forces that are responsible for high physical spalling rates that in turn drive relatively high rates of chemical leaching.

3-1. INTRODUCTION

Although the average surface temperature on Mars is -60°C (McKay et al., 1991), temperatures also rise above 0°C (Jakosky et al., 2003), and a growing body of evidence suggests that liquid water has been present on the surface of the planet (Ehlmann et al., 2011 and references within). Consistent with the presence of water, Martian rocks display a wide variety of surface features including surface flaking, dirt cracking, exfoliation, honeycomb weathering and the formation of what appear to be weathering rinds (Thomas et al., 2005; Hausrath et al., 2008a). Thermal emission spectrometer data from Mars further indicate the presence of both primary and secondary minerals, including plagioclase, pyroxene, olivine, phyllosilicates, zeolites, volcanic glasses, opaline silica and allophane (Rampe et al., 2012 and references within).

To understand whether Martian rocks retain features indicative of water-rock reactions (chemical weathering) requires understanding how basaltic material weathers on Earth. Weathering of volcanic soils has been investigated at sites from around the world, including the cold climates of Alaska (Ping et al., 1988; Ping et al., 1989) and Iceland (Arnalds et al., 1995). On Earth, the relative importance of chemical relative to physical weathering is thought to decrease from the tropics to the poles (Campbell and Claridge, 1987), an observation that is likely true for basaltic materials. However, measurements of riverine solutes suggest that substantial chemical weathering of basalts occurs even in very cold environments (Gislason et al., 1996; Dixon et al., 2002; Hall et al., 2002; Huh, 2003; Navarre-Sitchler and Brantley, 2007). Furthermore, Nesbitt and Wilson (1992) concluded that the relative release rates of major elements from weathered basalts do not vary substantially as a function of climate. In fact, studies of basalt weathering in Central Siberia document a similar relative elemental mobility series in arctic rivers to that found in other rivers around the world: Na + K > Ca > Mg > Si > Fe ≥ Mn ≥ Ti ≥ Al (Pokrovsky et al., 2005).

A variety of secondary minerals form during basalt weathering at sites around the world, including allophane (Colman, 1982; Stefansson and Gislason, 2001; Chadwick et al., 2003; Shikazono et al., 2005; Pokrovsky et al., 2005), halloysite (Shoji and Saigusa, 1977; Shikazono et al., 2005; Ziegler et al., 2003; Chadwick et al., 2003), Al-organic compounds (Ping et al., 1988; Pokrovsky et al., 2005), chlorite (Shoji and Saigusa, 1977; Ping et al., 1988) and smectite

(Nesbitt and Wilson, 1992; Stefansson and Gislason, 2001; Pokrovsky et al., 2005; Rasmussen et al., 2010). The abundance of these different phases varies considerably with climate and location. In volcanic settings, the rapid weathering of glass releases elements such as Si, Fe and Al that quickly become over-saturated with respect to the noncrystalline minerals allophane, imogolite, opaline silica and ferrihydrite (Ugolini and Dahlgren, 2002). In fact, because basaltic glass dissolves up to ten times faster than crystalline basalt (Gislason and Eugster, 1987), glass weathering is of particular importance during the early stages of weathering in volcanic environments. Based on studies of weathering rinds, Colman (1982) further observed the following order of mineral susceptibility during basalt dissolution: glass > olivine > pyroxene > plagioclase > K-feldspar.

Previous studies on basalts have focused on relatively wet environments with annual precipitation in excess of 700 mm/yr. Consequently, extrapolation from such studies to mineral weathering on relatively dry Mars is difficult. Hausrath et al. (2008a) attempted to bridge this gap by comparing Martian weathering with weathering at a Mars analog site at Sverrefjell volcano, located above the Arctic Circle. They documented weathering-related leaching of cations from glass to depths of ~250 μm in basalt samples collected from a rubbly weathered zone ~30 cm beneath the land surface. Following Hausrath et al. (2008a), we targeted this same dry (<200 mm/yr) and frigid site as an analog. The basaltic composition of the Sverrefjell volcano, the short 10,000 year period since deglaciation, as well as the cold, dry climate allow for insights into the early stages of regolith formation occurring on Mars.

The presence of unripened amorphous silicates on Mars has long puzzled researchers (Banin, 1996). Because the origin and age of these short-range ordered phases is not well understood, work at Mars analog sites may eludicate the mechanisms by which amorphous phases evolve and crystallize over time. In this contribution, we examine in greater detail the mechanisms that are associated with weathering at the Sverrefjell volcano. In particular, we are interested in the relative elemental loss over the entire regolith profile during weathering as well as secondary phase formation and mineralogical changes with depth. Finally, because volcanic ash soils are particularly rich in sub-micron sized particles (Dahlgren et al., 1993), we use short-term batch experiments to understand the colloidal size fractions in which different elements occur under oxic and anoxic conditions. To further investigate fine particle production, wetting,

freezing and drying experiments were completed on pristine Sverrefjell parent regolith in the laboratory.

3-2. MATERIALS AND METHODS

3-2.1. Field sampling:

Sverrefjell volcano is one of three Quaternary eruptive centers in northwestern Spitsbergen on the arctic archipelago of Svalbard that began most recent deglaciation ~10,000 years ago (Hausrath et al., 2008b). Based upon Ar-Ar age data, Treiman (2012) derived an eruption age of 1.05 ± 0.5 My, which would imply that it has experienced multiple glacial/interglacial cycles. The volcano extends from a 3 km cross-sectional diameter base at ~sea level to an elevation of 500 m at the summit (Skjelkvale et al., 1989). It is composed of sequences of primitive alkali basaltic flows and pyroclastics with abundant xenoliths (Skjelkvale et al., 1989). The basalts contain phenocrysts of olivine and augite in a fine-grained groundmass of olivine, augite, plagioclase laths and titanomagnetite along with varying amounts of basaltic glass (Skjelkvale et al., 1989). Precipitation is estimated at <200 mm/year, with an estimated average annual temperature of -5°C (Hausrath, 2007; Hausrath et al., 2008b).

The land surface at Sverrefjell volcano is characterized by a rocky, essentially bare basalt, covered occasionally by lichens and very limited plant cover. Two types of samples were collected during the summers 2004 and 2005: (a) fractured rock material and (b) loose regolith made up mostly of weathered cinder. The fractured rock samples were dug by hand from the landform surface in many locations on Sverrefjell. To ensure that our rock samples were not greatly affected by erosion, depth profiles were collected from flat, stable surfaces to the depth of shovel refusal (~30 cm). The second sample type consisted of a ~75-cm loose regolith core made up of volcanic cinders collected from the south side of the volcano at an elevation of ~300 meters (Site 1 in Figure 3-1). The land surface above the regolith core was composed of cinders that looked similar to those in the core. Using a hand auger, samples were collected until depth of refusal, presumably marking the contact between the weathered volcanic cinders and the underlying basalt flow. All samples were stored frozen in sterile Whirl-Pak® bags until analysis. A large and relatively pristine rock was selected from a basaltic dike at the Sverrefjell volcano for wetting/drying experiments.

3-2.2. Regolith Chemical Characterization:

The samples were defrosted and air dried for chemical analysis. One set of samples ("sieved" samples) was sieved to <2 mm, while another set was left unsieved and contained all collected rock fragments ("unsieved" samples). Both sample sets were ground in a mortar and pestle to a particle size <100 μm, while the clay-sized fraction (<2 μm) of each sample was isolated using a wet sieving technique (Jackson, 1956). For each sample type, 100 mg of ground material was fused with lithium metaborate at 850°C for 10 minutes, re-dissolved in dilute nitric acid and analyzed for total elemental concentrations on an inductively coupled plasma-atomic emission spectroscopy (Perkin-Elmer ICP-AES 5300DV). The estimated precision for most elements is ± 3% based on error associated with ICP-AES analysis.

The pH of the regolith sample (sieved to <850 μm) was measured in water (pH_{water}) and in 1.0 M KCl (pH_{KCl}) at a 1:1 g sample: g solution ratio after 10 minutes of stirring (Thomas, 1996). Solid phase total carbon (C) and nitrogen (N) concentrations were measured using the Dumas method of complete and instantaneous oxidation by flash combustion (Matejovic, 1996) on a CE Instruments EA 1110 CHNS-O elemental analyzer.

We used the sodium pyrophosphate method of McKeague (1967) to estimate the concentrations of organically-associated Al and Fe in the regolith profile and the ammonium oxalate method of McKeague and Day (1966) to quantify amorphous oxides and hydrous oxides. All extractions were performed on regolith sieved to <850 μm to minimize heterogeneity. Although ammonium oxalate is known to dissolve less crystalline lepidocrocite and magnetite, it primarily dissolves short-range order (SRO) phases such as ferrihydrite and allophane (Parfitt and Childs, 1988). The Al/Si molar ratio of allophanic material was estimated using the following formula: (mole Al_o-mole Al_p)/mole Si_o), which corrects for organic Al (Dahlgren, 1994). Here, Al_o and Si_o are acid-oxalate extractable concentrations (g/kg soil), and Al_p is the sodium pyrophosphate extractable Al (g/kg soil).

3-2.3. Microscopy and Mineral Identification Methods:

Two weathered rocks sampled from the 38-47 cm depth of the regolith core were embedded in epoxy to preserve the surface (Gordon et al., 2005), cut perpendicular to the surface and polished to a thickness of 1 μm. Elemental analysis was completed using energy dispersive X-ray spectroscopy with the FEI Quanta 200 environmental scanning electron microscope

(ESEM) at the Material Characterization Laboratory at Penn State University. Thin sections of weathered rocks obtained from the regolith core (from depths of 0-20 cm, 20-36 cm and 63-70 cm) were made by Spectrum Petrographics and imaged under an optical microscope and SEM. Images from the 0-3 cm depth of the Site A fractured rock sample were taken with the environmental secondary electron detector (ESED) detector on the Hitachi S-3500N variable pressure scanning electron microscope. For transmission electron microscope (TEM) analysis on the Philips EM 420 TEM (120 kV), samples sonicated and dispersed in ethanol and deposited onto a lacey carbon grid. Images and EDS data were collected from the sample in a Gatan double-tilt analytical holder with the holder tilted 30 degrees in the x-axis.

Fourier transform infrared (FTIR) spectra were collected on the clay-sized fraction of several regolith core samples by mixing 1 mg of sample with 40 mg KBr (International Crystal Laboratories, Garfield NJ) and pressing the mixture into a free-standing pellet using a Quick Press outfitted with a 7 mm die (International Crystal Laboratories, Garfield NJ). Pellets were analyzed in transmission geometry on a Bruker Vertex 70 spectrometer (Bruker Optics, Billerica MA) by averaging 100 scans acquired at 6 scans cm^{-1}. All spectra are referenced to a pure KBr pellet.

X-ray diffraction (XRD) patterns were collected using a PANalytical Empyrean theta-theta style goniometer with Cu-K-alpha radiation, with a fixed slit incidence (0.25 deg. divergence, 0.5 deg. anti-scatter, specimen length 10 mm) and diffraction optics (0.25 deg anti-scatter, 0.02 mm nickel filter). Regolith samples (sieved to <100 μm) were prepared by pressing a powder sample into the cavity of a silicon low-background support (e.g., backloading method). Clay-sized samples were prepared by thoroughly suspending the sample in water and then placing a drop on a glass slide (Whittig and Allardice, 1986). XRD data were collected at 45 kV and 40 mA from 5-70 deg 2-theta using a PIXcel detector in scanning mode with a PSD length of 3.35 deg. 2-theta, and 255 active channels for a duration time of ~16 minutes. The resulting patterns were then analyzed with Jade +9 software by MDI of Livermore, CA.

3-2.4. Determination of the point of zero net charge (PZNC):

The point of zero net charge of the 47-56 cm regolith core sample (<850 μm size fraction) was determined using the method of Zelazny et al. (1996). Briefly, the method involves analysis of both cation exchange capacity (CEC) and anion exchange capacity (AEC) at different

pH values. The point of zero net charge occurs at the pH at which AEC = CEC. The method involves adding a 1 M KCl solution to an air-dried soil sample in order to adsorb K^+ and Cl^-, which are later displaced with 0.5 N $NaNO_3$. Potassium concentrations in the final $NaNO_3$-displaced solution were measured with ICP-AES, while chloride concentrations were measured via ion chromatography.

3-2.5. Colloidal dispersion experiments:

Two sets of colloidal dispersion experiments were performed on the regolith sample from the 38-47 cm depth. The sample was first sieved to <850 μm to minimize size heterogeneity of the sample. To understand colloidal dispersion as a function of pH at a constant ionic strength, experiments were performed under both oxic and anoxic conditions. For both oxic and anoxic experiments, a mass of 0.4 grams of soil was added to a series of 50-mL Falcon tubes or anaerobic culture tubes to which a total volume of 20 mL of solution was added. The solution included distilled water, potassium lactate to achieve a 10 mM concentration of carbon as an energy source for growth of bacterial spores in the anoxic experiment, 0.02 N KOH and HCl to adjust the pH, as well as 0.5 N KCl to adjust the ionic strength to 23 mM.

For each oxic experiment, acid and base were added in triplicate to achieve pH values ranging from 4.5 to 10 after incubation on an end-to-end shaker for 2 h. For the anoxic experiments, all additions were made with N_2-purged reagents stored previously in an anoxic glove box for at least 2 weeks and sealed with butyl rubber septa and aluminum seals. Once prepared, sealed anoxic serum vials were removed from the glove box and incubated on an end-to-end shaker for one to three weeks. All processing of the anoxic samples was done in the glove box.

For both the oxic and anoxic samples, tubes were allowed to settle for a minimum of 5 minutes and then 1.5 mL of clear supernatant was collected and added to a series of acid-washed, 1.7-mL microcentrifuge tubes (National Scientific Supply Company, Inc.). Tubes were then centrifuged according to calculations based upon Stokes' law (Henderson et al., 2012), assuming spherical geometry of dispersed colloids and a mean density of 2.65 g cm^{-3}. Centrifugation was performed with the Eppendorf Microcentrifuge 5415 D and the Eppendorf F-45-24-11 rotor using centrifugation times of 1,000, 3,000 and 16,000 rcf to separate particles to <415 nm, <260

nm and <35 nm, respectively. 0.5 mL of the supernatant was removed from each tube, taking care not to disturb solid material, and added to 6 mL of 2% nitric acid for analysis with ICP-AES. In addition, a 1 mL aliquot of the <35 nm separated sample was passed through a Millipore Amicon® Ultra centrifugal filter to isolate the <3 kDa particle sizes, and 0.5 mL of the resulting filtrate was added to 6 mL of 2% nitric acid for analysis. After 15 minutes of centrifugation, pH and ionic strength were measured for the remaining non-centrifuged solution. During each experiment, a Mettler Toledo Education Line conductivity meter was used to ensure that all samples had ionic strengths within 5% of 23 mM (comparable to the ionic strength used by Thompson et al., 2006). Blanks were run to verify the purity of reagents, and metal-free centrifuge tubes were used for the experiment.

3-2.6. Calculations:

The mass transfer coefficient ($\tau_{i,j}$) for bulk soil samples was plotted to investigate the extent of chemical weathering. The $\tau_{i,j}$ parameter is defined as (Brimhall and Dietrich, 1987; Anderson et al., 2002):

$$\tau_{i,j} = \frac{C_{j,w}C_{i,p}}{C_{j,p}C_{i,w}} - 1 \qquad (3\text{-}1)$$

Here, C refers to the concentrations of the immobile (i) and mobile (j) elements in the weathered (w) or parent (p) material. For the bulk (or clay-sized) sample, the lowermost regolith (or clay-sized) sample was considered the parent. Ti was chosen as the immobile element, consistent with previous work indicating that Ti tends to be the least mobile element during basalt weathering, even relative to trace elements such as Zr (Nesbitt and Wilson, 1992; Sak et al., 2004; Neaman et al., 2005; Sak et al., 2010). Within the unweathered rocks at Sverrefjell, the bulk of the Ti is contained within pyroxene and primary Fe-Ti oxides (for example, ilmenite), while negligible amounts are present in volcanic glass (Hausrath, 2007). The goal behind normalizing a mobile element to an immobile element (in this case, Ti) is to account for concentration changes resulting from depletion and addition of other elements. Values of $\tau_{Ti,j} > 0$ indicate that element *i* is enriched in soil relative to Ti in bedrock, while $\tau_{Ti,j} < 0$ indicates depletion. The following equation was used to determine the error in $\tau_{i,j}$, $Er\left|\tau_{i,j}\right|$ (Herndon et al., 2011):

$$Er\left|\tau_{i,j}\right| = (\tau_{i,j}+1)\left[\left(er\left(C_{i,p}\right)\right)^2 + \left(er\left(C_{i,w}\right)\right)^2 + \left(er\left(C_{j,p}\right)\right)^2 + \left(er\left(C_{j,w}\right)\right)^2\right]^{1/2} \quad (3\text{-}2)$$

The error in $\tau_{i,j}$ for each sample is set equal to the ICP-AES analytical error for each element (~ 3%).

3-2.7. Wetting/drying/freezing experiments:

Rock collected from a basaltic dike on the Sverrefjell volcano was fractured to obtain pristine surfaces. Newly fractured samples ~1 cm^3 in volume were sonicated for 30 minutes, soaked in water for two days and weighed multiple times until the saturated mass was constant. The samples were then placed in the oven at 105°C for 2 days and weighed to determine the initial dry mass prior to experiments. The samples were then repeatedly subjected to one of two treatments over a 15-month period: 1) wetting for 1 min, followed by 24 h of drying at room temperature (referred to as the "wet/dry" experiments) and 2) wetting for 1 min, freezing at -20^0C for three h (Hall and Hall, 1996), and then drying for 21 h at room temperature (referred to as "wet/freeze/dry" experiments). Our intent was to subject the samples to cycles of wetting/drying $\pm$ freezing but not to simulate any particular seasonal timing. Manipulations were performed five days in a row and then the samples were stored in the air over the weekend over the course of 15 months. At the termination of the experiment, the final saturated and dry masses were again determined as described above.

Specific surface areas of the starting rock from the wet/freeze/dry experiments were also measuring using BET gas adsorption analysis. Prior to BET analysis, the pristine rock from the experiments was ground to <100 μm and then degassed at 105°C to ~0.01 Torr. Nitrogen gas adsorption was analyzed with the ASAP 2020 Automated Surface Area and Porosimetry System at the Penn State Material Characterization Laboratory by the multipoint method. This method measures sorption of N_2 on the material surface, including connected pores ranging in size from 3.5 to 5000 Å.

3-3. RESULTS

3-3.1. Clay-sized properties

Based on particle size analysis, the clay content of the regolith increases from 0.38% in the deepest sample (70.5-75 cm depth) to 1.02% at the most shallow depth (Table 3-1). At all depths, rocks and sand-sized particles make up >80% of the total mass. The pH of the 74-cm regolith core material decreases slightly from ~6.5 at the bottom of the profile to ~5.9 toward the surface (Table 3-2). Total carbon increases from 0.13 wt. % in the deepest sample to 1.05 wt. % at the surface, while nitrogen increases from 0.02 to 0.08 wt. % (Table 3-2). The C/N mass ratios vary from 6.4 in the lowermost sample to 12.7 in the surface sample (Table 3-2). Fractured rock samples measured at Site A have an order of magnitude more C and N than the regolith (Table 3-2).

The cation exchange capacity (CEC) was higher than the anion exchange capacity in regolith samples collected from the 38-47 cm depth range. The CEC ranged from ~4 $cmol_c\ kg^{-1}$ soil at pH 3 to ~20 $cmol_c\ kg^{-1}$ soil at pH 8 (Figure D-1; Table D-1). In contrast, the anion exchange capacity was much lower, reaching a maximum of ~3 $cmol_c\ kg^{-1}$ soil at a pH of 3 (Table D-1). The intersection between the two lines should provide an estimate of the point of zero net charge (Zelazny et al., 1996), which in this case is at a pH of ~2.5.

3-3.2. Microscopy:

SEM images of epoxied rind cross sections made from the regolith core (at 38-47 cm depth) showed weathered surfaces and occasional coatings ranging in thickness from 20-50 μm (Figure 3-2). EDS analysis of the outer 100 μm of the rock surface indicated that, relative to the inner portion of the rock, the surface was depleted in Na, Mg, K and Ca (Table D-2), while no significant differences were observed in Al, Fe and Si (Table D-2). Thin sections of all three weathered rocks obtained from the regolith core showed abundant silica coatings (found to be Si-rich based with SEM/ EDS) under the optical microscope.

TEM images of the clay-sized regolith fraction (38-47 cm depth) show several different shapes of particles, ranging from 200–300 nm in diameter. Some are amorphous and some crystalline based on electron diffraction patterns (Figure 3-3A). The electron diffraction pattern determined for particles in the 200–300 nm size range (Figure 3-3B) indicated diffuse rings

indicative of amorphous material, while EDS analysis documented that they are made up predominantly of Al, Si and Fe (Figure D-2). Particles with morphologies resembling imogolite threads or halloysite tubes (Gilkes, 1994) were not observed in any of the five samples analyzed (two regolith samples and three fractured rock samples). Darker areas within the images correspond to Fe-rich regions in many of the particles (Figure 3-3C), indicating that the element distribution is not homogenous.

3-3.3. Chemistry:

For the bulk chemistry of the 75-cm core, $\tau_{Ti,j}$ values normalized to the lowermost regolith sample for most elements suggest no gain or loss (e.g., $\tau_{Ti,j}$ ~0) throughout the profile for sieved (<2 mm) and unsieved samples (Table D-3). However, Na and K show slight depletion up to 15% in the upper 30 cm of the profile (Figure 3-4; Table D-3). In addition, the sieved samples exhibited slightly more element depletion than unsieved samples (Figure 3-4).

The chemistry of the clay-sized fraction is distinctly different in composition from the parent material (pristine rock collected from the regolith core). For instance, rock fragments contain an order of magnitude more Na than the clay-sized fraction by weight, even in the deepest regolith samples (Table D-3). Similar findings are also noted for K, Mg, Ca and Si (Table D-3). On the other hand, Al, Fe and Ti appear to be retained within the clay-sized fraction (Table D-3).

In contrast to the bulk sample showing minimal depletion compared to bulk parent material, the clay-sized fraction in surface samples of the regolith core becomes depleted in Na, K, Ca and Mg relative to Ti in the lowermost clay-sized (parent) sample, with $\tau_{Ti,j}$ values in the uppermost samples ranging from a maximum of -0.39 for Ca to a minimum of -0.70 for Na (Figure 3-5; Table D-4). In other words, up to 39% of the Ca and 70% of the Na in the clay-sized fraction has been removed from the surface sample. Si shows a moderate amount of depletion (up to 20%), while Fe and Al show little or no evidence for depletion (Table D-4). Phosphorus is the only element that shows slight enrichment in the uppermost clay-sized sample ($\tau_{Ti,P} = 0.11$). Based upon $\tau_{Ti,j}$, the general order of elemental loss from the clay-sized fraction of the regolith is as follows: Na, K > Ca, Mg > Si > Al, Fe.

Ammonium oxalate extracted 30-40% of the total Al, 25-30% of total Fe and 15-20% of the total Si (Table 3-3) from the <850 μm sieved samples. In contrast, sodium pyrophosphate

extracted only a small amount of Al, Fe and Si, suggesting very minimal association with organic matter (Table 3-3).

3-3.4 Mineral Identification:

Based on XRD, unweathered rock from the site contains augite, anorthite feldspar and olivine (Figure 3-6A) (see also, Hausrath (2007)). Although peaks consistent with quartz, muscovite and illite were not detected in the unweathered rock (Figure 3-6A), peaks for these phases are evident in the <850 μm portion of the regolith sample, with greater relative peak area in the surface samples (Figure 3-6A). In addition, the XRD patterns suggest some combination of vermiculite and/or chlorite in the sieved (<850 μm) regolith sample (Figure 3-6A). In contrast, XRD of the clay-sized fractions prepared by the dropper method (used to orient and thus discern clay minerals) shows no obvious peaks corresponding to phyllosilicate clays such as smectite, vermiculite or chlorite (Figure 3-6B). Instead, a broad hump in the 15-30° 2θ region is consistent with phases such as volcanic glass, allophane or ferrihydrite (Kawano and Tomita, 2001). Of these phases, allophane and ferrihydrite are known to be soluble in ammonium oxalate.

For the clay-sized fraction of the regolith samples, the presence of IR bands near 1010, 690, 570 and 480 cm^{-1} (Figure 3-7) is consistent with allophane ($(SiO_2)_{1-2}Al_2O_3*5H_2O$ (Kitagawa, 1974)) as an important phase (Parfitt et al., 1980). Allophane typically has a strong absorption band in the 1200-800 cm^{-1} region, with the absorption maximum decreasing from 1020 to 975 cm^{-1} with increasing Al/Si ratio from 1.0 to 2.0 (Parfitt et al., 1980; Wada et al., 1992). Toward the surface of the profile, the shift from 1010 to 980 cm^{-1} (Al or Si-O stretching), as well as a decrease in the intensity of the 470 cm^{-1} band (Si-O-X, where X: Si or Al stretching) is consistent with a possible shift from 1:1 to 2:1 allophane (ratio is the molar ratio of Al:Si) toward the surface of the profile.

3-3.5. Colloidal dispersion experiment:

Colloidal dispersion experiments were performed on the regolith sample collected from the 38-47 cm depth (sieved to <850 μm). The pH of this sample was ~5.7 (Table 3-2). In the supernatant, Mg, Ca and Na were present solely in the dissolved form (i.e., <3 kDa or ~2 nm (Verdugo et al., 2004)) across the entire pH range (Figure 3-8; Table 3-5). Dissolved Mg and Ca decreased dramatically over an order of magnitude in concentration from pH 4 to pH 10, while

Na stayed constant across the pH range (Table D-6). In contrast, Al, Fe and Ti were present predominantly in the 260-415 nm size fraction across the pH 4-8 range (Figure 3-8; Table D-5). At most pH values for Si, about half was present in the 260-415 nm size range and the other half present in the dissolved (<2 nm) range (Figure 3-8). Elevated concentrations of dissolved Al, Fe, and Ti were found both at pH 4 and 10, but not between pH 5-8 (Figure 3-9). In contrast, dissolved Si concentrations in excess of 2 mmol Si kg^{-1} soil were measured at all pH values (Figure 3-9).

In contrast to oxic conditions, the 3-week anoxic experiment performed at pH 6 indicated a shift toward smaller colloidal particles over time (Figure 3-10; Figure D-3). While the larger 260-415 nm particle range was the predominant size range of dispersed colloids in the three-week oxic experiment, the 35-260 nm size fraction predominated under anoxic conditions (Figure 3-10).

3-3.6. Wet/dry/freeze experiments:

The connected porosity based upon saturated and oven-dried masses of the basalt rocks ranged from 3-15% (see Table 3-4 for details). During the experiment, small pieces of rock occasionally spalled off the samples during both wet/dry and wet/freeze/dry cycles. Over the course of ~200 cycles, wet/dry and wet/freeze/dry samples showed similar mass losses such that 0.2% of the original mass of the material was lost (Table 3-4). These observations were transformed into a weathering advance rate (w) due to physical spalling over a 1-year period by assuming 100 cycles yr^{-1} using the following equation (Navarre-Sitchler and Brantley, 2007):

$$w = \frac{\Delta M}{\rho_{basalt} * S} \frac{1}{t} \qquad (3\text{-}3)$$

Here, w is the surface area-normalized weathering advance rate (mm ky^{-1}), ΔM is the fraction of mass lost during the experiments (~0.001 g g^{-1} rock, calculated by determining the oven-dried mass loss over the course of 100 cycles), and S is the specific surface area (m^2 g^{-1}) of the parent material at the start of the experiment (Navarre-Sitchler and Brantley, 2007). Using the BET surface area of the unweathered but laboratory-ground starting material (1.96 m^2 g^{-1}) and an assumed basalt density (2.8 g cm^{-3}), the weathering advance rate assuming ~100 cycles y^{-1} was 1.8 x 10^{-4} mm ky^{-1}. Alternately, using an estimate for the ratio of particle BET surface area to clast geometric surface area of 200 m^2 g^{-1} (Navarre-Sitchler and Brantley, 2007), the weathering

advance rate was 3.6 x 10^{-2} mm ky^{-1}. As shown by Navarre-Sitchler and Brantley (2007), this advance rate varies depending upon the scale of observation from BET to clast scale.

Chapter 3-4. DISCUSSION

3-4.1. Identity of secondary phases:

Despite the cold, dry climate (annual precipitation <200 mm) and the relatively short duration of time for weathering (~10,000 yr), a high abundance of secondary phases has formed in regolith at the Sverrefjell volcano. Concentrations of amorphous Al and Si (in material sieved to <850 μm) range from 20 to 40 g kg^{-1} dry soil and make up 20-40% of the total Al and Si. These values are higher than levels documented in somewhat older volcanic ash deposits in the much warmer, wetter climate of New Zealand where the percent of amorphous Al and Si was less than 20% and 10%, respectively (Parfitt et al., 1983). Similarly high concentrations of amorphous Al and Si (ranging from 10 to 30 g kg^{-1}) have been observed in Iceland pedons in which the mean annual precipitation ranged from 600-2000 mm (Arnalds and Kimble, 2001). Apparently, Svalbard's cold, dry climate does not hinder the formation of secondary phases.

XRD, FT-IR and TEM analysis of the clay-sized fraction of regolith documents allophane as a predominant secondary phase. Allophane is common in volcanic soils (Dahlgren et al., 1993), and it has been suggested based on thermal emission spectrometer data that allophane may be present at different latitudes across the surface of Mars (Rampe et al., 2012). While halloysite is a thermodynamically more stable phase than allophane (Ziegler et al., 2003), there is no evidence for it at the Sverrefjell volcano. Although it is generally thought that halloysite ripens from allophane over time in most locations (Parfitt et al., 1983), evidence also suggests that halloysite may form directly from volcanic glass in soil profiles (Bleeker and Parfitt, 1974; Parfitt et al., 1983; Parfitt and Wilson, 1985; Shikazono et al., 2005). For instance, Shikazono et al. (2005) found evidence for halloysite in soils of central Japan (average annual precipitation 1,700 mm) ranging in age from 200 to 6,000 years, while Bleeker and Parfitt (1974) documented the formation of halloysite in tephra from New Guinea (average annual precipitation > 3,400 mm) after only 800 years of weathering.

The direct formation of halloysite is noted particularly in soils characterized by elevated aqueous silica concentrations (Farmer et al., 1979; Parfitt and Wilson, 1985), a condition that tends to occur in drier climates where minimal silica is lost from the profile during leaching

(Dahlgren et al., 1993). In the case of the Sverrefjell volcano, extensive silica coatings on the surfaces of rocks from the regolith core suggest that silica concentrations often approach saturation in the regolith core. However, these conditions evidently do not lead to halloysite formation in the short time since deglaciation.

No consensus exists on the exact origin of layer silicates in volcanic soils, as these phases may result from eolian deposition and/or hydrothermal alteration (Dahlgren, 1993; Rasmussen et al., 2010). XRD analysis is consistent with the presence of an unknown phyllosilicate phase (likely chlorite/vermiculite based on Jade +9 software identification) in the upper 38 cm of the regolith profile (Figure 3-6A). On the other hand, the clay-sized fraction (<2 μm) below 38 cm is dominated instead by an amorphous hump and shows no evidence for phyllosilicates (Figure 3-6B). Along with the increase in the abundance of quartz and muscovite/illite toward the surface of the regolith profile (Figure 3-6A), these findings suggest a detectable contribution from eolian sources in particular. In addition to eolian deposition from remote sources, hydrothermal alteration may also have resulted in the formation of layer silicate minerals in the crater prior to eruption (Dahlgren et al., 1993).

Since sodium pyrophosphate extracted very low concentrations throughout the profile (0.5 to 2 g kg^{-1} soil extracted with sodium pyrophosphate), only a small fraction of the Al in the regolith core is likely present as Al-humus complexes. Low organic-associated Al concentrations are consistent with the circumneutral pH of the regolith core (pH~6), since Al-humic complexes are more common in in soils with pH < 5 (Ugolini and Dahlgren, 2002).

3-4.2. Chemistry:

Eggleton et al. (1987) noted that glass weathering in Australian basalts resulted in a notable loss of Si, K and Na, while olivine weathering in contrast led to the significant loss of Mg. Likewise, the observed depletion of Na and K, but not Mg, from the bulk regolith profile at Sverrefjell is attributed to more significant weathering of basaltic glass than olivine (Figure 4). These results are consistent with the general finding that basaltic glass dissolves faster than fully crystallized basaltic rocks (Stefansson and Gislason, 2001).

Based upon $\tau_{Ti,j}$ plots, the following relative order of elemental weathering is observed during clay weathering at Sverrefjell: Na, K > Ca, Mg > Si > Al, Fe, Ti (Figure 3-5). This sequence is somewhat similar to a previous study of basalt weathering:

Ca>Na>Mg>Si>Al>K>Fe>Ti (Shikazono et al., 2005). Minor differences in the relative order of weathering at different volcanic sites are likely due to differences in the abundance of volcanic glass, the mineralogical composition of the bedrock, vegetation uptake and climate.

Ash-derived soils often exhibit changes in mineral crystallinity as a function of depth, with some profiles exhibiting increased crystallinity toward the surface and other sites showing decreases (Arnalds et al., 1995; Broquen et al., 2005). These trends likely reflect a variety of factors including the climate, age of the tephra deposits and the influence of vegetation. Within the Sverrefjell regolith profile, the abundance of short-range-ordered (SRO) Al and Fe (i.e., around 25-40% extracted with ammonium oxalate) increases slightly from the bottom of the regolith profile to the surface (Table 3-3). Similar SRO-Al and -Fe trends have been documented in Icelandic pedons consisting of low organic carbon concentrations and high glass content (Arnalds et al., 1995); in contrast, SRO-Si is roughly constant throughout the Sverrefjell regolith profile (Table 3-3).

Molar ratios of SRO Al/Si in regolith samples at our site (between 0.65 to 0.95 in the < 850 μm fraction, Table 3-5) are substantially lower than ratios observed at other sites dominated by allophane mineralogy (Arnalds and Kimble, 1995) and considerably lower than the 1.0-2.0 molar Al/Si ratio for pure allophane and imogolite (Dahlgren et al., 1993). In fact, most allophanes tend to exhibit a Al/Si ratio near 2.0, as Si-rich allophanes are relatively rare (Dahlgren et al., 1993). We suggest that the low carbon concentrations (~1%) in the Sverrfjell regolith and cold, dry climate of Svalbard may have promoted the formation of Si-rich allophanes, as similar observations were made in Icelandic volcanic ash soils which had carbon concentrations <5% (Arnalds, 2004). Alternatively, the low SRO Al/Si ratios at Sverrefjell may be related to the abundant Si coatings we observe on all weathered rock samples in the regolith profile. As these secondary silica coatings are more likely to dissolve in the ammonium oxalate extractant than Si in primary mineral phases, this may result in anomalously low Al/Si ratios. In addition to the coatings, the adsorption and polymerization of H_4SiO_4 onto ferrihydrite surfaces may also increase Si concentrations in ammonium oxalate extractions (Carlson and Schwertmann, 1981; Swedlund and Webster, 1999; Arnalds and Kimble, 2001).

Silica coatings or glazes have been observed in a wide variety of different climates and locations around the world including deserts, glaciers, Hawaiian drylands, temperate-humid environments and Antarctica (Dorn, 1998). There is also evidence that silica glazes exist on

Martian rocks (Kraft et al., 2003; Michalski et al., 2005) and speculation that they indicate prior presence of water. However, the presence of silica coatings on Martian rocks cannot be taken as direct evidence for the presence of liquid water. Dorn (2012) demonstrated that silica coatings can form in 20 years on dry basalts rocks exposed to 80% relative humidity.

Dixon et al. (2002) attributes silica glazes in northern Scandinavia to the dissolution of underlying bedrock coupled to subsequent precipitation of a SRO-Si phase. As discussed below, our colloidal mobilization experiments on Sverrefjell regolith samples document significant solubilization of Si (>2 mmol Si kg^{-1} soil) across the entire pH 4-10 range (Figure 3-9). Subsequent precipitation of this Si during drier periods may explain Si glazes in our samples. However, the mechanisms by which silica glazes form are not well understood and most silica glazes, including those observed in Antarctica, appear to contain large detrital particles derived from eolian sources (Dorn, 1998; Dixon et al., 2002). Micron-sized detrital material trapped within the silica coatings at our site (Figure 3-2) could be dust, and if so, suggest a potential contribution of Si from eolian sources.

Circumstantial evidence suggests that lichens may also influence the formation of silica coatings. The SEM images of the upper 3 cm of fractured rock collected from Site A indicate an abundance of fungal hyphae as well as what appear to be oxalate crystals associated with lichens (Figure D-4). Previous research has also documented the association of residual silica layers with crustose lichens (Wilson and Jones, 1983). At the Sverrefjell volcano, 20-µm Si-rich coatings are observed between the unweathered rock surface and what appears to be a lichen layer in SEM images (Hausrath 2007). However, we observe an abundance of silica coatings deeper in the regolith samples, where photosynthetic lichens do not grow. We therefore conclude that most Si glazes at this site form independently of lichens.

3-4.3. Colloidal dispersion:

The majority of colloids dispersed in our study were between 260-415 nm in size (Figure 3-8). Colloids of similar size (100-400 nm) were dispersed from Japanese volcanic ash soils and identified as allophane (Karube et al. 1996). Despite the fact that allophane is made up of unit spherical particles 3.5-5.5 nm in diameter (Karube et al., 1996), it evidently aggregates to form larger particles of similar size both at Sverrefjell volcano and in Japan.

Molar ratios of Al, Si and Fe in colloids dispersed under oxic conditions in the 260-415 nm size fraction were consistent from pH 4-10 (Figure 3-11). The approximate 1.4/1 Al/Si ratio of the dispersed particles (Table D-8) is consistent with allophane (Parfitt and Furkert, 1980), but too low for imogolite (Al/Si~2) and too high for kaolinite-halloysite (Al/Si~1) or for 2:1 silicates such as smectite and vermiculite (Al/Si <1; Essington, 2004).

Colloidal dispersion by electrostatic repulsion is favored as the solution pH moves away from the zero point of charge (ZPC) of the colloids, whereas coagulation is promoted in the vicinity of the zero point of charge (Seta and Karathanasis, 1996). Our regolith samples have a point of zero net charge at pH ~2.5. Since the inferred point of zero net charge of regolith is ~2.5, well below the pH range explored in this study (Figure D-1), we do not expect dramatic changes in the concentrations of dispersed elements from pH 4-8 (Figure 3-9). At pH 10, we suspect that the low concentrations of colloidal-sized particles (Figure 3-9) reflect the complete dissolution of allophane at this very high pH, consistent with the high dissolved Al and Si concentrations we measure at pH 10.

Under anoxic conditions, the majority of dispersed particles were smaller than in the oxic experiment, ranging in size from 35-260 nm (Figure 3-10; Table D-7). We initially suspected that the longer incubation in the anoxic experiments (1 to 3 weeks) relative to the 2-hour oxic experiments influenced this difference in colloid size. However, subsequent oxic experiments carried out for two weeks also produced larger-sized colloids (260-415 nm) (Figure 3-10), and thus differences in colloidal sizes at pH 6 between oxic and anoxic conditions can therefore be attributed to the mechanism of dispersion as opposed to differences in incubation times.

Rapid redox shifts have previously been associated with colloidal dispersion, but in several cases the influence of Fe(III) reduction could not be clearly separated from the influence of the pH increase associated with Fe-reduction, which can also drive changes in colloid composition through electrostatic repulsion (Ryan and Gschwend, 1990; Ryan and Gschwend, 1994; Thompson et al., 2006). The low PZNC of the Sverrefjell regolith sample allows the influence of Fe reduction on colloid dispersion to be discerned from general electrostatic mechanisms. A key difference between the oxic and anoxic experiments is that the concentrations of dissolved Fe (<2 nm) increased over the 3-week incubation time in the anoxic experiments (Table D-7), which we attribute to reductive dissolution of Fe(III)-rich phases. As discussed above, anoxic conditions also resulted in smaller colloidal-sized particles, which we

likewise attribute to the dissolution of Fe oxide cements and subsequent release of fines. Recent work has also found greater dispersion of P-bearing (Henderson et al., 2012) and C-bearing colloids (Buettner et al., in press) during anoxic incubation than during equivalent increases in pH under oxic conditions.

The very high correlation between dispersed Fe and Ti across the pH range (R^2= 0.995, $p<0.001$) suggests a close association between Ti and Fe in dispersed colloids (Table D-9). TEM/EDS analysis of colloidal-sized particles (200-400 nm in diameter) from Sverrefjell document Fe-rich clusters ~30 nm in size (Figure 3C and Figure D-2). In synthetic allophane studies spanning a range of Fe/Si ratios, McBride et al. (1984) concluded that little or no Fe(III) was incorporated into the allophane. Instead, a separate SRO Fe-rich product precipitated on the allophane particles. TEM/EDS data suggest that the colloids present at Sverrefjell are likewise heterogeneous in composition, with separate Fe- and Si-rich regions (Figure 3-3C). These findings are further consistent with findings from another TEM study of colloids dispersed from highly weathered ultisols in which 50-nm aluminosilicate flakes were studded with smaller Fe and Ti-rich clusters <10 nm in diameter (Henderson et al., 2010). This clustering of Fe and Ti may help to explain the finding that Fe and Ti tend to be even less mobile than Al during basalt weathering (Colman, 1982; Gislason et al., 1996).

The tendency of Fe, Al and Ti to readily form colloidal particles may further help to explain why these elements tend to be retained in the dry regolith profile at the Sverrefjell volcano. On the other hand, dissolved elements such as Na, Ca and Mg are more likely to be leached from the profile, even under the relatively dry conditions present at Sverrefjell. Although Si can be mobilized as a colloid, some fraction of mobilized Si is also present as solute, which explains intermediate loss of this element from the soil profile. Elevated concentrations of dissolved silica in incubation experiments were observed across the entire pH range from 4-10. Re-precipitation of such silica dissolved from the regolith during intermittent dry periods may explain the presence of Si-rich coatings on weathered rocks from the regolith profile. Based on findings from the Sverrefjell volcano, we expect that colloidal material is abundant in Martian regolith, with similar elemental fractionation to that observed in the colloidal dispersion experiments.

3-4.4. Frost action versus hydration:

While wetting and drying over 200 cycles released an average of ~0.2% of the total rock mass in our study, these rocks did not disaggregate as much as other lithologies. For example, Dunn and Hudec (1972) reported that carbonate rocks treated in a similar manner lost 3-10% of their mass after 25 cycles of wetting and drying. Basalt likely disintegrates less quickly because it lacks clays and argillaceous partings, which may accelerate splitting due to wetting-drying (Dunn and Hudec, 1972).

The percent mass lost was no higher in our wet/freeze/dry experiments than under the wet/dry scenario (Table 3-4), a finding that may be surprising considering the 9% volumetric increase that occurs when water changes to ice in rock pores and cracks (Fahey and Dagesse, 1984). Indeed, an experimental study of schist weathering revealed that frost action was three to four times more effective than hydration alone in causing rock disintegration (Fahey, 1983). Consistent with our study however, Fahey and Dagesse (1984) failed to note greater mass loss across freezing conditions in comparison to similar temperature shifts above and below freezing for argillaceous carbonate rocks. Likewise, Dunn and Hudec (1972) concluded that sorptive interactions with water vapor and liquid water were more destructive than freezing and thawing in clay-rich rocks from New York.

While it is commonly asserted that frost action is the major weathering process of consequence in cold climates, this belief has also been questioned (Dunn and Hudec, 1972; Thorn, 1979; Fahey, 1983; Hall and Hall, 1996; Hall et al., 2002). Wetting and drying alone is thought to be of particular importance when clay minerals are present, perhaps because the highly polar water molecule links to clay layers and leads to repulsive forces that break the rock (Fahey, 1983). Furthermore, this adsorbed water has been shown to resist freezing at temperatures as low as -40^0C (Dunn and Hudec, 1972), perhaps explaining why freezing does not always lead to additional disintegration beyond wetting and drying.

We attempted to calculate the weathering advance rate due to freeze/thaw cycles. The frequency of freeze/thaw cycles in the ground cannot be gauged from air surface temperatures (Hall and Hall, 1996), and thus it is difficult to extrapolate weathering advance rates due to spalling in the field. In an alpine environment of Colorado, Thorn (1979) estimated the annual number of freeze/thaw cycles to range from 40-150 depending upon the location. On the other

hand, Fraser (1959) argued that the frequency of freeze/thaw cycles decreases from ~60 in southern Canada to ~20 in northern regions. For Sverrefjell, we assume ~100 cycles yr^{-1} to extrapolate rates, noting this value could vary between 20 to 150 cycles yr^{-1}. This yields a BET-normalized spalling advance rate of ~2 $x10^{-4}$ mm ky^{-1}. Based on reaction transport modelling for one Svalbard clast, a surface retreat of 400 μm due to physical weathering was estimated previously (Brantley and White, 2009; Hausrath et al., 2008a): such physical weathering at Sverrefjell therefore results in a total retreat of 400 μm over 10,000 years, yielding a physical weathering advance rate of ~$2.0*10^{-4}$ mm ky^{-1}. This value incorporates a conversion from the clast to BET surface area scale using a scaling factor of 200 (Navarre-Sitchler et al., 2007). This value is the same as the approximate physical loss rates calculated from the wet/dry experiments. It therefore appears that wetting and drying alone may reasonably simulate physical weathering rates estimated in the field.

At the Sverrefjell volcano, Hausrath et al. (2008a) previously documented that several samples (collected from 17 cm at Site A) show chemical weathering-related leaching of Na from glass to depths of ~250 μm. If weathering is assumed to have occurred for 10,000 years since deglaciation and if clast rates are again converted to the BET scale using a conversion factor of 200 (Navarre-Sitchler et al., 2007), then this yields a chemical weathering advance rate of ~$1.2x10^{-4}$ mm ky^{-1}. In comparison, when basaltic clasts from four different studies in temperate environments in Japan and the western United States were scaled by BET surface area according to Navarre-Sitchler and Brantley (2007), the estimated chemical weathering advance rates were ~1 x 10^{-4} mm ky^{-1}. In those studies, however, alteration rinds built up on the clast surfaces: in contrast, at Svalbard, only very thin chemical leaching rinds are observed. These weathering rates are consistent with observations of high concentrations of amorphous phases at Sverrefjell and confirm very high chemical weathering rates at this site despite the cold, dry climate.

In conclusion, chemical and physical weathering of basalts at Sverrefjell appears to proceed at surprisingly fast rates given the cold, dry climate. Relatively fast chemical leaching could be related to the fast rates of spalling and exposure of fresh surfaces to repeated wetting/drying cycles. Given that our experiments are inconsistent with an added impact from freezing, perhaps the wet/dry process is enhanced at Sverrefjell due to the dry regolith profile, which may allow for more significant disintegration of the rock when small amounts of water are occasionally adsorbed onto dry surfaces.

3-5. Conclusions

Despite the cold, dry climate (annual precipitation <200 mm) and the relatively short duration of time for weathering (~10,000 years), secondary phases are forming in regolith at the Sverrefjell volcano. In fact, concentrations of short-range-ordered Al, Fe and Si are higher than those in older volcanic ash deposits in the much warmer, wetter climate of New Zealand (Parfitt et al., 1983). The cold, dry climate of Sverrefjell therefore appears to facilitate the rapid formation and retention of secondary phases in regolith. The predominant weathering product at Sverrefjell appears to be allophane, with no evidence for halloysite or extensive phyllosilicate clays. The lack of these latter phases is likely due to the short weathering time. Relative to other volcanic soils in warmer, wetter climates, SRO phases from the Sverrefjell regolith have low Al/Si ratios, either indicating a high-silica allophane or reflecting the abundance of silica glazes present at Sverrefjell. Based on the chemistry of the clay-sized fraction, the relative order of loss of elements from regolith was observed to be: (Na, K) > (Ca, Mg) > Si > (Fe, Al, Ti). If the Sverrefjell volcano is indeed a good Mars analog site, then we can expect a similar relative loss of elements from circumneutral Mars regolith. Moreover, we would expect that Martian regolith would be made up predominantly of primary minerals with some secondary allophane and an abundance of Si coatings on weathered rocks. The fact that allophane and Si coatings are prevalent at Sverrefjell lends further support for the argument based on thermal emission spectrometer data that allophane and Si-rich coatings are common on the surface of Mars (Kraft et al., 2003).

TEM/EDS data suggest that the colloids present at Sverrefjell are heterogeneous in composition, with separate Fe- and Si-rich regions. Based on the colloidal batch experiments, we expect the regolith weathering at pH~6 to release Al, Fe and Ti as colloids (35 and 450 nm) rather than as solutes. In contrast, elements such as Na, Ca and Mg are mobilized largely as solutes. Based upon estimates of from the advance rates of chemical and physical weathering, we infer high rates of chemical weathering at this site that are comparable to rates observed in temperate climates. The high rate of leaching is attributed to the continual exposure of fresh surfaces due to physical spalling. Cyclic freezing experiments did not disintegrate the rock faster than wetting and drying alone: all treatments resulted in ~0.2% mass loss over ~200 cycles. These experiments are in agreement with previous research suggesting that extensive weathering

in cold, dry climates such as Sverrefjell volcano and Mars need not be attributed exclusively to freeze/thaw processes.

Acknowledgements: We thank Henry Gong for assistance with ICP-AES, Beth Jones for assistance with XRD and Trevor Clark for help with the TEM. Funding was provided by the Penn State Astrobiology Research Center grant NNA04CC06A.

References:

Anderson, S.P., Dietrich, W.E., and Brimhall, G.H., 2002, Weathering profiles, mass-balance analysis, and rates of solute loss: Linkages between weathering and erosion in a small, steep catchment. Geol. Soc. Am. Bull. 114: 1143-1158.

Arnalds, O., Hallmark, C.T., and Wilding, L.P., 1995, Andisols from four different regions of Iceland. Soil Sci. Soc. Am. J. 59: 161-169.

Arnalds, O., and Kimble, J., 2001, Andisols of deserts in Iceland. Soil Sci. Soc. Am. J. 65: 1778-1786.

Arnalds. O., 2004, Volcanic soils of Iceland. Catena. 56: 3-20.

Banin, A., 1996, The missing crystalline minerals in Mars soil. Adv. Space Res. 18: 233-240.

Bleeker, P., and Parfitt, R.L., 1974, Volcanic ash and its clay mineralogy at Cape Hoskins, New Britain, Papua New Guinea. Geoderma. 11: 123-135.

Brantley, S.L., and White, A.F., 2009, Approaches to modeling weathered regolith. Reviews in Mineralogy & Geochemistry. Vol. 70: Thermodynamics and Kinetics of Water-Rock Interaction. Eds. Oelkers, E.H., and Schott, J., pp.435-484.

Brimhall G.H., and Dietrich, W.E., 1987, Constitutive mass balance relations between chemical composition, volume, density, porosity, and strain in metasomatic hydrochemical systems: Results on weathering and pedogenesis. Geochim. Cosmochim. Ac. 51: 567-587.

Broquen, P., Lobartini, J.C., Candan, F., and Falbo, G., 2005, Allophane, aluminum, and organic matter accumulation across a bioclimatic sequence of volcanic ash soils of Argentina. Geoderma. 129: 167-177.

Buettner, S., Kramer, M., Chadwick, O.A., and Thompson, A., in press, Mobilization of colloidal carbon during reduction events in basaltic soils. Geoderma.

Campbell. I.B., and Claridge, G.G.C., 1987, Antarctica: Soils, Weathering Processes and Environment. Developments in Soil Science 16. Elsevier Science Publishing Company Inc. New York, NY.

Carlson, L., and Schwertmann, U., 1981, Natural ferrihydrites in surface deposits from Finland and their associations with silica. Geochim. Cosmochim. Ac. 45: 421-429.

Chadwick, O.A., Gavenda, R.T., Kelly, E.F., Ziegler, K., Olson, C.G., Elliott, W.C., and Hendricks, D.M., 2003, The impact of climate on the biogeochemical functioning of volcanic soils. Chem. Geol. 202: 195-223.

Colman, S.M., 1982, Chemical Weathering of Basalts and Andesites: Evidence from Weathering Rinds. Geological Survey Professional Paper 1246. U.S. Department of the Interior. United States Government Printing Office, Washington.

Dahlgren, R., Shoji, S., and Nanzyo, M., 1993, Chapter 5: Mineralogical characteristics of volcanic ash soils. In Volcanic Ash Soils: Genesis, Properties and Utilization. Eds. Shoji, S., Nanzyo, M., and Dahlgren, R.A. Developments in Soil Science 21. Elsevier. Amsterdam, The Netherlands. 101-143.

Dahlgren, R.A., 1994, Quantification of allophane and imogolite. Methods in Soil Mineralogy, SSSA Miscellaneous Publication. pp. 430-451. Eds. J.E. Amonette and L.W. Zelazny. Soil Science Society of America, Inc. Madison, Wisconsin, USA.

Dixon, J.C., Thorn, C.E., Darmody, R.G., Campbell, S.W., 2002, Weathering rinds and rock coatings from an Antarctic alpine environment, northern Scandinavia. Geol. Soc. Am. Bull. 114: 226-238.

Dorn, R.I., 1998, Chapter 13: Silica Glaze. Rock Coatings. Developments in Earth Surface Processes 6. Elsevier, Amsterdam.

Dorn, R.I., 2012, Formation of silica glaze rock coatings through water vapor interactions. Phys. Geogr. 33: 21-31.

Dunn, J.R., and Hudec, P.P., 1972, Frost and sorption effects in argillaceous rocks. Highway Res. Record. 393: 65-78.

Ehlmann, B.L., Mustard, J.F., Murchie, S.L., Bibring, J., Meunier, A., Fraeman, A.A., and Langevin, Y., 2011, Subsurface water and clay mineral formation during the early history of Mars. Nature. 479: 53-60.

Eggleton, R.A., Foudoulis, C., Varkevisser, D., 1987, Weathering of basalt: Changes in rock chemistry and mineralogy. Clays Clay Miner. 3: 161-169.

Essington, M.E., 2004, Soil and Water Chemistry: An Integrative Approach. Boca Raton, CRC Press, p. 328.

Fahey, B.D., 1983, Frost action and hydration as rock weathering mechanisms on schist: A laboratory study. Earth Surf. Proc. and Land. 8: 535-545.

Fahey, B.D., and Dagesse, D.F., 1984, An experimental study of the effect of humidity and temperature variations on the granular disintegration of argillaceous carbonate rocks in cold climates. Arctic Alpine Res. 16: 291-298.

Farmer, V.C., Smith, B.F.L., and Tait, J.M., 1979, The stability, free energy and heat of formation of imogolite. Clay Miner. 14: 103-107.

Fraser, J., 1959, Freeze-thaw frequencies and mechanical weathering in Canada. Arctic.12: 40-53.

Gilkes, R.J., 1994, Transmission electron microscope analysis of soil materials. Quantitative Methods in Soil Mineralogy, SSSA Miscellaneous Publication. pp. 177-204. Eds. J.E. Amonette and L.W. Zelazny. Soil Science Society of America, Inc. Madison, Wisconsin, USA.

Gislason, S.R., and Eugster, H.P., 1987, Meteoric water-basalt interactions. I: A laboratory study. Geochim. Cosmochim. Ac. 51: 2827-2840.

Gislason, S.R., Arnorsson, S., and Armannsson, H., 1996, Chemical weathering of basalt in southwest Iceland: effects of runoff, age of rocks and vegetative/glacial cover. Am. J. Sci. 296: 837-907.

Gordon, S.J., and Dorn, R.I., 2005, In situ weathering erosion. Geomorphology, 67: 97-113.

Hall, K., and Hall, A., 1996, Weathering by wetting and drying: Some experimental results. Earth Surf. Proc. and Land. 21: 365-376.

Hall, K., Thorn, C.E., Matsuoka, N., and Prick, A., 2002, Weathering in cold regions: some thoughts and perspectives. Prog. Phys. Geog. 26: 577-603.

Hausrath, E.M., 2007, Basalt Weathering on Earth and Mars. Ph.D. Thesis. College of Earth and Mineral Sciences. The Pennsylvania State University.

Hausrath, E.M., Navarre-Sitchler, A.K., Sak, P.B., Steefel, C.I., Brantley, S.L., 2008a, Basalt weathering rates on Earth and the duration of liquid water on the plains of Gusev Crater, Mars. Geology. 30: 67-70.

Hausrath, E.M., Treiman, A. H., Vicenzi, E., Bish, D.L., Blake. D., Sarrazin, P., Hoehler, T., Midtkandal, I., Steele, A., and Brantley, S.L., 2008b, Short- and long-term olivine weathering in Svalbard: Implications for Mars. Astrobiology. 8: 1079-1092.

Henderson, R., Kabengi, N., Mantripragada, N., Cabrera, M., Hassan. S., and Thompson, A., 2012, Anoxia-induced release of colloid- and nanoparticle-bound phosphorus in grassland soils. Environ. Sci. Technol. 46:11727-11734.

Herndon, E.M., Jin, L., and Brantley, S.L., 2011, Soils reveal widespread manganese enrichment from industrial inputs. Environ. Sci. Technol. 45: 242-247.

Huh, Y., 2003, Chemical weathering and climate-a global experiment: A review. Geosci. J. 7: 277-288.

Jackson M.L., 1956, Soil Chemical Analysis-Advanced Course. Chapter 3. University of Washington, Dept. of Soils, Madison, Wisconsin. pp. 101-168.

Jakosky, B.M., Nealson, K.H., Bakermans, C., Ley, R.E., Mellon, M.T., 2003, Subfreezing activity of microorganisms and the potential habitability of Mars' polar regions. Astrobiology. 3: 343-350.

Karube, J., Nakaishi, K., Sugimoto, H., and Fujihira, M., 1996, Size and shape of allophane partices in dispersed aqueous systems. Clays Clay Miner. 44: 485-491.

Kawano, M., and Tomita, K., 2001, TEM-EDX study of weathered layers on the surface of volcanic glass, bytownite, and hypersthene in volcanic ash from Sakurajima volcano, Japan. Am. Mineral. 86: 284-292.

Kitagawa, Y., 1974, Dehydration of allophane and its structural formula. Am. Mineral. 59: 1094-1098.

Kraft, M.D., Michalski, J.R., and Sharp, T.G., 2003, Effects of pure silica on thermal emission spectra of basaltic rocks: Considerations for Martian surface mineralogy. Geophys. Res. Lett. 30: 2288, doi:10.1029/2003GL018848.

McBride, M.B., Farmer, V.C., Russell, J.D., Tait, J.M., and Goodman, B.A., 1984, Iron substitution in aluminosilicate sols synthesized at low pH. Clay Miner. 19: 1-8.

McKay, C.P., Toon, O.B., and Kasting, J.F., 1991, Making Mars habitable. Nature. 352:489-496.

McKeague, J.A., 1967, An evaluation of 0.1 M Pyrophosphate and pyrophosphate-dithionite in comparison with oxalate as extractants of the accumulation products in podzols and some other soils. Can. J. Soil Sci. 47: 97-99.

McKeague, J.A., Day, J.K., 1966, Dithionite- and oxalate-extractable Fe and Al as aids in differentiating various classes of soils. Can. J. Soil Sci. 46: 13-22.

Matejovic, I., 1996, The application of Dumas method for determination of carbon, nitrogen, and sulphur in plant samples. Rost. Vyroba. 42:313-316.

Michalski, J.R., Kraft, M.D., Sharp, T.G., Williams, L.B., and Christensen, P.R., 2005, Mineralogical constraints on the high-silica martian surface component observed by TES. Icarus. 174: 161-177.

Navarre-Sitchler, A., and Brantley, S.L., 2007, Basalt weathering across scales. Earth Planet. Sci. Lett. 261: 321-334.

Neaman, A., Chorover, J., and Brantley, S.L., 2005, Implications of the evolution of organic acid moieties for basalt weathering over geological time. Am. J. Sci. 305: 147-185.

Nesbitt, H.W., and Wilson, R.E., 1992, Recent chemical weathering of basalts. Am. J. Sci. 292: 740-777.

Parfitt, R.L., Furkert, R.J., and Hemni, T., 1980, Identification and structure of two types of allophane from volcanic ash soils and tephra. Clays Clay Miner. 28: 328-334.

Parfitt, R.L., Russell, M., and Orbell, G.E., 1983, Weathering sequence of soils from volcanic ash involving allophane and halloysite, New Zealand. Geoderma. 29: 41-57.

Parfitt, R.L., and Wilson, A.D., 1985, Estimation of allophane and halloysite in three sequences of volcanic soils, New Zealand. In: Caldas, E.F., Yaalon, D.H. (Eds.), Volcanic Soils. Catena Supplement 7, pp.1-8.

Parfitt, R.L., and Childs, C.W., 1988, Estimation of forms of Fe and Al: A review, and analysis of contrasting soils by dissolution and Moessbauer methods. Aust. J. Soil Res. 26: 121-144.

Ping. C.L., Shoji, S., and Ito, T., 1988, Properties and classification of three volcanic ash-derived pedons from Aleutian Islands and Alaska Peninsula, Alaska. Soil Sci. Soc. Am. J. 52: 455-462.

Ping, C.L., Shoji, S., Ito, T., Takahashi, T., and Moore, J.P., 1989, Characteristics and classification of volcanic-ash-derived soils in Alaska. Soil Sci. 148: 8-28.

Pokrovsky, O.S., Schott, J., Kudryavtzev, D.I., Dupre, B., 2005, Basalt weathering in Central Siberia under permafrost conditions. Geochim. Cosmochim. Ac. 69: 5659-5680.

Rampe, E.B., Kraft, M.D., Sharp, T.G., Golden, D.C., Ming, D.W., and Christensen, P.R., 2012, Allophane detection on Mars with thermal emission spectrometer data and implications for regional-scale chemical weathering processes. Geology. 40: 995-998.

Rasmussen, C., Dahlgren, R.A., and Southard, R.J., 2010, Basalt weathering and pedogenesis across an environmental gradient in the southern Cascade Range, California, USA. Geoderma. 154: 473-485.

Ryan, J.N., and Gschwend, P.M., 1990, Colloid mobilization in two Atlantic Coastal Plain aquifers: Field Studies. Water Resour. Res. 26: 307-322.

Ryan, J.N., and Gschwend, P.M., 1994, Effect of solution chemistry on clay colloid release from an iron oxide-coated aquifer sand. Environ. Sci. Technol. 28: 1717-1726.

Sak, P.B., Fisher, D.M., Gardner, T.W., Murphy, K., and Brantley, S.L., 2004, Rates of weathering rind formation on Costa Rican basalt. Geochim. Cosmochim. Ac. 68: 1453-1472.

Sak, P.B., Navarre-Sitchler, A.K., Miller, C.E., Daniel, C.C., Gaillardet, J., Buss, H.L., Lebedeva, M.I., and Brantley, S.L., 2010, Controls on rind thickness on basaltic andesite clasts weathering in Guadeloupe. Chem. Geol. 276: 129-243.

Seta, A.K., and Karathanasis, A.D., 1996, Water dispersible colloids and factors influencing their dispersibility from soil aggregates. Geoderma. 74: 255-266.

Shikazono, N., Takino, A., Ohtani, H., 2005, An estimate of dissolution rate constant of volcanic ash soil from the Mt. Fuji area, central Japan. Geochem. J. 39: 85-196.

Shoji, S., and Saigusa, M., 1977, Amorphous clay materials of Towada ando soils. Soil Sci. Plant Nutr. 23: 437-455.

Skelkvale, B.L., Amundsen, H.E.F., O'Reilly, S.Y., Griffin, W.L., and Gjelsvik, T., 1989. A primitive alkali basaltic stratovolcano and associated eruptive centres, Nothwestern Sptisbergen: Volcanology and tectonic significance. J. Volcanol. Geoth. Res. 37: 1-19.

Stefansson, A., and Gislason, S.R., 2001, Chemical weathering of basalts, southwest Iceland: effect of rock crystallinity and secondary minerals on chemical fluxes to the ocean. Am. J. Sci. 301: 513-556.

Swedlund, P.J., and Webster, J.G., 1999, Adsorption and polymerization of silicic acid on ferrihydrite, and its effect on arsenic adsorption. Water Res. 33: 3413-3422.

Thomas, M., Clarke, J.D.A., and Pain, C.F., 2005, Weathering, erosion and landscape processes on Mars identified from recent rover imagery, and possible Earth analogues. Aust. J. Earth Sci. 52: 365-378.

Thomas, G.W., 1996, Chapter 16. Soil pH and soil acidity. pp. 487-488. Methods of Soil Analysis Part 3: Chemical Methods. Soil Science Society of America, Inc. Madison, Wisconsin. Book Series No. 5. Sparks, D.L.

Thompson, A., Chadwick, O.A., Boman, S., Chorover, J., 2006, Colloid mobilization during soil iron redox oscillations. Environ. Sci. Technol. 40: 5743-5749.

Thorn, C.E., 1979, Bedrock freeze/thaw weathering regime in an alpline environment, Colorado Front Range. Earth Surf. Proc. Land. 4: 211-228.

Treiman, A.H., 2012, Eruption age of the Sverrefjellet volcano, Spitsbergen Island, Norway. Polar Res. 31:17320.

Ugolini, F.C., and Dahlgren, R.A., 2002, Soil development in volcanic ash. Global Environ. Res. 6: 69-81.

Verdugo, P., Alldredge, A.L., Azam, F., Kirchman, D.L., Passow, U., and Santschi, P.H., 2004, The oceanic gel phase: a bridge in the DOM-POM continuum. Mar. Chem. 9: 67-85.

Wada, K., Arnalds, O., Kakuto, Y., Wilding, L.P., and Hallmark, C.T., 1992, Clay minerals of four soils formed in eolian and tephra materials in Iceland. Geoderma. 52: 351-365.

Whittig, L.D., and Allardice, W.R., 1986, X-ray diffraction techniques. *In* A. Klute (ed.) Methods of soil analysis. Part 1. Physical and mineralogical methods 2nd ed. ASA and SSSA, Madison, WI.

Wilson, M.J., and Jones, D., 1983, Lichen weathering of minerals: implications for pedogenesis. Geological Society, London, Special Publications. 11: 5-12.

Zelazny, L.W., He, L., and Vanmormhoudt, A., 1996, Charge analysis of soils and anion exchange. p. 1231-1253. In D.L. Sparks et al. (ed.) Methods of soil analysis. Part III. SSSA Book Ser. 5. SSSA, Madison, WI.

Ziegler, K., Hsieh, J.C.C., Chadwick, O.A., Kelly, E.F., Hendricks, D.M., and Savin, S.M., 2003, Halloysite as a kinetically controlled end product of acid-zone basalt weathering. Chem. Geol. 202: 461-478.

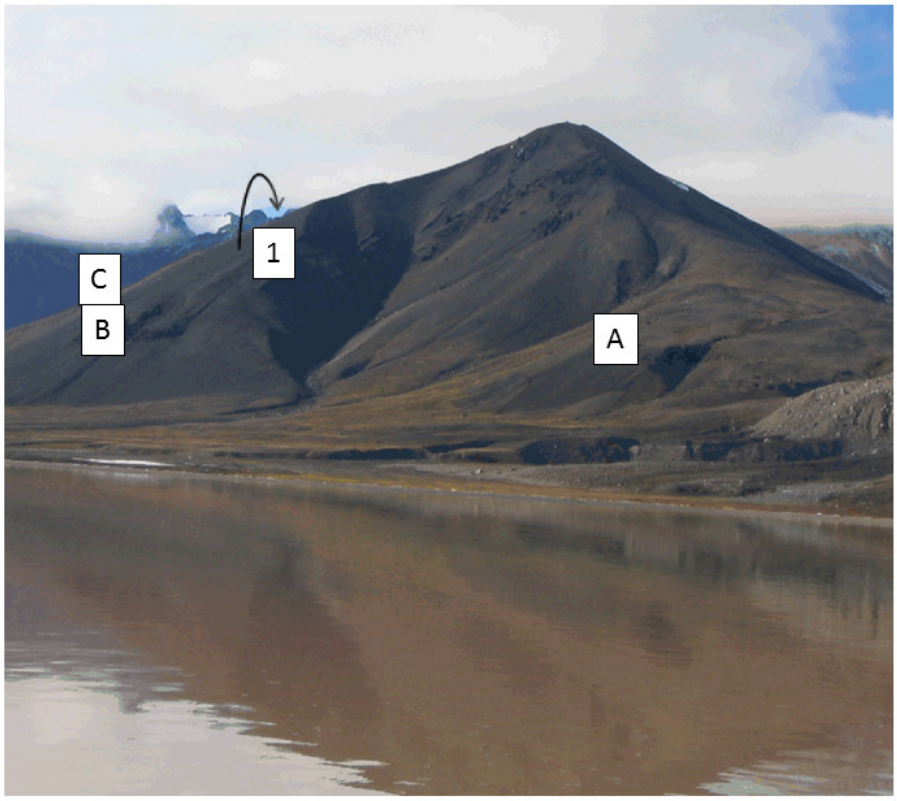

Figure 3-1. The 500-m Sverrefjell volcano. Sites A-C (respective elevations of 162 m, 157 m and 175 m) are the locations from which fractured rock samples were obtained in the summer of 2005. Site 1 indicates location of the 74-cm loose regolith core collected during the summer of 2004 (elevation=365 m).

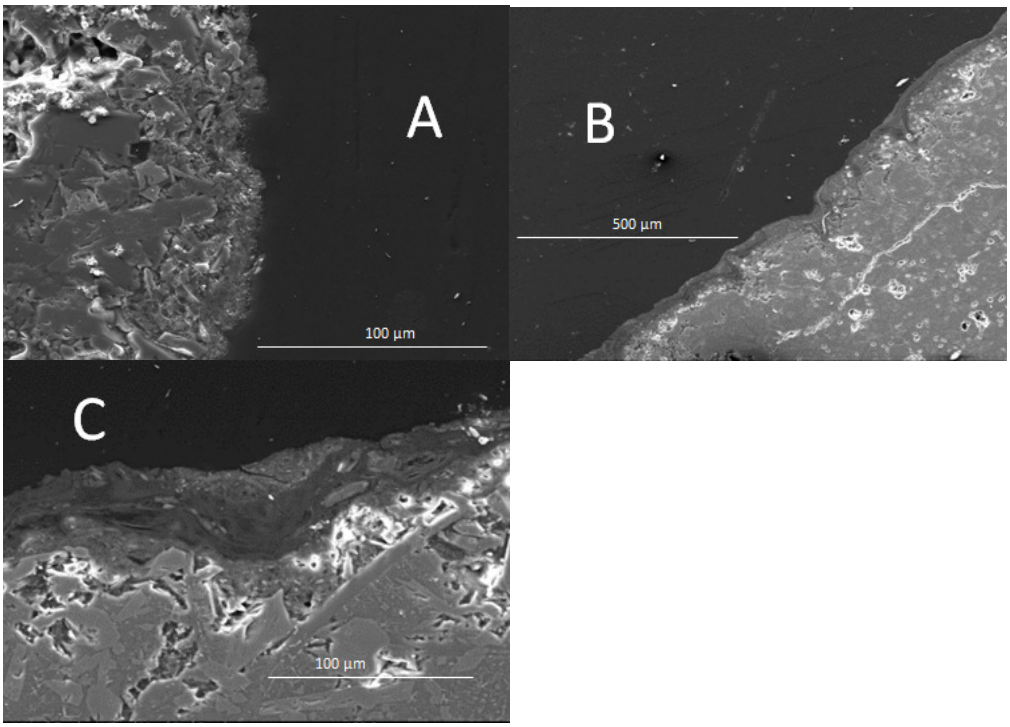

Figure 3-2. Secondary electron images (Everhart-Thornley Detector, 20 kV) of epoxied surfaces of two rocks taken from the regolith core (38-47 cm depth) showing: A) the ~50 µm surface of Rock 1, which is depleted in Ca, K, Na and Mg based upon EDS data (Table D-2), B) a silica-rich coating on Rock 2, and C) a closer view of another part of the thick Si coating (~40 µm thick here) from Rock 2. Micron-sized detrital particles are evident in C, while an incipient, surface-parallel fracture is evident in B. EDS data for Rocks 1 and 2 are given in Table D-2.

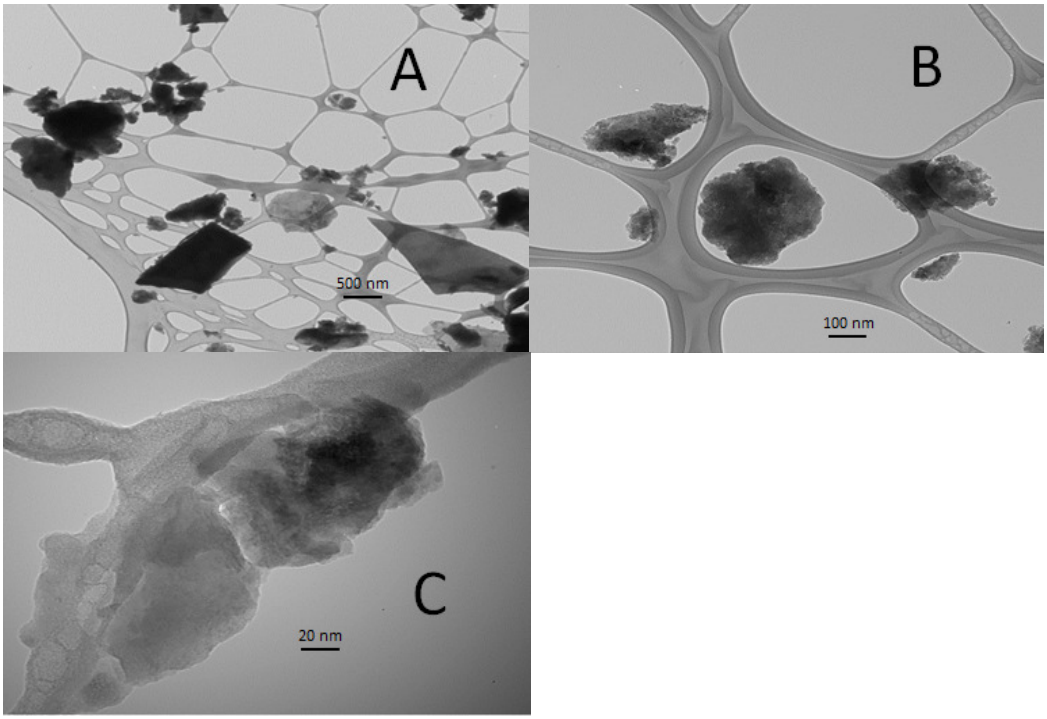

Figure 3-3. A) TEM image of the clay-sized (<2 μm) fraction from the regolith core (38-47 cm depth) showing a wide variety of different morphologies, with the lacey carbon grid in the background. B) TEM micrograph showing the clay-sized (<2 μm) fraction of regolith core. The electron diffraction pattern determined for three of the particles shown in the image indicated diffuse rings documenting amorphous material. EDS analysis further indicated that the particles are made up primarily of Al, Si and Fe (Supplemental Figure 2). C) TEM image of a colloidal-sized particle ~400 nm in length from the regolith core. The darker ~30 nm region in the upper right contains much more iron and less silica compared to the rest of the particle (Figure D-2).

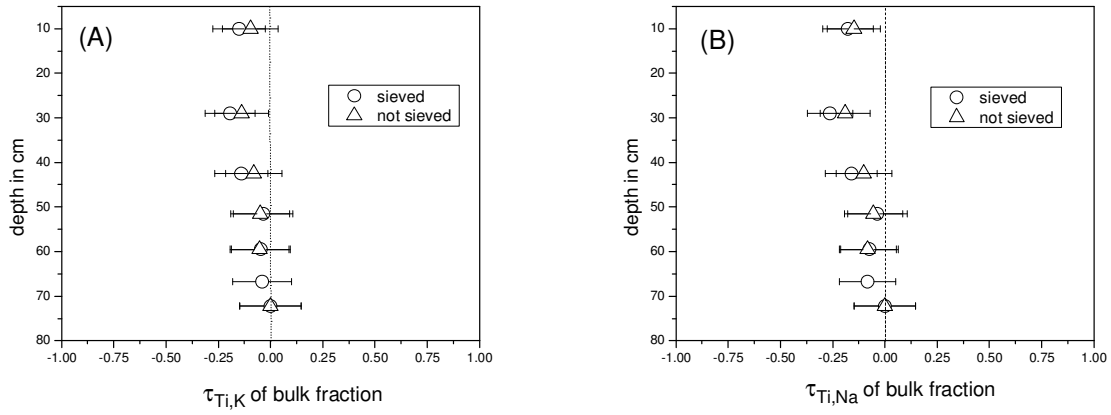

Figure 3-4. Bulk profile of $\tau_{Ti,X}$ plotted versus depth as analyzed in the 75-cm loose regolith core for sieved (<2 mm) and unsieved bulk samples. The parent material ($\tau_{Ti,X}$=0) is taken to be the lowermost regolith sample. Error bars calculated using Equation (3-2) in text. Profiles for all other elements analyzed (Al, Ca, Fe, Mg, Mn, P, Si) did not vary significantly from 0 at any depth (Table D-3).

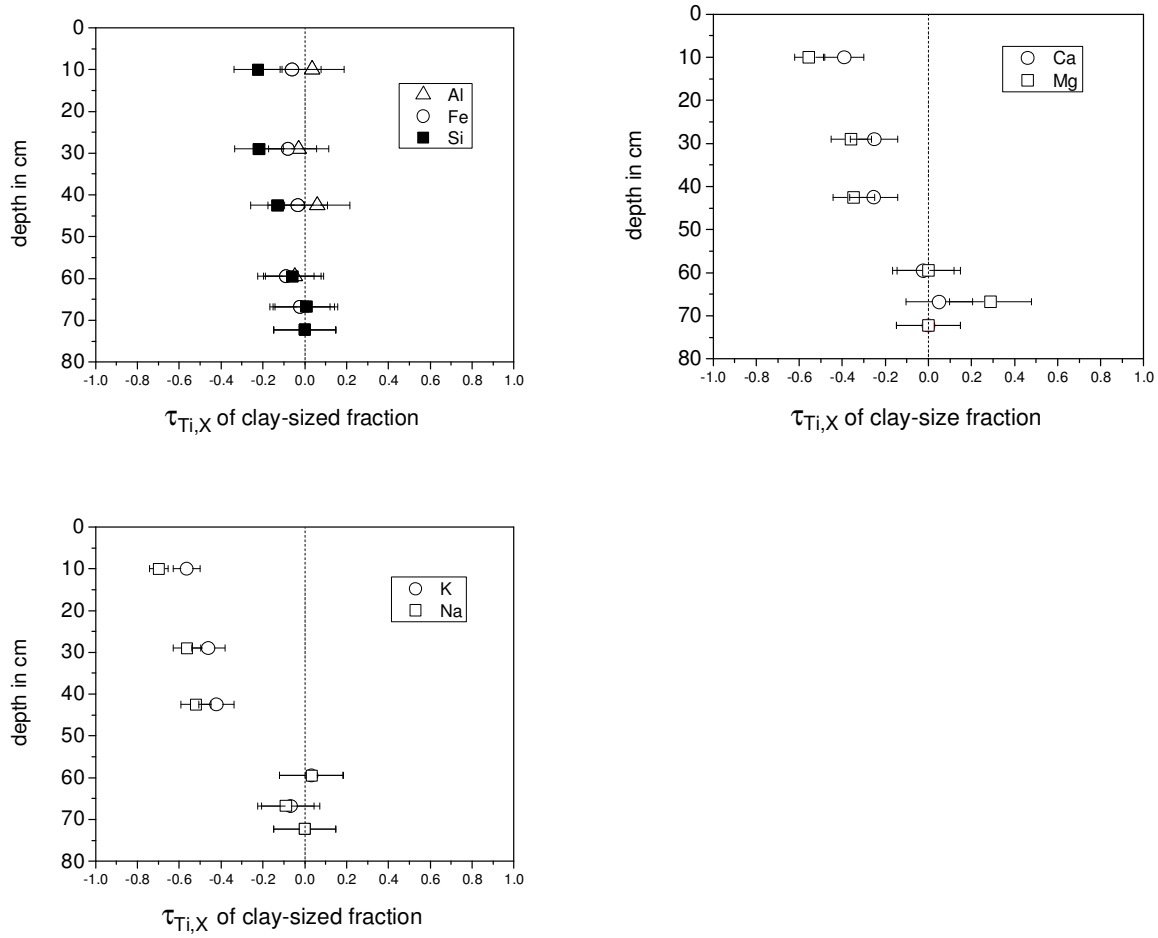

Figure 3-5. $\tau_{Ti,X}$ values for the clay-sized (<2 μm) fraction of the loose regolith core plotted versus depth. The parent material is taken to be the clay-sized fraction of the lowermost regolith sample. Error bars from Equation (3-2) in text.

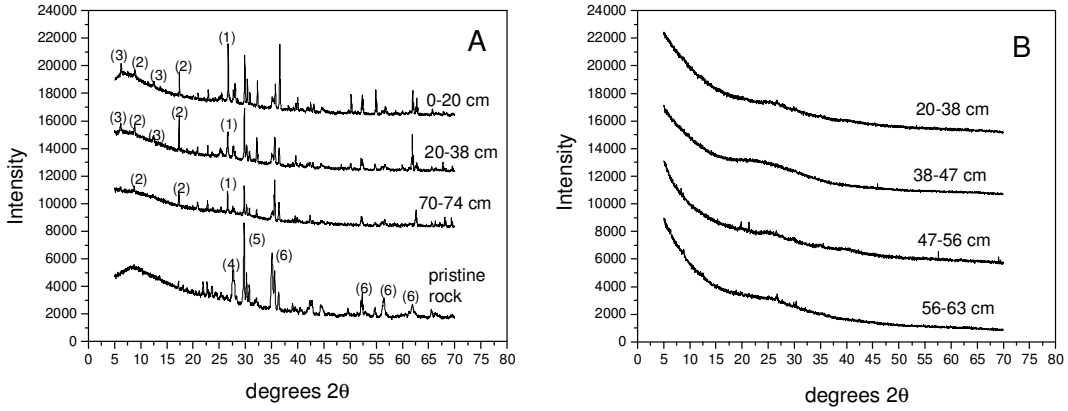

Figure 3-6. A) XRD scans of the sieved (<850 μm) sample with depth in the regolith core. Samples were ground to <100 μm prior to analysis. Labels indicate 2θ values of (1) quartz, (2) muscovite, (3) an unidentified phyllosilicate, (4) plagioclase, (5) augite and (6) forsterite. B) Scans of the clay-sized fraction of two sample depths from the regolith core. Clay-sized samples were prepared by the dropper method, as explained in the text.

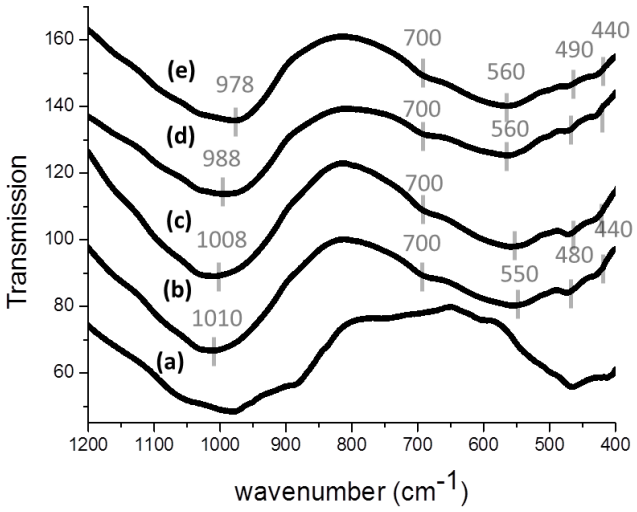

Figure 3-7. IR spectra for the clay-sized fraction of a) material recovered from a pristine rock from the regolith core, b) the 70.5-74 cm regolith core sample, c) the 63-70.5 cm regolith core sample, d) the 38-47 cm regolith core sample and e) the 0-20 cm regolith core sample. The gray vertical lines indicate characteristic bands expected for allophane (Parfitt et al., 1980).

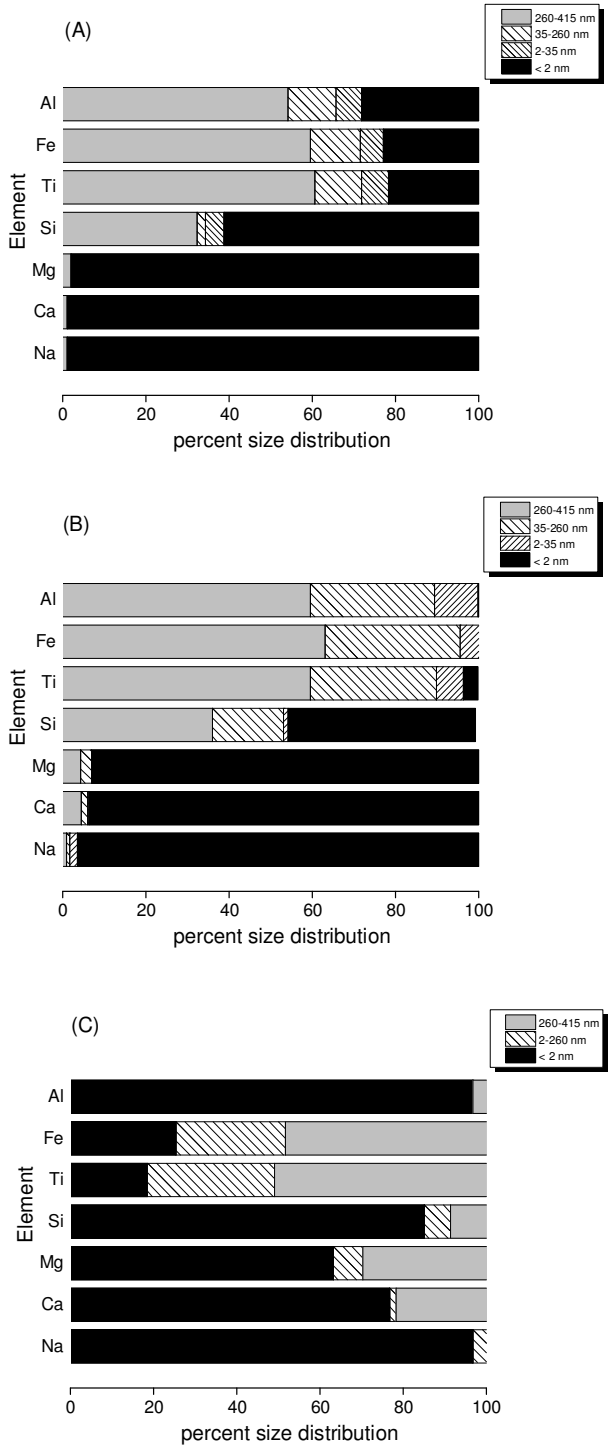

Figure 3-8. Elemental size distributions of dispersed colloidal particles under oxic conditions at A) pH=4, B) pH=5-8, and C) pH=10. B) shows the average values for five samples measured in the 5-8 pH range. See Supplemental Table 5 for raw data.

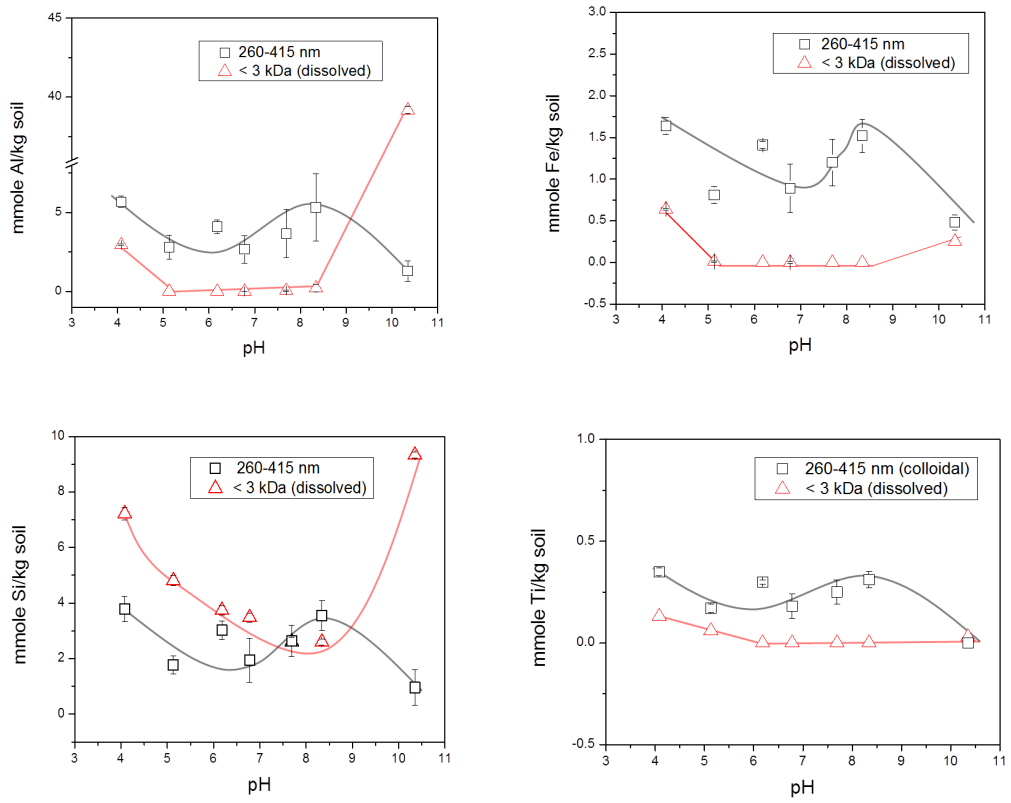

Figure 3-9. Concentrations of dispersed elements as a function of pH under oxic conditions in the larger colloidal (260-415 nm) and dissolved (<3 kDa) fractions. Error bars show the 1σ variation for triplicate experiments. See Table D-7 for raw data.

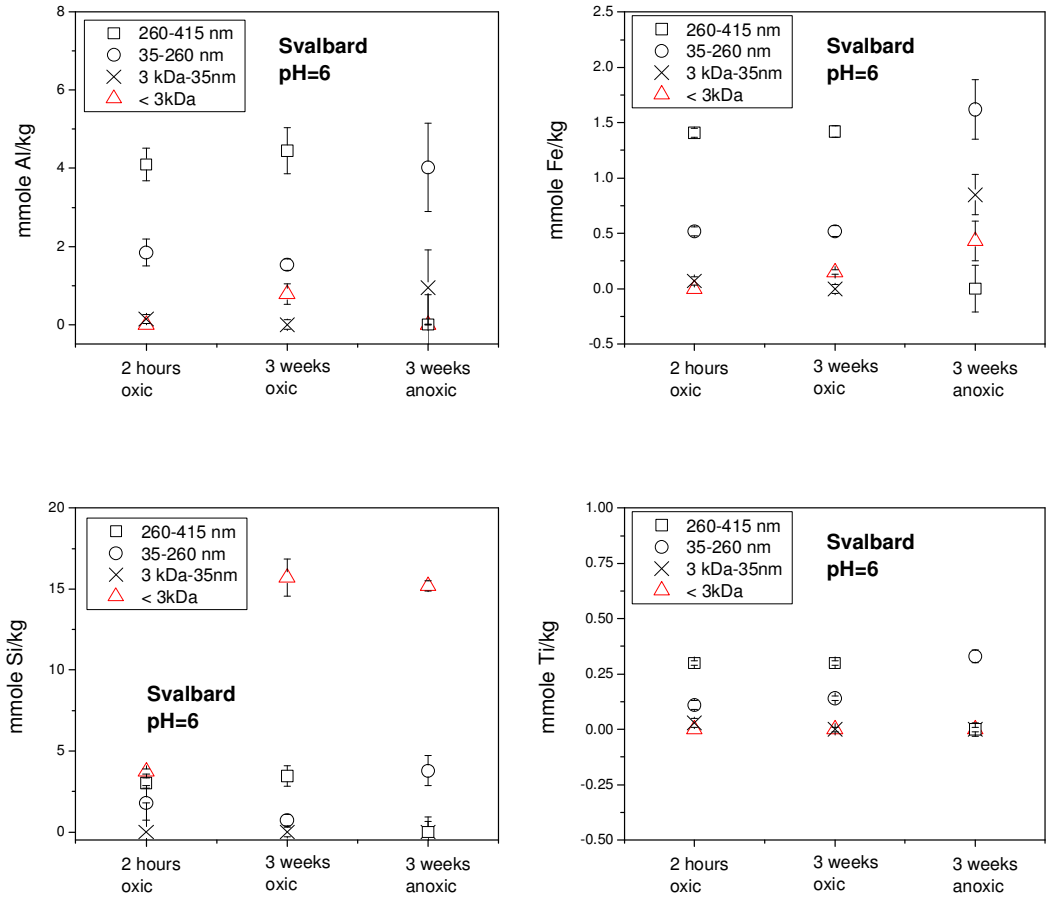

Figure 3-10. Concentration of dispersed elements as a function of time for oxic and anoxic experiments performed at pH 6. Error bars show the 1σ variation for triplicate experiments. See Table D-7 for raw data.

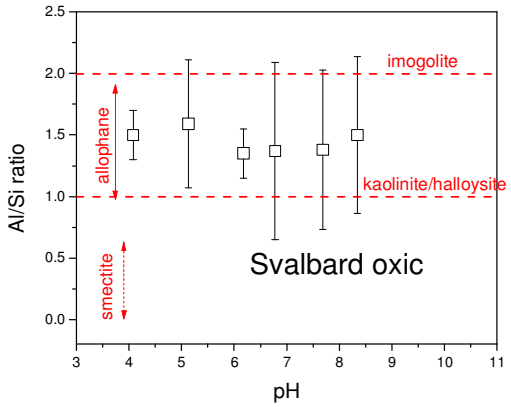

Figure 3-11. Molar ratio of Al/Si dispersed in the 260-415 nm size fraction as a function of pH under oxic conditions. Error bars show the 1σ variation for triplicate experiments. See Table D-8 for raw data.

Tables:

Table 3-1: Particle size data for Svalbard core[1]

depth	mid-depth	% rock	% sand	% silt	% clay
0-20 cm	10	31.20	52.32	3.45	1.02
20-38 cm	29	24.94	63.86	9.77	1.43
38-47 cm	42.5	39.40	47.85	17.57	0.60
47-56 cm	51.5	45.72	48.84	4.81	0.63
56-63 cm	59.5	72.38	21.29	3.13	0.29
63-70.5 cm	66.75	41.67	49.57	8.16	0.61
70.5-74 cm	72.25	43.21	47.63	6.46	0.38

1) Separated with wet sieving method of Jackson (1956)

Table 3-2: Total soil carbon and nitrogen of regolith core[1]

Site	depth (cm)	pH (H_2O)	pH (KCl)	weight percent total carbon	weight percent total nitrogen	C/N
regolith	0-20	5.9	6.0	1.05	0.08	12.7
regolith	20-38			0.71	0.06	12.0
regolith	38-47	5.7		0.47	0.04	11.1
regolith	47-56			0.41	0.03	11.8
regolith	56-63	6.3		0.47	0.04	10.8
regolith	63-70.5			0.31	0.03	9.7
regolith	70.5-74	6.5	6.3	0.13	0.02	6.4
Site A	0-3 cm			6.73	0.49	13.6
Site A	14 cm			2.31	0.20	11.2
Site A	16-18 cm			2.96	0.26	11.3

1) Measured with a CE Instruments EA 1110 CHNS-O elemental analyzer

Table 3-3: Sequential extractions of regolith core samples[1]

	g/kg soil								
	$Al_{oxalate}$	$Fe_{oxalate}$	$Si_{oxalate}$	Al_{pyro}	Fe_{pyro}	Molar ratio amorphous Al/Si[2]	% Al in amorphous form[3]	% Fe in amorphous form[4]	% Si in amorphous form[5]
0-20 cm	31.6 ± 1.4	24.1 ± 0.9	32.6 ± 1.4	1.8	0.8	0.95	40	32	16
20-38 cm	29.5	22.5	31.4	1.8	0.8	0.92	36	29	15
38-47 cm	30.3	22.9	35.6	-	-	-	-	-	17
47-56 cm	22.9	17.6	33.0	1.1	0.5	0.69	29	23	16
56-63 cm	25.2	19.5	34.3	1.2	0.6	0.73	32	27	17
63-70.5 cm	27.1	21.6	39.2	0.8	0.3	0.70	35	29	19
70.5-74 cm	23.9	19.0	38.2	0.5	0.3	0.64	32	27	19

1) sieved to < 850 µm

2) Ratio amorphous Al: (moles Al_{ox}-moles Al_{pyro})/moles Si_{ox}

3) Amorphous Al: $(Al_{ox}-Al_{pyro})/Al_{ox}$

4) Amorphous Fe: $(Fe_{ox}-Fe_{pyro})/Fe_{ox}$

5) Amorphous Si: Si_{ox}

Table 3-4: Results of wetting/drying experiment[1]

	Percent mass loss (wet/dry)[1]	Percent mass lost (wet/freeze/dry)[1]	percent porosity, ϕ (wet/dry)[2]	percent porosity, ϕ (wet/freeze/dry)[2]
Replicate 1	0.315	0.119	7.8	6.3
Replicate 2	0.202	0.154	14.6	5.7
Replicate 3	0.224	0.238	6.1	7.2
Replicate 4	0.190	0.072	10.1	2.7
Replicate 5	0.055	1.167	3.2	4.5
Replicate 6	-	0.279	-	16.1
Average	0.34 ± 0.41	0.20 ± 0.09	8.3 ± 4.3	7.1 ± 4.7
Median	0.20 ± 0.41	0.20 ± 0.09	7.8 ± 4.3	6.0 ± 4.7

1) Percent mass lost over 200 cycles

2) $\phi=((\text{mass saturated rock-mass dry rock})/\rho_{water})/(\text{dry mass rock}/\rho_{basalt})$

Chemical Weathering and Fe Isotope Fractionation in Regolith Overlying a Diabase: Fe Cycling at the Bedrock/Regolith Interface in Pennsylvania (U.S.A)

Tiffany Yesavage[1*], Gary E. Stinchcomb[1], Peter Sak[2], Matthew S. Fantle[1], Alexander Kasznel[3]

and Susan L. Brantley[1]

[1]Department of Geosciences, the Pennsylvania State University, University Park, Pennsylvania 16802, USA

[2]Department of Earth Sciences, Dickinson College, Carlisle, PA 17013, USA

[3]Department of Chemistry, Dickinson College, Carlisle, PA 17013, USA

**Corresponding author: tay120@psu.edu*

4. Abstract:

Although deep horizons have often been ignored in many studies pertaining to soil weathering, a growing body of evidence indicates that important chemical and biological reactions occur deep within the regolith profile. The goal of this study is to understand changes in mineralogy, chemistry and Fe isotope signatures in a 4-m thick regolith profile in Pennsylvania that is underlain entirely by rocks of basaltic composition (diabase). Here, regolith is defined as hand-augerable material overlying relatively intact rock. We document important chemical and isotopic reactions taking place in the deep regolith at the bedrock-regolith interface. Total sulfur concentrations decrease from 1,000 ppm in the bedrock to 0-150 ppm in the regolith, indicating that the oxidation of sulfides has occurred below the bedrock/regolith interface. While total Fe is largely retained in the lower portion of the profile, Fe(II) is oxidized in the lowermost 30 cm of the profile. Elevated concentrations of amorphous Fe are observed both toward the surface of the profile and at depth near the bedrock-regolith interface. Similar trends in a Puerto Rico quartz diorite soil highlight the process of spheroidal weathering, which may release Fe(II) that is rapidly oxidized in the profile and precipitated as amorphous Fe oxides. Values of δ^{56}Fe from bulk samples show very little variation with depth, whereas δ^{56}Fe values of amorphous Fe (extracted with 0.5 N HCl) are isotopically depleted both in the upper meter and near the bedrock-regolith interface. Although we cannot rule out biological mechanisms, we attribute isotopically light Fe at depth largely to kinetic isotope effects during the rapid abiotic precipitation of Fe(III) to form Fe oxides.

In addition to Fe chemistry, we are also interested in understanding changes that occur in pore-water chemistry in the deeper B and C horizons. The pH values of pore water samples decrease from the B to C horizons, presumably due to higher concentrations of soil atmosphere carbon dioxide at depth. Elevated concentrations of DOC, Fe and Al near the Bt/BC horizon are consistent with preferential flowpaths, likely resulting from the lower hydraulic conductivity of the underlying BC horizon. Pore-water data from the upper two meters are used in conjunction with solid-state chemistry data to derive two different time-integrated dissolution rates for the diabase. A comparison of these rates suggests that the diabase regolith has attained steady state at this site (i.e., constant regolith thickness with time).

4-1. Introduction:

Although the C horizon has often been ignored in many studies pertaining to soil weathering (Richter and Markewitz, 1995), a growing body of evidence indicates that important chemical and biological reactions occur deep within the regolith profile (White et al., 1998; Buss et al., 2005; Jin et al., 2011; Minyard et al., 2012; Bazilevskaya et al., 2013). While researchers have been studying reactions in deep regolith since the 1970s (e.g., Eswaran and Bin, 1978; Gilkes and Suddhiprakan, 1979; Calvert et al., 1980; Rice et al., 1985; Graham et al., 1989; Buol and Weed, 1991), the more recent studies cited here set the stage for quantitative interpretation of mineral weathering near the bedrock-regolith interface. Recent research shows that weathering reactions can remove specific minerals entirely from the deep regolith near the bedrock-regolith interface. In the Rio Icacos watershed of Puerto Rico, intense weathering of a quartz diorite results in the near complete loss of plagioclase, K-feldspar and hornblende at the bedrock-regolith interface (White et al., 1998). In a Pennsylvania watershed underlain by shale, Jin et al. (2011) likewise argued that significant illite weathering initiates within 15 cm of the bedrock-regolith interface of a shallow soil profile (<2 m) but that carbonate dissolution has occurred at depths of ≥20 meters. In addition to mineral losses at Rio Icacos, Buss et al. (2005) observed an increase in the abundance of amorphous Fe along with notable changes in Fe isotope signatures near the bedrock-regolith interface. Bazilevskaya et al. (2013) further reported distinct zones of Fe(II) oxidation and sulfur depletion near this interface in a diabase and a granite soil profile in Virginia. In contrast to crystalline igneous rocks, Brantley et al. (2013) reported the rapid oxidation of Fe(II) and sulfur in shales of a Pennsylvania watershed at depths ranging from 6 to 36 m below the bedrock-regolith interface. One of the goals of the current study is to test the hypothesis that the regolith-bedrock interface is an important location for Fe cycling in basaltic regolith profiles in humid-temperate climates. Of further interest is the question of how Fe chemistry, pore-water chemistry and mineralogy evolve from the deep regolith toward the surface.

The weathering of mafic rocks impacts both the carbon cycle and the composition of natural waters due to the higher solubility and reactivity of mafic minerals (Dessert et al., 2003). The goal of the current study is to investigate a 4-m regolith profile developed entirely upon a diabase (a mafic rock of tholeiitic composition) that is found in Pennsylvania as sills and dikes in

large swarms often extending for kilometers (Smith et al., 1975; Mottana et al., 1977). Previous work at this site indicates that the primary minerals plagioclase and augite are weathering within the soil profile to form smectite and kaolinite as secondary minerals (Hausrath et al., 2011). This weathering profile does not show a smooth upward decrease in elemental concentrations, but rather zones corresponding to intense weathering. Prior analysis of the regolith chemistry revealed two distinct weathering fronts around which extensive chemical weathering occurs. These two zones of extensive weathering occur i) in the lowermost 50 cm of the profile above the bedrock-regolith interface and ii) in a zone extending from 50 to 150 cm below the surface. Weathering in the lowermost portion was discussed in the context of spheroidal weathering (Hausrath et al., 2011).

In addition to amorphous extractions and Fe(II) measurements, we report several methods to understand changes in chemistry and mineralogy throughout the profile in order to understand Fe cycling deep in the regolith profile. The clay-sized fraction was isolated and analyzed with X-ray diffraction (XRD) and transmission electron microscopy (TEM) to characterize secondary phases throughout the profile. Porous suction cup lysimeters, installed at various depths in the regolith, were used to monitor pore-water chemistry in the upper two meters of regolith. To elucidate whether Fe isotope fractionation accompanies Fe cycling with depth, we analyzed the stable isotope values of Fe (δ^{56}Fe values) in both bulk and amorphous (HCl-extracted) samples. Many pedogenic processes may contribute to Fe isotope fractionation. For instance, mineral incubation experiments indicate that organic ligand-promoted dissolution preferentially releases isotopically light Fe into solution relative to the starting material (Brantley et al., 2001; Brantley et al., 2004; Liermann et al., 2011). Bacterially-mediated reductive dissolution may also cause Fe isotopic variations. For example, dissimilatory iron reduction of Fe (oxyhydr)oxides occurs when microorganisms use Fe(III) as an electron acceptor, resulting in the release of isotopically light Fe into solution (Beard et al., 1999). Finally, inorganic reactions such as precipitation and adsorption have also been shown to fractionate Fe isotopically (Skulan et al., 2002; Icopini et al., 2004). Although several studies have analyzed Fe isotope values within soils (e.g., Brantley et al., 2001; Fantle and DePaolo, 2004; Emmanuel et al., 2005; Thompson et al., 2007; Wiederhold et al., 2007a; Wiederhold et al., 2007b; Poitrasson et al., 2008), many of these studies were limited in nature. For instance, in some cases fewer than three samples were analyzed from the soil profile (Brantley et al., 2001; Thompson et al., 2007) or the parent material was poorly

constrained (Wiederhold et al., 2007a, 2007b). In the current study in contrast, samples were collected from a series of different depths from a site underlain entirely by diabase bedrock, and this sample set therefore allows for a greater understanding of the bedrock to saprolite transformation. We investigated weathering at a ridge top, where sediment input is insignificant and where weathering advance can be considered to progress downward.

4-2. Methods:

4-2.1. Study site and sample collection:

The regolith profile was developed on a dike of basaltic composition, which is part of the ca. 200 my Gettysburg diabase sheet (Mesozoic basin) (Sutter, 1988). The soil is mapped as the Neshaminy series, which is described as a deep, well-drained Alfisol formed from diabase and other dark-colored basic rocks (Soil Survey Staff, 2013). Previous work within the Appalachian mountain range indicates an erosion rate of ~5 mm/ky (references within Hausrath et al., 2011).

Samples were collected from a forested ridge-top site to avoid contributions from downslope mass movements at a location along the Appalachian Trail (40°13′14.0″N/77°6′14.2″W) (Fig. 4-1) that is not currently highly disturbed by human impact. A four-inch diameter stainless stell hand auger was used to collect samples as a function of depth (see Hausrath et al. (2011) for details), with the bedrock-regolith interface defined as the depth of auger refusal. Samples analyzed in the current study correspond to Core 1 of Hausrath et al. (2011), which was collected in 2006 and analyzed for bulk chemistry, mineralogy and water content. All samples were thoroughly dried shortly upon collection and stored for several years at room temperature prior to analysis. An additional core (not analyzed here) was sampled in the spring of 2013 for identifying soil horizons delineated in Table 4-1. Few if any outcrops of diabase are observed near the regolith profile site; therefore, samples of largely unweathered rock, inferred to be similar to the parent lithology, were collected from a nearby roadcut along the Pennsylvania Turnpike (40°13′16.0″N/77°6′11.2″W). Previous analysis of the bedrock sampled along the turnpike (Hausrath et al., 2011) indicates the following mineralogy: 66% plagioclase (bytownite) ($Ca_{07}Na_{0.3}Al_{1.7}Si_{2.3}O_8$), 24% augite ($Ca_{0.33}Mg_{2.67}Fe_{0.33}Si_{3.01}Al_{0.99}O_{1.0}((OH)_2)$, 5% magnetite and 1% ilmenite ($FeTiO_3$).

4-2.2. Soil sampling:

Elemental concentrations of soil samples as a function of depth were previously determined (Hausrath et al., 2011). In the current study we used the sodium pyrophosphate method of McKeague (1967) to estimate the organically-associated Al and Fe and the ammonium oxalate method of McKeague and Day (1966) to determine the abundance of amorphous oxides and hydrous oxides. Concentrations of FeO (wt. %) in soils were also determined using a method that involves boiling 1 g of soil in the presence of HF and sulfuric acid and titrating with potassium dichromate (Goldich, 1984). Precision for these analyses was estimated at 20% based multiple measurements on individual samples, and matrix effects were shown to be minimal in organic-poor samples such as those reported here (Yesavage et al., 2011). Total sulfur (S) concentrations were determined with a LECO Sulfur Analyzer (see Brantley et al. (2013) for further details regarding method).

4-2.3. Microscopy and Mineral Identification Methods:

The clay-sized fractions of regolith samples from depths of 30, 70 and 340 cm were obtained by wet sieving (Jackson, 1956). Material was analyzed with TEM analysis on a Philips EM 420 TEM (120 kV). Samples were prepared by sonicating each sample in ethanol and dispersing the solution onto a lacey carbon grid. Images and EDS data were collected from the sample in a Gatan double-tilt analytical holder with the holder inclined 30° in the x-axis.

XRD patterns were collected using a PANalytical Empyrean theta-theta style goniometer with Cu-K-α radiation, with a fixed slit incidence (0.25° divergence, 0.5° anti-scatter, specimen length 10 mm) and diffraction optics (0.25° anti-scatter, 0.02 mm nickel filter). Regolith samples (sieved to <100 μm) were prepared by the back-loading method in which a powder sample is pressed into the cavity of a silicon low-background support. Clay-sized samples were prepared by the dropper method, which involves thoroughly suspending the sample in water and then dropping it on a glass slide (Whittig and Allardice, 1986). Data were collected at 45 kV and 40 mA from 5-70° 2θ using a PIXcel detector in scanning mode with a PSD length of 3.35° 2θ, and 255 active channels for a duration time of ~16 minutes. Resulting patterns were analyzed with Jade +9 software by MDI of Livermore, CA.

4.2.4. Pore-water sampling:

To sample soil pore waters, porous cup tension lysimeters (Soil Moisture Inc., 1900 and 1920 F1 Series) were installed in November 2010 at depths of 15, 60, 95 and 125 cm. Lysimeters were preconditioned by washing with dilute nitric acid (10%) overnight and then rinsing in deionized water before installation. Each hole was augered to the desired depth, and a 2-mm sieve was used to disaggregate soil, which was then added back into the hole in the same order in which it was removed. Another lysimeter was installed at 205 cm in April of 2013. These lysimeters consist of a ceramic cup with 1.3-µm pores through which soil water is drawn with the creation of a vacuum in the lysimeter tube. To avoid disturbances associated with zero-tension lysimeter installation (Currie et al., 1996), sample collection did not commence until Fall 2011, although the deepest lysimeter was sampled within a couple of weeks of installation. One week prior to sampling, the lysimeters were pumped to -0.5 centibars; samples were then collected the following week using PVC tubing and plastic syringes. No samples were collected during the late summer due to dryness, nor during the winter due to sub-freezing temperatures.

In the field, a portable pH meter (Symphony SP70P) was calibrated daily and used to measure pH on all soil pore-water samples. Samples for cation and anion analysis were filtered and added to 15-mL metal-free Falcon tubes. For this study, dissolved cations were defined operationally as the fraction that passed through VWR International 25-mm (0.45-µm pore size) Nylon syringe filters (North American Cat. No. 28145-489). To minimize precipitation, a few drops of Ultrex® Ultrapure HNO_3 from J.T. Baker were added to filtered samples on the day of collection. Cation concentrations were analyzed with inductively-coupled plasma atomic emission spectroscopy (ICP-AES, Perkin-Elmer ICP-AES 5300DV). DOC samples were filtered (<0.45 µm), stored in combusted glass vials and acidified with HCl on the day of analysis. All water samples were stored in a refrigerator between sampling and analysis. DOC samples were measured with a Shimadzu TOC-5000A Analyzer. With this instrument, carbon in the sample is combusted to CO_2, which is detected with a non-dispersive infrared gas analyzer. Filtered anion concentrations were analyzed with a Dionex 2500 ICS under isocratic conditions and an eluent concentration of 39 nM KOH using an Ion Pac AS18 4 x 250 mm column and Ion Pac AG18 4 x 50 mm guard column.

4-2.5. Iron isotope analysis:

All soils were digested in a perchloric acid hood, within a clean box. Prior to Fe isotope analysis, ~100 mg of air-dried bulk soil were digested at 90°C for 24 hours in acid-washed Savillex vials using a 1 mL: 3 mL mixture of HNO_3 (16 N): HF (29 N). One mL of concentrated perchloric acid ($HClO_4$, 11.6 N) was subsequently added to the dissolved sample, which was evaporated at 120°C until ~1 mL of solution remained, at which point the vessels were resealed and digested an additional 24 hours at 150°C. Samples were resuspended in 3:1:1 HNO_3 (16 N): HF (29 N): HCl (12 N), reacted for 2 hours at room temperature, sealed, and heated overnight at 150°C. Finally, samples were evaporated to dryness and redissolved in 0.5 N HNO_3. Even after addition of perchloric acid, samples containing large amounts of organic matter required up to 15 mL H_2O_2 to remove all visible organic matter. Upon removal of organic matter, samples were dried down in HNO_3 (16 N) to ensure oxidation of Fe and resuspended in 2 mL of 7 N HCl prior to ion exchange chemistry. All reagents used were ultrapure grade (e.g., Aristar®ultra HF, OmniTrace Ultra™ high purity $HClO_4$ and Ultrex® Ultrapure HCl, H_2O_2 and HNO_3 from J.T. Baker); Millipore 18.3 MΩ deionized water was used for all dilutions. Process blanks for the digestion procedure had Fe concentrations below the detection limit of ICP-AES of 50 ppb, about three orders of magnitude lower than Fe concentrations in digested samples.

Poorly crystalline Fe oxides were extracted using 0.5 N HCl, a method that has been demonstrated not to fractionate Fe (Wiederhold et al., 2007a; 2007b). First, 0.2 grams of sample were weighed into 15-mL metal-free tubes and 4 mL of 0.5 N HCl added. The tubes were then shaken on an end-over-end shaker for 24 hours at room temperature and centrifuged at 3,400 g for 15 minutes. The resulting supernatant was decanted and filtered through DI-rinsed 0.45-µm VWR Nylon filters. The centrifugate was then washed with distilled water, centrifuged a second time, and the resulting supernatant filtered and combined with the first supernatant. The combined supernatant was then dried down on a hotplate and resuspended in 7 N HCl for Fe isotope analysis.

Iron in all digested and extracted samples was chromatographically purified prior to isotopic analysis using BioRad's AG MP-1 anion exchange resin. Each column (bed volume =

~2 mL) was rinsed (7 mL 0.5 N HCl) and conditioned (9 mL 7 N HCl) prior to sample loading. Approximately 90 µg Fe in 7 N HCl was loaded onto each column, rinsed three times with 9 mL 7 N HCl, and the Fe eluted in 9 mL 0.5 N HCl. All Fe cuts were dried and resuspended in 0.45 N HNO_3. Yields were always >95%, as determined by analysis of aliquots of all sample solutions before and after column chemistry. Fe concentrations in post-column blanks fell below the detection limit of ICP-AES of 50 ppb, which is two orders of magnitude lower than post-column sample concentrations.

The iron isotopic composition was measured by multiple collector-inductively coupled plasma-mass spectrometry (MC-ICP-MS) using a Thermo Scientific Neptune Plus at Penn State University's Metal Isotopes Laboratory (MIL). Samples were introduced using an ESI SSI quartz dual cyclonic spray chamber (i.e., under wet plasma conditions), a 100 µl/min nebulizer flow rate (ESI PFA-100 microflow nebulizer), 1200 W power, and a high mass resolution mode at Fe concentrations of 3 ppm. Delta values were determined by standard-sample-standard bracketing and reported relative to IRMM-014, which is the bracketing standard. Two laboratory standards were run in each analytical session: NIST SRM-3126a ($\delta^{56}Fe_{IRMM014}$=0.35 ± 0.03‰ 1SD, *n*=14; *accepted value*: 0.35‰, personal comm., T. Bullen, 11-06-2012), and HPS-UW ($\delta^{56}Fe_{IRMM014}$=0.58 ± 0.03‰ 1SD, *n*=10, *accepted value*: 0.58‰, personal comm., C. Johnson, 11-2012). Single-element Fe standards from High-Purity Standards™ were run before and after ion exchange separation to verify that column chemistry did not result in fractionation; analysis of a ~3 ppm Fe standard run before and after column chemistry yielded δ^{56}Fe values within 0.05‰, thus demonstrating minimal fractionation with column chemistry.

4-2.6. Calculations.

Plots of the mass transfer coefficient ($\tau_{i,j}$) in bulk soil samples were made to investigate extent of chemical weathering. The $\tau_{i,j}$ parameter is defined as (Brimhall and Dietrich, 1987; Anderson et al., 2002):

$$\tau_{i,j} = \frac{C_{j,w} C_{i,p}}{C_{j,p} C_{i,w}} - 1 \qquad (4\text{-}1)$$

Here, *C* refers to the concentrations of the immobile (*i*) and mobile (*j*) elements in the weathered (*w*) or parent (*p*) material. Diabase bedrock collected from the Pennsylvania Turnpike was used as the parent material. Due to its general insolubility and immobility throughout the regolith, Zr was chosen as the immobile element at this site (Hausrath et al., 2011). The goal behind normalizing to an immobile element is to account for concentration changes resulting from depletion and addition of other elements. Values of $\tau_{Zr,j,} > 0$ indicate that the element of interest (j) is enriched in soil relative to parent material, while $\tau_{Zr,j} < 0$ indicates depletion or loss from the profile.

4-3. Results:

4-3.1. Soil description:

As reported by Hausrath et al. (2011), the depth of refusal based on hand augering was 401 cm; in 2013, we hand augered a second profile at the same site to 385 cm for the purposes of identifying soil horizons. The following horizons were identified from the land surface downward (Table 4-1): A (0-22 cm), Bt (22-60 cm), BC (60-90 cm), Cr1 (90-160 cm), Cr2 (160-230 cm), Cr3 (230-340 cm), Cr4 (340-365 cm), Cr5 (365-395 cm), R (>395 cm). Notable horizon features include a strong brown (7.5YR 5/6) silty clay loam Bt horizon, which begins at 20 cm below surface and has a medium subangular blocky structure (Table 4-1). At a depth of ~60 cm, a transition is noted toward the yellowish brown (10YR 5/8) sandy loam of the BC horizon with a weak, medium subangular blocky structure. Also at the Bt/BC interface, distinct black manganese coatings (N 2.5/) are observed along ped faces and tubular pores. The Cr horizon is located between 0.9 to 4 meters and varies from olive yellow (2.5Y 6/6) sandy loam to strong brown (7.5YR 5/6) silt loam with an overall massive structure.

4-3.2. Trends in Fe and S chemistry with depth:

Previous work by Hausrath et al. (2011) indicates that bulk Fe depletion profiles for Fe exist both in the lower 50 cm of the 4-m profile as well as in the upper 50-150 cm. In the current study, we observed that the percent of Fe present as Fe(II) decreases markedly from the value measured in parent material (86%) to the values in deep regolith just above augering refusal: 56% at 401 cm and 13% at 379 cm (Table 4-2; Figure 4-2A). Although both total Fe and Fe(II) show strong depletion profiles with losses of >80%, the overall depletion pattern differs. While

Fe(II) is largely depleted toward the bottom of the profile, the majority of the total Fe depletion occurs in the upper meter (Figure 4-2A).

Amorphous Fe concentrations are high toward the top and bottom of the profile and lower in the middle (Figure 4-2B; Table 4-3). Concentrations of amorphous Fe and Al are 3 to 10 times higher than the organically-extracted fraction and make up between 1-10% of the total bulk analysis of Al and Fe (Table 4-3). Sulfur concentrations throughout the regolith were about an order of magnitude lower than those of the bedrock (Table 4-2; Figure 4-2A).

4-3.3. Fe isotope chemistry, XRD and microscopy:

Bulk δ^{56}Fe values within the regolith average ~-0.02‰, with minimal variation throughout the profile (Table 4-4; Figure 4-3A); bulk Fe values throughout the regolith profile are similar to the measured composition for the diabase parent rock of -0.01‰. In contrast, HCl-extracted δ^{56}Fe values show a U-shaped relationship with depth of isotopically depleted values (approaching ~-0.3‰) both in the lowermost sample and toward the surface, with values of ~0‰ in the middle (Figure 4-3B).

XRD diffractograms of clay-sized material isolated as part of the current study indicate the presence of a 14 Å phyllosilicate mineral (smectite/vermiculite/chlorite), 7 Å halloysite/kaolinite and quartz. The 14 Å phyllosilicate mineral was also present throughout the profile, whereas quartz was most abundant toward the surface of the profile (Figure 4-4). TEM images of the clay-sized fraction of diabase samples from three depths (30, 70 and 340 cm) show a variety of different morphologies (Figure 4-5A), including tube-like structures ~100 nm in diameter and up to 1 μm in length (Figure 4-5B). TEM diffraction patterns indicated that some of these tubes are amorphous while others are polycrystalline (Figures 4-5B and 4-5C). Rose-shaped morphologies that were amorphous based on diffraction patterns were also noted. TEM/EDS analysis indicated that both the tubes and the rose-like structures were made up predominantly of Si and Al, with smaller amounts of Fe (Figure E-1), a composition consistent with both halloysite and newly-formed kaolinite (Papoulis et al., 2004).

4-3.4. Lysimeter chemistry:

Pore water collected from the 60-cm depth often had a yellow color in contrast to the clear color observed at all other depths. The pH of the pore water decreased from ~6.3 at the surface of the profile to ~5.6 at depth (Figure 4-6A; Table 4-5). This decrease in pH was accompanied by a corresponding increase in the percent of soil gas carbon dioxide (Figure 4-6B). The concentration of dissolved silica increases gradually from ~10 mg/L at the surface to ~30 mg/L at 205 cm (Figure 4-6C). In contrast, elements such as Mg, Na, K and Ca show greater variability and therefore less apparent trends with depth (Table 4-5; Table E-1). DOC concentrations range from 0 to 200 mg/L, and tend to decrease with depth toward the surface, although a great deal of variation is observed (Figure 4-6D). Nitrate concentrations range from 0-20 mg/L, with average values decreasing with depth (Figure 4-6E; Table 4-5). Although a great deal of variation occurs, concentrations of dissolved Al and Fe are highest at a depth of 60 cm (Figures 4-6F and 4-6G). Chloride concentrations remain roughly constant with depth (Figure 4-6H). No significant differences are observed in the concentrations of DOC as a function of season nor are DOC concentrations related to the amount of precipitation in the days and weeks prior to sample collection (Table E-2). Concentrations of DOC and nitrate are nonetheless more elevated in some years than others (i.e., higher concentrations in fall of 2011 and spring of 2012) (Figure E-2). DOC concentrations are well correlated with concentrations of Fe and K in particular, and moderately correlated with Al and Na ($p<0.001$ in all cases).

4-4. Discussion:

4-4.1. Soil chemistry and Fe isotopes:

Based upon XRD analysis of the bulk bedrock sample (Hausrath et al., 2011), most of the Fe(II) in the diabase parent material is in pyroxene (augite) and to a lesser extent, in magnetite and ilmenite. Fe(II) titrations indicate that ~80% of the bedrock Fe is made up of Fe(II), which decreases to ~40% at a depth of 3 meters in the profile (Figure 4-2B); consequently, we infer that significant Fe(II) oxidation is occurring at the bottom of the profile as Fe(II) in augite is oxidized and precipitated as secondary Fe oxide phases (Hausrath et al., 2011). The percent of Fe present as Fe(II) remains constant at ~20-40% in the upper 3 m of the profile, which is likely due to the persistence of magnetite and/or ilmenite. Similar to the above observations, Bazilevskaya (2013)

likewise noted a zone of Fe(II) oxidation in the lowermost 20 cm of a 100-cm thick regolith profile in Virginia soils developed on diabase. The collective findings of Bazilevskaya et al. (2013) and the current study suggest that the bedrock-regolith interface is an important location for Fe(II) oxidation in temperate diabase weathering.

In contrast to the two diabase profiles discussed above, the Fe(II) oxidation front was noted many meters below the bedrock-regolith interface in a Pennsylvania shale (Brantley et al., 2013). In the shale profiles, pyrite and ankerite were oxidatively dissolved and lost from the shale at a depth of 23 m beneath the ridge, while further oxidation of Fe(II) in chlorite, illite and feldspar was noted at a depth of 5-6 m below the bedrock/regolith interface (Brantley et al., 2013). These differences suggest that lithology plays a major role in determining the location of Fe(II) oxidation fronts, with Fe(II) oxidation in shale occurring in a more gradual manner that is not associated with the bedrock/soil interface. In the case of shale, partings and cleavage planes may alter the extent to which oxygen may diffuse at depth. In contrast, Fe(II) oxidation fronts appear to be more closely associated with the bedrock-regolith interface in crystalline rocks, perhaps consistent with saprolite or soil formation driven by the oxidation process. The depth of the oxidation front in all these rocks is also presumably related to the depth of the water table: While the water table lies at tens of meters below the shale ridgetop, the water table may be much higher at the Pennsylvania diabase site. This higher water table may result from the lower porosity and permeability of the diabase and the lower abundance of microfractures (Bazilevskaya et al., 2013).

In the Pennsylvania diabase, spheroidal weathering is thought to be of particular importance (Hausrath et al., 2011). Fletcher et al. (2006) have argued that spheroidal weathering can occur when the diffusion of oxygen into bedrock along fractures initiates oxidation of Fe(II) minerals. A volumetric increase accompanying oxidation then results in an elastic strain energy in the rock that creates a concentric set of rock layers (subtended by fractures) referred to as rindlets that slowly transform to saprolite (Fletcher et al., 2006). Spheroidal weathering in the diabase regolith could therefore be related to the rapid oxidation of Fe(II) near the bedrock-regolith interface.

The amorphous Fe (as measured with acid ammonium oxalate extractions) displays a U-shaped trend, with higher concentrations both at depth and toward the surface (Figure 4-2C; Table 4-3). Similar trends were noted in the Puerto Rico granodiorite profile analyzed by Buss et

al. (2005). Although elevated amorphous Fe concentrations near the surface of the profile may result from vegetation cycling and litter decomposition (Buss et al., 2010), higher concentrations at depth are likely the result of rapid Fe oxidation in the rindlet zone during spheroidal weathering (Fletcher et al., 2006). Whether this Fe oxidation is facilitated by microorganisms in the diabase cannot yet be tested; however, Minyard et al. (2012) documented circumneutral Fe-oxidizing bacterial species in the lower portion of the Puerto Rico soil profile using 16S rRNA clone libraries, pointing toward a possible contribution from microorganisms. On the other hand, the abiotic oxidation of Fe(II) also proceeds rapidly under neutral pH conditions (Emerson et al., 2010). Future work at the diabase profile will be necessary to gain a fuller understanding of the extent to which Fe-oxidizing bacteria may enhance spheroidal weathering at this site.

Sulfur, which is presumably present solely in the form of an iron sulfide mineral in the parent material, is also highly depleted in the profile relative to the bedrock; concentrations throughout the regolith are an order of magnitude lower than in the parent material (Figure 2A). These findings indicate that sulfide oxidation is occurring at a depth greater than the depth of refusal. As we have no drill core from the diabase ridgetop, we do not know exactly where the sulfur depletion front occurs at this site. In a study of a diabase drill core in Virginia, Bazilevskaya et al. (2013) observed rapid sulfide oxidation within 0.5 meters of the bedrock-saprolite interface; given the similarities between the two sites, the sulfur depletion front may likewise be located within a meter of the bedrock-regolith interface at this Pennsylvania site as well. Consistent with observations from the VA diabase, it is also likely that the bedrock-regolith interface corresponds to the depth of the water table at the Pennsylvania site as well.

4-4.2. Fe Isotope Analysis:

Fe has four naturally occurring isotopes: ^{54}Fe (5.85%), ^{56}Fe (91.75%), ^{57}Fe (2.12%) and ^{58}Fe (0.28%) (Dauphas and Rouxel, 2006). Variations among these isotopes are reported as δ^{56}Fe values (‰):

$$\delta^{56}Fe = \left(\frac{\left(\frac{^{56}Fe}{^{54}Fe} \right)_{sample}}{\left(\frac{^{56}Fe}{^{54}Fe} \right)_{std}} - 1 \right) * 10^{3} \qquad (4\text{-}2)$$

The international Fe reference material IRMM-014 is used as a standard, which is ~0.09‰ lighter than the average of igneous rocks (Beard and Johnson, 2004). The precision of δ^{56}Fe values is generally reported at ±0.05 to ±0.15‰ (Beard and Johnson, 2004). While the extent of Fe isotopic variation is limited in bulk igneous rocks (which cluster around 0‰), soils often show a greater degree of fractionation. For instance, the range of δ^{56}Fe values measured for bulk Fe in different soil samples is ~1.5‰ (Wiederhold et al., 2007a).

Bulk δ^{56}Fe values show very little variation throughout the diabase soil profile (Figure 3a; Table 4). In contrast, variations of up to 1‰ have been noted in soils from Hawaii and Germany (Thompson et al., 2007; Wiederhold et al., 2007a; Wiederhold et al., 2007b). Thompson et al. (2007) and Wiederhold et al. (2007) attributed isotopically enriched zones in Hawaiian basaltic soils and in a saturated German Inceptisol as resulting from bacterially-mediated Fe(III) reduction, which releases isotopically light Fe to solution under anoxic conditions (Beard et al., 1999). In the case of a German Spodosol, Wiederhold et al. (2007) explained an isotopically heavy E horizon as resulting from organic complexation associated with podsolization, a pedogenic process that results when Fe and Al are mobilized from the E horizon and redeposited in a zone of illuviation where clays accumulate (Lundstrom et al, 2000). More specifically, organic ligands, which have been shown to preferentially complex isotopically light Fe (Brantley et al., 2001), could explain the isotopically heavy residual in the E horizon.

The lack of Fe fractionation in the diabase profile is consistent with a lack of detectable effects from dissimilatory processes in the oxic, well-drained diabase profile, as well as the minimal extent of podsolization. In their analysis of Cameroon laterites, Poitrasson et al. (2008) likewise observed minimal fractionation of bulk Fe, with δ^{56}Fe variations of <0.2‰ over a 36-m drill core including parent granodiorite, saprolite and Fe-rich horizons. The authors attributed this lack of fractionation to minimal active redox cycling (all Fe was present as Fe(III)) and the low concentrations of organic carbon present in the profile. Wiederhold et al. (2007) also observed minimal fractionation of Fe in a well-drained German Inceptisol. In the case of the diabase, oxygen concentrations remain above 14% by volume in the late summer even near the bedrock-regolith interface (Stinchcomb et al., in prep.), perhaps limiting the extent of Fe redox cycling in the regolith.

In contrast to bulk Fe, amorphous (HCl-extracted) Fe varies in isotopic composition, showing a U-shaped relationship similar to the pattern associated with amorphous Fe. Similar trends for amorphous δ^{56}Fe values were also observed in the Puerto Rico granodiorite by Buss et al. (2010). As was suggested by Buss et al. (2010), the isotopic depletion of Fe in the upper portion of the profile could be explained by i) the decomposition of vegetation containing isotopically light Fe, ii) organic-promoted dissolution of Fe-bearing phases, or iii) plant-mediated reductive dissolution of Fe(III) oxides.

Isotopically light Fe near the bottom of the profile is more difficult to explain. Given the similarities between the isotopic profiles in Puerto Rico and Pennsylvania, it is possible that Fe-oxidizing bacteria may be active near the bedrock-regolith interface in the diabase, just as they are in the Puerto Rico quartz diorite. However, we have not yet performed any microbiological analyses at this site. Nonetheless, such bacteria are unlikely to explain the pattern of isotopically light amorphous Fe isotope fractionation because circumnuetral Fe-oxidizing bacteria in batch studies have been observed to precipitate Fe oxides that are up to 3‰ *heavier* than the starting Fe(II) in solution (Kappler et al., 2010). As an alternative to bacterial recations, Buss et al. (2010) attributed isotopic depletion of amorphous Fe in the Puerto Rico profile as resulting from the organic-promoted dissolution of hornblende in the quartz diorite, a process that preferentially releases isotopically light Fe into solution (Brantley et al., 2001; Brantley et al., 2004). However, hornblende is not present as a primary mineral in the parent diabase studied here, and the bedrock at this site contains minimal Fe(III) (Figure 4-2B).

Rapid abiotic precipitation of Fe oxides has also been shown to produce isotopically light products. For instance, in batch experiments in which hematite was rapidly precipitated from aqueous Fe(III), Skulan et al. (2002) demonstrated that kinetic processes lead to fractionation in which $10^3\ln\alpha_{Fe(III)\text{-hematite}} = -1.32 \pm 0.12‰$ (where $10^3\ln\alpha_{Fe(III)\text{-hematite}}$ is approximately equal to $\Delta_{Fe(III)\text{-hematite}}$). The key feature here is the rate of precipitation: only minimal Fe isotopic fractionation between $Fe(III)_{aq}$ and hematite ($10^3\ln_{Fe(III)\text{-hematite}} = 0.1 \pm 0.20‰$) was observed under conditions of slow precipitation during which equilibrium fractionation was inferred (Skulan et al., 2002). A second possible mechanism may involve the preferential transport of isotopically light Fe along a preferential flow zone near the bedrock-regolith interface. This isotopically light

Fe, which may exist in an organically complexed form (Brantley et al., 2001, Wiederhold et al., 2007b), might then be occasionally oxidized and precipitated at the bottom of the profile.

The fact that analogous trends are noted both in the Puerto Rico quartz diorite investigated by Buss et al. (2010) and in the Pennsylvania diabase may indicate that the processes responsible for Fe isotope fractionation are similar despite differences in climate and vegetation. Specifically, a mechanism consistent with all observations here and in the literature is release of Fe(II) to solution at the bedrock-regolith interface (perhaps mediated by bacteria) followed by rapid precipitation of isotopically light amorphous Fe oxide. In contrast, ridge-top soils from a shallow (25 cm) shale-derived Pennsyvania watershed indicate no significant depletion of Fe isotope values near the bedrock-regolith interface (Yesavage et al., 2012); these differences highlight the importance of lithology and/or the process of spheroidal weathering in controlling Fe isotope signatures in regolith profiles.

4.-4.3. Identification of clay-sized fraction:

Based upon XRD analysis of bulk samples by Hausrath et al. (2011), kaolinite and smectite both occur throughout the diabase profile. XRD diffractograms of clay-sized material from the regolith core more specifically indicate the following secondary weathering products: 1) a 14 Å phyllosilicate clay, 2) 7 Å kaolinite/halloysite and 3) quartz. The intensity of the 14 Å peak in the clay-sized fraction does not change notably from 340 cm to 8 cm (Figure 4-5), indicating that this phyllosilicate phase forms at the bedrock-regolith interface and is present throughout the profile. Greater intensities of quartz toward the surface of the profile likely document eolian deposition at this site. In their study of a North Carolina diabase, Oh and Richter (2005) suggested that elevated Zr concentrations toward the surface of the profile may also be the result of eolian deposition. A similar elevation in Zr is noted in the upper 50 cm of the diabase profile as well (Hausrath et al., 2011). However, we argue that elevated Zr toward the surface at this site is mostly the result of weathering rather than eolian deposition. While the XRD quartz peak rapidly attenuates from 8 to 30 cm (Figure 4-4), Zr concentrations in the upper 50 cm increase by only 20% toward the surface (Hausrath et al., 2008).

XRD peaks corresponding to halloysite/kaolinite indicate a 7 Å d-spacing that does not shift notably throughout the profile (Figure 4-4). Halloysite, identified throughout the profile

with TEM, has a 1:1 Al:Si ratio and exhibits a wide variety of different morphologies, including tubular and spherical forms (Tazaki, 2005). Electron microscope images from other sites indicate that halloysite may form directly from plagioclase (Jeong et al., 2000; Papoulis et al., 2004). Other work has indicated an intimate association between halloysite and microorganisms (Tazaki, 2005; Minyard et al., 2011). The latter study is perhaps of particular interest here because Minyard et al. (2001) documented formation of halloysite in the zone where Fe oxidation occurred at the base of saprolite on the quartz granodiorite discussed previously. Further microbiological work is needed to characterize those organisms living near the bedrock-regolith interface in the diabase profile.

Thermodynamic considerations predict that halloysite will convert into kaolinite with aging according to the following sequence observed in soils via electron microscopy: spherical halloysite → tubular halloysite → interconnected tubular halloysite → platy halloysite → newly formed kaolinite (Papoulis et al., 2004). In an investigation of regolith from the Piedmont of Virginia, Pavich et al. (1989) noted that halloysite, which was often present toward the bottom of the soil profile, tended to recrystallize to kaolinite toward the surface. This finding was true for regolith overlying metapelite, metagraywacke and granite. In contrast, we found morphological evidence of halloysite throughout the entire profile at the diabase site, with no obvious transition to kaolinite toward the surface. Lack of transformation of halloysite in Pennsylvania could be explained, for example, if the rate of erosion in Pennsylvania is faster, causing the residence time of diabase in the weathering zone to be lower than in Virginia. Alternately, the lack of transformation could relate to the lower temperature (10-12°C versus 12-14°C) and precipitation (104 cm/y versus 114 cm/y) in PA compared to VA based on Prism estimates (Daly, 1994).

The lack of Si in the acid oxalate extractions is consistent with a lack of allophane, a common amorphous phase with a 1:1 molar ratio of Al:Si. The lack of allophane may be due to lack of volcanic glass (Dahlgren et al., 1993), a common precursor of allophane (Hausrath et al., 2011).

4-4.4. Pore-water chemistry:

Of all measurements, pore-water silica concentrations showed the most significant changes with depth (Figure 6C). Only a very weak correlation was observed between dissolved

silica concentrations and DOC in the profile (R^2=0.07, p<0.05). In contrast, a very modest inverse correlation was noted between dissolved silica and pH (R^2=0.27, p<0.001), with higher silica concentrations at greater depth where the average pH was lower.

The soil pore-water pH as measured in the field roughly decreases from ~6.3 toward the surface to ~5.6 at 205 cm (Table 4-4; Figure 4-6A), a finding that is somewhat at odds with higher levels of organic matter and with the presence of low-pH rainwater expected toward the surface. Silicate weathering in the deep regolith is also expected to increase the pH. In contrast to these expectations, the pH at a depth of two meters is significantly *lower* than toward the surface (Figure 6A). These decreases in pH with depth may be explained by corresponding increases in the concentrations of soil gas carbon dioxide with depth (Stinchcomb et al., in prep; Figure 6B).

Apparently, decreases in soil pH with depth are not unusual. Using the National Resource Conservation Service online characterization website, we examined soil pH versus depth for seven soils classified as Neshaminy series (National Cooperative Soil Survey, 2013). In five of the seven profiles, pH decreases at ~100 cm below the surface. As with our study site, the pH decrease was often associated with a transition from the B to C horizon. In these soils, the BC horizon may be acting as a restrictive barrier that limits upward diffusive loss of carbon dioxide (Richter and Markewitz, 1995; Schulz et al., 2011). For example, in a study of three soil profiles underlain by three lithologies (gneiss, metavolcanic rock and gabbro), a dramatic decrease in hydraulic conductivity was noted at the BC horizon (Buol and Week, 1991).

Although there is a great deal of variation, average DOC and nitrate concentrations decrease with depth in the profile (Figures 4-6D and 4-6E; Table 4-5). Elevated nitrate concentrations at this site (of up to 30 mg/L) may be the result in part of anthropogenic nitrogen, which is high in the northeastern United States (Hedin et al., 1995). A decrease in DOC levels with depth has been observed in a wide variety of different studies and is likely the result of precipitation, adsorption and decomposition of organic matter during downward migration (Dijkstra and Fitzhugh, 2003). Maximum DOC concentrations are also higher at this site (reaching values of 190 mg/L) than has typically been observed (1-50 mg/L) in many soil pore waters (Andrews et al., 2011 and references within), a finding that is particularly apparent in the fall of 2011 and the spring of 2012 (Figure E-2). At the moment, is it unclear as to why we observed higher DOC concentrations in the fall of 2011 and the spring of 2012 but not in the fall of 2012 and the spring of 2013. One possibility involves disturbance effects from lysimeter

installation. However, average annual precipitation may have also been somewhat higher during the first year of sampling (Figure E-3).

Although DOC export often increases during the fall in temperate climate soils as a result of increased litter production and decomposition during this time of the year (Dijkstra and Fitzhugh, 2003; Kalbitz et al., 2000), DOC concentrations were not elevated during fall months of 2012 (Figure E-2). This observation is consistent with observations of pore waters from a shale-derived watershed of central Pennsylvania (Andrews et al., 2011) that show no consistent relationship between DOC and season. Furthermore, while previous research has indicated increases in DOC release with large rainfall events (Kalbitz et al., 2000), no correlation was observed between DOC concentrations and precipitation either on the day of collection or on the seven days prior to collection (Table E-2).

Elevated dissolved Al and Fe concentrations at this site of up to 1.2 mg/L were observed during different seasons at the 60-cm depth (Table E-1). Lysimeter pore-water samples collected from the 60-cm depth also had a distinct yellow hue unlike that from any other sample depth. In contrast, the dissolved Al and Fe concentrations at depths below 60 cm were always ≤0.1 mg/L, while concentrations at the 16-cm depth never exceeded 0.26 mg/L (Table E-1; Figures 4-6F and 4-6G). Although metal concentrations generally tend to decrease with depth in pore waters (Tolpeshta and Sokolova, 2009), elevated concentrations at 60 cm may be the result of preferential flow along the Bt/BC horizon interface. More specifically, low hydraulic conductivities have been documented in the BC horizon of several other soil profiles (Buol and Weed, 1991). These low hydraulic conductivites have been attributed to a lack of continuous pores at this depth due to fewer root channels and worm holes, as well as thick cutans of clay translocated from the overlying soil (Buol and Weed, 1991). Prominent black Mn coatings along ped faces in the BC horizon (Table 4-1) further support the notion that this interval experiences frequent water movement (Ross et al., 1976), a phenomenon that would be associated with preferential flow. In the Shale Hills watershed of Pennsylvania, Andrews et al. (2011) likewise observed elevated DOC and metals concentrations near certain horizon boundaries.

Within pore water samples, DOC was more highly correlated with Fe and K (R^2=0.60, $p<0.001$ and R^2=0.66, $p<0.001$, respectively) than with Al and Na (R^2=0.35, $p<0.001$ and R^2=0.24, $p<0.001$, respectively). In contrast to Al, Fe, K and Na, no significant correlation was

found between DOC and Mg (p=0.46). Although the mobilization of Al by DOC has been well documented within pore waters (Dijkstra and Fitzhugh, 2003; Tolpeshta and Sokolova, 2009), the correlation between DOC and Al is weaker at this site than for Fe and K. Nonetheless, these results suggest the important role of organic ligand complexation in the mobilization of dissolved Al and Fe in the diabase profile.

4-4.5. Calculating diabase dissolution rates from solute chemistry:

To understand the weathering system, we compare solid- and solute-based weathering rates in the upper 2 m of the diabase profile from which pore waters were sampled. In theory, steady state conditions in which the bedrock has attained a constant thickness over time would result in similar values for both of these rates (White et al., 2002). The following equation was used to calculate the diabase weathering rate based upon pore-water gradients in the upper two meters of regolith (White et al., 2002):

$$R_{solute} = 1000 \frac{1}{S_{BET} \beta} \frac{q_h}{b_p} \tag{4-3}$$

Here R_{solute} (mol m^{-2} s^{-1}) is the surface-area normalized weathering rate, S_{BET} (m^2 m^{-3}) is the specific surface area, β (mol mol^{-1}) is the stoichiometric coefficient for the element in a mineral or rock, q_h is the flux density of water through the profile (m s^{-1}), and b_p (m L mol^{-1}) is the solute weathering gradient. For the bulk rock, the stoichiometric coefficient was assumed to be one Si atom per diabase formula unit (β=1). The approximate formula unit of the diabase is $Ca_{0.23}Na_{0.08}Mg_{0.36}Fe_{0.11}Si_{1.00}Al_{0.57}O_{3.51}(OH)_{0.27}$ (Hausrath et al., 2011). Based upon Si solute chemistry with depth, the average solute weathering gradient b_p ($\Delta z/\Delta c$) is equal to ~1,600 m L mol^{-1} (Figure E-4). The maximum flux density was set equal to the difference between average annual precipitation and average annual evapotranspiration (Brantley and White, 2009). Estimated mean annual precipitation ranges from 100-125 cm/yr in subcentral Pennsylvania, while evapotranspiration averages ~60 cm/year (Sanford and Selnick, 2013); these values would suggest a value of ~50 cm/year (40-65 cm/year) or ~1.6 x 10^{-8} m/s for the flux density. Based upon microscopic measurements of grain diameters and surface roughness, Hausrath et al. (2011) estimated plagioclase (~66% abundance) and pyroxene (~34% abundance) surface areas in the

parent rock equal to 24,100 m^2/m^3 and 10,200 m^2/m^3 respectively. Based on an assumption of 66% plagioclase and 34% pyroxene, we calculate a bulk rock surface area (S_{BET}) of ~19,000 m^2/m^3.

The solute-based weathering rate of diabase based on Si can then be compared with the solid-state rate in the upper two meters for which pore-water measurements were available based on the following equation (White et al., 2002):

$$R_{solid} = 1000 \frac{\rho_w}{S_{BET} \beta} \frac{\omega}{b_s} \quad (4\text{-}4)$$

Here, R_{solid} (mol m^{-2} s^{-1}) is the surface-area normalized weathering rate based on solid regolith chemistry. A weathering advance rate (ω) of 5 mm/ky or 1.6 *10^{-13} m/s was assumed for the Appalachian mountain range based on a compilation of erosion rate studies (references within Hausrath et al., 2011), while the average bulk density (ρ_w) of the profile was assumed to be 1 g/cm^3 (Hausrath et al., 2011). We used the same S_{BET} value as assumed for the solute-based calculation above (19,000 m^2/m^3), and the Zr-normalized Si weathering gradient was calculated to equal 0.4 m kg/mol^{-1} in the upper two meters (Table E-2).

Using the above values, the time-integrated dissolution rate of diabase based on pore-water chemistry (log rate = -12.3 (mol diabase m^{-2} s^{-1})) is about an order of magnitude faster than the rate calculated from solid chemistry in the upper two meters (log rate = -13.7 (mol diabase $m^{-2}s^{-1}$)). One possibility for the discrepancy between the solid- and solute-based calculations may involve an overestimation of the flux density due to a failure to account for loss from lateral flow (Brantley and White, 2009) or an underestimation of the weathering advance rate used above. It is also possible that the higher solute-based rate is consistent with a weathering profile that has not attained steady state since the Last Glacial Maximum. For example, the time-integrated values of dissolution calculated here from solute fluxes could be high because they are still perturbed by the recent period of periglacial conditions during glacial retreat. However, in agreement with previous work in the central Appalachian Mountains (Potter et al., 2009; White et al., 2009), it is more likely that the relatively similar values are evidence that the diabase profile is at steady state.

4-6. Conclusions:

The goal of this study was to understand weathering reactions and Fe cycling in deep regolith, with a particular focus upon understanding processes important at the bedrock-regolith interface overlying rock of basaltic composition. Transmission electron microscopy (TEM) and EDS data for the clay-sized fraction of the regolith developed on diabase on a Pennsylvania ridge indicate a 14 Å phyllosilicate phase and halloysite/kaolinite as the main secondary weathering products throughout the profile. Trends of Fe(II) concentrations, amorphous Fe and HCl-extracted δ^{56}Fe in the Pennsylvania diabase are similar to those previously observed in other sites underlain by crystalline rocks in Pennsylvania and Puerto Rico. More specifically, Fe(II) is rapidly oxidized in the lowermost 20 cm of the profile near the bedrock-regolith interface, as was observed for a Virginia diabase by Bazilevskaya et al. (2013).

Dissolved Fe(II) near the bedrock-regolith interface is likely precipitated initially as amorphous Fe oxides in the bottom of the profile during spheroidal weathering, which may then re-crystallize toward the middle section of the profile. Complexation of Fe by vegetation may likewise increase the concentration of amorphous Fe toward the surface, thus resulting in similar trends for amorphous Fe at both the Pennsylvania diabase as well as at a Puerto Rico site. Near the bedrock-regolith interface, the amorphous δ^{56}Fe values show trends that we attribute to rapid precipitation of Fe oxides from aqueous Fe(III) under kinetically-controlled conditions at the bedrock-regolith interface. Similar Fe isotope profiles in diabase and quartz diorite (Pennsylvania and Puerto Rico) document a trend that may be common in profiles underlain by crystalline rocks undergoing speroidal weathering.

In addition to Fe chemistry, we are also interested in understanding changes that occur in pore-water chemistry in the deeper B and C horizons. Average nitrate and dissolved organic concentrations (DOC) in regolith pore fluids decrease with depth in the profile. The pH values of pore water samples decrease from the B to C horizons, presumably due to higher concentrations of soil atmosphere carbon dioxide at depth. Pore-water cation concentrations (especially Fe and Al) correlate with DOC throughout the year, as expected given that these metals are generally held in solution by complexation in soils. Elevated concentrations of DOC, Fe and Al near the Bt/BC horizon are consistent with preferential flowpaths, likely resulting from the lower hydraulic conductivity of the underlying BC horizon. Pore-water data from the upper two meters

are used in conjunction with solid-state chemistry data to derive two different time-integrated dissolution rates for the diabase. A comparison of these rates suggests that the diabase regolith has attained steady state at this site (i.e., constant regolith thickness with time).

Acknowledgements: We thank Beth Jones for assistance with XRD and Trevor Clark for help with the TEM. Funding was provided by the Penn State Astrobiology Research Center grant NNA04CC06A. We also acknowledge permission from the National Park Service to sample along the Appalachian Trail Easement.

References:

Anderson, S.P., Dietrich, W.E., and Brimhall, G.H., 2002, Weathering profiles, mass-balance analysis, and rates of solute loss: Linkages between weathering and erosion in a small, steep catchment. Geological Society of America Bulletin. 114: 1143-1158.

Andrews, D.M., Lin, H., Zhu, Q., Jin, L., and Brantley, S.L., 2011, Hot spots and hot moments of dissolved organic carbon export and soil organic carbon storage in the Shale Hills Catchment. Vadose Zone J. 10: 943-954.

Anbar, A.D., Roe, J.E., Barling, J., and Nealson, K.H., 2000, Nonbiological fractionation of iron isotopes. Science. 288: 126-128.

Bazilevskaya, E., Lebedeva, M., Pavich, M., Rother, G., Parkinson, D.Y., Cole, D., Brantley, S.L., 2013, Where fast weathering creates thin regolith and slow weathering creates thick regolith. Earth Surface Processes and Landforms. 38: 847-858.

Beard, B.L., Johnson, C.M., Cox, L., Sun, H., Nealson, K.H., and Aguilar, C., 1999, Iron isotope biosignatures. Science. 285: 1889-1892.

Beard, B., and Johnson, C., 2004. Chapter 10A: Fe isotope variations in the modern and ancient Earth and other planetary bodies, Reviews in Mineralogy and Geochemistry: Geochemistry of Non-traditional Stable Isotopes, pp. 319-357.

Brantley, S.L., Liermann, L., Bullen, T.D., 2001, Fractionation of Fe isotopes by soil microbes and organic acids. Geology. 29: 535-538.

Brantley, S.L., Liermann, L.J., Guynn, R.L., Anbar, A., Icopini, G.A., Barling, J., 2004, Iron isotope fraction during mineral dissolution with and without bacteria. Geochim. Cosmochim. Acta. 68: 3189-3204.

Brantley, S.L., and White, A.F., 2009, Approaches to modeling weathered regolith. Reviews in Mineralogy & Geochemistry. Mineralogical Society of America. 70: 435-484.

Brantley, S.L., Holleran, M.E., Jin, L., and Bazilevskaya, E., 2013, Probing deep weathering in the Shale Hills Critical Zone Observatory, Pennsylvania (USA): the hypothesis of nested chemical reaction fronts in the subsurface. Earth Surface Processes and Landforms. 38: 1280-1298.

Brimhall G.H., and Dietrich, W.E., 1987, Constitutive mass balance relations between chemical composition, volume, density, porosity, and strain in metasomatic hydrochemical systems: Results on weathering and pedogenesis. Geochimica et Cosmochimica Acta. 51: 567-587.

Buol, S.W., and Weed, S.B., 1991, Saprolite-soil transformations in the Piedmont and Mountains of North Carolina. Geoderma. 51: 15-28.

Buss, H.L., Bruns, M.A., Schultz, M.J., Moore, J., Mathur, C.F., Brantley, S.L., 2005, The coupling of biological iron cycling and mineral weathering during saprolite formation, Luquillo Mountains, Puerto Rico. Geobiology. 3: 247–260.

Buss, H.L., Mathur, R., White, A.F., and Brantley, S.L., 2010, Phosphorus and iron cycling in deep saprolite, Luquillo Mountains, Puerto Rico. Chemical Geology. 269: 52-61.

Calvert, C.S., Buol, S.W., and Weed, S.B., 1980, Mineralogical characteristics and transformations of a vertical rock-saprolite-soil sequence in the North Carolina Piedmont: II. Feldspar alteration products-their transformations through the profile. Soil Sci. Soc. Am. J. 44: 1104-1112.

Currie, W.S., Aber, J.D., McDowell, W.H., Boone, R.D., and Magill, A.H., 1996, Vertical transport of dissolved organic C and N under long-term amendments in pine and hardwood forests. Biogeochemistry. 35: 471-505.

Dahlgren, R., Shoji, S., and Nanzyo, M., 1993, Chapter 5: Mineralogical characteristics of volcanic ash soils. In Volcanic Ash Soils: Genesis, Properties and Utilization. Eds. Shoji, S., Nanzyo, M., and Dahlgren, R.A. Developments in Soil Science 21. Elsevier. Amsterdam, The Netherlands. 101-143.

Daly, C., Neilson, R.P., and Phillips, D.L., 1994, A statistical-topographic model for mapping climatological precipitation over mountainous terrain. Journal of Applied Meteorology, 33: 140-158.

Dauphas, N., and Rouxel, O., 2006, Mass spectrometry and natural variations of iron isotopes. Mass Spectrom. Rev. 25: 831-832.

Dessert, C., Dupre, B., Gaillardet, J., Francois, L.M., Allegre, C.J., 2003, Basalt weathering laws and impact of basalt weathering on the global carbon cycle. Chemical Geology. 202: 257-272.

Emerson, D., Fleming, E.J., and McBeth, J.M., 2010, Iron-oxidizing bacteria: An environmental and genomic perspective. Annu. Rev. Microbiol. 64: 561-583.

Emmanuel, S., Erel, Y., Matthews, A., and Teutsch, N., 2005, A preliminary mixing model for Fe isotopes in soils. Chemical Geology. 222: 23-34.

Eswaran, H., and Bin, W.C., 1978, A study of a deep weathering profile on granite in Penninsular Malaysia: III. Alteration of feldspars. Soil Sci. Soc. Am. J. 42: 154-158.

Fantle, M.S., and DePaolo, D.J., 2004, Iron isotopic fractionation during continental weathering. Earth and Planetary Science Letters. 228: 547-562.

Fletcher, R.C., Buss, H.L., Brantley, S.L., 2006, A spheroidal weathering model coupling porewater chemistry to soil thickness during steady-state denudation. Earth and Planetary Science Letters. 244: 444-457.

Gilkes, R.J., and Suddhiprakarn, A., 1979, Biotite alteration in deeply weathered granite. Morphological, mineralogical, and chemical properties. Clays and Clay Minerals. 5: 349-360.

Goldich S. S., 1984, Determination of ferrous iron in silicate rocks. Chem. Geol. 42: 343-347.

Graham, R.C., Weed, S.B., Bowen, L.H., Amarasiriwardena, D.D., and Buol, S.W., 1989, Weathering of iron-bearing minerals in soils and saprolite on the North Carolina Blue Ridge Front: II. Clay mineralogy. Clays and Clay Minerals. 37: 29-40.

Hausrath, E.M., Navarre-Sitchler, A.K., Sak, P.B., Williams J.Z., and Brantley, S.L., 2011, Soil profiles as indicators of mineral weathering rates and organic interactions for a Pennsylvania diabase. Chemical Geology. 290: 89-100.

Hedin, L.O., Armesto, J.J., and Johnson, A.H., 1995, Patterns of nutrient loss from unpolluted, old-growth temperate forests-evaluation of biogeochemical theory. Ecology. 76: 493-509.

Icopini G.A., Anbar A.D., Ruebush S.S., Tien, M., and Brantley S. L., 2004, Iron isotope fractionation during microbial reduction of iron: the importance of adsorption. Geology. 32: 205–208.

Jackson M.L., 1956, Soil Chemical Analysis-Advanced Course. Chapter 3. University of Washington, Dept. of Soils, Madison, Wisconsin. pp. 101-168.

Jeong, G.Y., 2000, The dependence of localized crystallization of halloysite and kaolinite on primary minerals in the weathering profile of granite. Clays and Clay Minerals. 48: 196-203.

Jin, L., Rother, G., Cole, D.R., Mildner, D.F.R., Duffy, C.J., Brantley, S.L., 2011, Characterization of deep weathering and nanoporosity development in shale—a neutron study. American Mineralogist. 96: 498-512.

Johnson-Maynard, J.L., Graham, R.C., Shouse, P.J., and Quideau, S.A., 2005, Base cation and silicon biogeochemistry under pine and scrub oak monocultures: implications for weathering rates. Geoderma. 126: 353-365.

Kappler, A., Johnson, C.M., Crosby, H.A., Beard, B.L., and Newman, D.K., 2010, Evidence for equilibrium iron isotope fractionation by nitrate-reducing Fe(II)-oxidizing bacteria. Geochimica et Cosmochimica Acta. 74: 2826-2842.

Kautz, C.Q., and Ryan, P.C., 2003, The 10 Å to 7 Å halloysite transition in a tropical soil sequence, Costa Rica. Clays and Clay Minerals. 51: 252-263.

Kiczka, M., Wiederhold, J.G., Frommer, J., Kraemer, S.M., Bourdon, B., and Kretzschmar, R., 2010. Iron isotope fractionation during proton- and ligand-promoted dissolution of primary phyllosilicates. Geochimica et Cosmochimica Acta. 74: 3112-3128.

Liermann L.J., Mathur, R., Wasylenki, L.E., Nuester J., Anbar A.D., and Brantley S.L., 2011, Extent and isotopic composition of Fe and Mo release from two Pennsylvania shales in the presence of organic ligands and bacteria. Chem. Geol. 281: 167-180.

Lundstrom, U.S., van Breemen, N., and Bain, D., 2000, The podzolization process. A review. Geoderma. 94: 91-107.

McKeague, J.A., 1967, An evaluation of 0.1 M Pyrophosphate and pyrophosphate-dithionite in comparison with oxalate as extractants of the accumulation products in podzols and some other soils. Can. J. Soil Sci**.** 47: 97-99.

McKeague, J.A., Day, J.K., 1966, Dithionite- and oxalate-extractable Fe and Al as aids in differentiating various classes of soils. Can. J. Soil Sci. 46: 13-22.

Minyard, M.L., Bruns, M.A., Liermann, L.J., Buss, H.L., and Brantley, S.L., 2011, Halloysite nanotubes and bacteria at the saprolite-bedrock interface, Rio Icacos watershed, Puerto Rico. Soil Sci. Soc. Am. J. 75: 348-356.

Minyard, M.L., Bruns, M.A., Liermann, L.J., Buss, H.L., and Brantley, S.L., 2012, Bacterial associations with weathering minerals at the regolith-bedrock interface, Luquillo Experimental Forest, Puerto Rico. Geomicrobiology Journal. 29: 792-803.

Mottana, A., Crespi, R., and Liborio, G., 1977, Simon & Schuster's Guide to Rocks and Minerals. Eds. Prinz, M., Harlow, G., and Peters, J., Simon & Schuster Inc. The American Museum of Natural History. p.319.

National Oceanic and Atmospheric Administration (NOAA) website: http://www.ncdc.noaa.gov/cdo-web/

Neaman, A., Chorover, J., and Brantley, S.L., 2005, Implications of the evolution of organic acid moieties for basalt weathering over geological time. American Journal of Science. 305: 147-185.

Papoulis, D., Tsolis-Katagas, P., Katagas, C., 2004, Progressive stages in the formation of kaolin minerals of different morphologies in the weathering of plagioclase. Clays and Clay Minerals. 52: 275-286.

Pavich, M.J., Leo, G.W., Obermeier, S.F., and Estabrook, J.R., 1989, Investigations of the characteristics, origin, and residence time of the upland residual mantle of the Piedmont of Fairfax County, Virginia. U.S. Geological Survey Professional Paper 1352.

Poitrasson, F., Viers, J., Martin, F., and Braun, J.J., 2008, Limited iron isotope variations in recent lateritic soils from Nsimi, Cameroon: Implications for the global Fe geochemical cycle. Chemical Geology. 253: 54-63.

Potter, N., Niemitz, J.W., Sak, P.B., 2009, Long-term field-based studies in teaching geology. In: Whitmeyer, S.J., Mogk, D.W., Pyle, E.J. (Eds.), Field Geology Education: Historical Perspectives and Modern Approaches: Geological Society of America Special Paper, 461.

Rice, T.J., Buol, S.W., and Weed, S.B., 1985, Soil-saprolite derived from mafic rocks in the North Carolina Piedmont: I. Chemical, morphological, and mineralogical charateristics and transformations. Soil Sci. Soc. Am. J. 49: 171-178.

Riebe, C.S., Kirchner, J.W., and Finkel, R.C., 2003, Long-term rates of chemical and physical erosion from cosmogenic nuclides and geochemical mass balance. Geochimica et Cosmochimica Acta. 67: 4411-4427.

Richter, D.D., Markewitz, D., 1995, How deep is soil? BioScience. 45: 600-609.

Ross, S.J., Franzmeier, D.P., and Rorn, C.B., 1976, Mineraology and chemistry of manganese oxdies in some Indiana soils. Division S-9L–Soil Minerology. Soil Sci. Soc. Am. J. 40: 137-143.

Sanford, W.E., and Selnick, D.L., 2013, Estimation of evapotranspiration across the conterminous United States using a regression with climate and land-cover data. Journal of the American Water Resources Association. 49: 217-230.

Schulz, M., Stonestrom, D., Von Kiparski, G., Lawrence, C., Masiello, C., White, A., and Fitzpatrick, J., 2011, Seasonal dynamics of CO_2 profiles across a soil chronosequence, Santa Cruz, California. Applied Geochemistry. 26: S132-S134.

Skulan, J.L., Beard, B.L., and Johnson, C.M., 2002b, Kinetic and equilibrium Fe isotope fractionation between aqueous Fe(III) and hematite. Geochimica et Cosmochimica Acta, 66: 2995-3015.

Smith, R.C., Rose, A.W., Lanning, R.M., 1975, Geology and geochemistry of Triassic diabase in Pennsylvania. Geological Society of America Bulletin. 86: 943-955.

Soil Survey Staff, National Resources Conservation Service, United States Department of Agriculture. Web Soil Survey. Available online at http://websoilsurvey.nrcs.usda.gov.

Stinchcomb, G. E., et al., in prep., Quantitative links between biota, mass-balance geochemistry and the soil atmosphere: An example from a diabase weathering profile in northeastern USA.

Sutter, J.F., 1988, Innovative approaches to the dating of igneous events in the early Mesozoic basins of the Eastern United States. U. S. Geological Survey Bulletin Report:

B 1776, 194–200.

Tazaki, K., 2005, Microbial formation of halloysite-site mineral. Clays and Clay Minerals. 53: 224-233.

Thompson, A., Chadwick, O.A., Boman, S., Chorover, J., 2006, Colloid mobilization during soil iron redox oscillations. Environ. Sci. Technol. 40: 5743-5749.

Tolpeshta, I.I., and Sokolova, T.A., 2009, Aluminum compounds in soil solutions and their migration in podzolic soils in two-layered deposits. Eurasian Soil Science. 42: 24-35.

White, W.B., 2009. The evolution of Appalachian fluviokarst: competition between stream erosion, cave development, surface denudation, and tectonic uplift. Journal of Cave and Karst Studies. 71: 159–167.

White, A.F., Blum, A.E., Schulz, M.B., Vivit, D.V., Stonestrom, D.A., Larsen, M., Murphy, S.F., and Eberl, D., 1998, Chemical weathering in a tropical watershed, Luquillo Mountains, Puerto Rico: I. Long-term versus short-term weathering fluxes. Geochimica et Cosmochimica Acta. 62: 209-226.

Wiederhold, J.G., Teutsch, N., Kraemer, S.M., Halliday, A.N., and Kretzschmar, R., 2007a, Iron isotope fractionation during pedogenesis in redoximorphic soils. Soil Science Society of America Journal. 71: 1840-1850.

Wiederhold, J.G., Teutsch, N., Kraemer, S.M., Halliday, A.N., and Kretzschmar, R., 2007b, Iron isotope fractionation in oxic soils by mineral weathering and podzolization. Geochimica et Cosmochimica Acta. 71: 5821-5833.

Yesavage, T.A., Fantle, M.S.,Vervoort, J., Mathur, R., Jin, L., Liermann, L.J., and Brantley, S.L., 2012, Fe cycling in the Shale Hills Critical Zone Observatory, Pennsylvania: an analysis of biogeochemical weathering and Fe isotope fractionation. Geochimica et Cosmochimica Acta. 99: 18-38.

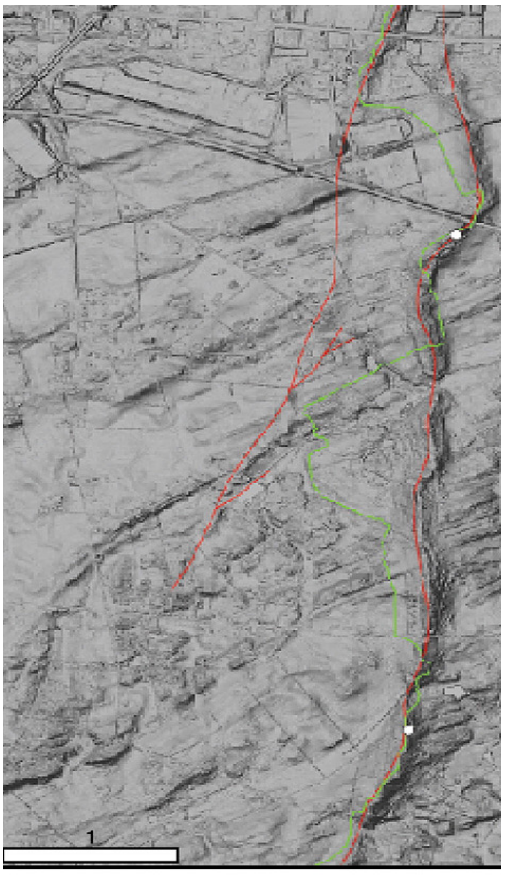

Figure 4-1. Map indicating sampling locations on the Gettysburg diabase indicated as white points, overlain by inferred locations of the diabase dike in red. The northern white point indicates the location of the turnpike road cut, while the lower white point indicates the location from which soil cores was obtained. The scale bar is 1 km.

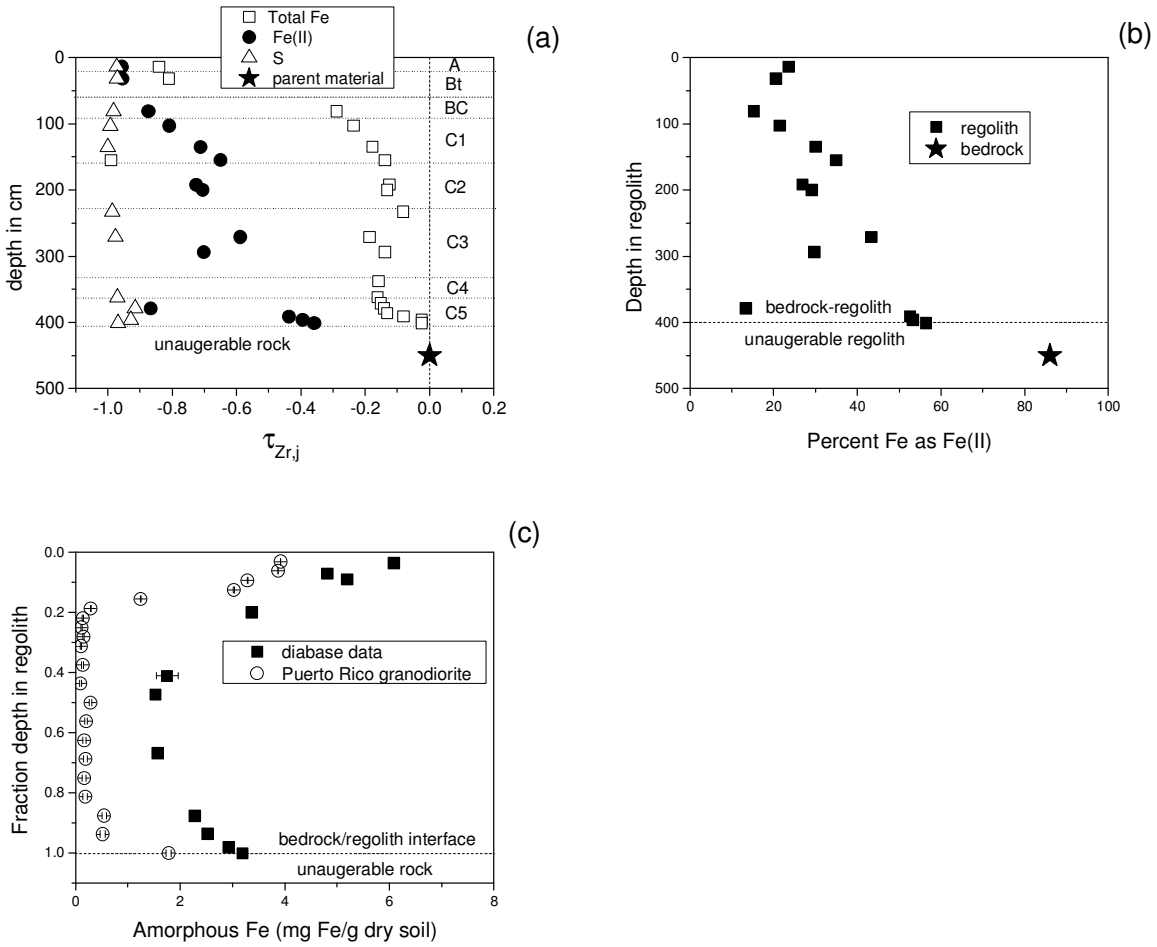

Figure 4-2. a) $\tau_{Zr,j}$ values with depth for total Fe (from Hausrath et al., 2011), Fe(II) and sulfur in the diabase regolith profile of the current study, b) the percent of Fe present as Fe(II) in regolith with depth (with an estimated precision of 20%) and c) the abundance of amorphous Fe with depth based upon extractions with acid ammonium oxalate (black squares) and for a Puerto Rico granodiorite (circles; Buss et al., 2010). Error bar in c) based on 1σ variation for samples preformed in triplicate. The black stars in a) and b) indicate the composition of inferred bedrock material.

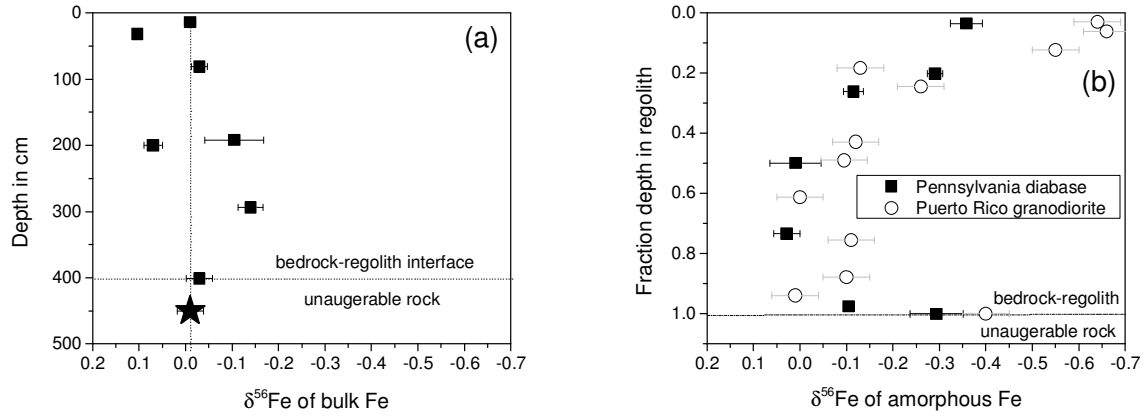

Figure 4-3. δ^{56}Fe values of a) bulk Fe and b) amorphous (HCl-extracted) Fe as a function of depth in the regolith. Error bars show 1σ variation of replicate analyses. The lowermost points (stars) indicate the isotopic composition of bulk Fe in bedrock taken from along the Pennsylvania Turnpike. Horizontal lines in a) and b) indicate the depth of auger refusal, interpreted as the bedrock-regolith interface. Vertical line in a) indicates the isotopic composition of parent material. Circles in Figure 3b are data from Buss et al. (2010).

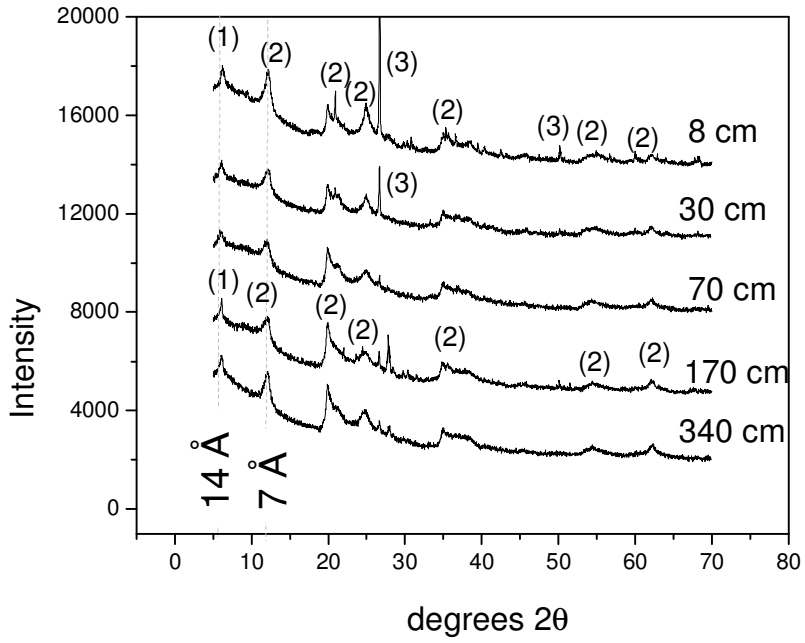

Figure 4-4. XRD diffractograms of the clay-sized fraction (<2 μm) of the regolith at different depths. Peaks include: (1) a 14-Å clay (chlorite/vermiculite/smectite), (2) 7-Å kaolinite/halloysite and (3) quartz. Vertical gray lines indicate 7 and 14 Å peaks. Peaks are identified for only a few scans.

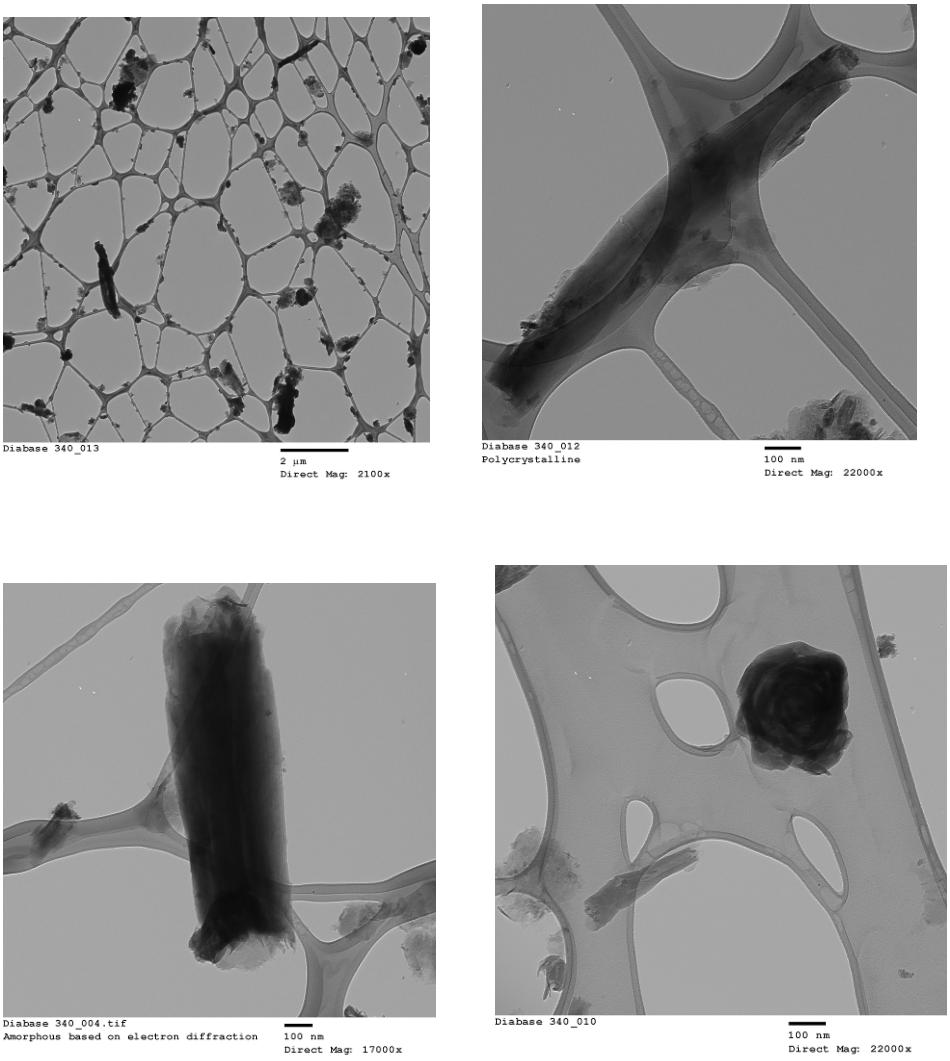

Figure 4-5. TEM images of the clay-sized fraction of the 340-350 cm diabase sample. Images include: A) a lower magnification image to demonstrate the heterogeneous morphology, B) a polycrystalline tube similar to reported halloysite morphology, C) an amorphous tube-like structure, and D) a rose-shaped morphology characteristic of halloysite. Tubular and rose-shaped halloysite were also observed in the clay-sized fraction of samples from 30 cm and 70 cm.

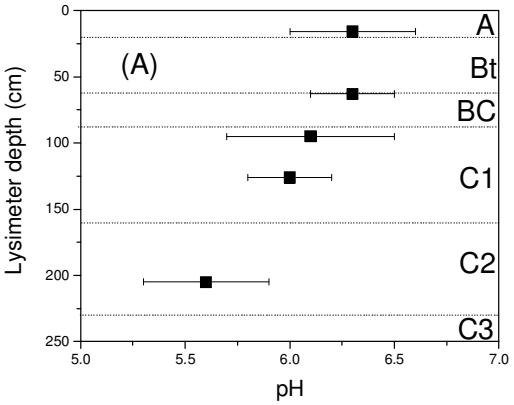
(A)
A
Bt
BC
C1
C2
C3
Lysimeter depth (cm)
pH
0
50
100
150
200
250
5.0
5.5
6.0
6.5
7.0

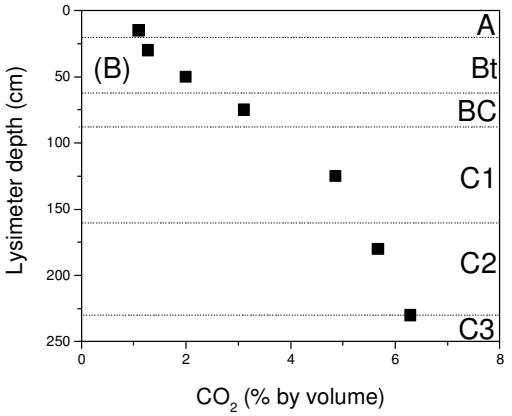
(B)
A
Bt
BC
C1
C2
C3
Lysimeter depth (cm)
CO2 (% by volume)
0
50
100
150
200
250
0
2
4
6
8

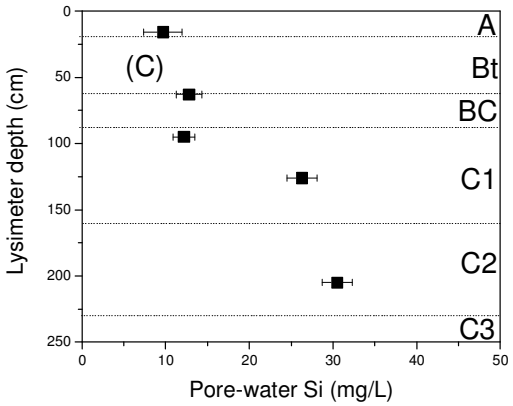
(C)
A
Bt
BC
C1
C2
C3
Lysimeter depth (cm)
Pore-water Si (mg/L)
0
50
100
150
200
250
0
10
20
30
40
50

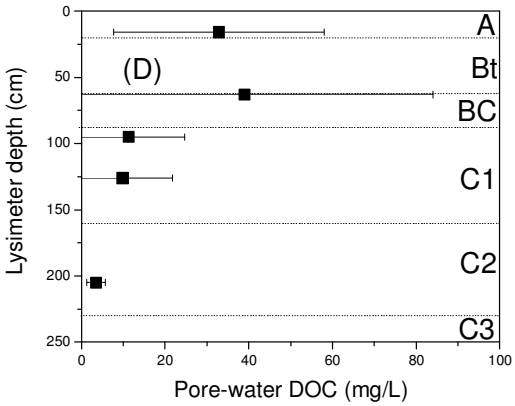
(D)
A
Bt
BC
C1
C2
C3
Lysimeter depth (cm)
Pore-water DOC (mg/L)
0
50
100
150
200
250
0
20
40
60
80
100

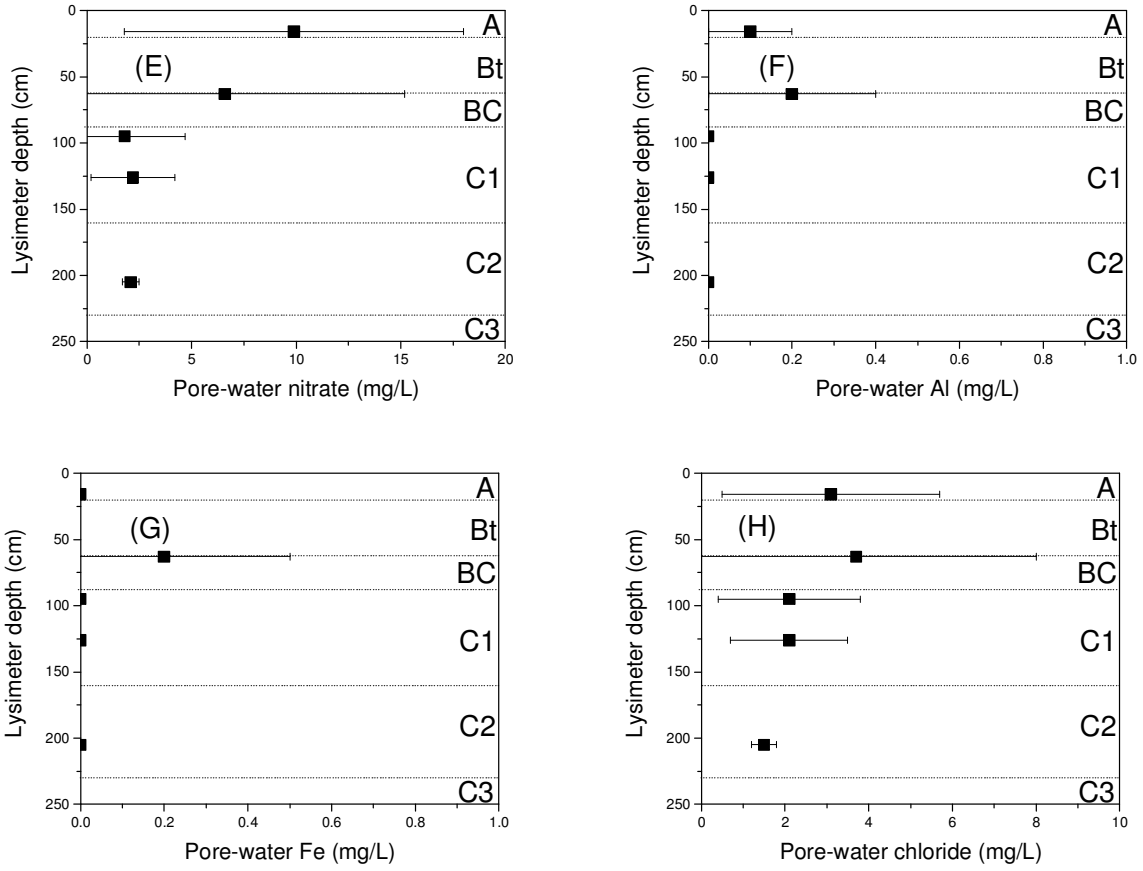

Figure 4-6. Average pore-water data with standard deviations plotted as a function of profile depth. A) pH, B) soil carbon dioxide (percent by volume) C) pore-water silica, D) pore-water dissolved organic carbon, E) pore-water nitrate, F) pore-water Al, G) pore-water Fe and H) pore-water chloride. Error bars indicate the 1σ variation over time for each depth.

Table 4-1: Description of diabase soil profile

Depth (m)	Horizon	
0-0.22	A	very dark grayish brown (10YR 3/2) silt loam with moderate, fine, subangular blocky structure; very friable; slightly sticky; common fine to medium roots throughout; clear lower boundary
0.22-0.60	Bt	strong brown (7.5YR 5/6) silty clay loam with moderate, medium, subangular blocky structure; friable; slightly sticky; common fine to medium roots throughout; few, distinct, discontinuous strong brown (7.5YR 5/6) clay films coating ped faces; clear lower boundary
0.60-0.90	BC	yellowish brown (10YR 5/8) sandy loam with weak, medium subangular blocky structure; very friable; slightly sticky; few fine roots; few yellowish red (5YR 5/8) clay films along ped faces; few, distinct black (N 2.5/) Mn coatings along ped faces and possibly tubular pores; clear lower boundary
0.9-1.60	C1	olive yellow (2.5Y 6/6) sandy loam, massive with zones of moderate, medium, angular blocky structure; laminated Fe concentrations (relict?); clear lower boundary
1.60-2.05	C2	strong brown (7.5YR 5/6) silt loam, common, distinct, black (N 2.5/) Mn coatings; auger boring terminated because of lystimer installment
2.05-2.30	C2	yellowish brown (10 YR 5/6) sandy loam
2.30-3.40	C3	olive yellow (2.5Y 6/6) sandy loam to loamy sand
3.40-3.65	C4	strong brown (7.5YR 5/6) silt loam; alternating layers of red (2.5YR 4/6) alternating with white (7.5YR 8/1) layers (rindlets?); red layers had possible pressure faces and black mottles along surfaces. This could be from augering.
3.65-3.95	C5	olive yellow (2.5Y 6/6) sandy loam to loamy sand
>3.95	R	bedrock

Table 4-2: Chemistry of regolith

depth (cm)	total Fe (wt. %)[1]	total Al (wt. %)[1]	Zr (ppm)[1]	Fe (II) (wt.%)[2]	% Fe as Fe(II)	S (ppm)[3]	$\tau_{Zr,Fe}$	$\tau_{Zr,Fe(II)}$	$\tau_{Zr,S}$
14	6.46	7.52	247	1.5	23.6	151	-0.84	-0.96	-0.97
32	7.08	8.28	227	1.5	20.5	142	-0.81	-0.95	-0.97
81	9.72	10.43	83.5	1.5	15.3	33	-0.29	-0.87	-0.98
103	9.44	9.87	75.5	2.0	21.5	14	-0.24	-0.81	-0.99
135	8.88	9.1	66	2.7	30.1	0	-0.18	-0.71	-1.00
155	8.74	8.84	62	3.1	34.9	14	-0.14	-0.65	-0.99
192	8.81	8.71	61.5	2.4	26.9	-	-0.12	-0.73	-
200	8.81	8.79	62	2.6	29.2	-	-0.13	-0.70	-
233	8.71	8.52	58	-	-	17	-0.08	-	-0.99
271	8.39	8.52	63	3.6	43.4	33	-0.19	-0.59	-0.98
294	8.88	9	63	2.6	29.7	-	-0.14	-0.70	-
338	8.81	8.76	64	-	-	-	-0.16	-	-
362	8.92	8.76	65	-	-	42	-0.16	-	-0.97
371	9.02	8.89	65	-	-	-	-0.15	-	-
379	8.85	8.68	63	1.2	13.4	115	-0.14	-0.87	-0.92
386	8.67	8.47	61	-	-	-	-0.13	-	-
391	8.57	8.15	57	4.5	52.6	-	-0.08	-0.44	-
396	8.46	7.83	53	4.5	53.3	81	-0.02	-0.39	-0.93
401	8.46	7.83	53	4.8	56.4	36	-0.02	-0.36	-0.97
bedrock	7.69	7.78	47	6.6	86.0	1011	0.00	0.00	0.00

1) Data from Hausrath et al. (2011)

2) Data from Fe(II) titrations as described in methods section

3) Data from sulfur titrations as detailed in methods section

Table 4-3: pH and sequential extraction data from regolith sieved to <850 µm

depth (cm)	Al_{ox} (mg/g soil)[1]	Fe_{ox} (mg/g soil)[1]	Si_{ox} (mg/g soil)[1]	Al_{pyro} (mg/g soil)[2]	Fe_{pyro} (mg/g soil)[2]	% amorphous Al[1]	% amorphous Fe[1]	% amorphous Si[1]
8-19 cm	2.21	6.09	0.39	0.91	1.84	2.9	9.4	0.2
23-30 cm	1.95	4.82	0.38	0.76	1.25	2.5	7.1	0.1
30-37 cm	2.20	5.20	0.62	0.67	0.81	2.5	7.1	0.2
71-77 cm	1.65	3.37	0.64	0.46	0.45	1.5	3.4	0.3
144-160 cm	1.18 ± 0.07	1.75 ± 0.21	0.44 ± 0.02	0.29 ± 0.02	0.21 ± 0.02	1.3 ± 0.08	2.0 ± 0.24	0.19 ± 0.01
170-180 cm	1.18	1.53	0.40	0.41	0.37	1.4	1.7	0.2
242-252 cm	1.49	1.57	0.54	0.31	0.15	1.7	1.8	0.2
319-329 cm	1.21	2.28	0.50	0.41	0.39	1.4	2.6	0.2
341-351 cm	1.28	2.52	0.58	0.37	0.35	1.5	2.9	0.3
358-367 cm	1.30	2.93	0.59	0.59	0.68	1.5	3.3	0.3
367-373 cm	1.45	3.19	0.64	0.43	0.49	1.6	3.5	0.3

1) Measured with ammonium oxalate extraction as described in methods

2) Measured with sodium pyrophosphate extraction as described in methods

Table 4-4: δ^{56}Fe values of bulk and amorphous Fe in diabase regolith

	average	standard deviation	n
Bulk samples:			
14 cm	-0.01	0.01	2
32 cm	0.10	-	1
81 cm	-0.03	0.02	3
192 cm	-0.11	0.06	2
200 cm	0.07	0.02	2
271 cm	-0.14	0.03	2
401 cm	-0.03	0.03	2
bedrock	-0.01	0.03	2
Amorphous (HCl-extracted) samples:			
14 cm	-0.36	0.03	2
81 cm	-0.29	0.02	2
105 cm	-0.12	0.02	2
200 cm	0.01	0.05	2
294 cm	0.03	0.03	2
391 cm	-0.11	0.01	2
401 cm	-0.29	0.06	3
bedrock	-0.17	0.02	2
Standards:			
NIST SRM-3126a	0.35	0.03	14
HPS-UW	0.58	0.03	10

Table 4-5: Averaged pore-water data from fall of 2011 to the summer of 2013, with 1 standard deviation variation[1]

depth (cm)	pH	DOC (mg/L)	Al (mg/L)	Ca (mg/L)	Fe (mg/L)	K (mg/L)	Mg (mg/L)	Mn (mg/L)	Na (mg/L)	Si (mg/L)	nitrate (mg/L)	sulfate (mg/L)	chloride (mg/L)
16	6.3 ± 0.3	32.9 ± 25.2	0.1 ± 0.1	12.3 ± 3.0	0.0 ± 0.0	2.9 ± 3.1	2.8 ± 0.6	0.0 ± 0.1	1.2 ± 1.7	9.7 ± 2.3	9.9 ± 8.1	5.3 ± 2.3	3.1 ± 2.6
63	6.3 ± 0.2	39.0 ± 45.0	0.2 ± 0.2	7.5 ± 3.2	0.2 ± 0.3	7.2 ± 7.0	3.6 ± 1.4	0.0 ± 0.1	4.2 ± 3.0	12.8 ± 1.5	6.6 ± 8.6	10.7 ± 4.8	3.7 ± 4.3
95	6.1 ± 0.4	11.3 ± 13.4	0.0 ± 0.0	10.1 ± 1.9	0.0 ± 0.0	1.4 ± 0.6	2.3 ± 0.4	0.0 ± 0.0	1.2 ± 0.4	12.2 ± 1.3	1.8 ± 2.9	6.2 ± 1.4	2.1 ± 1.7
126	6.0 ± 0.2	9.9 ± 11.9	0.0 ± 0.0	9.1 ± 0.7	0.0 ± 0.0	0.2 ± 0.1	5.7 ± 0.4	0.0 ± 0.0	3.6 ± 0.3	26.3 ± 1.8	2.2 ± 2.0	12.1 ± 2.9	2.1 ± 1.4
205	5.6 ± 0.3	3.5 ± 2.2	0.0 ± 0.0	9.5 ± 0.4	0.0 ± 0.0	0.2 ± 0.1	5.5 ± 0.2	0.0 ± 0.0	3.2 ± 0.1	30.5 ± 1.8	2.1 ± 0.4	11.0 ± 0.8	1.5 ± 0.3

1) All analytical methods discribed in text in greater detail.

Appendix A: Summary of Colloidal Dispersion experiments

As was described in Chapter 3, colloidal dispersion experiments were performed to understand the size fractions in which different elements exist in regolith. These experiments were performed not only for a Sverrefjell regolith sample (38-47 cm), but also for a Shale Hills toeslope sample (78-87 cm) and two Pennsylvania diabase samples (from depths of 30-37 cm and 70-71 cm). At both pH 5 and 7, the Sverrefjell regolith dispersed more total colloidal Al, Fe and Si (2-415 nm in size) than the other two sites (Figure A-1; Table A-1). This finding is likely the result of elevated concentrations of amorphous (and likely colloidal-sized) Al, Fe and Si at Sverrefjell relative to other two sites (Table A-3; Chapter A-3).The higher abundance of non-crystalline phases at Sverrefjell is likely due to a) the presence of volcanic glass, a precursor to amorphous allophane (Dahlgren et al., 1993), and b) the short time since deglaciation at Sverrefjell, which would limit crystallization of allophane into halloysite.

Interestingly, the overall patterns of colloidal dispersion are very similar at all three sites, with Na, Ca and Mg being present in the dissolved form and Al and Fe existing largely in the 260-425 nm fraction (Figure A-2). While measurable concentrations of Ti were observed for Sverrefjell regolith, concentrations of Ti in dispersion experiments at the other two sites were below the ICP-AES detection limit of 1 ppb. At all sites, Si appears to be present simultaneously as larger colloidal particles (260-415 nm) and in the dissolved form (Figure A-2). Similar elemental dispersion patterns for all three locations suggest that Al, Fe and Si tend to form colloidal particles of similar size despite mineralogical differences in soils.

Molar ratios of Al/Si in the 260-415 nm fraction aid in the identification of specific minerals that are being dispersed. For instance at the Sverrefjell volcano, molar Al/Si ratios ranged from 1.0 to 2.0, a ratio that is consistent with allophane as the predominant phase (Figure A-3). In contrast, the molar Al/Si ratio in the Pennsylvania diabase ranges between 0.5 and 1.0, consistent with some combination of halloysite/kaolinite and/or smectite as the dispersed phases (Figure 3). The molar ratios of Al:Fe:Si of dispersed colloidal material in the 260-415 nm size fraction remain constant as a function of pH both for the Sverrefjell volcano (Chapter 3) and for the Pennsylvania diabase (Figure A-4).

At all three sites, minimal amounts of dissolved Al and Fe (< 3 kDa) were released in experiments performed between pH 5 to 8 m, although the dissolved fraction increased significantly below pH 4.5 at Sverrefjell and Shale Hills (Figures A-5 and A-6). These findings imply that significant concentrations of Al and Fe dissolve only when the regolith pH drops to below 4.5, a scenario that is only likely at Shale Hills. Although not likely to be environmentally relevant, significant Al was also dissolved above pH 10 (Figures A-5 and A-6). In contrast to Al and Fe, significant Si (in excess of 1 mmole/kg soil) was solubilized in all experiments performed regardless of pH (Figure A-7); the amount of dissolved Si tended to increase at both high and low pH (Figure A-7).

Concentrations of colloidal Al, Fe and Si (260-415 nm) are relatively constant across the pH range at Sverrefjell and the Pennsylvania diabase site, with dramatic changes being noted only above pH 10 (Figures A-5, A-6 and A-7). In the case of Sverrefjell, the amorphous dispersed phase is likely very soluble at pH 10, thus resulting in no measurable colloidal material above pH 10. In contrast, the more crystalline products inferred at the diabase site (halloysite/kaolinite and smectite) are apparently insoluble above pH 10. However, a pH above 10 is not likely at either of these sites. In the Shale Hills samples, the amount of colloidal Al, Fe and Si increases dramatically at a pH~7 (Figure A-5). The pH in the Shale Hills watershed ranges from ~4 at the ridges to ~5 in the valley floor (Jin et al., 2010), implying that valley floor conditions are more conducive toward colloidal dispersion.

In the case of the Shale Hills watershed, lysimeter pore-water data suggest that minimal Fe exists in the dissolved state (Chapter 2). The apparent loss of Fe from the watershed based upon $\tau_{Zr,Fe}$ values seems therefore to require loss of colloidal-sized material that is too large to be introduced into the 1.3-μm ceramic cup pores of the lysimeters. However, results from the colloidal dispersion experiments show only minimal dispersion of colloidal Fe compared with the Sverrefjell site, for instance. It is therefore not clear why Fe appears to be lost from the Shale Hills watershed but not from Sverrefjell. One possibility involves abundant preferential flow pathways throughout the Shale Hills watershed that facilitate loss of colloidal-sized Fe from this site. A second possibility may involve eolian deposition of Zr at Shale Hills, which would overestimate the extent to which Fe appears to be depleted based on $\tau_{Zr,Fe}$ values. Finally, the possibility exists that Fe loss from the Shale Hills catchment occurred mostly during some earlier

point of time in the history of the catchment. For instance, if the pH was once significantly lower, this would enhance the dissolution of Fe based on results from the dispersion experiments.

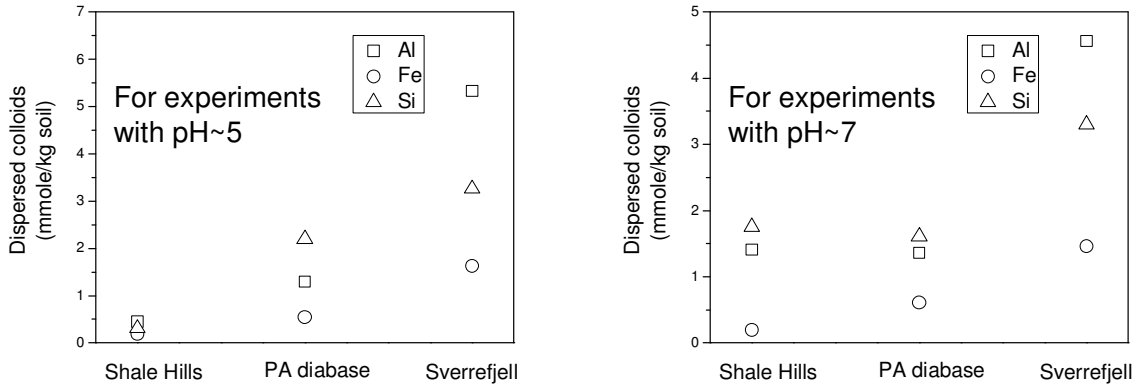

Figure A-1. Total amounts of dispersed colloidal material (ranging between 2-415 nm in size) from colloidal dispersion experiments performed at the three different sites at pH~5 (to the left) and pH~7 (to the right).

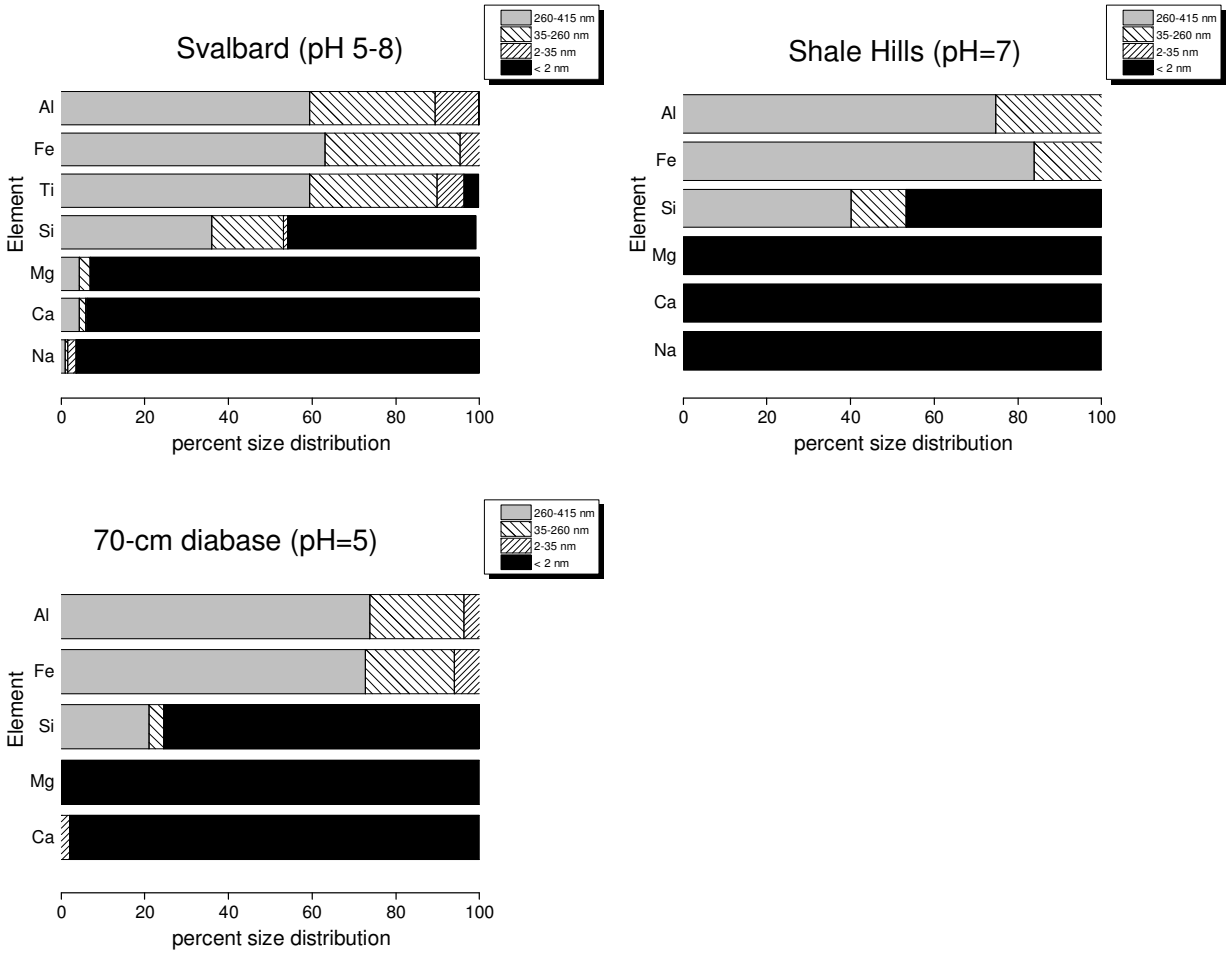

Figure A-2. Elemental size distributions of dispersed elements from the three different sites.

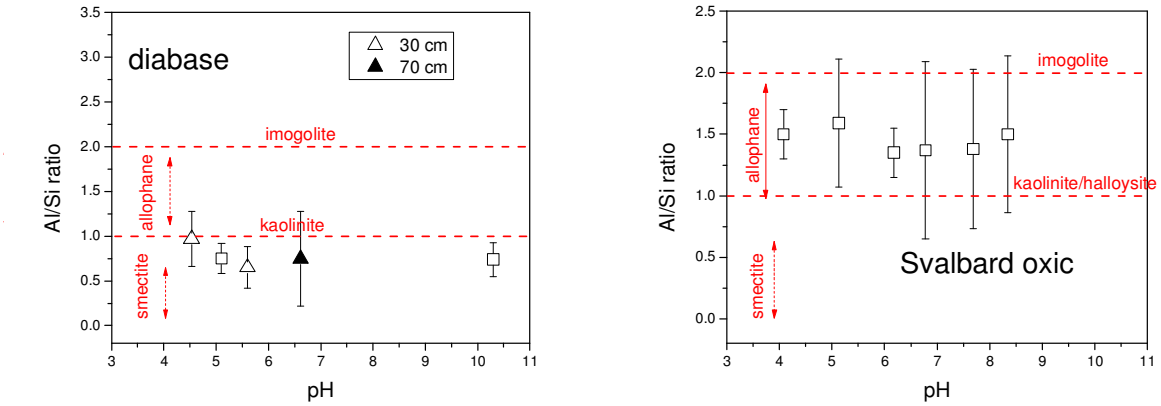

A-3. Molar ratio of Al/Si dispersed from the 260-415 nm size fraction of the diabase regolith samples (to the left) and the Sverrefjell regolith (to the right) as a function of pH under oxic conditions. Error bars show the 1σ variation around triplicate experiments.

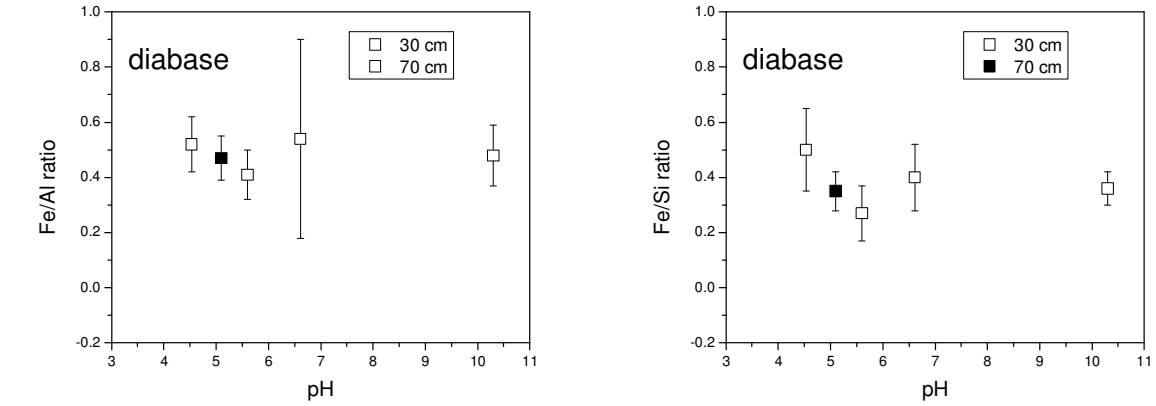

Figure A-4. Ratios of Fe/Al and Fe/Si remain constant across the pH range analyzed for the diabase colloidal experiments, in accordance with similar findings from the Sverrefjell volcano documented in Chapter 3.

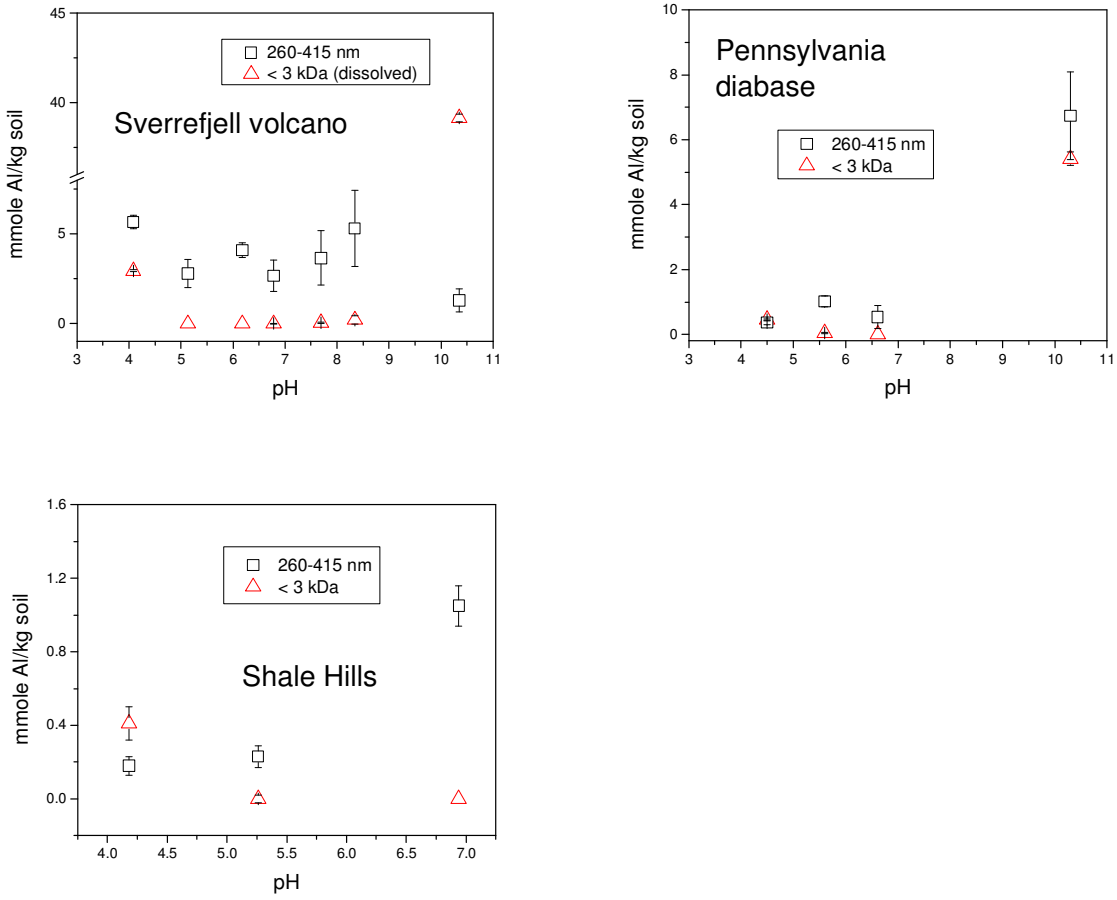

Figure A-5. Concentrations of dissolved (< 3 kDa) and larger colloidal (260-415 nm) Al measured in colloidal dispersion experiments at the three sites.

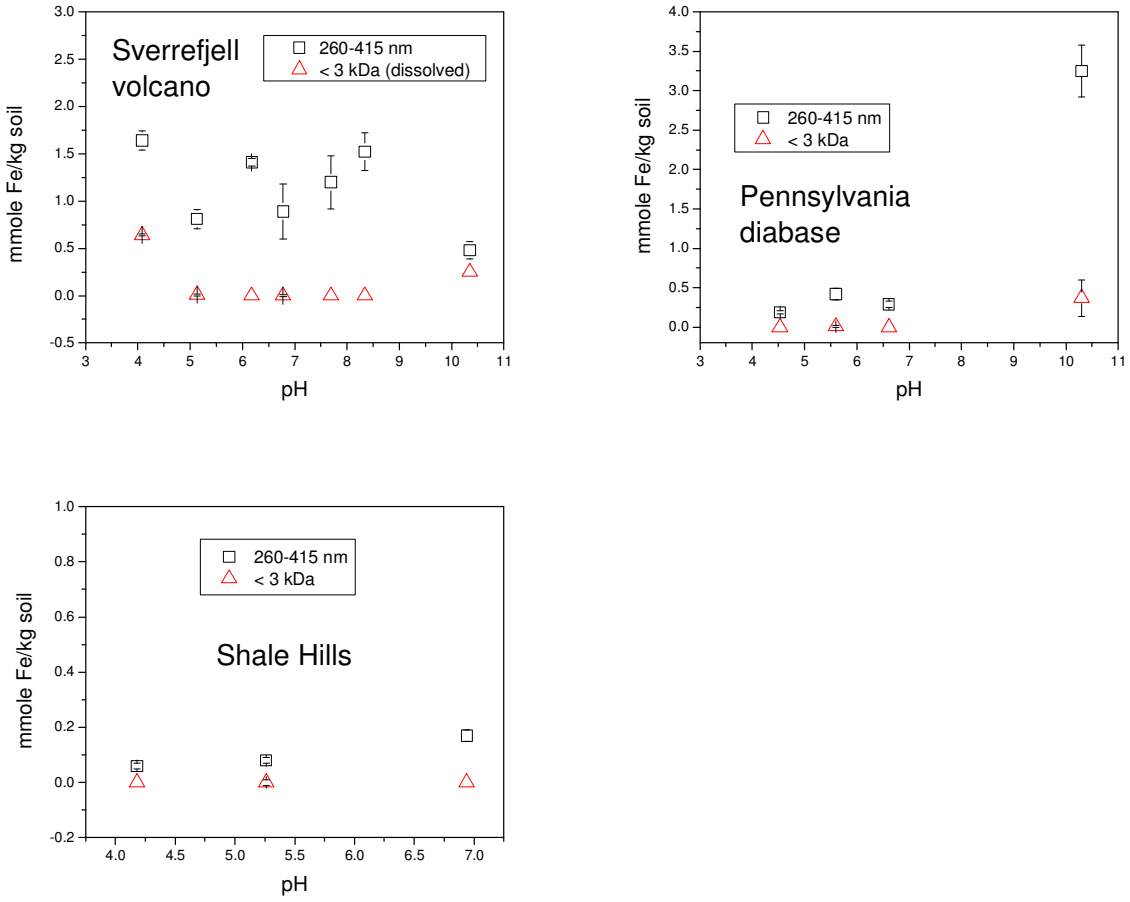

Figure A-6. Concentrations of dissolved (< 3 kDa) and larger colloidal (260-415 nm) Fe measured in colloidal dispersion experiments at the three sites.

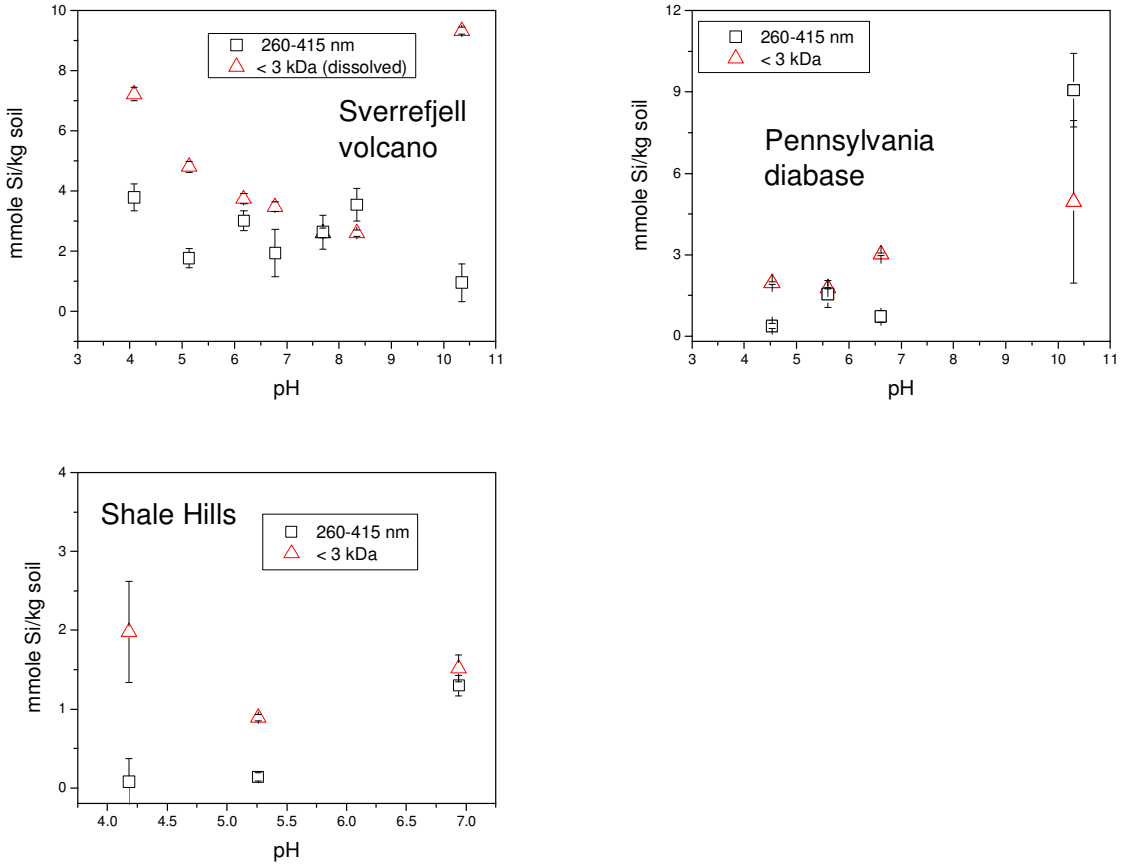

Figure A-7. Concentrations of dissolved (< 3 kDa) and larger colloidal (260-415 nm) Si measured in colloidal dispersion experiments at the three sites.

Table A-1: Chemistry of colloidal dispersion experiments[1]

Al (mmole/kg soil):	<3 kDa	error	<3 kDa-35 nm	error	35-260 nm	error	260-415 nm	error	sum of colloids (3 kDa-415 nm)
Sverrefjell 2-hr oxic (pH 4.08)	2.95	0.06	0.65	0.22	1.20	0.38	5.67	0.37	7.53
Sverrefjell 2-hr oxic (pH 5.13)	0.00	0.00	0.39	0.25	2.14	0.35	2.80	0.77	5.33
Sverrefjell 2-hr oxic (pH 6.18)	0.00	0.00	0.14	0.12	1.84	0.34	4.10	0.42	6.08
Sverrefjell 2-hr oxic (pH 6.78)	0.00	0.01	0.14	0.03	1.75	0.87	2.67	0.87	4.56
Sverrefjell 2-hr oxic (pH 7.69)	0.05	0.04	0.96	0.47	1.71	1.07	3.66	1.52	6.33
Sverrefjell 2-hr oxic (pH 8.34)	0.21	0.23	1.51	0.34	2.05	0.54	5.32	2.13	8.88
Sverrefjell 2-hr oxic (pH 10.3)	39.20	0.21	-	-	0.02	0.47	1.30	0.65	1.32
Sverrefjell 1 week anoxic (pH=5.97)	2.08	3.60	0.00	3.61	0.98	0.32	0.76	0.56	1.74
Sverrefjell 2 week anoxic (pH=5.91)	0.07	0.07	0.28	0.19	1.56	0.45	2.84	3.59	4.68
Sverrefjell 3 weeks anoxic (pH=5.98)	0.00	0.01	0.95	0.96	4.02	1.13	0.00	0.76	4.97
Sverrefjell 3 weeks oxic (pH 6.28)	0.78	0.26	0.00	0.28	1.53	0.15	4.45	0.59	5.98
diabase2-hr oxic (pH 4.5)	0.46	0.02	0.08	0.04	0.16	0.04	0.37	0.06	0.61
diabase2-hr oxic (pH 5.6)	0.04	0.02	0.00	0.00	0.29	0.14	1.02	0.16	1.30
diabase 2-hr oxic (pH 7)	0.00	0.00	0.12	0.21	0.69	0.23	0.54	0.36	1.36
diabase 70 cm 2-hr oxic (pH 5.1)	0.00	0.01	0.14	0.02	0.22	0.05	0.73	0.10	1.10
Shale Hills 2-hr oxic (pH 4)	0.41	0.09	0.06	0.10	0.11	0.05	0.18	0.05	0.35
Shale Hills 2-hr oxic (pH 5)	0.00	0.02	0.06	0.03	0.16	0.04	0.23	0.06	0.45
Shale Hills 2-hr oxic (pH 7)	0.00	0.00	0.00	0.00	0.36	0.03	1.05	0.11	1.41

Fe (mmole/kg soil):	<3 kDa	error	<3 kDa-35 nm	error	35-260 nm	error	260-415 nm	error	sum of colloids (3 kDa-415 nm)
Sverrefjell 2-hr oxic (pH 4.08)	0.64	0.01	0.15	0.06	0.33	0.11	1.64	0.10	2.12
Sverrefjell 2-hr oxic (pH 5.13)	0.01	0.01	0.14	0.07	0.69	0.12	0.81	0.10	1.63
Sverrefjell 2-hr oxic (pH 6.18)	0.00	0.00	0.07	0.04	0.52	0.04	1.41	0.04	2.00
Sverrefjell 2-hr oxic (pH 6.78)	0.00	0.01	0.02	0.01	0.55	0.29	0.89	0.29	1.46
Sverrefjell 2-hr oxic (pH 7.69)	0.00	0.00	0.12	0.17	0.61	0.33	1.20	0.28	1.93
Sverrefjell 2-hr oxic (pH 8.34)	0.00	0.00	0.02	0.01	0.65	0.20	1.52	0.20	2.20
Sverrefjell 2-hr oxic (pH 10.3)	0.25	0.00	-	-	0.26	0.09	0.48	0.09	0.74
Sverrefjell 1 week anoxic (pH=5.97)	0.00	0.00	0.24	0.03	0.27	0.06	0.22	0.05	0.73
Sverrefjell 2 week anoxic (pH=5.91)	0.11	0.02	0.13	0.04	0.45	0.12	0.39	0.12	0.96
Sverrefjell 3 weeks anoxic (pH=5.98)	0.43	0.18	0.85	0.25	1.62	0.27	0.00	0.21	2.48
Sverrefjell 3 weeks oxic (pH 6.28)	0.15	0.02	0.00	0.05	0.52	0.05	1.42	0.05	1.94
diabase2-hr oxic (pH 4.5)	0.00	0.00	0.01	0.01	0.08	0.02	0.19	0.02	0.28
diabase2-hr oxic (pH 5.6)	0.01	0.01	0.00	0.00	0.13	0.07	0.42	0.07	0.55
diabase 2-hr oxic (pH 7)	0.00	0.00	0.05	0.08	0.28	0.09	0.29	0.04	0.61
diabase 70 cm 2-hr oxic (pH 5.1)	0.00	0.01	0.03	0.01	0.10	0.03	0.34	0.03	0.47
Shale Hills 2-hr oxic (pH 4)	0.00	0.00	0.02	0.01	0.03	0.01	0.06	0.01	0.10
Shale Hills 2-hr oxic (pH 5)	0.00	0.01	0.02	0.01	0.09	0.02	0.08	0.01	0.19
Shale Hills 2-hr oxic (pH 7)	0.00	0.00	0.00	0.00	0.03	0.02	0.17	0.02	0.20

Si (mmole/kg soil):	<3 kDa	error	<3 kDa-35 nm	error	35-260 nm	error	260-415 nm	error	sum of colloids (3 kDa-415 nm)
Sverrefjell 2-hr oxic (pH 4.08)	7.22	0.22	0.52	0.27	0.24	0.23	3.79	0.45	4.55
Sverrefjell 2-hr oxic (pH 5.13)	4.81	0.18	0.06	0.37	1.44	0.35	1.77	0.32	3.26
Sverrefjell 2-hr oxic (pH 6.18)	3.74	0.17	0.00	1.79	1.07	1.80	3.02	0.33	4.09
Sverrefjell 2-hr oxic (pH 6.78)	3.48	0.16	0.00	0.23	1.36	0.77	1.94	0.79	3.30
Sverrefjell 2-hr oxic (pH 7.69)	2.61	0.16	0.23	0.33	1.30	0.58	2.64	0.56	4.18
Sverrefjell 2-hr oxic (pH 8.34)	2.60	0.11	0.00	0.14	1.34	0.49	3.55	0.55	4.89
Sverrefjell 2-hr oxic (pH 10.3)	9.33	0.11	-	-	0.68	0.50	0.96	0.63	1.64
Sverrefjell 1 week anoxic (pH=5.97)	10.80	0.71	1.13	1.01	0.27	1.00	0.55	0.82	1.95
Sverrefjell 2 week anoxic (pH=5.91)	13.87	0.13	0.00	0.66	1.10	0.91	0.96	0.82	2.06
Sverrefjell 3 weeks anoxic (pH=5.98)	15.19	0.32	0.00	0.71	3.78	0.93	0.00	0.94	3.78
Sverrefjell 3 weeks oxic (pH 6.28)	15.71	1.16	0.00	1.20	0.73	0.35	3.46	0.63	4.19
diabase2-hr oxic (pH 4.5)	1.96	0.05	0.02	0.10	0.13	0.10	0.38	0.10	0.53
diabase2-hr oxic (pH 5.6)	1.77	0.03	-	-	0.64	0.47	1.55	0.49	2.20
diabase 2-hr oxic (pH 7)	3.01	0.05	0.26	0.21	0.62	0.24	0.73	0.21	1.61
diabase 70 cm 2-hr oxic (pH 5.1)	3.54	2.07	0.00	2.07	0.17	0.07	0.98	0.18	1.15
Shale Hills 2-hr oxic (pH 4)	1.98	0.64	0.00	0.64	0.37	0.29	0.08	0.29	0.45
Shale Hills 2-hr oxic (pH 5)	0.89	0.04	0.02	0.06	0.15	0.05	0.14	0.05	0.31
Shale Hills 2-hr oxic (pH 7)	1.52	0.17	0.01	0.18	0.43	0.08	1.30	0.13	1.75

1) mmol element/kg soil

Appendix B: Summary of Sverrefjell DNA and microbial work

Introduction:

The archipelago of Svalbard, which lies north of the Arctic Circle, is a Mars analog field site chosen due to its cold, dry climate and the presence of carbonate globules within basaltic rocks similar to those found in Martian meteorites (Treiman et al., 2002). As part of AMASE (Arctic Mars Analogue Svalbard Expedition), we studied olivine- and glass-containing basaltic rocks from the Sverrefjell volcano of Svalbard to determine weathering characteristics. To gain insight into olivine and glass weathering on Mars, 1-year burial experiments were conducted in which olivine and glass were subjected to the cold, dry climate of Svalbard.

Further studies are now underway to characterize microbial communities present at Sverrefjell, which will aid in understanding potential biological contributions to weathering and trace element cycling in this arctic ecosystem; we are further interested in any biosignatures at the Sverrefjell volcano that may be relevant to Mars. To explore the microbial ecosystem at Sverrefjell, fractured rock samples and cinder (in which the burial experiments took place) were analyzed for a wide variety of different microbiological parameters. Moreover, metagenomic analysis was performed upon selected samples from five locations to gain an understanding of the types of organisms present as well as community diversity.

Methods

Site characteristics and sampling

The Sverrejell volcano is one of three quaternary eruptive centers in Northwest Spitsbergen on the Svalbard archipelago composed of primitive alkali basalt flows, pyroclastics, and intrusives (Skjelkvale et al, 1989). The precipitation is estimated at <200 mm/year, with an average temperature of -5°C (Hausrath, 2007). Fractured rock samples were collected aseptically for use in DNA extraction and culturing studies for characterization of microbial communities (marked A, B, and C on Figure B-1). For the burial studies, pieces of forsterite and manufactured glass were buried at 30-cm depths at four locations representing different weathering conditions: 1) a dry streambed subject to seasonal snow melt (BR1), 2) a flat, vegetated marine terrace

(BR2), 3) a vegetated basaltic cinder of Sverrefjell volcano (BR3), and 4) an unvegetated volcanic cinder at the summit of Sverrefjell (BR4; numbers 1-4 on Fig. B-1). Material for microbiological analysis from the burial sites was collected aseptically at 30-cm depths.

DNA extractions and metagenomics analysis

Metagenomic analysis was performed on fractured rock samples from sites A (14 cm), B (15 cm) and C (20 cm), as well as on cinder from burial sites 2 and 3 (Figure B-1). DNA was extracted by Laura Liermann (as described in Liermann et al., in review) from ~10 g samples from each depth by the method of Zhou et al. (1996). Aliquots of each extraction were run on a 0.8% (w/v) agarose gel in Tris-acetate-EDTA buffer to check for successful DNA yields. The DNA was stored in 10 mM Tris-HCl, pH 8.0 at -20° C. DNA samples selected for use in metagenomics analysis were further purified using the PowerClean® DNA Clean-Up kit (MoBio Laboratories). DNA successfully extracted and purified from five samples was submitted to the Genomics Core Facility (The Pennsylvania State University) for amplicon library construction and sequence analysis (see Liermann et al. for further details).

Cell enumeration

To minimize sample handling and the potential for contamination, approximately 1 g of sample from each depth was thoroughly suspended in 9 ml of phosphate-buffered saline (PBS), and this suspension was used for direct cell counting by acridine orange staining, heterotrophic plate counts on R2A agar, and iron-related bacterial activity reaction tests (IRB-BART; LaMotte Co.). Direct cell counts were carried out by Laura Liermann on formalin-preserved cell suspensions, which could be prepared and then stained at a later time. To prepare the formalin suspensions, 2.7 ml of sample suspension in PBS was added to 0.3 ml of 37% formalin in a sterile tube (final formalin concentration 3.7%). For acridine orange staining, 100 µl of formalin-preserved cell suspension was added to 1 ml of sodium dithionite (0.1 g) in 0.2 M sodium citrate/0.35 M sodium acetate buffer to dissolve Fe oxide particulates. The cell suspension/dithionite solution was then vacuum filtered onto a Whatman Nucleopore 0.2-µm black filter, and stained with a 0.01% solution of acridine orange for 1 minute. After removal of excess stain by vacuum-filtration, the filter was placed on a borosilicate glass slide with a cover

slip, and viewed under oil immersion on a Nikon Eclipse 80I light microscope using a blue FITC light cube and a counting grid. For heterotrophic plate counts, serial dilutions were made starting from 100 µl of the sample suspension in PBS, and dilutions were plated onto R2A agar plates (Liermann et al., in review). R2A is a medium designed for growth of difficult-to-culture heterotrophic organisms. The plates were incubated at 30° C for 3 days and the colonies counted.

IRB-BART

The iron-related bacterial activity reactions tests (IRB-BART) were performed by Laura Liermann to detect the presence of iron-related bacteria, which include both iron-reducing and iron-oxidizing bacteria. These tests could also indicate the presence of anaerobic bacteria, pseudomonads and enteric bacteria, as well as heterotrophic bacteria. To set up the tests, 13 ml of sterile phosphate-buffered saline (PBS) was added to each IRB-BART tube, and 2 ml of sample suspension in PBS was added to the tube. The samples were incubated in the dark and checked every 1-2 days for 9 days.

Results

Cell enumeration

Cells were present at all locations sampled, with total cell numbers ranging from 10^8 – 10^9 cells/g dry soil mass (Figure B-2). However, culturable heterotrophic cell numbers were much lower, generally in the 10^4–10^6 cells/g range, with only ~100 cells/g at burial site 1 (stream bed BR1; Fig. B-3). At fractured rock site A, both total and heterotrophic cell counts decreased with increasing depth from the surface, but at sites B and C, cell numbers were similar at all depths sampled (Figures B-2 and B-3). Although all four burial site samples (BR1–BR4) were obtained from a 30-cm depth, site BR2 had approximately one order of magnitude more cells than the other three sites (Figure B-2); this is likely due to the vegetated nature of the BR2 site. Although site BR1 had only ~100 culturable heterotrophic cells/g, sites BR2, BR3, and BR4 had ~1–2 x 10^4 culturable heterotrophs/g (Figure B-3). Several types of colony morphologies (raised and shiny, flat and dull, wrinkled, spreading) and colors (translucent white, cream, brown, yellow, pink) were present on the R2A plates.

IRB-BART

Results from iron-related bacterial activity reaction tests (IRB-BART) indicated the likely presence of iron-related bacteria at sites A, B, and C at $\geq$ 10 cm depth, and at burial site 2 (BR2; Table B-1).

Soil moisture and pH

The pH of the pore waters was estimated by adding 2.5 mL of deionized water to 1 gram of soil and then measuring the pH of the slurry (Hausrath, 2007). Pore-water chemistry of the samples was determined as explained in Table 2. The soil pH in water ranged from 6.5 to 8.5 (Figure B-4), while the gravimetric soil moisture ranged from 0.04 to 0.4 (Figure B-5). There is no apparent correlation between soil moisture or pH and cell numbers, heterotrophs, anaerobes, or iron-related bacteria. Furthermore, soil moisture and pH do not appear to change in a consistent way with depth (Supplemental Figures B-4 and B-5). As expected, heterotrophic and total cell counts were correlated for the 12 fractured rock and cinder samples analyzed (R^2=0.58, p=0.002). Total cell count was most highly correlated with the gravimetric soil moisture (R^2=0.58, p=0.002), while soil pH, pore-water acetate, nitrate and phosphorus did not show significant relationships with the total cell count (p>0.05 in all cases). These findings suggest that soil moisture is a major predictor of total cell count in a cold, dry climate such as Sverrefjell.

Rarefaction curves are used to determine how well a system under study has been sampled and sequenced (Liermann et al., in review); the rarefaction curve indicates the number of operational taxonomic units (OTU) identified as a function of the number of sequences analyzed. If the rarefaction curve flattens as the sample number increases, a reasonable number of samples have been studied. Here, rarefaction curves generated for samples with a distance value of 0.03 (97% similarity) indicated that the regolith was more adequately sampled for sites C, 2 and 3 than for sites A and B in terms of estimating species richness (Figure B-7).

The predominant phyla present at the five sequenced sites included Proteobacteria, Bacteroidetes, Actinobacteria and Acidobacteria (Table B-4), groups that tend to be common in soil samples from around the world (Liermann et al. and references within). Site C was unique in that it contained a high abundance of Bacteroidetes (47%) relative to the other four sites. Both the very high nitrate concentration (195 uM; Table B-2) and the higher pH value of this site (8.2)

may be responsible for these differences. α-Proteobacteria made of 40-60% of the Proteobacteria at all five sites (Table B-5). β-Proteobacteria was the second most common group, making up 20-40% of the total; β-Proteobacteria were more common at Site C (40% of the total) than at the other four sites. Sites A (14 cm) and B (15 cm) had the lowest Berger-Parker and Simpson indices (Table B-6), indicative of higher diversity in these two sites. In contrast, the 30-cm cinder sample from Site 3 had higher indices, indicating lower diversity.

Figures:

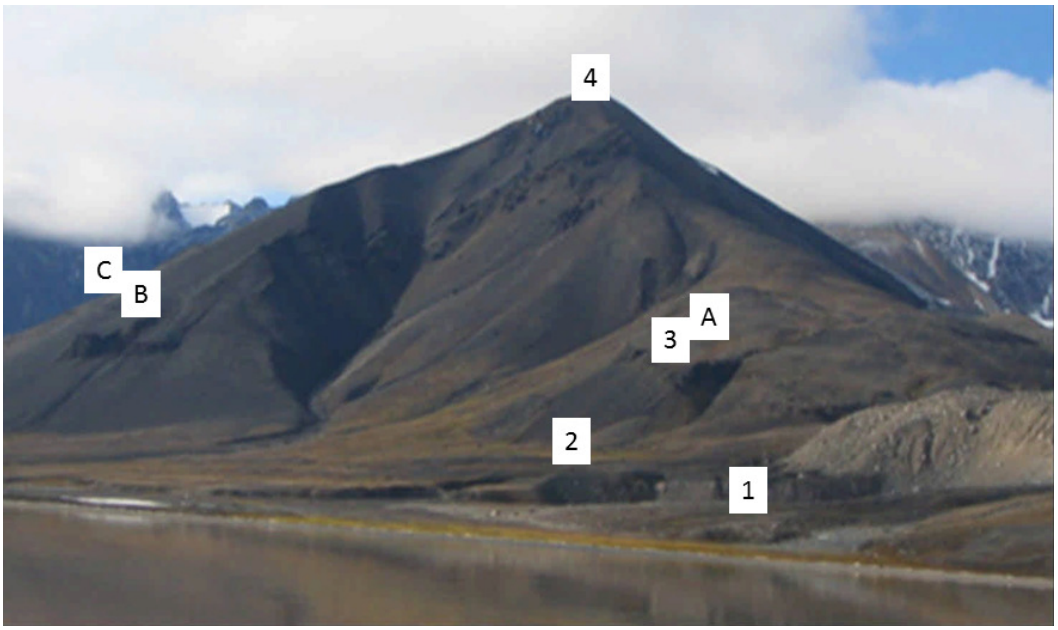

Figure B-1. The locations of fractured rock samples (A, B and C) and burial ash sites (BR1-BR4).

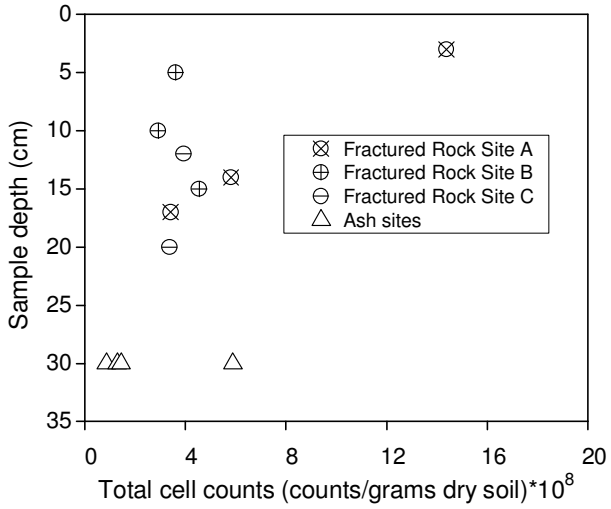

Figure B-2. Total cell count/gram of dry soil with depth for fractured rock and ash samples. Cell counts were made using an acridine orange stain.

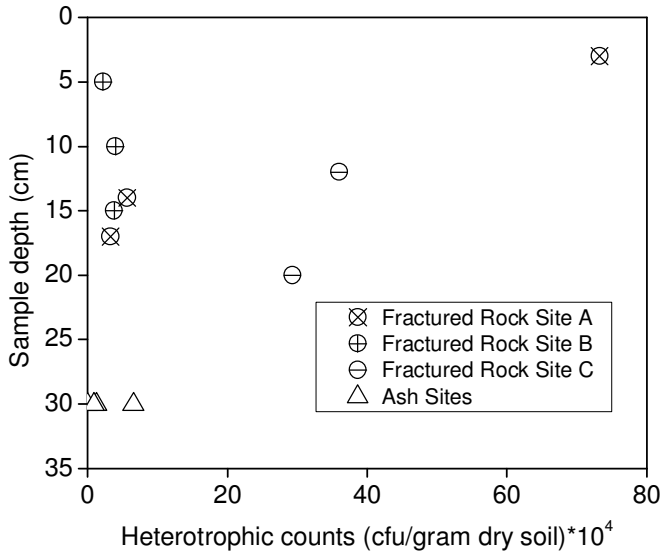

Figure B-3. Heterotrophic counts made on R2A agar plates with depth for fractured rock and ash samples.

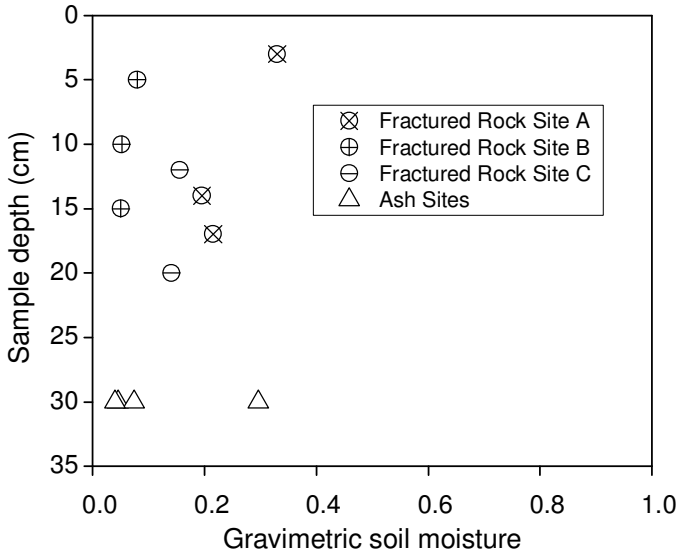

Figure B-4. Gravimetric soil moisture with depth for fractured rock and ash samples.

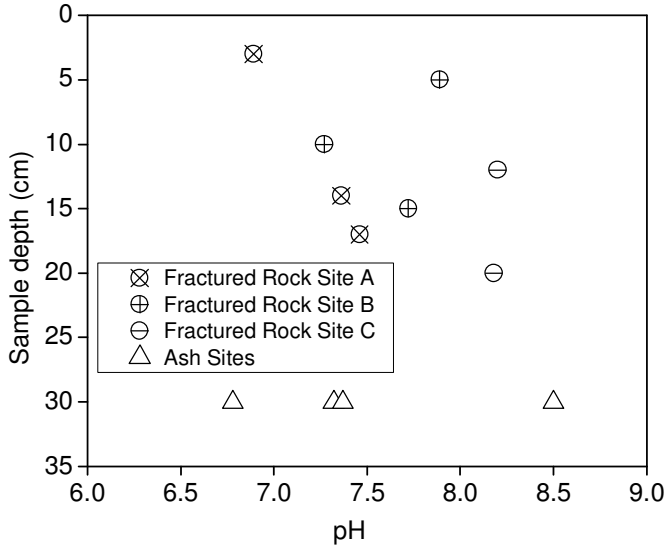

Figure B-5. pH with depth for fractured rock and ash samples.

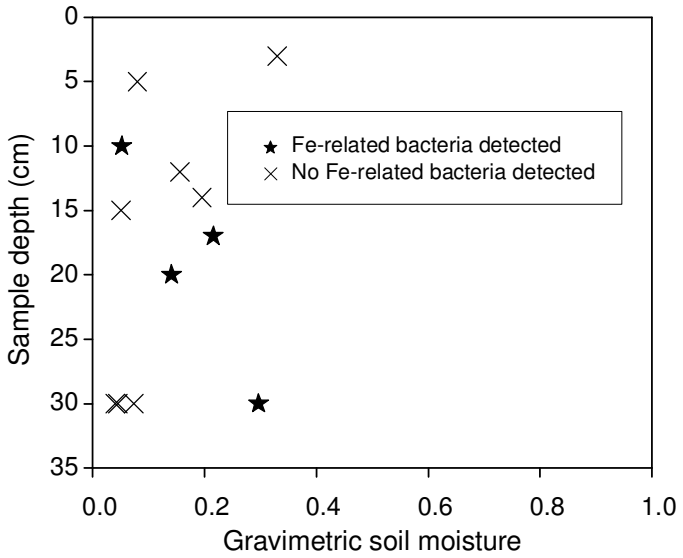

Figure B-6. The presence of Fe-related bacteria in fractured rock and ash samples. Stars indicate locations from which Fe-related bacteria were found using the BART™ test. No Fe-related bacteria were observed for the other sites.

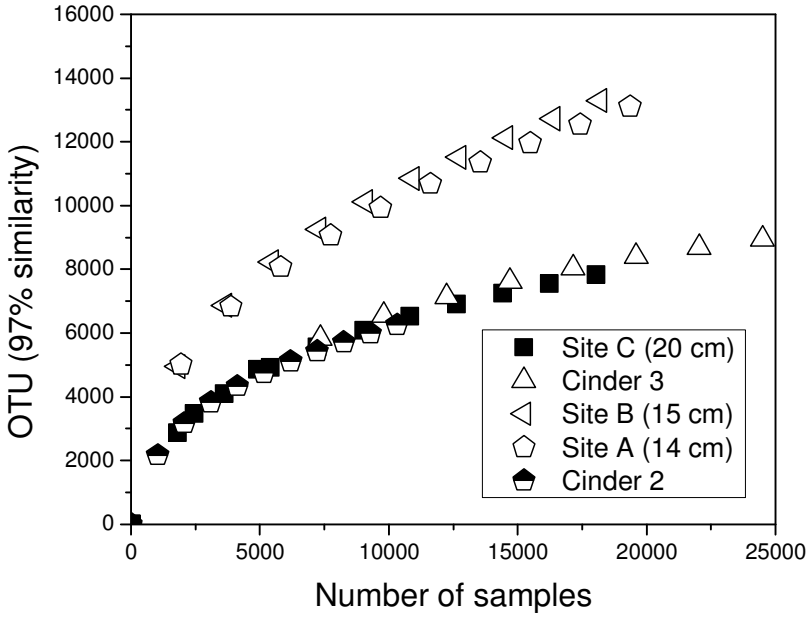

Figure B-7. Operational taxonomic units (OTU) versus number of sequences at 97% similarity for the five samples analyzed at the Sverrefjell volcano.

Tables:

Table B-1: Sample characteristics

	Elevation (m)	Gravimetric soil moisture[1]	pH[2]	Heterotrophic cell count[3]	Total cell count[4]	Iron-related bacteria	Heterotrophs	Anaerobes
Site A, 3 cm	162	0.330	6.9	73.3	14.4	-	++	+
Site A, 14 cm	**162**	**0.195**	**7.4**	**5.7**	**5.8**	**NA**	**NA**	**NA**
Site A, 17 cm	162	0.215	7.5	3.3	3.4	++	++	++
Site B, 5 cm	NA	0.080	7.9	2.2	3.6	-	+	-
Site B, 10 cm	NA	0.052	7.3	4.0	2.9	++	++	++
Site B, 15 cm	**NA**	**0.050**	**7.7**	**3.8**	**4.6**	**-**	**+**	**-**
Site C, 12 cm	175	0.156	8.2	36.0	3.9	NA	NA	NA
Site C, 20 cm	**175**	**0.141**	**8.2**	**29.3**	**3.4**	**+**	**++**	**++**
Site 1	21	0.045	8.5	0.0	0.9	-	+	+
Site 2	**34**	**0.297**	**7.3**	**1.3**	**5.9**	**++**	**++**	**++**
Site 3	**168**	**0.074**	**7.4**	**6.6**	**1.3**	**-**	**++**	**-**
Site 4	506	0.040	6.8	0.9	1.5	-	+	-

1) Field samples were weighed, oven dried at 60°C until dry, and then reweighed

2) The pH of the pore water was estimated by adding 2.5 mL of deionized water to 1 gram of soil and then measuring pH of the slurry

3) Heterotrophic count in colony forming units/gram dry soil $*10^4$

4) Total cell count in counts/gram dry soil $*10^8$

Table B-2: Pore-water chemistry[1]

	Al (μM)[2]	Fe (μM)[2]	P (μM)[2]	Si (μM)[2]	Acetate (μM)[3]	Nitrate (μM)[3]
Site A, 3 cm	10	5.2	3.6	350	54	2.9
Site A, 14 cm	**15**	**5.5**	**1.5**	**435**	**33**	**50**
Site A, 17 cm	18	7.1	1.4	694	19	33
Site B, 5 cm	17	5.4	2.6	217	47	18
Site B, 10 cm	24	7.9	2.0	182	20	10
Site B, 15 cm	**11**	**3.6**	**1.7**	**184**	**2.0**	**11**
Site C, 12 cm	43	7.6	2.6	171	4.7	42
Site C, 20 cm	**33**	**4.9**	**3.9**	**246**	**34**	**195**
Site 1	5	1.7	1.3	116	2	22
Site 2	**24**	**10.3**	**1.4**	**338**	**37**	**6.7**
Site 3	**11**	**3.9**	**0.9**	**149**	**34**	**4.4**
Site 4	2	1.2	0.8	130	60	4.1

1) Pore waters for cation and anion analysis were extracted by adding 5 mL MilliQ deionized water to 15 g of wet sample. The slurry was then centrifuged at 4,500 rpm for 35 minutes at 5°C and syringe filtered (0.22 μm) into a sterile container

2) Cations measured with ICP-MS using a Finnigan Element 1

3) Measured by ion chromatography using a Dionex 100

Table B-3: Correlations between different parameters in fractured rock and cinder samples[1]

	R^2	p value
pore-water Al and Fe	0.43	0.013
total and heterotrophic cell counts	0.58	0.002
total cell count and gravimetric soil moisture	0.58	0.002
total cell count and pore-water pH	0.16	0.194
total cell count and pore-water acetate	0.03	0.272
total cell count and pore-water nitrate	-0.09	0.734
total cell count and pore-water phosphorus	0.24	0.060

1) All values from Table 1, chemistry from Hausrath (2007)

Table B-4: Percent of all sequence reads classified within major phyla

	burial site 2	burial site 3	Site A (14 cm)	Site C (20 cm)	Site B (15 cm)
Proteobacteria	22.60	29.14	30.25	23.26	22.70
Bacteroidetes	20.24	2.81	4.27	47.44	7.02
Actinobacteria	12.37	19.97	15.74	7.75	13.31
Acidobacteria	11.27	11.76	18.64	6.80	24.26
Firmicutes	0.21	0.19	0.16	0.24	0.25
TM7	0.58	0.07	0.24	0.10	0.67
Chloroflexi	0.08	0.19	0.55	0.22	0.24
Verrucomicrobia	0.36	0.52	0.42	0.15	2.41
Planctomycetes	0.53	0.58	2.09	0.56	1.23
Cyanobacteria	0.03	0.08	0.13	0.13	0.01
WS3	0.01	0.07	0.20	0.00	0.01
Nitrospira	2.18	0.66	1.06	0.18	0.22
Gemmatimonadetes	8.74	2.81	1.64	0.70	0.98
Unclassified Bacteria	20.80	31.15	24.60	12.50	26.70

Table B-5: Distibution of Proteobacteria

	burial site 2	burial site 3	Site A (14 cm)	Site C (20 cm)	Site B (15 cm)
alpha	40.01	65.57	60.80	49.09	49.25
beta	29.40	18.24	23.82	41.54	24.32
gamma	23.37	9.56	7.00	4.72	18.59
delta	1.24	1.94	2.35	0.77	1.39
unclassified	5.98	4.69	6.02	3.89	6.44

Table B-6: Berger-Parker and Simpson index summary values for depths sequenced from Svalbard, calculated at 97% sequence similarity

	Berger-Parker dominance index	Simpson index
Site 2, 30 cm	0.022	0.002
Site 3, 30 cm	0.070	0.016
Site A, 14 cm	0.014	0.001
Site B, 15 cm	0.015	0.001
Site C, 20 cm	0.039	0.009

References:

Hausrath, E.M., 2007, Basalt Weathering on Earth and Mars. Ph.D. Thesis. College of Earth and Mineral Sciences. The Pennsylvania State University.

Liermann, L.J., Brantley, S.L., Istvan Albert, I., Heather L. Buss, H.L., and Minyard, M., in prep. Relating microbial community structure and geochemistry in deep regolith developed on volcaninclastic rock in the Luquillo Mountains, Puerto, Rico.

Skelkvale, B.L., Amundsen, H.E.F., O'Reilly, S.Y., Griffin, W.L., and Gjelsvik, T., 1989. A primitive alkali basaltic stratovolcano and associated eruptive centres, Nothwestern Sptisbergen: Volcanology and tectonic significance. Journal of Volcanology and Geothermal Research. 37: 1-19.

Treiman A.H., Amundsen H.E.F., Blake D.F., and Bunch T., 2002, Hydrothermal origin for carbonate globules in Martian meteorite ALH84001: a terrestrial analogue from Spitsbergen (Norway). Earth and Planetary Science Letters. 204: 323-332.

Appendix C: Supplementary material for Chapter 2

Table C-1: Standard addition data for a spike of 1000 ppm Fe(II)[1]

Volume added (mL) as ferrous ammonium sulfate	% FeO measured in standards	% FeO measured in sample	% FeO: theoretical[2]
0.0		1.47	0.00
5.0		2.45	1.07
10.0	2.34		2.14
20.0		5.45	4.29
30.0	6.29	7.36	6.43

(1) Standard additions involved adding known amounts of a ferrous ammonium sulfate standard to a sample

(2) Assuming no interference

Table C-2: Fe(II) concentrations of stream sediment sample stored in different ways[1]

drying method	Fe in wt. %
freeze dried	1.48
freeze dried	1.98
freeze dried	1.53
oven dried at 40°C	1.16
oven dried at 40°C	1.55
air dried	1.55

(1) Using method of Goldich (1984)

Table C-3: Fe/Cr ratios of post-column samples[1]

post-column sample:	ratio of Fe:Cr
SPRT (0-10 cm)	18600
SPRT (0-10 cm) duplicate	116000
SPRT (10-20 cm)	31600
SPMS2 (45-47 cm)	15100
SPVF(TS1) (89-92 cm)	142000
SPMS (50-59 cm)	111000
SPMS (0-10 cm)	193000
SPRT (20-30 cm)	114000

(1) Measured on a Thermo Scientific XSERIES 2 ICP-MS
at the Penn State Material Characterization Laboratory

Table C-4: Elution profiles of a ~500 ppm Fe/Cr mixture[1]

total volume eluted (mL	mass Cr eluted (µg)	mass Fe eluted (µg)
10.1	<0.01	174.21
15.9	<0.01	35.26
21.4	<0.01	1.65
25.6	<0.01	<0.01
31.4	<0.01	<0.01
34.6	<0.01	<0.01
36.8	0.19	<0.01
39.0	130.97	<0.01
40.7	56.60	<0.01
44.8	36.50	<0.01

(1) 0.5 N HCl added at ~35 mL to elute Fe

Table C-5: Comparison of Zr concentrations measured with ICP-AES and ICP-MS[1]

Sample identity:	ICP-AES	ICP-MS
SPVF (TS1) (24-30 cm)	263	289
SPVF (TS1) (57-64 cm)	197	200
SPVF(TS1) (78-87 cm)	207	214
SPVF(TS1) (51-57 cm)	197	195
SPVF(TS1) (64-72 cm)	209	208

1) Using a Perkin-Elmer ICP-AES 5300DV and a Thermo Scientific XSERIES 2

ICP-MS from the Penn State Materials Characterization Laboratory

Table C-6: Chemistry data

		Elemental concentration[1]								$\tau_{Zr,x}$						
	mid-depth (cm)	Al (%)	Fe (%)	Fe(II) (%)	K (%)	Mg (%)	Si (%)	Ti (%)	Zr (ppm)	$\tau_{Zr,Al}$	$\tau_{Zr,Fe}$	$\tau_{Zr,Fe(II)}$	$\tau_{Zr,K}$	$\tau_{Zr,Mg}$	$\tau_{Zr,Si}$	$\tau_{Zr,Ti}$
ridgetop:																
SPRT2 (0-5 cm)	2.5	8.11	4.23	-	2.63	0.58	22.15	0.50	163	-0.18	-0.16	-	-0.24	-0.33	-0.10	-0.15
SPRT2 (5-10 cm)	7.5	9.94	4.87	0.8	3.31	0.72	27.56	0.60	194	-0.15	-0.19	-0.39	-0.19	-0.30	-0.05	
SPRT2 (10-15 cm)	12.5	10.24	4.90	0.4	3.39	0.73	27.92	0.62	192	-0.12	-0.18	-0.68	-0.17	-0.29	-0.03	-0.10
SPRT2 (15-20 cm)	17.5	9.93	4.79	0.7	3.27	0.72	28.14	0.62	196	-0.16	-0.21	-0.49	-0.21	-0.32	-0.04	-0.12
SPRT2 (20-25 cm)	22.5	10.13	5.14	0.9	3.61	0.78	27.51	0.58	183	-0.08	-0.09	-0.25	-0.07	-0.20	0.00	-0.11
middle slope:																
SPMS2 (0-10 cm)	5	8.68	4.29	0.6	2.77	0.57	27.35	0.62	220	-0.35	-0.37	-0.62	-0.40	-0.51	-0.17	-0.22
SPMS2 (10-20 cm)	15	8.87	4.44	0.9	2.89	0.64	29.64	0.65	249	-0.41	-0.42	-0.49	-0.45	-0.52	-0.21	-0.27
SPMS2 (20-30 cm)	25	9.31	4.40	1.0	3.14	0.73	29.71	0.63	233	-0.34	-0.39	-0.35	-0.36	-0.42	-0.15	-0.25
SPMS2 (30-36 cm)	33	9.83	5.15	0.8	3.41	0.80	28.75	0.60	208	-0.22	-0.20	-0.44	-0.22	-0.28	-0.08	-0.20
SPMS2 (36-45 cm)	41	9.19	4.80	1.2	3.20	0.77	29.40	0.61	212	-0.28	-0.27	-0.20	-0.29	-0.32	-0.08	-0.20
SPMS2 (45-47 cm)	46	9.82	5.04	1.3	3.42	0.84	28.67	0.59	200	-0.19	-0.19	-0.08	-0.19	-0.22	-0.05	-0.18
SPMS2 (lowermost)	47	9.06	4.71	1.6	3.10	0.75	28.39	0.61	217	-0.31	-0.30	0.06	-0.32	-0.35	-0.13	-0.22
footslope:																
SPVF(FS1) (0-10 cm)[2]	5	5.28	2.50	0.6	1.64	0.36	31.88	0.70	349	-0.75	-0.77	-0.75	-0.78	-0.81	-0.39	-0.44
SPVF(FS1) (10-20 cm)[2]	15	6.88	3.31	0.8	2.24	0.52	31.83	0.68	318	-0.64	-0.66	-0.64	-0.67	-0.69	-0.33	-0.41
SPVF(FS1) (20-30 cm)[2]	25	8.63	4.08	0.9	2.80	0.72	30.20	0.65	258	-0.45	-0.49	-0.50	-0.49	-0.48	-0.22	-0.30
SPVF(FS1) (30-40 cm)[2]	35	9.05	4.45	1.2	3.05	0.78	28.33	0.62	219	-0.32	-0.34	-0.21	-0.34	-0.33	-0.14	-0.21
SPVF(FS1) (40-50 cm)[2]	45	9.74	4.79	1.2	3.22	0.85	28.70	0.64	208	-0.22	-0.25	-0.17	-0.27	-0.23	-0.08	-0.14
SPVF(FS1) (50-60 cm)[2]	55	10.21	5.04	1.3	3.35	0.89	27.67	0.61	182	-0.07	-0.10	0.06	-0.13	-0.08	0.01	-0.07
SPVF(FS1) (60-67 cm)[2]	64	10.32	5.22	1.3	3.50	0.92	26.93	0.61	191	-0.11	-0.12	-0.02	-0.13	-0.10	-0.06	-0.11
toeslope:																
SPVF(TS1) (0-6 cm)	3	7.91	4.11	-	2.09	0.58	19.52	0.50	193	-0.32	-0.31	-	-0.49	-0.44	-0.18	-0.28
SPVF(TS1) (6-12 cm)	9	8.80	4.87	0.5	2.32	0.64	21.60	0.54	217	-0.33	-0.27	-0.67	-0.49	-0.45	-0.19	-0.30
SPVF(TS1) (12-18 cm)	15	9.09	5.05	0.6	2.51	0.64	22.61	0.59	238	-0.37	-0.31	-0.63	-0.50	-0.50	-0.23	-0.31
SPVF(TS1) (18-24 cm)	21	8.59	4.41	1.1	2.57	0.60	24.14	0.63	256	-0.44	-0.44	-0.39	-0.52	-0.56	-0.24	-0.31
SPVF(TS1) (24-30 cm)	27	8.21	5.04	0.5	2.62	0.58	24.61	0.66	263	-0.48	-0.38	-0.72	-0.53	-0.59	-0.25	-0.31
SPVF(TS1) (30-36 cm)	33	8.16	5.85	0.6	2.64	0.57	24.47	0.65	285	-0.53	-0.33	-0.69	-0.56	-0.62	-0.31	-0.37
SPVF(TS1) (51-57 cm)	54	10.20	5.19	0.7	3.50	0.73	22.94	0.56	197	-0.14	-0.15	-0.45	-0.16	-0.31	-0.06	-0.21
SPVF(TS1) (57-64 cm)	61	10.49	4.37	0.9	3.60	0.69	23.35	0.57	197	-0.12	-0.28	-0.37	-0.14	-0.34	-0.04	-0.19
SPVF(TS1) (64-72 cm)	68	9.52	7.76	0.8	3.40	0.70	21.16	0.57	209	-0.25	0.20	-0.43	-0.23	-0.37	-0.18	-0.25
SPVF(TS1) (72-78 cm)	75	10.05	5.41	0.8	3.56	0.72	22.81	0.59	189	-0.12	-0.07	-0.38	-0.11	-0.29	-0.02	-0.13
SPVF(TS1) (78-87 cm)	83	10.00	4.99	0.9	3.61	0.77	23.42	0.58	207	-0.20	-0.22	-0.39	-0.17	-0.31	-0.08	-0.22
SPVF(TS1) (87-89 cm)	88	9.61	4.55	0.8	3.43	0.70	23.25	0.59	232	-0.31	-0.37	-0.49	-0.30	-0.44	-0.19	-0.29
SPVF(TS1) (89-92 cm)	91	10.07	5.80	0.9	3.61	0.75	24.44	0.62	242	-0.31	-0.22	-0.45	-0.29	-0.42	-0.18	-0.28
SPVF(TS1) (lowermost)	92	9.24	4.91	1.0	3.23	0.73	23.99	0.61	253	-0.40	-0.37	-0.42	-0.40	-0.46	-0.23	-0.33
stream:	-	7.50	4.46	-	2.37	0.60	24.88	0.53	220	0.56	0.66	-	0.51	0.51	0.75	-0.33
north drill core:																
average drill core[3]	-	10.75	5.50	1.2	3.76	0.95	26.70	0.64	178	-	-	-	-	-	-	
DC1-8 (1.1-1.2 m depth)[2]	115	11.33	5.44	1.2	3.98	0.92	26.83	0.67	179	-	-	-	-	-	-	
DC1-26 (6.1-6.3 m depth)[2]	620	11.06	5.97	1.1	3.93	1.05	27.25	0.67	172	-	-	-	-	-	-	

(1) As weight percent, measured with ICP-AES

(2) Elemental concentration data from Jin et al. (2010)

(3) Average for samples between 0.30 and 20 m from Jin et al. (2010), excluding 4.3-4.5 m

Table C-7: Concentration of filtered and unfiltered stream-water samples[1]

Date	Sample type and location	Sample preparation	Al (µM)[2]	Ca (µM)	Fe (µM)[3]	K (µM)	Mg (µM)	Na (µM)	P (µM)	Si (µM)	Ti (µM)
4/17/2010	Stream mouth[4]	unfiltered	6.75	-	2.13	-	-	-	-	-	-
4/17/2010	Stream mouth[4]	filtered[6]	0.76	-	0.60	-	-	-	-	-	-
4/18/2010	Stream mouth[4]	unfiltered	11.82	-	3.51	-	-	-	-	-	-
4/18/2010	Stream mouth[4]	filtered[6]	1.45	-	0.62	-	-	-	-	-	-
5/14/2010	Stream mouth[4]	unfiltered	3.64	-	1.38	-	-	-	-	-	-
5/14/2010	Stream mouth[4]	filtered[6]	0.81	-	0.55	-	-	-	-	-	-
6/10/2010	Stream mouth[4]	unfiltered	3.06	246.9	2.35	-	-	-	-	-	-
6/10/2010	Stream mouth[4]	filtered[6]	0.52	241.5	0.70	-	-	-	-	-	-
7/10/2010	Stream mouth[4]	unfiltered	4.55	-	3.55	-	-	-	-	-	-
7/10/2010	Stream mouth[4]	filtered[6]	0.68	-	1.14	-	-	-	-	-	-
7/14/2010	Stream mouth[4]	unfiltered	7.75	-	6.12	-	-	-	-	-	-
7/14/2010	Stream mouth[4]	filtered[6]	1.62	-	2.87	-	-	-	-	-	-
6/10/2010	middle stream[4]	unfiltered	9.16	69.2	3.40	-	-	-	-	-	-
6/10/2010	middle stream[4]	filtered[6]	0.33	60.9	0.15	-	-	-	-	-	-
6/10/2010	lysimeter (SSVF 80 cm)[4]	unfiltered	0.78	17.4	0.02	-	-	-	-	-	-
6/10/2010	lysimeter (SSVF 80 cm)[4]	filtered[6]	0.79	16.8	0.01	-	-	-	-	-	-
6/10/2010	lysimeter (SPVF 40 cm)[4]	unfiltered	1.29	68.8	0.04	-	-	-	-	-	-
6/10/2010	lysimeter (SPVF 40 cm)[4]	filtered[6]	1.31	66.1	0.03	-	-	-	-	-	-
7/1/2010	lysimeter (NSVF 220 cm)[4]	unfiltered	1.10	17.5	<DL	-	-	-	-	-	-
7/1/2010	lysimeter (NSVF 220 cm)[4]	filtered[6]	1.07	17.8	0.01	-	-	-	-	-	-
7/1/2010	lysimeter (NSVF 260 cm)[4]	unfiltered	0.93	34.9	0.02	-	-	-	-	-	-
7/1/2010	lysimeter (NSVF 260 cm)[4]	filtered[6]	0.95	34.9	0.01	-	-	-	-	-	-
summer 2010	groundwater well 1[4]	unfiltered	41.14	-	6.22	-	-	-	-	-	-
summer 2010	groundwater well 1[4]	filtered[6]	34.46	-	3.63	-	-	-	-	-	-
summer 2010	groundwater well 2[4]	unfiltered	2.45	-	0.80	-	-	-	-	-	-
summer 2010	groundwater well 2[4]	filtered[6]	1.17	-	0.28	-	-	-	-	-	-
summer 2010	groundwater well 3[4]	unfiltered	3.91	-	3.55	-	-	-	-	-	-
summer 2010	groundwater well 3[4]	filtered[6]	1.54	-	1.84	-	-	-	-	-	-
spring 2011	macropore April[5]	unfiltered	1.60	51.8	0.46	28.0	70.8	19.9	3.0	97.0	0.04
spring 2011	macropore April[5]	filtered[6]	0.25	50.0	0.16	26.4	68.4	19.2	2.2	92.0	0.02
spring 2011	stream head[5]	unfiltered	3.62	49.6	1.08	28.0	68.9	16.1	2.3	93.1	0.08
spring 2011	stream head[5]	filtered[6]	0.02	49.1	0.16	27.4	68.1	16.1	2.4	87.1	0.02
spring 2011	above macropore[5]	unfiltered	3.32	53.0	0.90	27.5	70.4	18.6	2.3	96.5	0.06
spring 2011	above macropore[5]	filtered[6]	0.50	51.5	0.26	26.5	68.3	18.2	3.0	90.2	0.02
spring 2011	macropore[5]	unfiltered	3.39	53.1	0.97	28.1	71.5	19.2	2.5	97.8	0.06
spring 2011	macropore[5]	filtered[6]	0.57	50.6	0.31	26.1	67.2	17.9	1.3	89.4	0.03
spring 2011	mid-stream[5]	unfiltered	5.46	53.4	1.39	27.4	72.0	20.0	2.7	101.0	0.10
spring 2011	mid-stream[5]	filtered[6]	0.65	52.4	0.38	25.9	70.0	19.4	2.7	92.1	0.02
spring 2011	stream mouth[5]	unfiltered	12.70	112.1	3.61	27.6	75.5	21.3	2.6	119.7	0.21
spring 2011	stream mouth[5]	filtered[6]	1.06	107.2	0.83	24.4	71.2	20.1	1.2	92.1	0.03
	Det. Limit for ICP-AES		0.2	0.1	0.1	0.1	0.2	0.2	0.3	0.2	0.1

(1) All locations shown in Figure 1

(2) Estimated method detection limit of 0.03 µM for ICP-MS

(3) Estimated method detection limit of 0.01 µM for ICP-MS

(4) Measured with a Thermo Scientific XSERIES 2 ICP-MS

(5) Measured with a Perkin-Elmer ICP-AES 5300DV

Table C-8: Total C and N concentrations (wt. %)[1]

Sample	mid-depth	% Total nitrogen	% Total carbon
ridgetop:			
SPRT1 (0-10 cm)[2]	5	0.17	1.76
SPRT1 (10-20 cm)[2]	15	0.11	0.79
SPRT1 (20-30 cm)[2]	25	0.08	0.37
middle slope:			
SPMS1 (0-10 cm)[2]	5	0.12	1.07
SPMS1 (10-20 cm)[2]	15	0.09	0.63
SPMS1 (20-30 cm)[2]	25	0.07	0.34
SPMS1 (30-40 cm)[2]	35	0.07	0.41
SPMS1 (40-50 cm)[2]	45	0.07	0.22
SPMS1 (50-59 cm)[2]	55	0.06	0.11
footslope:			
SPVF(FS1) (0-10 cm)[2]	5	0.21	2.94
SPVF(FS1) (10-20 cm)[2]	15	0.09	0.68
SPVF(FS1) (20-30 cm)[2]	25	0.09	0.45
SPVF(FS1) (30-40 cm)[2]	35	0.09	0.51
SPVF(FS1)(40-50 cm)[2]	45	0.08	0.24
SPVF(FS1) (50-60 cm)[2]	55	0.08	0.23
SPVF(FS1) (60-67 cm)[2]	64	0.08	0.26
drill core:			
DC1-17 (3.4-3.5 m)[3]	345	0.06	0.05
DC1-20 (4.3-4.5 m)[3]	440	0.05	0.05
DC1-29 (10.7-10.9 m)[3]	1080	0.07	0.03
DC1-32 (15.2-15.4 m)[3]	1530	0.07	0.04

(1) Typical error with the Elementar vario MAX Macro analyzer is ± 5% at concentrations specified above

(2) Samples from Jin et al. (2010)

(3) North drill core samples from Jin et al. (2010) from depth range as indicated

Table C-9: Observations from redox gradient and soils moisture measurements

	Mid-depth	Redox gradient test results	BART™ test ranking #[1]	Heterotrophic count/gram dry soil * 10^7	Cell count/gram dry soil * 10^9	Gravimetric soil moisture (g/g)[2]
ridge top (May 2009):						
SPRT2 (0-5 cm)	2.5	light brown throughout	1	1.7	0.99	0.16
SPRT2 (5-10 cm)	7.5	yellow with brown tinges	2	0.6	1.15	0.14
SPRT2 (10-15 cm)	12.5	yellow with slight brown	4	0.9	0.26	0.09
SPRT2 (15-20 cm)	17.5	yellow with slight brown	3	2.1	0.52	0.07
SPRT2 (20-25 cm)	22.5	yellow with slight brown	4	2.0	0.50	0.13
middle slope (May 2009):						
SPMS2 (0-10 cm)	5	yellow with brown tinge	2	4.0	0.49	0.13
SPMS2 (10-20 cm)	15	yellow	5	0.4	0.19	0.10
SPMS2 (20-30 cm)	25	yellow	5	1.8	0.37	0.09
SPMS2 (30-36 cm)	33	yellow with slight brown	3	0.1	0.11	0.07
SPMS2 (36-45 cm)	40.5	yellow	5	0.6	0.16	0.09
SPMS2 (45-47 cm)	46	yellow with slight brown	4	1.0	0.19	0.11
SPMS2 (lowermost)	47	yellow with brown tinge	1	0.9	0.53	0.12
footslope (July 2008):						
SPVF(FS2) (0-6 cm)	3	dark brown, cloudy	1			0.24
SPVF(FS2) (6-14 cm)	10		-			0.26
SPVF(FS2) (14-22 cm)	18		-			0.18
SPVF(FS2) (22-28 cm)	25	light brown	4			0.18
SPVF(FS2) (28-36 cm)	32		-			0.18
SPVF(FS2) (36-41 cm)	38.5		-			0.16
SPVF(FS2) (41-53 cm)	47	light brown	4			0.13
SPVF(FS2) (53-59 cm)	56		-			0.13
SPVF(FS2) (59-62 cm)	60.5		-			0.12
SPVF(FS2) (62-66 cm)	64	ligth brown, cloudy	2			0.12

(1) BART™ test rankings for Fe-oxidizing bacteria from 1=highest reactivity to 9=lowest reactivity

(2) Gravimetric soil moisture in units of g water/g dry soil

Table C-9: Observations from redox gradient and soils moisture measurements, continued

	Mid-depth	Redox gradient test results	BART™ test ranking #[1]	Heterotrophic count/gram dry soil * 10^7	Cell count/gram dry soil * 10^9	Gravimetric soil moisture (g/g)[2]
footslope (October 2009):						
SPVF(FS3) (0 to 3 cm)	1.5			0.4	0.8	0.13
SPVF(FS3) (3 to 15 cm)	9.0			1.2	1.3	0.16
SPVF(FS3) (15 to 26 cm)	20.5			0.5	0.7	0.10
SPVF(FS3) (26 to 35 cm)	30.5			2.5	0.6	0.07
SPVF(FS3) (35 to 44 cm)	39.5			0.2	0.4	0.07
SPVF(FS3) (44 to 50 cm)	47.0			0.4	0.3	0.07
SPVF(FS3) (50 to 62 cm)	56.0			0.6	0.3	0.10
SPVF(FS3) (62 to 71 cm)	66.5			0.1	0.2	0.08
toeslope (May 2009):						
SPVF(TS1) (0-6 cm)	3	pale brown throughout	3	1.4	2.4	0.72
SPVF(TS1) (6-12 cm)	9	dark gray/black	1	0.4	0.8	0.49
SPVF(TS1) (12-18 cm)	15	pale brown	4	0.0	0.5	0.35
SPVF(TS1) (18-24 cm)	21	yellow with slight brown	6	0.2	0.1	0.29
SPVF(TS1) (24-30 cm)	27	yellow with slight brown	6	0.1	0.3	0.27
SPVF(TS1) (30-36 cm)	33	yellow with slight brown	7	0.1	0.2	0.28
SPVF(TS1) (51-57 cm)	54	yellow with slight brown	8	0.0	0.0	0.19
SPVF(TS1) (57-64 cm)	60.5	yellow with slight brown	7	0.0	0.1	0.29
SPVF(TS1) (64-72 cm)	68	yellow with slight brown	8	0.0	0.1	0.19
SPVF(TS1) (72-78 cm)	75	yellow	9	0.0	0.1	0.21
SPVF(TS1) (78-87 cm)	82.5	yellow with brown tinge	6	0.1	0.1	0.10
SPVF(TS1) (87-89 cm)	88	yellow with brown tinge	5	0.0	0.2	0.14
SPVF(TS1) (89-92 cm)	90.5	yellow with slight brown	8	0.0	0.0	0.12
SPVF(TS1) (lowermost)	92	light brown	2	1.5	0.0	0.20
toeslope (October 2009):						
SPVF(TS2) (0 to 3 cm)	1.5				1.9	0.53
SPVF(TS2) (3 to 13 cm)	8.0				0.8	0.39
SPVF(TS2) (13 to 22 cm)	17.5				0.6	0.18
SPVF(TS2) (22 to 34 cm)	28.0				0.4	0.25
SPVF(TS2) (34 to 44 cm)	39.0				0.3	0.08
SPVF(TS2) (44 to 54 cm)	49.0				0.4	0.18
SPVF(TS2) (54 to 66 cm)	60.0				0.1	0.42
SPVF(TS2) (66 to 78 cm)	72.0				0.0	0.15
SPVF(TS2) (78 to 81 cm)	79.5				0.1	0.08

(1) BART™ test rankings for Fe-oxidizing bacteria from 1=highest reactivity to 9=lowest reactivity

(2) Gravimetric soil moisture in units of g water/g dry soil

Table C-10: Concentration of Fe and Al extracted into solution during 0.5 N HCl extraction[1]

Sample:	% Fe of total Fe[2]	extracted Fe mass/soil mass (%)	% Al of total Al[2]	extracted Al mass/soil mass (%)
DC1-8 (1.1-1.2 m)	5.7	0.31	2.8	0.31
DC1-26 (6.1-6.3 m)	8.8	0.52	4.6	0.50
stream	13.8	0.61	2.9	0.21
SPRT2 (0-5 cm)	6.5	0.28	5.0	0.41
SPRT2 (0-5 cm) duplicate	6.7	0.29	5.8	0.47
SPRT2 (5-10 cm)	6.8	0.33	3.4	0.33
SPRT2 (15-20 cm)	8.0	0.38	3.1	0.31
SPRT2 (15-20 cm) duplicate	7.5	0.36	3.0	0.30
SPMS2 (10-20 cm)	5.5	0.25	3.0	0.26
SPMS2 (36-45 cm)	3.7	0.18	2.7	0.25
SPMS2 (45-47 cm)	3.6	0.18	2.3	0.22
SPVF(FS1) (10-20 cm)	10.9	0.36	5.6	0.38
SPVF(FS1) (40-50 cm)	7.6	0.36	3.8	0.37
SPVF(FS1) (60-67 cm)	7.0	0.36	3.8	0.39
SPVF(TS1) (0-6 cm)	13.3	0.55	4.1	0.33
SPVE(TS1) (30-36 cm)	4.2	0.24	2.6	0.21
SPVF(TS1) (51-57 cm)	3.9	0.20	2.0	0.20
SPVF(TS1) (64-72 cm)	3.1	0.36	2.1	0.34
SPVF(TS1)(78-72 cm)	7.2	0.24	3.4	0.20
SPVF(TS1) (89-92 cm)	3.3	0.19	2.0	0.20

(1) Measured on a Perkin-Elmer ICP-AES 5300DV

(2) Mass of each element extracted with 0.5 N HCl/total mass of element * 100

Table C-11: Mass balance calculations

	Constant soil production rate, P				Varying soil production rate, P[1]			
	Ridgetop	Middle slope	Footslope	Toeslope	Ridgetop	Middle slope	Footslope	Toeslope
P ($g*m^{-2}yr^{-1}$)	36	36	36	36	122	64	38	19
W ($g*m^{-2}yr^{-1}$)	1.8	13.1	12.9	-1.5	6.0	32.2	19.0	-14.0
E ($g*m^{-2}yr^{-1}$)	34.2	22.9	23.1	37.5	115.5	31.7	18.5	32.7
W_{Fe} ($g*m^{-2}yr^{-1}$)	0.32	1.00	1.17	-0.80	1.09	2.30	-0.13	-2.42
$W_{Fe(II)}$ ($g*m^{-2}yr^{-1}$)	0.18	0.16	-0.24	0.75	0.59	0.27	-0.68	1.27

(1) Soil production rate is assumed to vary as a function of depth of soil column according to regression from Ma et al. (2010)

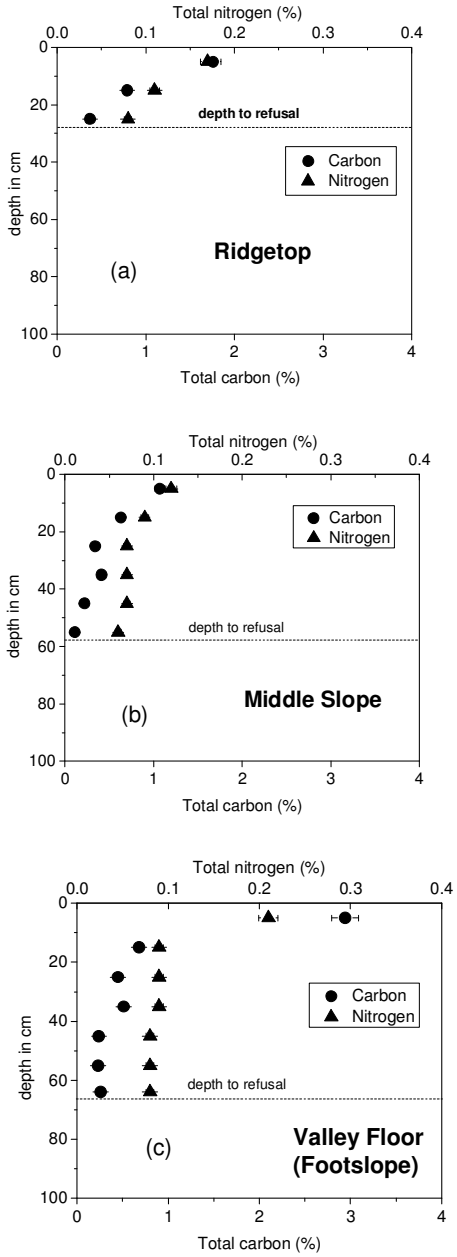

Figure C-1. Total carbon and nitrogen concentrations along the south planar transect at the ridge top (a), middle slope (b) and valley floor footslope (c). Horizontal lines indicate depth to refusal. Total carbon and nitrogen (wt. %) were measured with an Elementar vario MAX Macro Nitrogen Analyzer at the Agricultural Analytical Service Lab of Penn State University. Error was estimated equal to $\pm$ 5% at the concentration levels reported here.

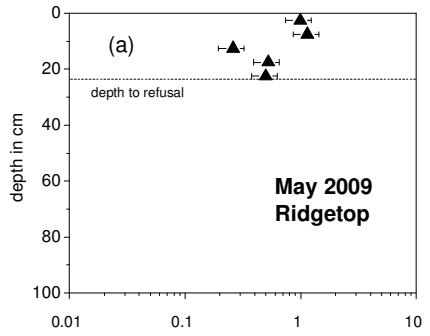
(a)
depth to refusal
May 2009
Ridgetop
depth in cm
0
20
40
60
80
100
0.01
0.1
1
10

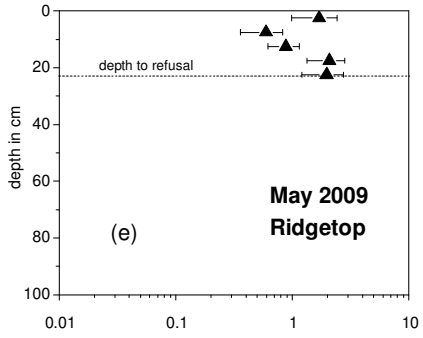
depth to refusal
May 2009
Ridgetop
(e)
depth in cm
0
20
40
60
80
100
0.01
0.1
1
10

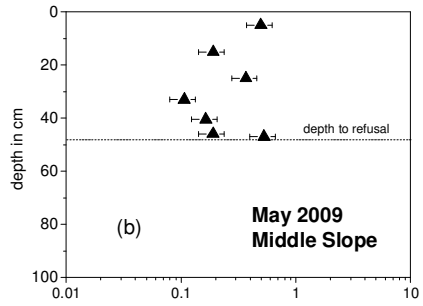
depth to refusal
(b)
May 2009
Middle Slope
depth in cm
0
20
40
60
80
100
0.01
0.1
1
10

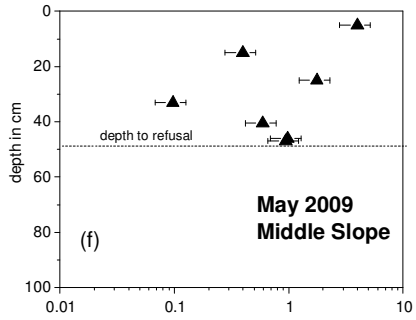
depth to refusal
May 2009
Middle Slope
(f)
depth in cm
0
20
40
60
80
100
0.01
0.1
1
10

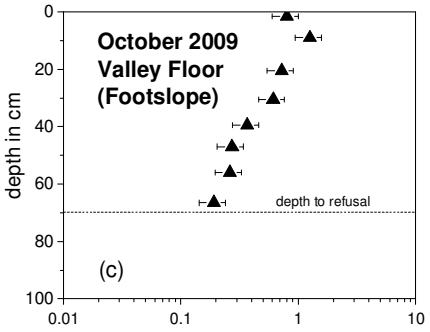
October 2009
Valley Floor
(Footslope)
depth to refusal
(c)
depth in cm
0
20
40
60
80
100
0.01
0.1
1
10

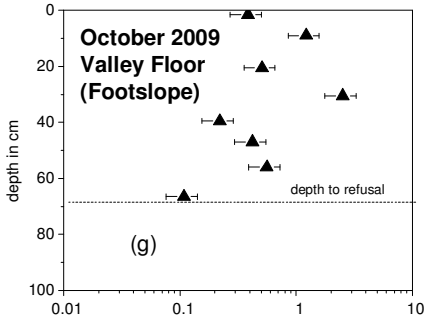
October 2009
Valley Floor
(Footslope)
depth to refusal
(g)
depth in cm
0
20
40
60
80
100
0.01
0.1
1
10

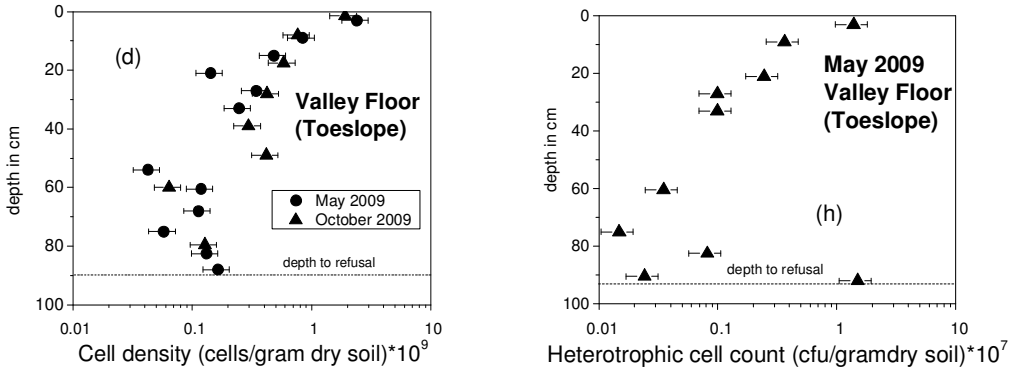

Figure C-2. To the left: Cell density in cells/gram of dry soil plotted versus depth at the ridge top (a), middle slope (b), valley floor footslope (c) and valley floor toeslope (d). Horizontal lines indicate depth to refusal. To the right: Heterotrophic cell counts/gram of dry soil plated on R2A agar at the ridge top (a), middle slope (b), valley floor footslope (c) and valley floor toeslope (d). Horizontal lines indicate depth to refusal.

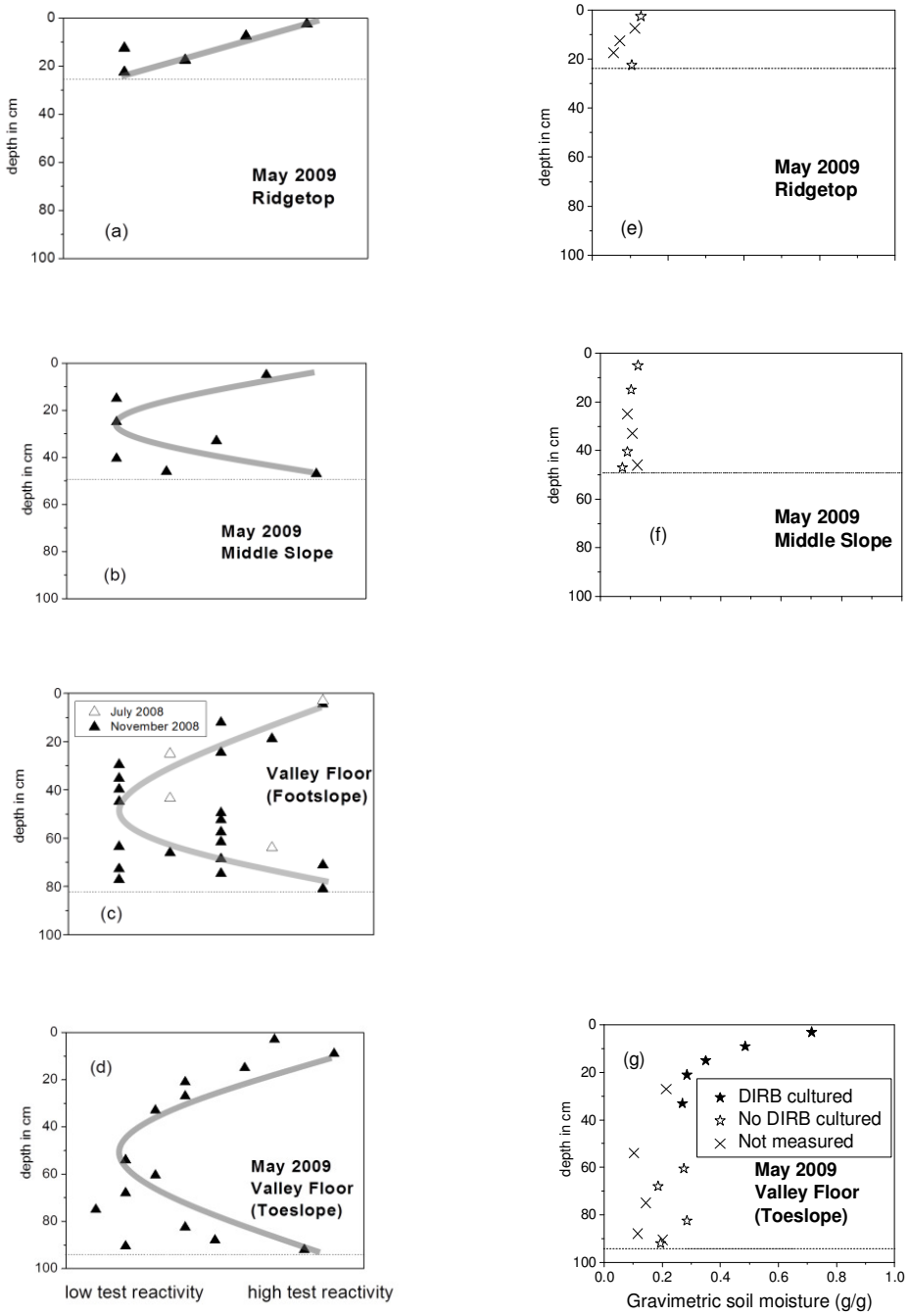

Figure C-3. Left column of panels: Observations from redox gradient (BART™) tests for iron-related bacteria along the south planar transect at the ridge top (a), middle slope (b), valley floor footslope (c) and valley floor toeslope (d). The extent of reactivity is ranked on a scale from 1 as the highest to 9 as the lowest relative to a control buffer. Right column of panels: growth of DIRBs plotted versus gravimetric soil moisture content measured along the catena at the ridge top (e), middle slope (f) and valley floor toeslope (g). Horizontal lines indicate depth to refusal.

Description of Steady State Model:

Assuming that the soils are at steady state, the following equation can be written following the methodology of Jin et al. (2010):

$$D = P = W + E \tag{C-1}$$

Here, D is the denudation rate (in units of $gm^{-2}yr^{-1}$), P is the soil production rate, W is the weathering rate and E is the erosion rate. It is assumed that the soil propagation rate for the Shale Hills watershed is ~15 m/My Jin et al. (2010).

Explanation of Ridge top Equations:

At the ridgetop, it is assumed that sediment input does not occur, that the mass of biota have largely been maintained at steady state over the exposure age of the regolith and that loss occurs only through chemical and physical weathering. For the case of an immobile element like Zr, the sole mechanism for loss involves physical weathering whereas a mobile element like Fe may be lost from ridge tops through a combination of physical and chemical weathering. Assuming steady state conditions, the mass flux of Zr, which does not experience chemical weathering, can be expressed as:

$$P^{ridgetop} * C_{Zr}^{parent} = E^{ridgetop} * C_{Zr}^{ridgetop} \tag{C-2}$$

The mass flux for a mobile chemical element like Fe can be expressed as:

$$P^{ridgetop} * C_{Fe}^{parent} = E^{ridgetop} * C_{Fe}^{ridgetop} + W_{Fe} \tag{C-3}$$

Substituting E=P-W into the right-hand side of Equation (2) then gives:

$$P^{ridgetop} * C_{Zr}^{parent} = (P^{ridgetop} - W^{ridgetop}) * C_{Zr}^{ridgetop} \tag{C-4}$$

Rearranging (4) to solve for W (the weathering flux at the ridge top) gives:

$$W^{ridgetop} = P^{ridgetop} - \left(P^{ridgetop} * \left(\frac{C_{Zr}^{parent}}{C_{Zr}^{ridgetop}} \right) \right) = P^{ridgetop} * \left(1 - \left(\frac{C_{Zr}^{parent}}{C_{Zr}^{ridgetop}} \right) \right) \quad \text{(C-5)}$$

In an analogous way, the weathering flux for Fe at the ridge top can be calculated by substituting E=P-W into Equation (3) to get:

$$W_{Fe}^{ridgetop} = P^{ridgetop} * \left(C_{Fe}^{parent} - \left(\frac{C_{Zr}^{parent}}{C_{Zr}^{ridgetop}} \right) * C_{Fe}^{ridgetop} \right) \quad \text{(C-6)}$$

As discussed in Jin et al. (2010), analogous mass balance equations can also be written for the middle slope by incorporating a term that includes an influx into the profile resulting from erosion at the ridge top. The following equation results for the chemical weathering flux at the middle slope:

$$W_{Fe}^{middle} = P^{middle} * C_{Fe}^{parent} \left(1 - \left(\frac{C_{Fe}^{middle} * C_{Zr}^{parent}}{C_{Fe}^{parent} * C_{Zr}^{middle}} \right) \right) + E^{ridge} * C_{Fe}^{ridge} \left(1 - \left(\frac{C_{Fe}^{middles} * C_{Zr}^{ridge}}{C_{Fe}^{ridge} * C_{Zr}^{middle}} \right) \right)$$

Analogous equations can also be written for the footslope and toeslope, where the erosion is taken to be equal to the total amount of erosion derived from all upslope sites. Two assumptions were used in the calculations regarding the bedrock propagation rate. The first assumption involved assuming a constant rate along the entire transect of 15 m/My, while the second approach involved varying the bedrock propagation rate according to estimates from Ma et al. (2010).

Appendix D: Supplementary Material for Chapter 3

Table D-1: Cation and anion exchange capacity of 38-47 cm sample[1]

pH	Anion exchange capacity (cmole/kg soil)	Cation exchange capacity (cmole/kg soil)
3.0	2.8	4.1
4.1	1.3	7.4
6.4	1.4	16.8
8.5	1.0	22.3
8.0	1.0	-
10.1	1.2	-
11.4	1.0	-
11.7	1.0	48.9

1) Based upon the method of Zelazny et al. (1996)

Table D-2: SEM-EDS data on rim of rock thin sections from the regolith core at 38-47 cm (in atomic percent)

	Al	Ca	Fe	K	Mg	Na	Si	Ti
rock 1, inner	8.16 ± 1.42	4.23 ± 1.24	2.31 ± 1.15	0.86 ± 0.39	2.36 ± 1.19	3.56 ± 0.96	16.09 ± 0.96	0.68 ± 0.36
rock 1, outer 100 µm	10.64 ± 2.70	2.43 ± 1.71	2.62 ± 0.63	0.65 ± 0.37	1.77 ± 1.09	1.47 ± 1.60	14.56 ± 1.87	0.55 ± 0.29
rock 2 inner	6.31 ± 3.14	2.32 ± 1.49	2.81 ± 0.40	0.70 ± 0.46	7.51 ± 9.54	2.89 ± 2.30	16.96 ± 2.32	0.46 ± 0.24
rock 2, outer 100 µm	10.13 ± 2.86	1.13 ± 1.53	2.34 ± 1.49	0.35 ± 0.31	0.75 ± 1.50	0.61 ± 1.88	20.25 ± 6.11	0.38 ± 0.30
rock 2, coating[1]	8.63 ± 2.50	0.35 ± 0.5	1.06 ± 0.8	0.21 ± 0.01	0.17 ± 0.29	0.0 ± 0.0	25.73 ± 3.52	0.11 ± 0.19

1) Coating appears to be ~50 µm in thickness

Table D-3a: Chemistry of loose regolith core[1]

not sieved											
depth	Al	Ca	Fe	K	Mg	Mn	Na	P	Si	Ti	Zr (ppm)
0-20 cm	7.46	5.87	7.33	1.53	6.29	0.11	2.88	0.37	20.26	1.36	221
20-38 cm	7.27	5.39	7.14	1.38	6.33	0.12	2.59	0.34	19.72	1.28	216
38-47 cm	7.38	5.83	7.29	1.54	6.43	0.11	3.02	0.37	20.64	1.35	214
47-56 cm	7.41	5.89	7.32	1.60	6.33	0.11	3.18	0.37	20.52	1.35	215
56-63 cm	7.51	5.73	7.20	1.57	6.01	0.11	3.04	0.36	20.49	1.33	221
70.5-74 cm	7.38	6.03	7.29	1.68	6.35	0.11	3.36	0.37	21.00	1.35	218
sieved											
depth											Zr (ppm)
0-20 cm	7.48	5.61	7.27	1.40	6.25	0.12	2.65	0.36	19.81	1.34	229
20-38 cm	7.76	5.39	7.47	1.33	6.49	0.12	2.37	0.35	20.49	1.34	238
38-47 cm	6.83	5.16	6.69	1.30	5.76	0.11	2.48	0.33	18.30	1.23	206
47-56 cm	7.43	5.77	7.29	1.58	6.47	0.11	3.08	0.36	20.66	1.33	213
56-63 cm	7.48	5.57	7.14	1.54	6.07	0.11	2.91	0.36	20.28	1.31	218
63-70.5 cm	7.57	5.64	7.27	1.58	6.01	0.11	2.94	0.36	20.81	1.34	227
70.5-74 cm	7.28	5.73	7.04	1.60	6.12	0.11	3.12	0.35	20.44	1.30	221

(1) Measured with Perkin-Elmer ICP-AES 5300DV

Table D-3b: $\tau_{Ti,X}$ for regolith core[1]

depth	$\tau_{Ti,Al}$	$\tau_{Ti,Ca}$	$\tau_{Ti,Fe}$	$\tau_{Ti,K}$	$\tau_{Ti,Mg}$	$\tau_{Ti,Mn}$	$\tau_{Ti,Na}$	$\tau_{Ti,P}$	$\tau_{Ti,Si}$	$\tau_{Ti,Zr}$
unsieved										
0-20 cm	0.00	-0.03	0.00	-0.10	-0.02	0.00	-0.15	-0.01	-0.04	0.00
20-38 cm	0.04	-0.06	0.03	-0.14	0.05	0.10	-0.19	-0.02	-0.01	0.04
38-47 cm	0.00	-0.03	0.00	-0.08	0.01	0.04	-0.10	0.00	-0.02	-0.02
47-56 cm	0.00	-0.02	0.00	-0.05	0.00	0.03	-0.05	0.00	-0.02	-0.01
56-63 cm	0.03	-0.04	0.00	-0.05	-0.04	0.02	-0.08	-0.01	-0.01	0.03
70.5-74 cm	0.00	0.00	0.00	0.00	0.00	0.00	0.00	0.00	0.00	0.00
sieved										
0-20 cm	0.00	-0.05	0.00	-0.15	-0.01	0.00	-0.18	-0.02	-0.06	0.00
20-38 cm	0.03	-0.09	0.03	-0.19	0.03	0.01	-0.26	-0.05	-0.03	0.00
38-47 cm	-0.01	-0.05	0.00	-0.14	-0.01	0.03	-0.16	-0.02	-0.05	0.00
47-56 cm	0.00	-0.02	0.01	-0.03	0.03	0.00	-0.04	0.00	-0.01	0.00
56-63 cm	0.02	-0.04	0.00	-0.05	-0.02	0.01	-0.07	0.00	-0.02	0.00
63-70.5 cm	0.01	-0.04	0.00	-0.04	-0.05	-0.04	-0.08	0.00	-0.01	0.00
70.5-74 cm	0.00	0.00	0.00	0.00	0.00	0.00	0.00	0.00	0.00	0.00

1) From Equation 1 in text. Lowermost sample taken to be parent.

Table D-4a: Chemical composition of clay-sized fraction (<2 μm)[1,2]

mid-depth	Al (wt.%)	Ca (wt. %)	Fe (wt. %)	K (wt. %)	Mg (wt. %)	Mn (wt. %)	Na (wt. %)	P (wt. %)	Si (wt. %)	Ti (wt. %)	Zr (ppm)
10	10.9	0.8	7.5	0.2	0.3	0.2	0.1	0.5	9.2	1.2	191
29	10.5	1.1	7.6	0.2	0.4	0.2	0.1	0.5	9.6	1.3	200
42.5	11.0	1.0	7.6	0.2	0.4	0.2	0.1	0.5	10.2	1.2	179
59.5	10.4	1.4	7.5	0.4	0.7	0.2	0.3	0.5	11.6	1.3	158
66.8	10.5	1.5	7.8	0.4	0.9	0.2	0.2	0.4	12.0	1.2	211
72.25	10.5	1.4	8.0	0.4	0.7	0.2	0.3	0.5	11.9	1.2	176
rock fragment[3]	7.2	6.3	7.3	1.4	6.4	0.1	3.0	0.4	19.9	1.3	204
unsieved regolith[3]	7.4	5.8	7.3	1.5	6.4	0.1	3.0	0.4	20.6	1.3	214

1) Separated with wet sieving method of Jackson (1956)

2) Measured with Perkin-Elmer ICP-AES 5300DV

3) Taken from a depth of 38-47 cm

Table D-4b: $\tau_{Ti,X}$ values of clay-sized fraction (<2 μm)[1]

mid-depth	$\tau_{Ti,Al}$	$\tau_{Ti,Ca}$	$\tau_{Ti,Fe}$	$\tau_{Ti,K}$	$\tau_{Ti,Mg}$	$\tau_{Ti,Mn}$	$\tau_{Ti,Na}$	$\tau_{Ti,P}$	$\tau_{Ti,Si}$	$\tau_{Ti,Zr}$
10	0.04	-0.39	-0.06	-0.57	-0.55	-0.11	-0.70	0.11	-0.22	0.08
29	-0.03	-0.25	-0.08	-0.49	-0.36	-0.14	-0.56	0.04	-0.22	0.10
42.5	0.06	-0.25	-0.03	-0.40	-0.35	-0.03	-0.52	0.09	-0.13	0.04
59.5	-0.05	-0.02	-0.09	-0.04	0.00	-0.02	0.03	-0.01	-0.06	-0.13
66.8	-0.01	0.05	-0.02	-0.07	0.29	0.04	-0.09	-0.05	0.01	0.20
72.25	0.00	0.00	0.00	0.00	0.00	0.00	0.00	0.00	0.00	0.00

1) From Equation 1 in text with lowermost clay-sized fraction as parent

Table D-5: percent of each element present in different size fractions during colloidal dispersion experiments

pH=4							
	Al	Fe	Ti	Si	Mg	Ca	Na
260-415 nm	54.1	59.6	60.5	32.2	1.9	1.1	0.9
35-260 nm	11.5	11.9	11.4	2.0	0.0	0.0	0.0
2-35 nm	6.2	5.5	6.3	4.4	0.0	0.0	0.0
< 2 nm	28.2	23.0	21.8	61.3	98.1	98.9	99.1
pH=5							
	Al	Fe	Ti	Si	Mg	Ca	Na
260-415 nm	52.5	49.4	42.8	21.9	0.0	0.0	0.0
35-260 nm	40.1	41.8	35.6	17.8	0.0	0.2	0.2
2-35 nm	7.4	8.3	7.6	0.7	0.0	1.2	3.9
< 2 nm	0.0	0.6	13.9	59.6	100.0	98.6	95.9
pH=6							
	Al	Fe	Ti	Si	Mg	Ca	Na
260-415 nm	67.4	70.4	68.7	38.6	0.8	1.5	0.1
35-260 nm	30.3	26.2	24.7	13.6	1.1	0.0	0.8
2-35 nm	2.3	3.4	6.2	0.0	0.0	0.0	0.0
< 2 nm	0.0	0.0	0.3	47.8	98.1	98.5	99.1
pH=7							
	Al	Fe	Ti	Si	Mg	Ca	Na
260-415 nm	57.3	62.1	60.0	38.9	3.7	1.7	0.0
35-260 nm	26.7	31.8	32.0	19.2	4.3	3.1	1.9
2-35 nm	15.1	6.0	8.0	3.4	0.0	0.0	4.0
< 2 nm	0.8	0.0	0.0	38.5	91.9	95.1	94.2
pH=8							
	Al	Fe	Ti	Si	Mg	Ca	Na
260-415 nm	58.5	69.4	66.8	47.4	12.0	11.6	2.6
35-260 nm	22.6	29.6	29.2	17.9	5.2	2.9	0.0
2-35 nm	16.7	1.0	4.0	0.0	0.0	0.0	0.0
< 2 nm	2.3	0.0	0.0	34.7	82.8	85.5	97.4
average from pH 5 to pH 8							
	Al	Fe	Ti	Si	Mg	Ca	Na
260-415 nm	59.5	63.1	59.5	36.0	4.3	4.4	0.9
35-260 nm	29.9	32.4	30.4	17.1	2.7	1.6	0.7
2-35 nm	10.4	4.7	6.4	1.0	0.0	0.3	2.0
< 2 nm	0.8	0.1	3.6	45.1	93.2	94.5	96.7
pH=10							
	Al	Fe	Ti	Si	Mg	Ca	Na
260-415 nm	96.7	25.3	18.5	85.1	63.1	76.7	96.7
35-260 nm	0.1	26.4	30.5	6.2	7.1	1.6	3.3
2-35 nm	3.2	48.3	51.0	8.7	29.8	21.7	0.0

Table D-6: Chemistry of dissolved elements from colloidal dispersion experiments[1]

Ca (mmol/kg soil):	< 3 kDa	error
2-hr oxic (pH 4.08)	26.04	0.21
2-hr oxic (pH 5.13)	20.59	0.68
2-hr oxic (pH 6.18)	14.51	0.63
2-hr oxic (pH 6.78)	10.27	0.54
2-hr oxic (pH 7.69)	6.47	0.41
2-hr oxic (pH 8.34)	2.75	0.30
2-hr oxic (pH 10.3)	0.43	0.06
1 week anoxic (pH=5.97)	18.17	1.04
2 week anoxic (pH=5.91)	18.26	1.09
3 weeks anoxic (pH=5.98)	20.81	1.31
3 weeks oxic (pH 6.28)	15.95	0.81
Na (mmol/kg soil):	< 3 kDa	error
2-hr oxic (pH 4.08)	4.2	0.1
2-hr oxic (pH 5.13)	4.5	0.1
2-hr oxic (pH 6.18)	4.4	0.1
2-hr oxic (pH 6.78)	4.3	0.2
2-hr oxic (pH 7.69)	4.5	0.4
2-hr oxic (pH 8.34)	4.6	0.2
2-hr oxic (pH 10.3)	4.1	0.0
1 week anoxic (pH=5.97)	5.2	0.4
2 week anoxic (pH=5.91)	4.9	0.1
3 weeks anoxic (pH=5.98)	5.2	0.4
3 weeks oxic (pH 6.28)	-	-
Mg (mmol/kg soil):		
2-hr oxic (pH 4.08)	6.1	0.0
2-hr oxic (pH 5.13)	5.7	0.3
2-hr oxic (pH 6.18)	4.7	0.3
2-hr oxic (pH 6.78)	3.8	0.2
2-hr oxic (pH 7.69)	2.4	0.1
2-hr oxic (pH 8.34)	1.0	0.1
2-hr oxic (pH 10.3)	0.1	0.0
1 week anoxic (pH=5.97)	6.0	0.4
2 week anoxic (pH=5.91)	6.1	0.4
3 weeks anoxic (pH=5.98)	7.4	0.5
3 weeks oxic (pH 6.28)	6.3	0.3
K (mmol/kg soil):	< 3 kDa	error
2-hr oxic (pH 4.08)	949	17.8
2-hr oxic (pH 5.13)	928	8.5
2-hr oxic (pH 6.18)	953	25.0
2-hr oxic (pH 6.78)	970	6.5
2-hr oxic (pH 7.69)	950	27.5
2-hr oxic (pH 8.34)	961	14.9
2-hr oxic (pH 10.3)	1035	38.9
1 week anoxic (pH=5.97)	942	11.3
2 week anoxic (pH=5.91)	962	17.4
3 weeks anoxic (pH=5.98)	1004	40.6
3 weeks oxic (pH 6.28)	1053	5.8

1) mmol element/kg soil

Table D-7: Chemistry from colloidal dispersion experiments[1]

Al (mmole/kg soil):	<3 kDa	error	<3 kDa-35 nm	error	35-260 nm	error	260-415 nm	error	sum	sum colloids
2-hr oxic (pH 4.08)	2.95	0.06	0.65	0.22	1.20	0.38	5.67	0.37	10.48	7.53
2-hr oxic (pH 5.13)	0.00	0.00	0.39	0.25	2.14	0.35	2.80	0.77	5.33	5.33
2-hr oxic (pH 6.18)	0.00	0.00	0.14	0.12	1.84	0.34	4.10	0.42	6.08	6.08
2-hr oxic (pH 6.78)	0.00	0.01	0.14	0.03	1.75	0.87	2.67	0.87	4.56	4.56
2-hr oxic (pH 7.69)	0.05	0.04	0.96	0.47	1.71	1.07	3.66	1.52	6.38	6.33
2-hr oxic (pH 8.34)	0.21	0.23	1.51	0.34	2.05	0.54	5.32	2.13	9.09	8.88
2-hr oxic (pH 10.3)	39.2	0.21	-	-	0.02	0.47	1.30	0.65	-	-
1 week anoxic (pH=5.97)	2.08	3.60	0.00	3.61	0.98	0.32	0.76	0.56	3.83	1.74
2 week anoxic (pH=5.91)	0.07	0.07	0.28	0.19	1.56	0.45	2.84	3.59	4.75	4.68
3 weeks anoxic (pH=5.98)	0.00	0.01	0.95	0.96	4.02	1.13	0.00	0.76	4.98	4.97
3 weeks oxic (pH 6.28)	0.78	0.26	0.00	0.28	1.53	0.15	4.45	0.59	6.76	5.98
Fe (mmole/kg soil):	<3 kDa	error	<3 kDa-35 nm	error	35-260 nm	error	260-415 nm	error	sum	sum colloids
2-hr oxic (pH 4.08)	0.64	0.01	0.15	0.06	0.33	0.11	1.64	0.10	2.76	2.12
2-hr oxic (pH 5.13)	0.01	0.01	0.14	0.07	0.69	0.12	0.81	0.10	1.64	1.63
2-hr oxic (pH 6.18)	0.00	0.00	0.07	0.04	0.52	0.04	1.41	0.04	2.00	2.00
2-hr oxic (pH 6.78)	0.00	0.01	0.02	0.01	0.55	0.29	0.89	0.29	1.46	1.46
2-hr oxic (pH 7.69)	0.00	0.00	0.12	0.17	0.61	0.33	1.20	0.28	1.93	1.93
2-hr oxic (pH 8.34)	0.00	0.00	0.02	0.01	0.65	0.20	1.52	0.20	2.20	2.20
2-hr oxic (pH 10.3)	0.25	0.00	-	-	0.26	0.09	0.48	0.09	-	-
1 week anoxic (pH=5.97)	0.00	0.00	0.24	0.03	0.27	0.06	0.22	0.05	0.73	0.73
2 week anoxic (pH=5.91)	0.11	0.02	0.13	0.04	0.45	0.12	0.39	0.12	1.07	0.96
3 weeks anoxic (pH=5.98)	0.43	0.18	0.85	0.25	1.62	0.27	0.00	0.21	2.90	2.48
3 weeks oxic (pH 6.28)	0.15	0.02	0.00	0.05	0.52	0.05	1.42	0.05	2.09	1.94
Si (mmole/kg soil):	<3 kDa	error	<3 kDa-35 nm	error	35-260 nm	error	260-415 nm	error	sum	sum colloids
2-hr oxic (pH 4.08)	7.22	0.22	0.52	0.27	0.24	0.23	3.79	0.45	11.77	4.55
2-hr oxic (pH 5.13)	4.81	0.18	0.06	0.37	1.44	0.35	1.77	0.32	8.07	3.26
2-hr oxic (pH 6.18)	3.74	0.17	0.00	1.79	1.07	1.80	3.02	0.33	7.83	4.09
2-hr oxic (pH 6.78)	3.48	0.16	0.00	0.23	1.36	0.77	1.94	0.79	6.78	3.30
2-hr oxic (pH 7.69)	2.61	0.16	0.23	0.33	1.30	0.58	2.64	0.56	6.79	4.18
2-hr oxic (pH 8.34)	2.60	0.11	0.00	0.14	1.34	0.49	3.55	0.55	7.49	4.89
2-hr oxic (pH 10.3)	9.33	0.11	-	-	0.68	0.50	0.96	0.63	-	-
1 week anoxic (pH=5.97)	10.80	0.71	1.13	1.01	0.27	1.00	0.55	0.82	12.75	1.95
2 week anoxic (pH=5.91)	13.87	0.13	0.00	0.66	1.10	0.91	0.96	0.82	15.93	2.06
3 weeks anoxic (pH=5.98)	15.19	0.32	0.00	0.71	3.78	0.93	0.00	0.94	18.97	3.78
3 weeks oxic (pH 6.28)	15.71	1.16	0.00	1.20	0.73	0.35	3.46	0.63	19.90	4.19
Ti (mmole/kg soil):	<3 kDa	error	<3 kDa-35 nm	error	35-260 nm	error	260-415 nm	error	sum	sum colloids
2-hr oxic (pH 4.08)	0.13	0.00	0.04	0.01	0.07	0.02	0.35	0.02	0.58	0.45
2-hr oxic (pH 5.13)	0.06	0.00	0.03	0.01	0.14	0.02	0.17	0.02	0.40	0.35
2-hr oxic (pH 6.18)	0.00	0.00	0.03	0.02	0.11	0.02	0.30	0.01	0.43	0.43
2-hr oxic (pH 6.78)	0.00	0.00	0.00	0.00	0.11	0.06	0.18	0.06	0.29	0.29
2-hr oxic (pH 7.69)	0.00	0.00	0.03	0.04	0.13	0.07	0.25	0.06	0.41	0.41
2-hr oxic (pH 8.34)	0.00	0.00	0.02	0.00	0.13	0.04	0.31	0.04	0.46	0.46
2-hr oxic (pH 10.3)	0.03	0.00	-	-	0.05	0.02	0.08	0.02	-	-
1 week anoxic (pH=5.97)	0.00	0.00	0.06	0.01	0.06	0.02	0.04	0.02	0.16	0.16
2 week anoxic (pH=5.91)	0.01	0.01	0.02	0.02	0.10	0.02	0.08	0.01	0.20	0.19
3 weeks anoxic (pH=5.98)	0.00	0.00	0.00	0.01	0.33	0.03	0.00	0.03	0.34	0.34
3 weeks oxic (pH 6.28)	0.00	0.00	0.00	0.01	0.14	0.01	0.30	0.01	0.44	0.44

1) mmol element/kg soil

Table D-8: molar ratios of elements from colloidal dispersion experiments[1]

Al/Si ratio:	35-260 nm	error	260-415 nm	error
2-hr oxic (pH 4.08)			1.50	0.20
2-hr oxic (pH 5.13)	1.49	0.44	1.59	0.52
2-hr oxic (pH 6.18)			1.35	0.20
2-hr oxic (pH 6.78)			1.37	0.72
2-hr oxic (pH 7.69)			1.38	0.65
2-hr oxic (pH 8.34)	1.53	0.69	1.50	0.64
2-hr oxic (pH 10.3)			1.36	1.12
1 week anoxic (pH=5.97)				
2 week anoxic (pH=5.91)				
3 weeks anoxic (pH=5.98)	1.06	0.40		
3 weeks oxic (pH 6.28)	2.08	1.00	1.29	0.29
Fe/Si ratio:	35-260 nm	error	260-415 nm	error
2-hr oxic (pH 4.08)			0.43	0.06
2-hr oxic (pH 5.13)	0.48	0.14	0.46	0.10
2-hr oxic (pH 6.18)			0.47	0.05
2-hr oxic (pH 6.78)			0.46	0.24
2-hr oxic (pH 7.69)			0.45	0.14
2-hr oxic (pH 8.34)	0.48	0.23	0.43	0.09
2-hr oxic (pH 10.3)			0.50	0.34
1 week anoxic (pH=5.97)				
2 week anoxic (pH=5.91)				
3 weeks anoxic (pH=5.98)	0.43	0.13		
3 weeks oxic (pH 6.28)	0.71	0.34	0.41	0.08
Fe/Al ratio:	35-260 nm	error	260-415 nm	error
2-hr oxic (pH 4.08)	0.27	0.12	0.29	0.03
2-hr oxic (pH 5.13)	0.32	0.08	0.29	0.09
2-hr oxic (pH 6.18)	0.28	0.06	0.34	0.04
2-hr oxic (pH 6.78)			0.33	0.15
2-hr oxic (pH 7.69)			0.33	0.16
2-hr oxic (pH 8.34)	0.32	0.13	0.29	0.12
2-hr oxic (pH 10.3)			0.37	0.20
1 week anoxic (pH=5.97)	0.27	0.11		
2 week anoxic (pH=5.91)	0.29	0.11		
3 weeks anoxic (pH=5.98)	0.40	0.13		
3 weeks oxic (pH 6.28)	0.34	0.05	0.32	0.04

1) Reported only when error < 52% of value with exception of 2-hr oxic (pH 10.3)

Table D-9: Pearson correlation coeffiecients for elements dispersed in the 260-414 nm fraction under oxic and anoxic conditions[1]

	Al	Si	Fe	Ti
Al	-	0.933	0.907	0.910
Si	0.933	-	0.995	0.992
Fe	0.907	0.995	-	0.997
Ti	0.910	0.992	0.997	-

1) $p<0.001$ for all correlations

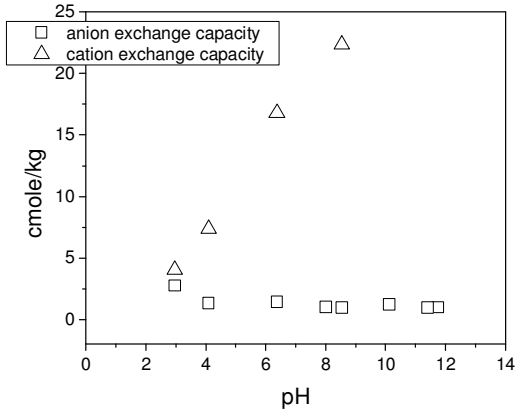

Figure D-1. Anion and cation exchange capacity for a regolith sample (38-47 cm). The zero point of charge can be determined from the intersection of the two curves.

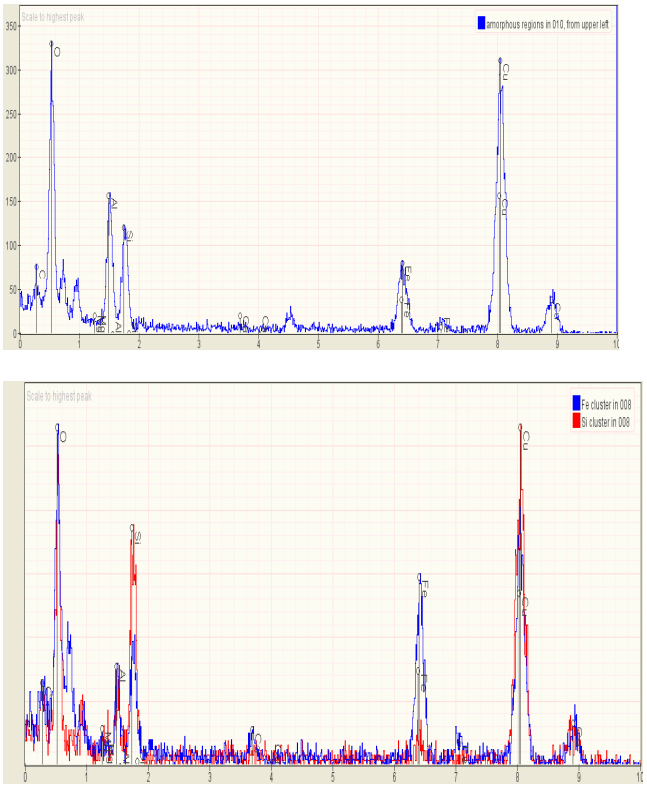

Figure D-2. EDS analysis for TEM images from Figures 3B (above) and 3C (below). Below: The darker Fe-rich region is in blue, while the lighter regions look like the spectrum in red.

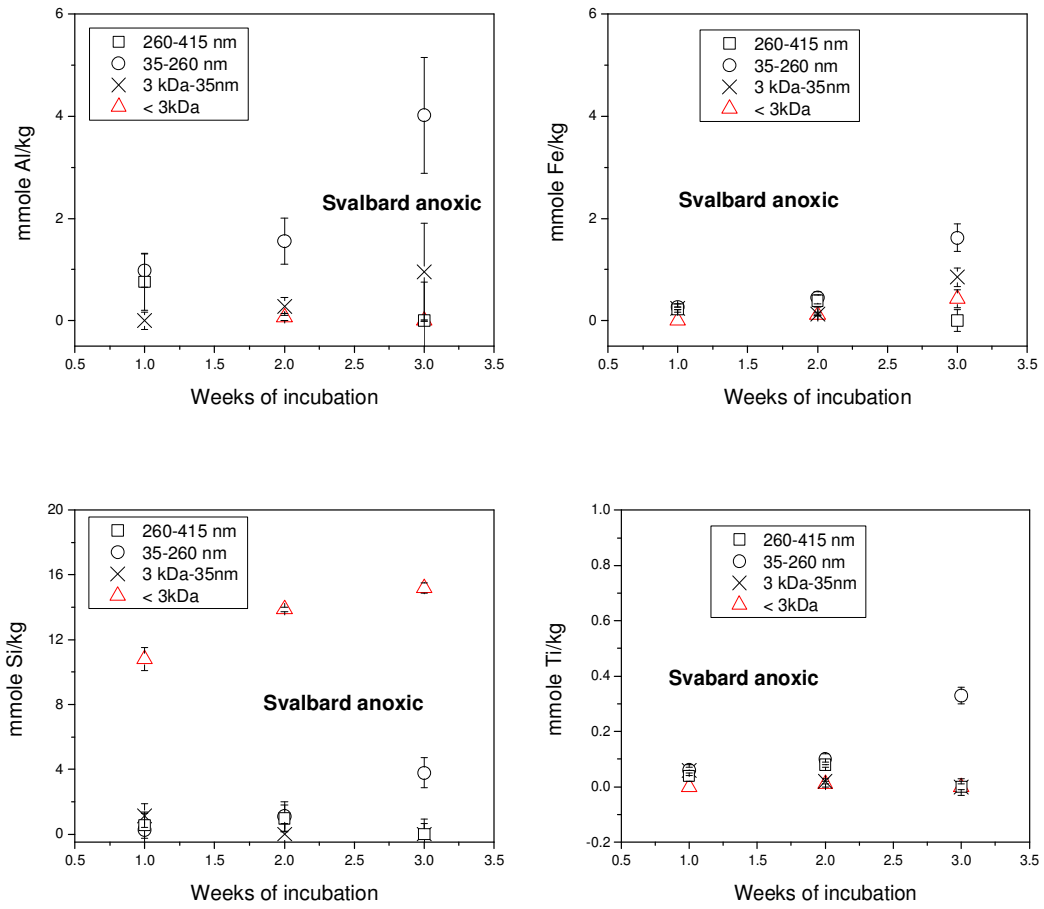

Figure D-3. Changes in size distribution over time in the anoxic particle experiment performed at pH 6. Error bars represent 1 standard deviation variation for triplicate.

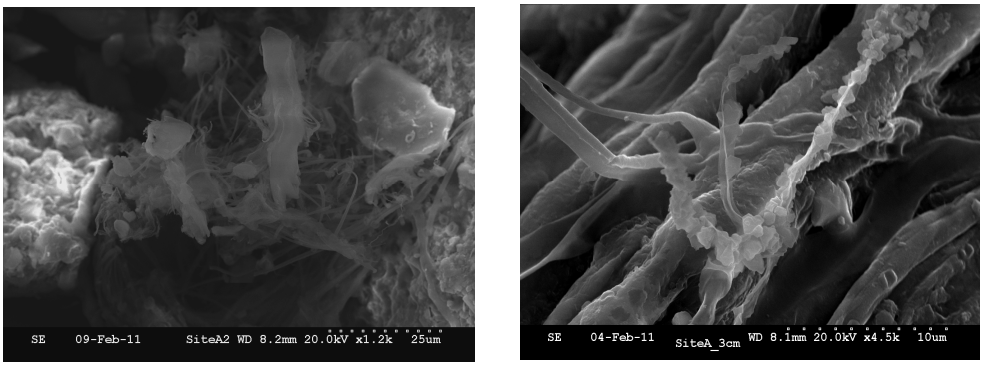

Figure D-4. Secondary electron images of regolith from the upper 3 cm of Site A (Figure 1) taken with the ESED detector on the Hitachi S-3500N variable pressure scanning electron microscope. Fungal Hyphae (left) and what appear to be oxalate crystals (right) are abundant.

Appendix E: Supplemental Material for Chapter 4

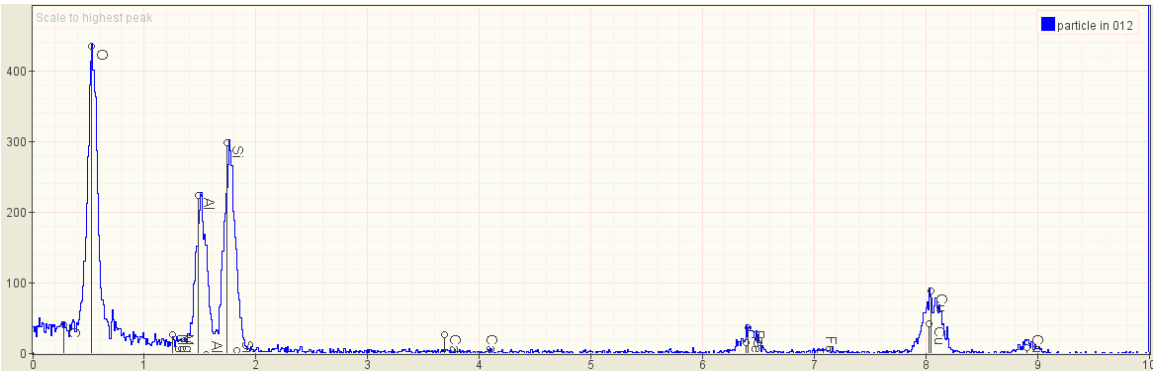

Figure E-1. TEM/EDS analysis of portion of polycrystalline particle in Figure 5b free from interference associated with underlying grid. EDS spectra of Figures 5c and 5d showed similar chemistry despite their amorphous character.

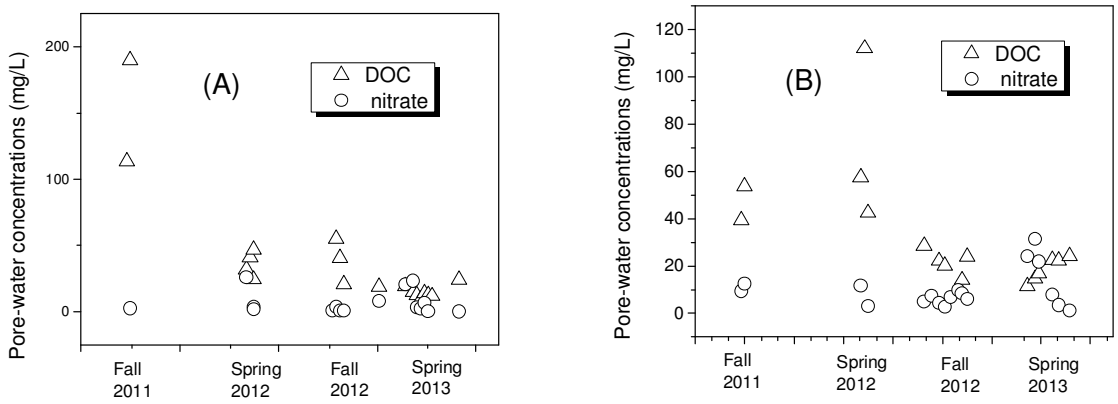

Figure E-2. Pore-water concentrations of DOC and nitrate with season at A) the 16-cm depth and B) the 63-cm depth.

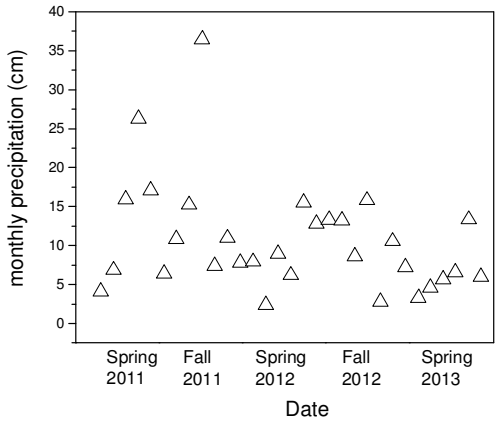

Figure E-3. Monthly precipitation near diabase site over time from a local weather station in Mechanicsburg, PA. Data obtained from the NOAA website (http://www.ncdc.noaa.gov/cdo-web/).

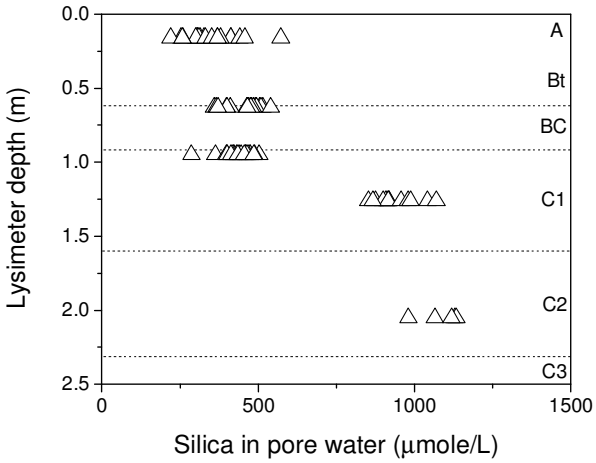

Figure E-4. The solute weathering gradient (b_p) for silica with depth in the diabase pore water. $b_p=\Delta z/\Delta c$=1,640 m L mol^{-1}.

Table E-1: Pore-water chemistry data[1]

Date	sampling depth (cm)	pH	DOC (mg/L)	Al (mg/L)	Ca (mg/L)	Fe (mg/L)	K (mg/L)	Mg (mg/L)	Mn (mg/L)	Na (mg/L)	Si (mg/L)	nitrate (mg/L)	sulfate (mg/L)	chloride (mg/L)
Oct 23, 2011	16	5.88	39	0.10	10.9	0.05	2.5	2.2	0.00	0.5	9.2	9.4	3.6	7.2
Oct 23, 2011	63	6.08	114	0.36	6.5	0.55	22.4	3.5	0.44	7.9	13.5	-	16.9	3.0
Oct 23, 2011	95	6.00	11	0.00	11.5	0.00	1.7	2.4	0.00	1.9	14.1	4.2	5.8	5.1
Oct 23, 2011	126	5.84	24	0.00	8.2	0.00	0.2	5.1	0.01	3.8	25.6	4.6	6.5	3.8
Oct 29, 2011	16	6.22	54	0.42	18.1	0.15	16.4	3.4	0.34	8.3	8.5	12.6	4.2	3.3
Oct 29, 2011	63		190	0.29	7.0	0.55	28.4	3.4	0.24	11.2	13.2	2.6	3.5	4.1
Oct 29, 2011	95	5.48	63	0.00	11.2	0.00	1.6	2.3	0.00	1.1	13.3	12.7	5.8	7.9
May 31, 2012	16	6.39	57	0.06	16.5	0.02	3.0	3.6	0.01	1.2	11.6	11.8	3.2	3.4
May 31, 2012	63	6.13	32	0.12	8.9	0.13	8.8	5.2	0.02	8.7	13.0	26.1	5.8	6.5
May 31, 2012	95	5.78	26	0.01	12.7	0.00	1.8	2.8	0.00	1.2	12.9	6.8	4.9	2.3
May 31, 2012	126	5.79	34	0.00	8.7	0.00	0.3	5.4	0.00	3.4	24.0	7.3	10.3	3.0
June 7, 2012	16	6.58	112	0.06	17.1	0.02	2.5	3.6	0.00	0.9	11.6	-	11.2	11.1
June 7, 2012	63	6.24	41	0.13	9.3	0.20	8.5	5.5	0.02	8.7	13.8	-	23.8	19.7
June 7, 2012	95	5.88	26	0.01	13.3	0.00	1.8	2.9	0.00	1.2	12.9	-	4.8	3.5
June 14, 2012	16	6.33	43	0.05	14.9	0.02	2.6	3.2	0.00	0.8	10.4	3.1	2.9	3.8
June 14, 2012	63	6.02	47	0.15	7.2	0.11	7.8	4.2	0.13	6.4	11.6	3.7	5.5	6.9
June 14, 2012	95	5.89	-	0.01	11.7	0.00	1.9	2.3	0.00	1.2	12.3	3.8	4.2	5.2
June 14, 2012	126	5.78	34	0.00	7.6	0.00	0.3	4.8	0.00	3.5	24.6	4.5	6.7	5.8
Sept. 25, 2012	16	-	29	0.09	13.7	0.05	1.8	2.9	0.00	1.4	12.4	5.1	9.3	6.3
Oct. 9, 2012	16	-	-	0.07	13.0	0.03	1.9	2.7	0.00	1.0	12.9	7.5	8.8	4.1
Oct. 23, 2012	16	6.31	22	0.06	11.0	0.02	2.5	2.3	0.00	0.7	8.6	4.4	6.9	3.6
Nov. 3, 2012	16	6.81	20	0.05	11.3	0.02	1.9	2.5	0.00	0.6	8.6	2.8	5.5	2.3
Nov. 3, 2012	63	-	-	1.09	19.1	1.23	9.1	8.0	0.00	5.7	14.2	-	-	-
Nov. 3, 2012	95	-	-	0.05	12.4	0.03	1.8	2.5	0.00	1.2	13.3	0.5	8.0	2.6
Nov. 6, 2012	63	-	-	0.41	9.9	0.52	6.7	4.5	0.00	4.1	14.4	0.9	10.1	2.8
Nov. 6, 2012	95	6.77	11	0.03	8.8	0.01	1.4	1.8	0.00	1.2	12.5	0.1	8.0	2.0
Nov. 13, 2012	16	-		0.05	10.1	0.03	1.6	2.1	0.00	0.5	8.8	7.0	5.3	1.9
Nov. 13, 2012	63	6.37	55	0.15	5.7	0.10	5.9	2.7	0.00	2.2	10.1	3.7	8.6	2.7
Nov. 13, 2012	95	6.19	8	-	-	-	-	-	-	-	-	0.0	7.9	1.8
Nov. 20, 2012	16	-	-	0.06	10.7	0.02	1.5	2.3	0.00	0.5	8.7	-	-	-
Nov. 20, 2012	63	6.68	41	0.28	7.0	0.24	7.0	3.5	0.00	3.0	13.8	0.8	12.0	2.7
Nov. 20, 2012	95	6.39	7	0.01	8.8	0.00	1.2	1.9	0.00	0.9	11.9	0.1	8.5	2.0
Nov. 27, 2012	16	-	-	0.04	9.3	0.02	1.4	2.1	0.00	0.5	8.4	9.9	5.1	1.9
Nov. 27, 2012	63	-	21	0.11	5.4	0.09	4.3	3.1	0.00	2.3	14.3	0.9	12.8	2.5
Nov. 27, 2012	95	6.85	6	0.01	8.6	0.00	1.1	1.8	-	0.9	12.1	0.2	8.3	1.4
Dec. 4, 2012	16	6.58	14	0.04	9.7	0.02	1.9	2.2	0.00	0.4	7.1	8.5	5.4	1.9
Dec. 4, 2012	95	6.23	-	0.00	9.6	0.00	1.2	2.2	0.00	1.1	13.1	0.4	8.1	2.0
Dec. 14, 2012	16	6.83	24	0.06	11.5	0.03	1.8	2.7	0.00	0.5	9.3	6.1	5.6	2.0
Dec. 14, 2012	63	6.42	24	0.23	7.4	0.13	6.7	3.6	0.00	4.2	13.9	2.0	11.3	2.8
Dec. 14, 2012	95	6.37	9	0.00	10.2	0.00	1.1	2.2	0.00	1.2	13.0	0.3	7.5	2.4
Dec. 14, 2012	126	6.00	4	0.01	9.7	0.00	0.6	5.9	0.00	4.1	29.3	2.2	13.5	3.7
Jan. 24, 2013	95	6.65	17	0.23	6.3	0.12	3.9	3.6	0.01	2.5	11.8	0.8	4.6	1.0
Jan. 31, 2013	63	6.51	19	0.01	8.2	0.00	0.9	1.8	0.00	0.8	10.3	8.1	11.0	2.2
Jan. 31, 2013	95	6.44	11	0.01	7.0	0.00	0.9	1.5	0.00	0.9	8.0	1.3	8.5	1.3
Jan. 31, 2013	126	6.29	13	0.00	9.1	0.00	0.2	5.9	0.00	3.4	25.8	2.1	16.8	1.6
Mar. 21, 2013	63	6.24	19	0.17	6.1	0.09	5.7	3.5	0.01	2.3	11.2	20.7	10.9	1.8
Mar. 21, 2013	95	6.26	7	0.00	9.1	0.00	1.1	2.1	0.00	0.9	11.7	2.9	5.7	0.9
Mar. 21, 2013	126	6.04	4	0.00	8.8	0.01	0.3	5.7	0.00	3.4	25.5	1.1	11.3	1.2
April 4, 2013	16	6.48	12	0.06	7.6	0.02	1.5	1.8	0.00	0.5	6.2	24.1	3.4	1.2
April 4, 2013	63	6.26	15	0.13	5.0	0.08	3.0	2.8	0.00	2.1	11.2	23.4	3.9	1.3
April 4, 2013	95	6.34	0	0.00	7.7	0.00	0.9	1.8	0.00	0.8	10.2	2.9	5.6	1.2
April 4, 2013	126	6.07	0	0.00	8.2	0.00	0.2	5.4	0.00	3.2	25.3	1.8	11.5	1.1
April 11, 2013	63	6.46	12	0.08	4.7	0.05	2.2	2.8	0.00	2.1	13.6	3.5	12.6	1.7
April 11, 2013	95	6.37	0	0.03	8.8	0.01	1.1	2.0	0.00	1.1	11.2	1.2	5.3	0.9
April 11, 2013	126	6.01	0	0.05	9.5	0.01	0.3	5.9	0.00	3.6	25.8	1.6	11.9	1.2

1) All analytical methods described in text

Table E-1: Pore-water chemistry data, continued[1]

Date	sampling depth (cm)	pH	DOC (mg/L)	Al (mg/L)	Ca (mg/L)	Fe (mg/L)	K (mg/L)	Mg (mg/L)	Mn (mg/L)	Na (mg/L)	Si (mg/L)	nitrate (mg/L)	sulfate (mg/L)	chloride (mg/L)
April 18, 2013	16	6.24	15	0.07	12.6	0.02	2.3	2.8	0.00	0.6	7.3	31.5	4.4	1.1
April 18, 2013	63	5.93	9	0.08	5.2	0.04	2.5	2.9	0.00	1.9	13.4	2.4	12.5	1.5
April 18, 2013	95	6.09	8	0.01	9.2	0.00	1.1	2.1	0.00	0.9	11.2	1.1	6.1	1.2
April 18, 2013	126	5.90	5	0.00	9.5	0.00	0.1	5.9	0.00	3.5	25.7	1.1	12.5	1.3
April 25, 2013	16	6.61	17	0.13	12.9	0.03	2.8	2.9	0.00	0.7	7.2	21.9	3.9	1.0
April 25, 2013	63	6.58	14	0.12	5.4	0.05	2.9	2.9	0.00	2.1	10.4	6.9	8.3	1.6
April 25, 2013	95	6.43	8	0.01	9.6	0.00	1.1	2.2	0.00	1.0	11.3	2.2	5.5	1.4
April 25, 2013	126	6.19	6	0.00	8.6	0.00	0.1	5.4	0.00	3.4	24.3	1.7	12.5	1.4
May 2, 2013	63	-	13	0.10	5.6	0.05	2.2	3.4	0.00	2.1	15.2	0.3	14.0	2.0
May 2, 2013	95	6.07	4	0.01	10.3	0.00	1.2	2.3	0.00	1.0	11.6	0.2	5.6	1.3
May 2, 2013	126	6.31	3	0.01	9.9	0.00	0.2	6.1	0.00	3.7	26.9	0.9	12.8	1.5
May 9, 2013	63	-	12	-	-	-	-	-	-	-	-	-	-	-
May 9, 2013	95	6.04	5	0.01	11.3	0.00	1.2	2.5	0.00	1.1	12.2	0.0	5.4	1.2
May 9, 2013	126	5.79	3	0.00	9.9	0.00	0.2	6.3	0.00	3.9	27.5	0.6	13.9	1.4
May 20, 2013	16	6.01	23	0.11	16.0	0.03	2.5	3.6	0.01	0.8	9.9	7.9	5.6	1.3
May 20, 2013	95	5.94	4	0.01	11.4	0.00	1.3	2.6	0.00	1.1	12.8	0.2	5.6	1.5
May 20, 2013	126	5.83	3	0.00	9.4	0.00	0.1	5.9	0.00	3.9	27.7	0.6	14.4	1.5
May 20, 2013	205	5.80	4	0.00	9.4	0.00	0.1	5.7	0.01	3.1	29.9	2.5	10.0	1.2
June 1, 2013	16	5.96	22	0.09	13.4	0.02	2.7	3.1	0.00	1.4	10.7	3.5	3.8	0.6
June 1, 2013	95	5.83	5	0.01	12.2	0.00	1.6	2.7	0.00	1.7	13.7	0.2	5.7	1.4
June 1, 2013	126	5.73	4	0.00	9.8	0.00	0.2	6.3	0.00	4.1	30.1	0.5	15.3	1.5
June 1, 2013	205	5.76	4	0.00	9.6	0.00	0.2	5.7	0.00	3.2	31.7	2.0	10.9	1.4
June 8, 2013	205	5.77	6	0.00	9.9	0.00	0.3	5.7	0.00	3.3	31.9	2.2	12.0	1.9
June 21, 2013	16	5.90	24	0.13	12.0	0.04	2.7	2.6	0.01	0.9	10.4	1.2	2.8	1.5
June 21, 2013	95	5.34	5	0.01	11.2	0.00	1.4	2.5	0.00	1.2	13.6	0.2	5.1	0.9
June 21, 2013	205	5.18	3	0.00	8.9	0.00	0.1	5.2	0.00	3.0	27.5	1.6	11.2	1.4
June 28, 2013	16	5.97	-	0.26	7.0	0.13	2.6	3.8	0.00	3.5	16.1	-	-	-
June 28, 2013	63	-	24	0.01	9.5	0.00	1.5	2.1	0.00	1.3	13.1	0.2	9.3	1.1
June 28, 2013	95	5.76	8	-	-	-	-	-	-	-	-	0.5	4.8	0.8
June 28, 2013	205	-	0	0.00	9.5	0.00	0.1	5.5	0.00	3.3	31.4	-	-	-

1) All analytical methods described in text

Table E-2:

depth in cm	Si (mole/kg)	Zr (ppm)	Si adjusted for Zr (mole/kg)
7	8.7	252	1.6
23	9.4	242	1.8
36	9.2	212	2.0
53	8.7	171	2.4
71	7.8	94	3.9
95	8.0	73	5.1
115	7.8	78	4.7
135	8.1	66	5.7
155	8.1	62	6.2
190	8.1	61	6.2
200	8.0	62	6.1
220.5	8.2	58	6.7
bedrock	8.4	47	8.4

$b_s = \Delta depth / \Delta adjusted\ Si = 0.43\ m*kg*mol^{-1}$

Tiffany Yesavage (tay120@psu.edu)

EDUCATION

Undergraduate:
University of Colorado, Boulder
B.A., Double Major in Biochemistry and Geology
GPA: 3.74

Graduate:
Colorado School of Mines
M.S., Geochemistry
GPA: 3.93

Graduate:
Penn State University
Ph.D., Geosciences and Biogeochemistry
Defense date: November 22, 2013
GPA: 3.94

HONORS

Undergraduate:
Golden Key International Honour Society (Fall 1999)
Estwing Award for top junior in geology (Spring 1999)
Phi Beta Kappa (inducted Spring 2000)
Vice President of the Geology Club (2001-2002)
Rocky Mountain Association of Geologists (RMAG) Award (Spring 2002)

Graduate:
Edna Bailey Sussman Environmental Fellowship Award (Summer 2003)
Honorable Mention, NSF Graduate Fellowship Award (2004)
I passed my Ph.D. comprehensive examination in Applied Chemistry (January 2006)
O.C. Hui Fellowship (September 2006-December 2007)
AWG Outstanding Woman Student Award (April 13, 2007)
Anne C. Wilson Graduate Research Award (September 2008)
Tait Scholarship for Microbial Biogeochemistry (Spring 2010)
P.D. Krynine Memorial Fund Research Grant (Fall 2011)

Publications

Yesavage, T.A., Fantle, M.S., Vervoort, J., Liermann, L.J., Jin, L., Mathur, R., and Brantley, S.L., 2012, Fe cycling in the Shale Hills Critical Zone Observatory, Pennsylvania: An analysis of biogeochemical weathering and Fe isotope fractionation. *Geochimica et Cosmochimica Acta*, 99: 18-38.

Yesavage, T.A., Thompson, A., Hausrath, E.M., Liermann, L.J., and Brantley, S.L., Basalt weathering in a Mars Analog Site. Submitted to *Icarus* on February 17, 2014.

Yesavage, T.A., and Humphrey, J.D., Sources and Transformations of Nitrate in the Turkey Creek Basin of Colorado. Submitted to *Environmental Science and Technology* on February 11, 2014.

Yesavage, T.A., Stitchcomb, G., Sak, P., Fantle, M., Kasznel, A., and Brantley, S.L.,
Chemical Weathering and Fe Isotope Fractionation in Regolith Overlying a Pennsylvania Diabase. Hoping to submit to *Chemical Geology* in March of 2014.